

INAUGURAL - DISSERTATION
zur
Erlangung der Doktorwürde
der
Naturwissenschaftlich-Mathematischen
Gesamtfakultät
der
Ruprecht-Karls-Universität
Heidelberg

vorgelegt von
Fabio Metlica
aus Vereeniging (Südafrika)
Tag der mündlichen Prüfung: 15. Juli 1998

**Produktion von Neutronen in
Vorwärtsrichtung durch $e - p$
Kollision bei HERA**

Gutachter:

Prof. Dr. Bogdan Povh

Prof. Dr. Hans-Wolfgang Siebert

Zusammenfassung

Am HERA-Experiment H1 werden in der tiefinelastischen Elektron-Proton-Streuung bei einer Schwerpunktsenergie von 300 GeV hochenergetische Neutronen beobachtet, welche unter kleinem Winkel ($\lesssim 1$ mrad) in Richtung des Protonenstrahls produziert werden. Ereignisse mit Neutronen der Energie $E > 100$ GeV bilden einen konstanten Anteil an allen tiefinelastischen Streueignissen, unabhängig von den kinematischen Variablen x_{BJ} und Q^2 im Bereich $2 < Q^2 < 100$ GeV² und $3.7 \cdot 10^{-5} < x_{BJ} < 5.5 \cdot 10^{-2}$. Wird das Monte-Carlo-Programm Lepto, welches das Konzept der weichen Farbwechselwirkung benutzt, zur Akzeptanzkorrektur verwendet, so haben $38^{+6}_{-4}\%$ der ep -Streueignisse ein Neutron mit $E > 100$ GeV. Für $E > 400$ GeV beträgt der Anteil an Neutronen $7.9^{+2.0}_{-1.5}\%$ unabhängig von der Akzeptanzkorrektur, die mit dem Lepto oder Pompyt (Ein Pion-Austausch) Monte Carlo ermittelt wird. Der totale semi-inklusive Wirkungsquerschnitt für die Reaktion $ep \rightarrow e'nX$ im oben angegebenen kinematischen Bereich wurde für $E > 100$ GeV und $E > 400$ GeV bestimmt. Der geringe Anteil von Ereignissen mit einem Neutron und gleichzeitig einer Rapiditätslücke zeigt, daß diffraktive Neutronenproduktion nicht den dominanten Prozeß darstellt. Für Neutronenenergien $E > 400$ GeV stimmen die gemessenen Energie, $|t|$, und p_T Verteilungen mit den Vorhersagen des Pion-Austausch-Modells (Pompyt) und dem auf der weichen Farbwechselwirkung basierenden Monte-Carlo-Modell (Lepto) überein.

Abstract

Production of Forward Neutrons in e – p Collisions at HERA

High energy neutron events produced at small angles ($\lesssim 1$ mrad) with respect to the proton beam direction have been observed in neutral current deep inelastic ep scattering at the center of mass energy of 300 GeV, by the H1 experiment at HERA. These events represent a fixed fraction of the total neutral current deep inelastic sample for neutron energies $E > 100$ GeV independent of the kinematical variables Q^2 and x_{BJ} in the range $2 < Q^2 < 100$ GeV² and $3.7 \cdot 10^{-5} < x_{BJ} < 5.5 \cdot 10^{-2}$. If the Lepto Monte Carlo which incorporates soft colour interactions is used to correct for acceptance, $38^{+6}_{-4}\%$ of the ep collisions have a neutron with $E > 100$ GeV, while for $E > 400$ GeV and $|t| < 0.5$ GeV² the percentage is $7.9^{+2.0}_{-1.5}\%$, independent of the Monte Carlo used to correct for the acceptance (Lepto or the one pion exchange Monte Carlo Pompyt). The total semi-inclusive cross section $ep \rightarrow e'nX$ has been measured in the above kinematical range for $E > 100$ GeV and $E > 400$ GeV. The small fraction of neutrons with a large rapidity gap indicates that diffractive neutron production is not the dominant mechanism. The observed energy, $|t|$, and p_T distributions are in general agreement with both the one pion exchange (Pompyt) and soft colour interaction (Lepto) Monte Carlo models for neutron energies $E > 400$ GeV.

Contents

CONTENTS	i
INTRODUCTION	v
1 THEORETICAL OVERVIEW	1
1.1 Deep Inelastic Scattering at HERA	2
1.2 DIS Kinematical Variables and Cross Section	3
1.3 Leading Neutrons	5
1.3.1 The Pion Exchange Model	5
1.3.2 Target Fragmentation: Soft Colour Interactions	8
2 THE H1 DETECTOR AT HERA	9
2.1 The HERA Storage Ring	9
2.2 The H1 Detector	12
2.2.1 Tracking Chambers	15
2.2.2 Calorimeters	17
2.2.3 Luminosity System	20
2.2.4 TOF-Detectors	22
2.2.5 Muon Detection	22
2.2.6 Very Forward Detectors	23
2.2.7 The H1 Trigger and Data Acquisition	24

3	THE FORWARD NEUTRON CALORIMETER- FNC	29
3.1	Brief Overview of Calorimetry	29
3.1.1	Electromagnetic Showers	31
3.1.2	Hadronic Showers	32
3.1.3	Energy Resolution	35
3.2	Modification	36
3.2.1	Lead-fiber matrix	38
3.2.2	Hodoscope	39
3.2.3	FNC layout	41
3.3	Test Beam Calibration	43
3.4	Installation	46
3.5	FNC Data Acquisition and Electronics	51
3.6	FNC Trigger	55
3.7	FNC Events	60
3.7.1	FNC Data Banks and Classification	60
3.7.2	FNC Variables	62
3.8	Hodoscope Efficiency	69
3.9	Monitoring System	75
3.10	Calibration	81
3.11	Energy Resolution and Linearity	84
3.11.1	Energy Resolution	84
3.11.2	Linearity	88
3.11.3	High Energy Tail	90
3.12	Position Resolution	96
3.13	Acceptance	99
4	PHYSICS RESULTS	103

4.1	Event Reconstruction and Selection	103
4.2	Properties of DIS Events with a Leading Neutron	109
4.2.1	Dependence on the Kinematical Variables	109
4.2.2	η_{max} Distribution	114
4.3	Leading Neutron Distributions	117
4.4	The Total $ep \rightarrow e'nX$ Cross Section	123
	CONCLUSIONS	125
A	Appendix: Energy Resolution	127
	Bibliography	129
	List of Figures	137
	List of Tables	143
	Acknowledgements	144

INTRODUCTION

In 1996 a new Forward Neutron Calorimeter (FNC) was installed in the H1 experiment at HERA, which started to collect data the same year, with the purpose of measuring the energy and angle of high energy leading neutrons (i.e. neutrons traveling very close to the proton beam direction) produced in the semi-inclusive reaction $ep \rightarrow e'nX$. The measurement of the leading neutron energy and angle by the FNC together with the measurement by H1 of the scattered electron and the hadronic final state, gives the possibility of studying the $ep \rightarrow e'nX$ process. This deep inelastic scattering process is of interest because one pion exchange is thought to be the dominant contribution at large z (ratio between outgoing neutron energy and incoming proton energy) at small momentum transfers $|t| < 0.5 \text{ GeV}^2$ (the four momentum transfer squared at the proton vertex). Since these neutrons are produced at small angles $\lesssim 1 \text{ mrad}$ with respect to the incident proton beam direction, the calorimeter was positioned in the tunnel at 107 m from the ep interaction point of the H1 experiment, where there is enough separation between the proton beam and the produced neutrons.

In the first chapter a theoretical introduction is given about deep inelastic scattering at HERA together with leading neutron production. The HERA collider and the H1 experiment are described in the second chapter. The third chapter gives a detailed description of the FNC; the modification of the spaghetti calorimeter (SPACAL) which was developed and built by the CERN/LAA project into the new FNC, the calibration, the installation, and the general characteristics and performance of the FNC are given. The last chapter reports on the properties of leading neutrons and displays the basic leading neutron distributions.

Chapter 1

THEORETICAL OVERVIEW

Scattering experiments have been used to probe the interactions and structure of matter, by sending a point-like probe particle into a target material and measuring its scattering angle and energy. Rutherford (1911) scattered α particles onto a gold metal foil to study the structure of the atom. The observation of large angle scatterings brought to the conclusion that the atom had a small but heavy positively charged nucleus. Later on in 1960's, the elastic scattering of electrons (~ 1 GeV) off protons demonstrated that a proton is not point-like but has a spatial extension of radius ~ 0.8 fm. The first deep inelastic scattering (DIS) experiments, so called because of the high beam energies with a high momentum transfer involved, took place in the late 1960's at SLAC¹, with the inelastic scattering of electrons (~ 20 GeV) on nucleons, revealing the existence of point-like constituents or *partons* in the nucleon confirming the partonic substructure of the proton (QPM-Quark Parton Model of Feynman 1972) and the *scaling* of the structure functions (Bjorken 1969). These experiments continued at CERN in the 1970's with neutrino and muon beams, further confirming the quark-parton model. The observation of scaling violations in the structure functions led Quantum Chromodynamics (QCD) to be established as the theory for strong interactions. With the recent HERA² electron³-proton storage ring, the proton can be studied using electron-proton deep inelastic scattering (*ep* DIS) with two orders of magnitude improved resolution. The semi-inclusive deep inelastic scattering off protons $ep \rightarrow e'nX$, also called leading neutron production, that can be studied at HERA, is of interest because pion exchange is believed to play a dominant role, opening the possibility for obtaining the pion structure function in a new kinematic region, up to now inaccessible. In this chapter a brief introduction to *ep* DIS at HERA will be given and then leading neutron production will be discussed.

¹Stanford Linear Accelerator Center.

²Hadron-Electron Ring Accelerator, see chapter 2.

³With the term "electrons" we refer to both electrons and positrons, since both particles can be used at HERA.

1.1 Deep Inelastic Scattering at HERA

Deep inelastic scattering (DIS)[1] is the scattering of a lepton from a nucleon at high particle energies, involving a high momentum transfer ($Q^2 \gtrsim 1 \text{ GeV}^2$)⁴. In ep DIS[2], the electron interacts with the proton by the exchange of a gauge boson, which normally breaks up the proton fragmenting it into various particles due to the high momentum transferred. The DIS events can be divided into two main classes (figure 1.1): neutral current events (NC) and charged current events (CC). For a NC event the exchanged boson is a photon (γ) or for higher Q^2 the Z^0 vector boson, giving an outgoing electron; while for a CC event the W^- (W^+) vector boson is exchanged, changing the electron (positron) into a neutrino (antineutrino). Only NC DIS processes, dominated by photon exchange will be considered⁵, since the studied leading neutrons originate from this process. According to the naive quark-parton model (QPM), which offers a qualitative picture, the scattering can be seen as an elastic scattering of the electron from a quark (antiquark) inside the proton. The incoming electron emits a gauge boson which strikes a quark. The struck quark then fragments into a jet of hadrons- *current jet*, while the other quarks remain practically unperturbed and move along the proton incident direction forming the *proton remnant jet*.

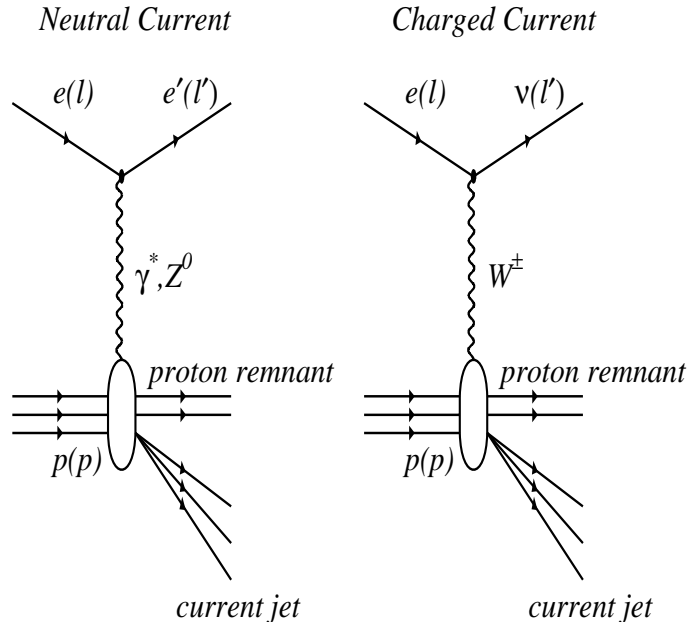


Figure 1.1: Feynman diagrams for NC and CC deep inelastic ep scattering.

⁴Interactions with low Q^2 ($Q^2 \ll 1 \text{ GeV}^2$) are termed photoproduction.

⁵ $Q^2 \ll M_{Z^0}^2$ is the range we are interested in.

1.2 DIS Kinematical Variables and Cross Section

The kinematics of inclusive ep scattering can be described fully at a given center of mass energy, \sqrt{s} , by using only two relativistic Lorentz invariants (inclusive process). The most commonly used variables are (x, Q^2) . These variables can be experimentally reconstructed utilizing various methods by combining the electron and hadronic system, angles and energies (see section 4.1). If l and l' are the initial and final four-momentum of the electron, p the initial proton four-momentum, p' the four-momentum of the hadronic final system (fig 1.2), the following relativistic invariants may be constructed:

$$s \equiv (p + l)^2; \quad (1.1)$$

$$Q^2 \equiv -q^2 \equiv -(l - l')^2 \approx 2EE'(1 - \cos \theta) \geq 0; \quad (1.2)$$

$$x \equiv \frac{Q^2}{2pq}; \quad 0 \leq x \leq 1; \quad (1.3)$$

$$y \equiv \frac{pq}{pl} \simeq \frac{Q^2}{xs}; \quad 0 \leq y \leq 1; \quad (1.4)$$

$$W^2 \equiv (p')^2 \equiv (p + q)^2 \simeq Q^2 \frac{(1-x)}{x}. \quad (1.5)$$

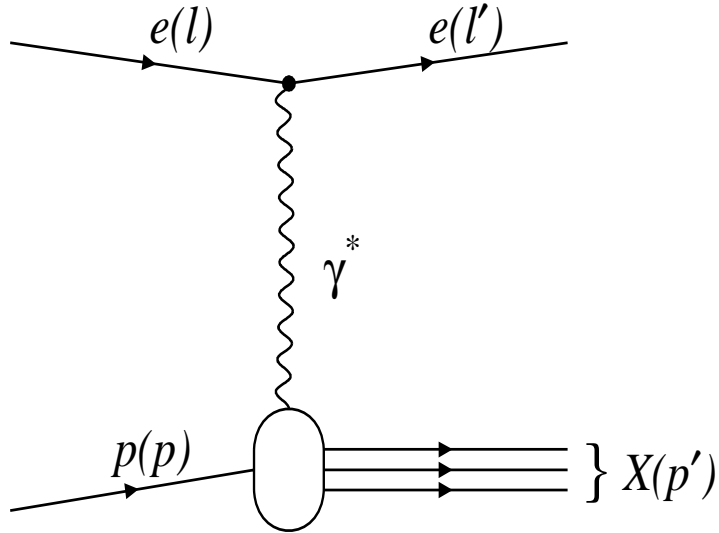


Figure 1.2: Feynman diagram for NC DIS.

The ep center of mass energy squared is s ; Q^2 is the four-momentum transfer squared at the lepton vertex, which gives the dimensions d of which an object can be resolved ($d \approx 1/Q$); x is the Bjorken scaling variable, which according to the quark-parton model, is the fraction of the proton's momentum carried by the struck quark in the proton (in the reference frame where the proton has a high momentum- infinite momentum frame); y is the inelasticity of the scattered electron, which is the fraction of energy transferred by the incoming electron to the proton in the proton's rest frame; W^2 is the invariant mass squared of the final state hadrons X .

The expression for the spin averaged neutral current differential cross-section for the $ep \rightarrow e'X$ process, in the one boson exchange approximation is:

$$\frac{d^2\sigma}{dx dQ^2} = \frac{4\pi\alpha^2}{xQ^4} [(1-y)F_2 + y^2 x F_1] = \frac{4\pi\alpha^2}{xQ^4} \left[(1-y) + \frac{y^2}{2} \frac{1}{1+R} \right] F_2 \quad (1.6)$$

where α is the electromagnetic coupling constant and $F_1(x, Q^2)$ and $F_2(x, Q^2)$ are two dimensionless independent structure functions⁶ of the two independent variables x and Q^2 , R is the ratio $\frac{F_L}{F_2 - F_L}$ with F_L the longitudinal structure function defined as $F_L := F_2 - 2xF_1$. In first approximation (QPM), the Callan-Gross relation, $2xF_1(x) = F_2(x)$, is satisfied, giving $F_L = 0$ and thus simplifying expression 1.6:

$$\frac{d^2\sigma}{dx dQ^2} = \frac{4\pi\alpha^2}{xQ^4} \left[(1-y + \frac{y^2}{2}) F_2 \right] \quad (1.7)$$

and F_2 can be written as:

$$F_2(x) = x \sum_i e_i^2 q_i(x) \quad (1.8)$$

where the sum is done over the different quark⁷ flavours in the proton, with e_i the quark charges and $q_i(x)$ the quark densities i.e. the number of quarks of flavour i having a momentum fraction of the proton in the interval $(x, x+dx)$. In the QCD improved QPM, quarks interact with each other by emitting or absorbing gluons; these gluons can give rise to quark-antiquark pairs ($g \rightarrow q\bar{q}$) or to gluon pairs ($g \rightarrow g\bar{g}$). The higher the Q^2 , the better these fluctuations may be resolved, showing a reduction of quarks at large x and an increase of quarks at low x , which gives rise to the F_2 structure function scaling violation i.e. F_2 log dependence on Q^2 .

⁶The F_3 structure function is omitted since Z^0 exchange is neglectable ($\sim 1\%$ correction at $Q^2 \approx 1000 \text{ GeV}^2$).

⁷With the term quark we include also the anti-quarks.

1.3 Leading Neutrons

A leading neutron, also called forward neutron, is a high energy neutron produced in ep scattering, which travels at small angles $\lesssim 1$ mrad with respect to the proton beam direction. The study of semi-inclusive leading neutron production $ep \rightarrow e'nX$, is of interest because the pion exchange mechanism for neutron production is thought to be the dominant one, at large z and small $|t|$ ($\ll 1$ GeV²) (see equations 1.9)[3]-[5]. Another possible leading neutron production mechanism is target fragmentation, i.e. hadronization of the proton remnant with the inclusion of soft colour interactions. These two models for leading neutron production will be compared to data, to possibly discriminate between them.

1.3.1 The Pion Exchange Model

Analogously to the pomeron exchange process occurring in diffraction (see section 1.3.2), pion exchange is believed to be a dominant mechanism for forward neutron production. By using the virtual pions present in the proton as a target in DIS, there is the possibility of measuring the pion structure function down to $x \sim 10^{-4}$, previously determined by πN Drell-Yan production in a limited kinematic region ($x > 0.1$)[3]-[11].

The kinematics of the $ep \rightarrow e'nX$ process (figure 1.3) is completely defined at a given center of mass energy \sqrt{s} , by taking four Lorentz invariants:

$$Q^2 \equiv -q^2 \equiv -(l - l')^2 \quad y \equiv \frac{pq}{pl} \simeq \frac{Q^2}{xs} \quad (1.9)$$

$$t \equiv (p - p')^2 \simeq \frac{-p_T^2}{z} - (1 - z)\left(\frac{M_n^2}{z} - M_p^2\right) \quad z \equiv 1 - 2k(p - p')/s \simeq E_n/E_p;$$

also some other additional kinematic variables are used to define the one-pion exchange process:

$$x \equiv \frac{Q^2}{2pq} \quad x_\pi \equiv (p - p')q/pq \simeq 1 - z \quad \beta \equiv x/x_\pi; \quad (1.10)$$

with Q^2, y, x defined previously for DIS; t is the four momentum transfer squared at the proton vertex, which can be seen as the invariant mass of the exchanged particle; z the neutron energy fraction i.e. the energy ratio between the leading neutron (E_n) and the incident proton (E_p); x_π can be seen as the momentum fraction carried by the pion in the proton; β the Bjorken scaling variable for the pion i.e. the momentum fraction of the struck quark in the pion; M_n, M_p are the neutron and proton mass respectively; and p_T^2 is the transverse momentum squared.

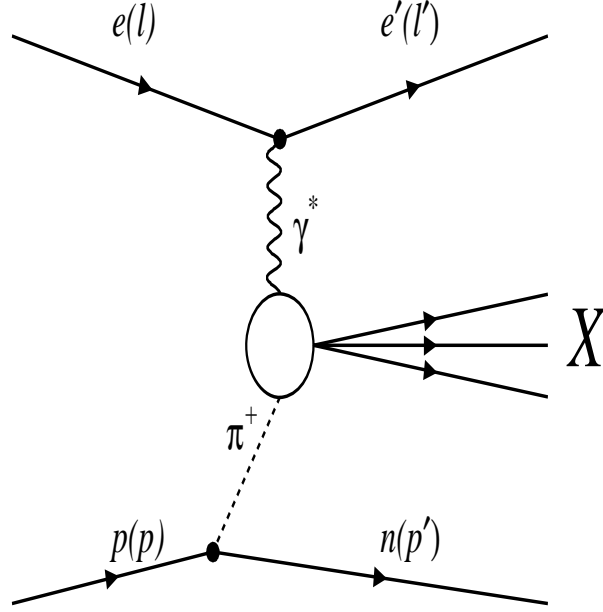


Figure 1.3: Feynman diagram for one pion exchange leading neutron production in DIS.

The DIS $ep \rightarrow e'X$ cross section (see equation 1.6) defines the proton structure function (R is put to zero for simplicity) $F_2^p(x, Q^2)$:

$$\frac{d^2\sigma(ep \rightarrow e'X)}{dx dQ^2} = K(x, Q^2) F_2^p(x, Q^2), \quad (1.11)$$

with $K(x, Q^2)$ the DIS kinematical factor introduced to simplify the equations,

$$K(x, Q^2) = \frac{4\pi\alpha^2}{Q^4 x} [1 - y + y^2/2]. \quad (1.12)$$

Analogously to the DIS cross section (equation 1.11) given above, the cross section for semi-inclusive neutron production $ep \rightarrow e'nX$ defines a "leading neutron structure function" $F_2^{LN}(x, Q^2, t, z)$ which is given as:

$$\frac{d^4\sigma(ep \rightarrow e'nX)}{dx dQ^2 dt dz} = K(x, Q^2) F_2^{LN}(x, Q^2, t, z). \quad (1.13)$$

According to the one-pion exchange model, the proton and pion vertexes are independent from each other i.e. factorization of the $ep \rightarrow e'nX$ cross section into a neutron flux factor and an $e\pi \rightarrow e'X$ cross section is assumed. This factorization hypothesis is supported by hadron-hadron scattering data[4], and can be written as:

$$F_2^{LN}(x, Q^2, t, z) = f_{n/p}(t, z) F_2^{e\pi}(\beta, Q^2), \quad (1.14)$$

- $f_{n/p}(t, z)$ - the neutron flux factor, which gives the flux of neutrons inside the proton with transverse momentum p_T ⁸ and fraction z of the proton's energy;
- $F_2^{\pi}(\beta, Q^2)$ - the pion structure function, function of β which is the Bjorken scaling variable for the pion, and of Q^2 .

So the semi-inclusive four differential cross section can be written as:

$$\frac{d^4\sigma(ep \rightarrow e'nX)}{dx dQ^2 dt dz} = \underbrace{f_{n/p}(t, z)}_{\text{flux factor}} \underbrace{K(x, Q^2) F_2^{\pi}(\beta, Q^2)}_{\pi \rightarrow e'X \text{ cross section}}. \quad (1.15)$$

The neutron flux factor $f_{n/p}(t, z)$ is a universal property of the proton, which is independent from the incident particle scattering on the proton, and can be written in the following form [5],[6]:

$$f_{n/p}(t, z) = \frac{2}{3} \frac{3g_{p\pi^0 p}^2}{16\pi^2} (1-z) \frac{-t}{(m_\pi^2 - t)^2} \exp\left\{\frac{t - m_\pi^2}{\Lambda^2(1-z)}\right\}, \quad (1.16)$$

with m_π the pion mass, $g_{p\pi^0 p}^2$ the coupling constant with $g_{p\pi^0 p}^2/4\pi = 13.6 \pm 0.8$ (from isospin relations $g_{p\pi^0 p}^2/g_{p\pi^+ p}^2=1/2$) and $\Lambda = 1.1 \pm 0.1 \text{ GeV}$. The values of $g_{p\pi^0 p}^2$ and Λ have been determined in previous experiments[9], [12].

The Monte Carlo program Pompyt[13] version 2.6 is used to simulate one pion exchange. It is expected to give a valid description of final state neutrons only for high energies ($z > 0.5$), because for low z other processes intervene substantially, which are not simulated by Pompyt. Pompyt simulates diffractive hard scattering processes for ep interactions⁹, with the emission of a pomeron by the beam proton ($p \rightarrow p\mathbb{P}$) which interacts with the virtual photon emitted from the beam electron; it includes also pion exchange, where the beam proton emits a virtual pion instead ($p \rightarrow \pi^+ n$) producing a leading neutron. PYTHIA 5.7[14] for the treatment of the hard scattering processes and JET-SET 7.4[14] for the hadronization following the Lund string model[15], are implemented in Pompyt. The flux factor is the one given in equation 1.16 and the GRV-P LO parton density function for the pion is used[16]. It is worth noting that the absolute normalization of the leading neutron cross section given by Pompyt is dependent on the value assumed by the pion structure function, which has not been measured at low x (< 0.1) and can only be extrapolated.

⁸The variable t can be written in terms of p_T and z , see equations 1.9.

⁹Also pp , γp and $p\bar{p}$ reactions can be simulated.

1.3.2 Target Fragmentation: Soft Colour Interactions

At HERA a new class of events in DIS ($\sim 10\%$ of the events) have been discovered in 1993, known as "rapidity gap events"[17], which are characterized by a large region of rapidity in the forward direction (the proton beam direction), where no hadronic activity is observed, i.e. no particles or energy deposit is observed- the so called rapidity gap. In normal DIS events a colour field is formed between the struck quark and the proton remnant (see figure 1.1), producing particles in the rapidity region between them, also in the forward direction near to the proton beam direction. It is unlikely that large rapidity gaps can be produced from normal proton fragmentation. These gaps are usually explained as pomeron exchange[2]. According to the Ingelman-Schlein model[18], a pomeron is exchanged in the t channel between the proton and virtual photon (also called diffractive process), giving rise to a rapidity gap because the proton remnant and the photon-pomeron systems are not colour connected. An alternative model[20] does not make use of the pomeron concept and explains the formation of rapidity gaps as changes in the colour topology of the event after the hard interaction has occurred. In this model additional non-perturbative soft colour interactions (SCI) are introduced, i.e. soft non perturbative gluon exchange, that do not change the momentum significantly, but change the colour topology modifying the hadronization, so that rapidity gap events may occur (see figure 1.4). This model of soft colour interactions can also give rise to leading neutrons without the concept of pion exchange, i.e. final state neutrons are produced as a result of the target fragmentation (proton) because of the soft colour interactions which change the hadronization of the proton remnant. This SCI model is implemented in the Lepto 6.5 Monte Carlo[19], which uses JETSET and PYTHIA and the Lund string model for hadronization with the addition of soft colour interactions.

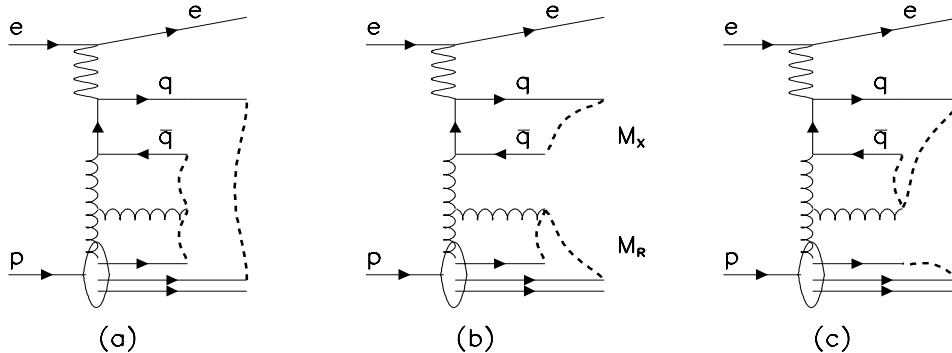


Figure 1.4: The string structure for a DIS boson-gluon-fusion event, which is the dominant contribution at low x : (a) the normal Lund string connections between partons, and (b),(c) the string connections after the string rearrangements due to soft colour interactions[20].

Chapter 2

THE H1 DETECTOR AT HERA

H1 is a general purpose detector situated at HERA, built to investigate the physics of ep interactions. The H1 detector is composed of various subdetectors, each optimized for retrieving specific information from the ep collisions. In this chapter an overview of HERA and the H1 detector with its various subdetectors will be given.

2.1 The HERA Storage Ring

The HERA[21] (Hadron-Electron Ring Accelerator) collider is situated at DESY (Deutsches Elektronen-Synchrotron) in Hamburg, Germany. On November 8, 1990 HERA was officially completed, after six and a half years of construction; the first ep (electron-proton) collisions took place on October 19, 1991, while regular data taking started in summer 1992 with two experiments H1[22] and ZEUS[23]. HERA is the first ep collider machine based on a concept unique in the world. It consists of two totally different independent storage rings which collide two completely diverse types of particles -electrons¹ and protons- which have to be accelerated and stored separately due to their big mass difference. These two separate accelerator rings are brought together just before the collision points, allowing ep collisions at zero crossing angle for the H1 and ZEUS detectors at a center of mass energy of $\sqrt{s} \simeq 300 \text{ GeV}$, equivalent to 48 TeV electron beam incident on a fixed proton target. This extends by two orders of magnitude the accessible kinematic range in Q^2 and x compared to fixed target experiments, as shown in figure 2.1.

¹Here "electrons" refers both to electrons and positrons. During the first years of HERA operation electrons were used. In 1994 the change over to positrons was made in order to achieve longer lepton beam lifetimes. Interactions with positively charged gas ions in the lepton beam-pipe, mainly originating from the HERA vacuum ion pumps, tends to defocus an electron beam, while for a positron beam the repulsive electromagnetic force prevents a pile-up of ions.

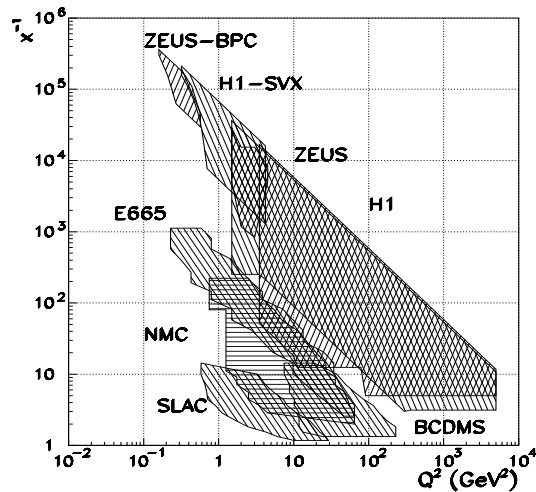


Figure 2.1: The Q^2-x^{-1} plane, showing the areas covered by the fixed target experiments and the HERA ones.

The two storage rings of HERA are contained in a tubular tunnel of 5.2 m in inner diameter and 6.3 km in circumference, positioned 10 to 25 m underground. The energy is 27.5 GeV for electrons or positrons and 820 GeV for protons, while the maximal achievable design luminosity is $\mathcal{L}=1.5 \cdot 10^{31} \text{ cm}^2\text{s}^{-1}$. The electrons and protons circulate in opposite directions. For protons the beam energy is limited by the magnetic field attainable by the dipole magnets, while for electrons the beam energy is limited by the synchrotron radiation loss. Therefore the proton ring requires the use of powerful magnetic fields to keep the 820 GeV protons in orbit, which can be achieved only with superconducting magnets (4.68 T); the electron ring needs only conventional magnets (0.165 T), since only a relatively weak field is necessary to keep electrons in their path. The electron's energy is mainly determined by the power of the rf (radio frequency) acceleration system, which compensates the energy lost by the beam through synchrotron radiation. HERA's electron ring is a scaled up version of the earlier storage ring PETRA. The increase in the electron's energy is due largely to the greater circumference of the accelerator (larger radius of curvature of the beam's orbit). Table 2.1 lists the basic parameters of HERA.

Figure 2.2 shows the DESY site accelerator complex for HERA. The electrons (positrons) and protons must be accelerated before injection into the HERA ring. This is done by using six other accelerators. The integrated HERA system is made up of a total of eight accelerators: three for protons, four for electrons, and the modified old PETRA ring- PETRA II, that is used alternately for injecting electrons and protons. A linac (linear accelerator) accelerates electrons to 500 MeV, then they are injected into the storage ring, where they are accumulated in a single bunch ($\sim 60 \text{ mA}$) and transferred to DESY II (a small synchrotron ring) and accelerated to 7 GeV. This bunch is transferred to PETRA II, where up to 70 of these bunches can be stored and accelerated to 14 GeV before injection into the electron ring of HERA. In the HERA electron ring eight superconducting cavities together with conventional rf cavities are used to accelerate the electrons to 27.5 GeV. In the case of protons, negatively ionized hydrogen is accelerated

Parameter	Proton Ring	Electron Ring
Energy(Gev)	820	30(27.5)
Center of Mass Energy(Gev)	314(300)	
Luminosity($cm^{-2}s^{-1}$)	$1.5 \cdot 10^{31} (\simeq 10^{31})$	
Crossing angle(mrad)	0	
Circumference(m)	6336	
Magnetic Field(T)	4.68	0.165
Beam Current(mA)	160($\sim 60-80$)	60(~ 30)
RF-Frequency(MHz)	52 \ 208	500
$\sigma_x \backslash \sigma_y$ at IP(mm)	0.29 \ 0.07	0.26 \ 0.02
σ_z at IP(mm)	110	8
Number of bunches	220	
Inter-Bunch distance(ns)	96	

Table 2.1: HERA design parameters. In brackets are the actual values for 1996-97.

by another linac, LINAC III, to 50 MeV, then it is stripped of its electrons leaving bare protons, which are bunched and accelerated to 7.5 GeV by a proton synchrotron, DESY III. As for the electrons, then the protons are transferred to PETRA II where up to 70 bunches are accelerated to 40 GeV and then are injected into the HERA proton ring. Here conventional rf cavities accelerate the protons from 40 GeV to 820 GeV.

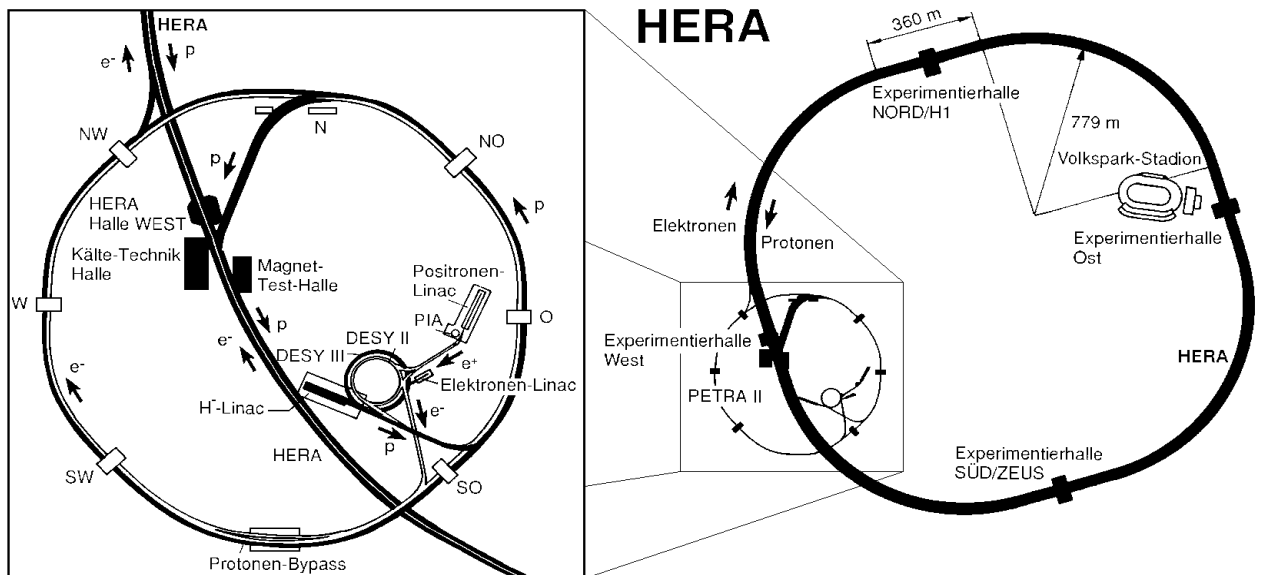


Figure 2.2: DESY site accelerator complex for HERA.

Four experiments are situated underground at the four interaction areas. H1 and ZEUS are general purpose collider experiments located in the North and South halls respectively, while HERMES[24] and HERA-B[25] are fixed target experiments, located in the East and West halls respectively. HERMES makes use of the electron beam (polarized longitudinally by a spin rotator) on polarised targets to study spin structure of the nucleon, while HERA-B uses the proton beam on internal wire targets to study CP-violation in the b-sector and rare b-decays.

Both beams contain 220 equidistant bunch buckets, which can be empty or filled by particles which are bundled into packets (bunches). In 1996-97 there were on average 174 colliding bunches (an electron bunch is paired to a proton bunch so that they collide in the interaction area), 10 proton pilot bunches (unpaired proton bunches), 15 electron pilot bunches (unpaired electron bunches) and 21 empty bunches. The pilot bunches are used to estimate the background rate; beam interactions with beam-pipe walls and with residual gas inside the beampipe. The bunch crossing frequency is 10.4 MHz or equivalently a bunch crossing every 96 ns or an inter-bunch distance of 28.8 m.

There are plans to upgrade HERA by increasing either its luminosity or its beam energies by the year 2000. Proposals for the luminosity upgrade are to increase the current (1997) annual integrated luminosity of $32.7 pb^{-1}$ to 150-170 pb^{-1} ; while proposals regarding the beam energies are to increase them from 27.5 GeV (e=electrons) and 820 GeV (p=protons), to 27.5 GeV (e) and 900 GeV (p) respectively and possibly to 30 GeV (e) and 1000 GeV (p). Concluding, in layman terms, HERA is a kind of super-electron microscope for taking a closer look at the basic constituents of matter, with a resolution of $\sim 10^{-18}$ m.

2.2 The H1 Detector

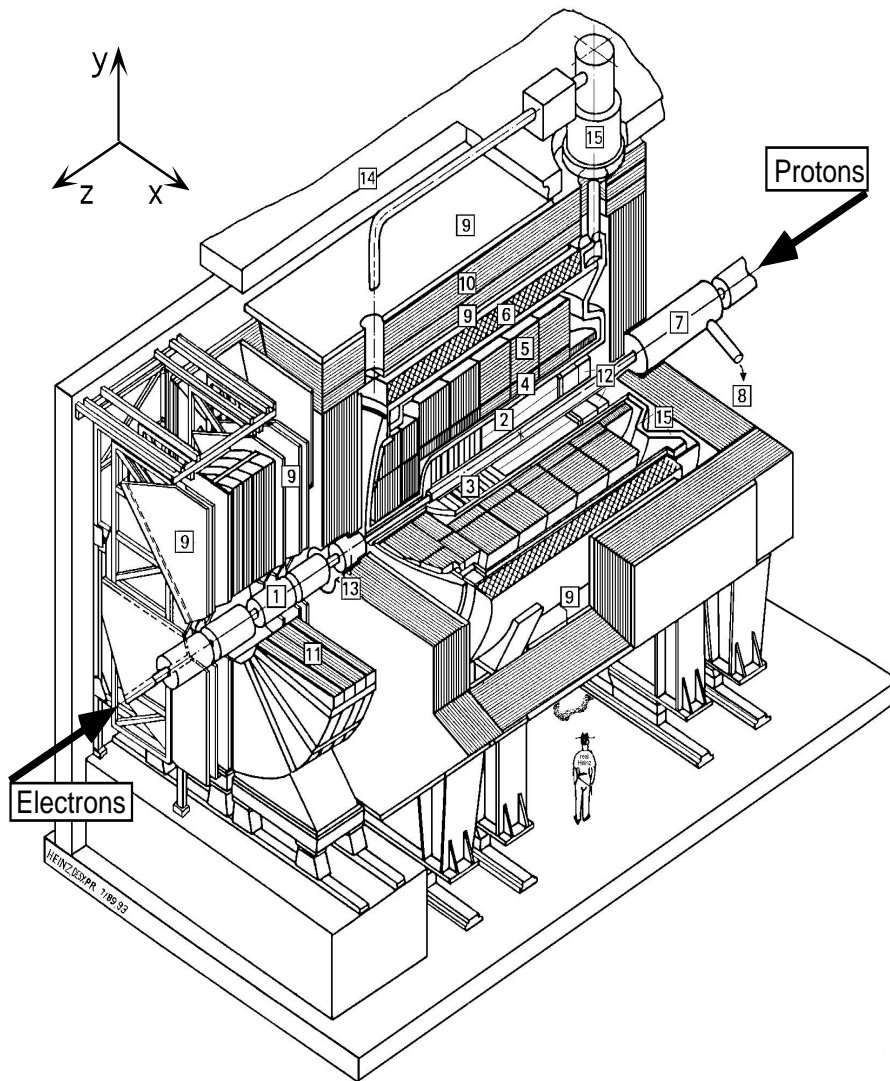
The H1[22] detector is a nearly hermetic general purpose collider apparatus, designed and built to investigate high energy electron-proton interactions at HERA. It measures the energies, angles, and possibly the identity of particles produced in the ep collision, with a near 4π solid angle coverage. The main limit to full solid angle coverage is the space occupied by the beampipe.

H1 is cylindrically symmetric around the beam axis. Due to the big energy difference between the two colliding beams, the center of mass of the ep collisions is boosted along the proton direction ($\gamma_{cm}=2.86$). Therefore H1 is an asymmetric detector, being more massive and instrumented in the outgoing proton direction. Apart from this forward-backward asymmetry, the H1 detector is similar to detectors used in e^+e^- or $p\bar{p}$ colliders. Tracking and calorimetry are the two main detection methods used in H1. A tracking detector reconstructs the trajectory of charged particles passing through it, from which

the momentum of a particle can be obtained. The trackers are placed in the magnetic field of H1, or otherwise the magnetic field is between the trackers and the interaction point. A calorimeter absorbs the incoming particle and converts its energy into a measurable signal. Neutral particles can be detected and hadrons can be distinguished from electrons or photons.

In the right-handed H1 reference frame coordinate system, the center corresponds to the nominal ep interaction point ($z=0$), the proton beam direction defines the positive z -axis, the x -axis is horizontal pointing towards the center of HERA and the y -axis points upwards. In the conventional spherical coordinate system (r, θ, φ) , θ is defined respect to the proton direction. H1 detector components situated on the positive side of the z -axis ($\theta < 90^\circ$) are referred to as "forward" detectors, and $\theta=0^\circ$ which corresponds to the proton direction defines the "forward direction"; while on the negative side of the z -axis ($\theta > 90^\circ$) the detectors are referred to as "backward" detectors, and the electron beam direction defines the "backward direction" ($\theta=180^\circ$).

Starting the description of H1 (figure 2.3) from the interaction vertex region going outwards, the detector consists of a central (2) and forward tracking system (3), composed of several layers of drift and proportional chambers, which measure momenta and reconstruct tracks of charged particles. These trackers are surrounded by a calorimetric system consisting of a fine grained liquid argon calorimeter (LAr), composed of an electromagnetic section (4) with lead absorber and a hadronic section (5) with steel absorber; ensuring good hermeticity in the central and forward regions for the measurement of energy and direction of charged and neutral particles. In the backward region (12) there is a backward drift chamber (BDC) and a lead-scintillating fiber calorimeter (SPACAL) for the measurement of the scattered electron and for the recognition of the background produced by the proton beam upstream of the H1 apparatus. The spaces around the beam pipe in the LAr calorimeter are filled with two small calorimeters, a silicon-copper (13) calorimeter in the very forward direction (PLUG) and a lead-scintillator in the very backward direction (SPACAL-Plug). A superconducting cylindrical coil (6) of diameter 6 m and length 5.75 m encloses the liquid argon calorimeter providing a 1.15 T uniform magnetic field parallel to the beams. A superconducting compensating magnet (7) is used in order not to influence the HERA beams. The magnetic flux is returned by the iron return yoke (10), which surrounds the detector and it is laminated and filled with streamer tubes. It is used as a Tail Catcher for the measurement of the hadronic energy leaking out of the calorimeter (hadronic shower tails), and for muon tracking. Muon tracking is supplemented by muon chambers (9), consisting of wire chambers, inside and outside the iron. Energetic forward muons are analyzed by a muon spectrometer, and by a toroidal magnet (11) sandwiched between drift chambers (Forward Muon System), placed outside the iron in the forward direction, where the particle density is highest. The luminosity system consists of an electron tagger and a photon detector placed in the tunnel respectively at $z=-33.4$ m and $z=-102.9$ m from the interaction point (ip). The luminosity



- | | |
|---|---|
| 1 Beam pipe and beam magnets | 9 Forward muon chambers |
| 2 Central tracking chambers | 10 Instrumented iron return yoke |
| 3 Forward tracking and Transition radiators | 11 Forward muon toroid magnet |
| 4 Electromagnetic calorimeter (Pb-LAr) | 12 SPACAL calorimeter |
| 5 Hadronic calorimeter (stainless steel-LAr) | 13 PLUG calorimeter |
| 6 Superconducting coil | 14 Concrete shielding |
| 7 Compensating magnet | 15 Liquid argon cryostat |
| 8 Helium cryogenics | |

Figure 2.3: Layout of the H1 detector. It has a size of $\sim 12\text{ m} \times 10\text{ m} \times 15\text{ m}$ and a weight of $\sim 2800\text{ t}$. The subdetectors placed in the tunnel are not shown.

measurement is done using the $ep \rightarrow ep\gamma$ bremsstrahlung process and measuring in coincidence the electron tagger and the photon detector. For the detection of leading baryons, a Forward Neutron Calorimeter (FNC)² and a Forward Proton Spectrometer (FPS)[26] are positioned in the tunnel. In the following pages a general description of the various components of H1 is given[22].

2.2.1 Tracking Chambers

The tracking detectors are located around the beam pipe. Their purpose is to trigger, reconstruct tracks and possibly identify particles emerging from the interaction area. Due to HERA kinematics many particles are produced in the forward direction. The tracking system has been divided therefore into two major mechanically distinct sections (figure 2.4): the central and the forward trackers. Each section, consisting of a number of subdetectors, is optimized for triggering and tracking in the specific angular region. The interaction region is enclosed by the Central Tracking Detectors (CTD) covering the angular range $15^\circ \leq \theta \leq 165^\circ$, while the forward area is covered by the Forward Tracking Detectors (FTD) with an angular range of $7^\circ \leq \theta \leq 25^\circ$. In addition, the Backward Drift Chamber (BDC) is mounted in front of the SPACAL calorimeter covering the backward region ($151^\circ \leq \theta \leq 177.5^\circ$)³.

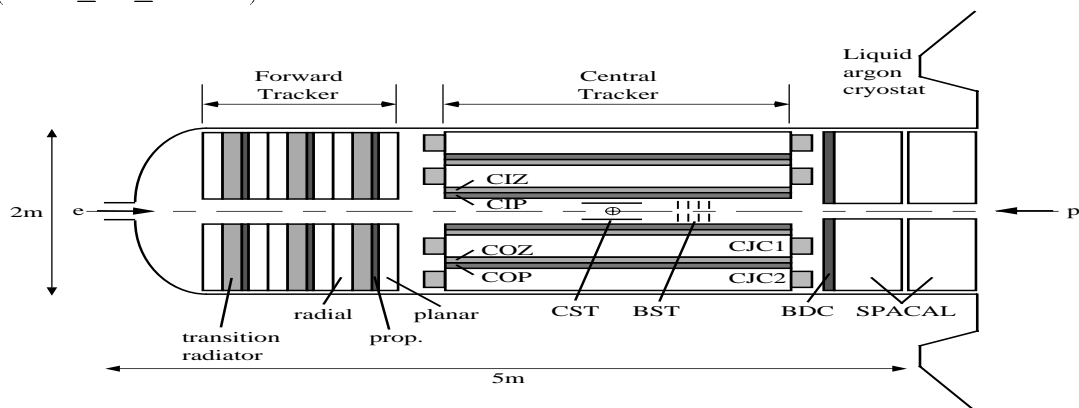


Figure 2.4: A side view of the H1 trackers.

Central Trackers

The superconducting magnet produces a uniform field parallel to the beam axis inside the tracking region. The central tracking system (figure 2.5) consists of six coaxial tracking chambers: two jet chambers *CJC1* and *CJC2* ($r\phi$ -drift chambers), two multiwire proportional chambers *CIP* (inner) and *COP* (outer) and the central inner and outer z chambers *CIZ* and *COZ* (r -drift chambers). The central jet chambers *CJC1* and *CJC2*

²A detailed description of the FNC detector will be given in chapter 3.

³In the 1994-95 winter shutdown upgrade of the H1 backward region, two silicon trackers were partially installed (figure 2.4 and 2.7), with the purpose of enhancing track measurements close to the interaction vertex. They are called central and backward silicon trackers (CST and BST) respectively[27].

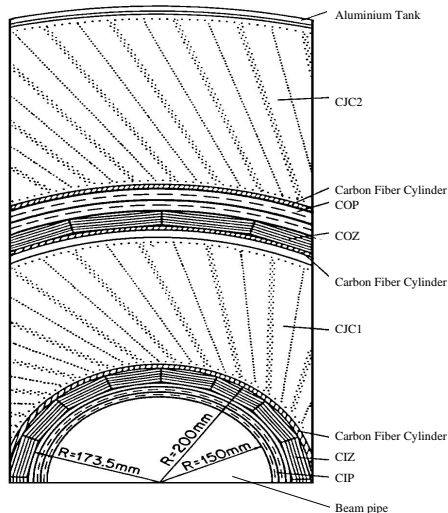


Figure 2.5: A $r - \phi$ view of the central trackers.

have drift cells with wires 2.2 m long strung parallel to the beam axis, so that r and ϕ are better determined, and inclined by $\simeq 30^\circ$ with respect to the radial coordinate to counteract the effect of the magnetic field, so that the drift direction is nearly perpendicular to high momentum tracks originating from the interaction region. The cell orientation and segmentation insure that the tracks are sampled a certain number of times and removes the problem of mirror tracks due to the drift cell ambiguity, i.e. the signal measured in a cell could originate from a drift particle coming from both sides of the wire. The wrong mirror track segments do not match and so they can be rejected. CJC1 has 30 cells, with 24 sense wires each, while CJC2 has 60 cells with 32 wires each. The track coordinates r/ϕ and z are measured with a spatial resolution of $\sigma_{r\phi} \simeq 170 \mu\text{m}$ and $\sigma_z \simeq 2.2 \text{ cm}$. The energy loss dE/dx along a track is used for particle identification, while particle momentum is obtained from the track curvature. The purpose of the central z chambers is to improve the z measurement provided by the CJC. They are thin drift chambers with the sense wires strung perpendicular to the beam axis. This provides a better measurement of the z track coordinate than from the charge division of signals in the CJC chambers, giving resolution in z of $\sigma_z \simeq 300 \mu\text{m}$ and $\sim 2\%$ in ϕ . The combined track measurements of the CJC and z chambers give a momentum resolution for the detected charged tracks of $\sigma(p)/p^2 \approx 3 \cdot 10^{-3} \text{ GeV}^{-1}$ and a polar angular resolution of $\sigma_\theta \approx 1 \text{ mrad}$. The MWPC chambers CIZ and COZ have fast response times ($\sim 20 \text{ ns}$ time resolution) and are used for triggering tracks starting at the interaction point, providing a fast signal used to differentiate successive bunch crossings on the first trigger level. They have wires strung parallel to the beam axis and consist of two layers of cells.

Forward Trackers

The Forward Tracker Detector (FTD) is made up of three identical subunits: called supermodules. Each supermodule consists of (in increasing z): three planar wire drift chambers rotated by 60° respect to each other in ϕ to provide an accurate θ measurement; a forward

multiwire proportional chamber (FMWPC) for fast triggering; a transition radiator for particle identification; and a radial wire drift chamber for accurate φ measurement.

Backward Tracker

The Backward Drift Chamber (BDC)[30] has been constructed and installed to replace the backward proportional chamber (BPC), as part of an upgrade of the backward region of the H1 Detector in the winter shutdown of 1994-95 and started data-taking in 1995. It is positioned in front of the SPACAL calorimeter, to improve the SPACAL measurement of the scattered electron angle in the backward region (figure 2.7).

2.2.2 Calorimeters

The H1 calorimeter system is designed to measure the total energy of charged and neutral particles produced in the ep interaction. It consists of a large liquid argon calorimeter (LAr) with an iron tail catcher, closed by a lead/scintillating fiber calorimeter (SPACAL) and the small SPACAL-Plug calorimeter in the backward region, and small the calorimeter (PLUG) in the forward region; and of a lead/scintillating fiber calorimeter (FNC) at $z=107$ m in the tunnel (see chapter 3). The LAr calorimeter is placed inside the magnet coil to minimize both the amount of dead material in front of the electromagnetic part of the calorimeter and the overall size and weight of the calorimeter (figure 2.6).

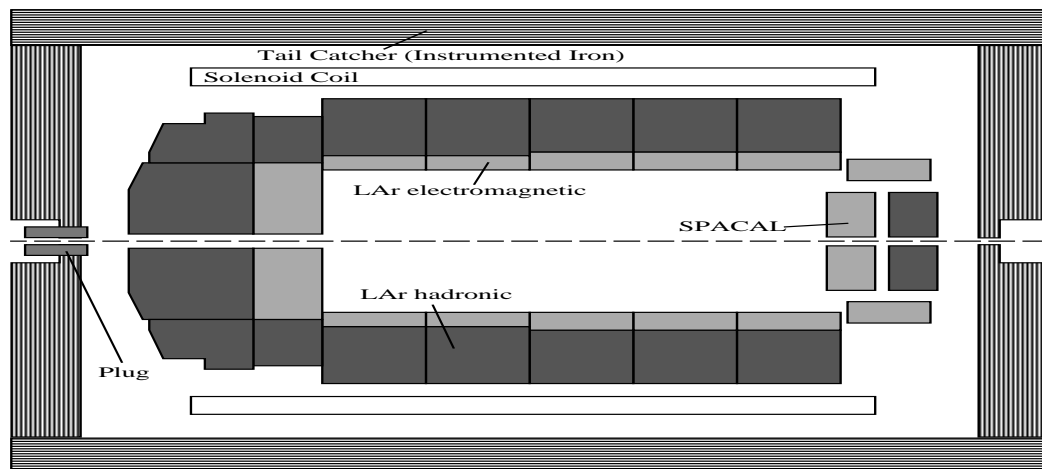


Figure 2.6: A $r - z$ view of the H1 calorimeters.

Liquid Argon Calorimeter

The LAr calorimeter is the main H1 calorimeter. It is used to detect the hadronic final state and high Q^2 ($\gtrsim 100 \text{ GeV}^2$) scattered electron events. The main reasons for choosing a LAr calorimeter is its stability, ease of calibration, homogeneity of response, fine granularity for e/π separation and energy flow, good angular and energy resolution. It is composed of two parts: the electromagnetic calorimeter (EMC) and the hadronic calorimeter (HAC). Argon is the active medium and both the EMC and HAC are contained in

a single cryostat. The LAr calorimeter is designed to optimize calorimeter homogeneity by minimizing cracks and support structures (dead material). It is composed of 8 independent self supporting modules- called wheels, lying along the beam-pipe. Each wheel is segmented in φ into 8 octants, and each octant has an electromagnetic and hadronic section, except for a section nearby the SPACAL, in the backward region (backward barrel electromagnetic- BBE), which has no hadronic counterpart (figure 2.6). The sampling structure of the electromagnetic section is built of 2.4 mm thick Pb absorber plates and 2.35 mm LAr gaps of active medium. The hadronic section sampling structure is composed of 16 mm thick stainless steel absorber and a double gap of LAr of 2.24 mm on both sides of the absorber, containing a double sided pad read out board. A high voltage is applied across the gap. The radiation length of the electromagnetic section of $20\text{-}30 X_0$ and the nuclear interaction length of the hadronic section of $4.5\text{-}8 \lambda$ ensures full absorption of the electromagnetic showers and nearly total absorption for the hadronic showers, with minimal leakage in the tail catcher. The LAr is highly segmented in both parts, consisting of about 45000 channels in total. The orientation of the absorber plates for both components is such that a particle originating from the vertex region has an angle of incidence always smaller than 45° , to maximize the number of absorber plates crossed by the particle. The hadronic section of the LAr calorimeter is not compensating, the e/π ratio is not one; in other words, the charge signal for hadrons is $\sim 30\%$ smaller than for electrons. Therefore a software weighting method is used, exploiting the fine longitudinal and lateral granularity and the fact that the energy deposits of high density are principally of electromagnetic origin, while the hadronic part of the shower is much more spread out. The LAr calorimeter covers the whole azimuthal range and the polar range of $4^\circ < \theta < 153^\circ$. Test beam measurements on the LAr modules give an energy resolution⁴ of $\sigma(E)/E \approx 0.12/\sqrt{E} \oplus 0.01$ for electrons and $\sigma(E)/E \approx 0.5/\sqrt{E} \oplus 0.02$ for pions. The absolute energy scale uncertainty for electrons is $\sim 3\%$, deduced by comparing the measured track momentum of the electron with its corresponding energy deposit in the LAr calorimeter. From the balance of transverse momentum between jets, the hadronic energy scale and resolution have an uncertainty of $\sim 5\%$.

SPACAL

The backward region of the H1 detector was upgraded, in the 1994-95 winter shutdown, with the scope of improving the measurement of the scattered electron in deep inelastic scattering and extending the range to low values of Q^2 and x . The principal component of this upgrade is the SPACAL (spaghetti calorimeter)[28] complemented by the BDC (see section 2.2.1) and the SPACAL-Plug. The SPACAL consists of two sections (figure 2.7): an inner electromagnetic and an outer hadronic section. The hadronic section is complemented by the SPACAL-Plug, a backward plug calorimeter positioned in the iron of the return yoke of the main magnet. The hadronic section provides coarse hadronic energy measurement and precise time information ($\lesssim 1$ ns) to suppress proton beam induced

⁴The energies (E) are always given in GeV.

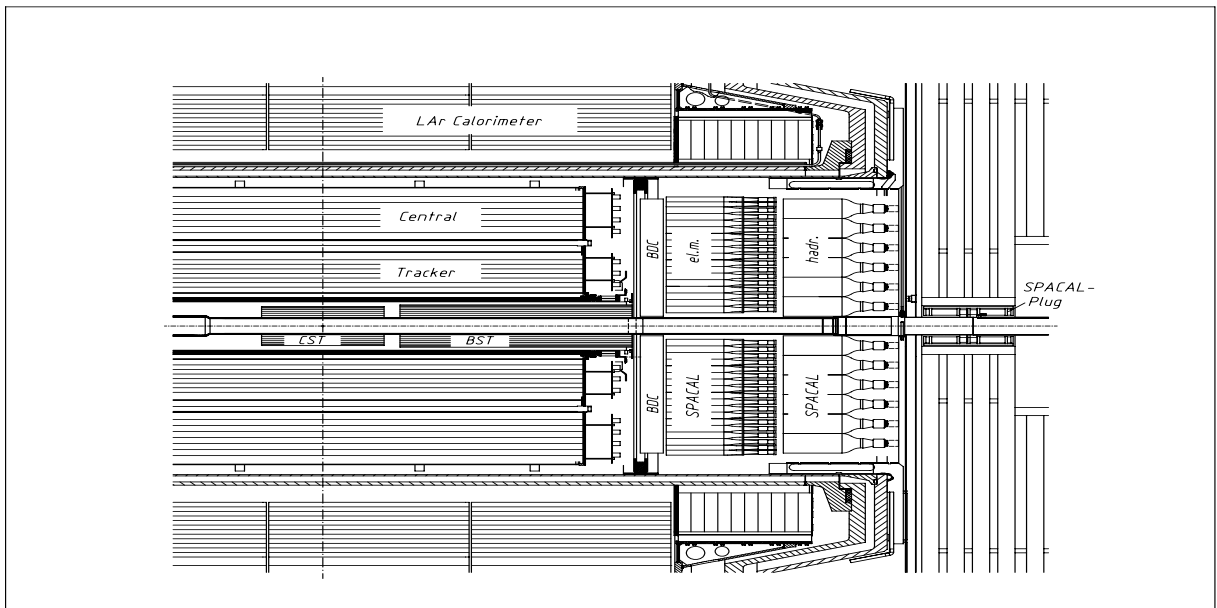


Figure 2.7: Partial side view of the H1 detector, showing the position of the electromagnetic and hadronic section of the SPACAL, the SPACAL-Plug and the BDC.

background from upstream, replacing the previous TOF system. The electromagnetic section consists of 0.5 mm scintillating plastic fibers embedded in a lead matrix, with a lead to fiber volume ratio of 2.3:1, while the hadronic section consists of 1.0 mm scintillating plastic fibers with a lead to fiber volume ratio of 3.4:1. The electromagnetic section is 28 radiation lengths deep, while the hadronic section adds 1.02 interaction lengths to the electromagnetic section, which is 1.0 interaction length deep. The SPACAL-Plug is made of the same material as the hadronic section and is positioned at $z = -2.6\text{ m}$. It extends the acceptance of the SPACAL into the transition region between deep inelastic scattering and photoproduction, covering a Q^2 range $\sim 0.1\text{--}0.5\text{ GeV}^2$ and extends the polar angle θ up to 178.7° . Since the SPACAL-Plug is positioned distant from the interaction point, it also provides additional veto information by discriminating out of time proton beam backgrounds. The angular acceptance of the SPACAL is $153^\circ \leq \theta \leq 177.5^\circ$. The electron detection by the SPACAL detector has a time resolution of $\approx 0.4\text{ ns}$, a position resolution of $\sim 2\text{ mm}$ ($\sim 2\text{ mrad}$), and an energy resolution of $\sigma/E = 7.1/\sqrt{E} \oplus 1.0\%$, while the hadronic energy resolution is $\sigma/E \approx 30\%/\sqrt{E}$ [29].

Plug

The Plug is a small Si–Cu calorimeter built and installed to close the acceptance gap between the beam pipe ($\theta \simeq 0.7^\circ$) and the forward part of the LAr calorimeter ($\theta \simeq 3.4^\circ$). Its aim is to minimize the missing part of the total transverse momentum due to hadrons emitted close to the beam axis, from proton fragmentation. It is also used to veto beam-wall and beam-gas backgrounds. The energy resolution for hadronic showers is moderate

($\sigma(E)/E \simeq 150\%/\sqrt{E}$), because of dead material in front of it and energy leakage. The Plug has a compact design due to space limitations. It is a sampling calorimeter made of 9 copper absorber plates (7.5 cm) alternated with 8 sensitive layers of Silicon-pad detector (300 μm). Its length is 65 cm (4.3 λ) and its radial acceptance is $0.7^\circ \leq \theta \leq 3.3^\circ$.

Tail Catcher

The hadronic showers leaking out from the main calorimeters are detected by the limited streamer tubes (11 layers) which are positioned in the slits of the iron yoke of the main magnet (instrumented iron) giving 4.5 λ . The instrumented iron is divided into central barrel, front and back end-cap regions giving nearly 4π coverage ($6^\circ < \theta < 172^\circ$). The energy resolution is moderate ($\sigma(E)/E \approx 100\%/\sqrt{E}$), but anyway only a small fraction of the total energy leaks out. The energy scale is obtained from cosmic muon calibration and it has an uncertainty of $\sim 35\%$.

2.2.3 Luminosity System

The luminosity system has several tasks. The principal task is an accurate measurement of the luminosity delivered by HERA, which is of paramount importance for the determination of the cross section of physics interactions. It also serves the purpose of electron beam monitoring for HERA, tagging photoproduction⁵ events and measuring photon (from initial state radiation) and small angle scattered electron energies. Luminosity is defined by the following formula:

$$N = L\sigma,$$

where N is the rate of events of a given process and σ is its cross section. Luminosity is determined from the rate of the Bethe-Heitler bremsstrahlung reaction $ep \rightarrow ep\gamma$, which has a large and precisely calculable cross-section. The main source of background is bremsstrahlung from residual gas in the beam pipe, $eA \rightarrow eA\gamma$. This can be corrected by using the electron pilot bunches to determine the background. Luminosity is therefore calculated by:

$$L = \frac{R_{tot} - (I_{tot}/I_0)R_0}{\sigma_{vis}},$$

where R_{tot} is the total rate of bremsstrahlung events, R_0 is the rate in the electron pilot bunches, I_{tot} and I_0 are the corresponding electron beam currents and σ_{vis} is the visible part of the $ep \rightarrow ep\gamma$ cross section with acceptance and trigger efficiency included.

The luminosity system is built to detect in coincidence photons and scattered electrons originating from the interaction region. There are two crystal calorimeter detectors:

⁵In the 1994-95 winter shutdown an additional electron tagger -ET44- was installed in the HERA tunnel at $z=-44$ m, to extend the acceptance for tagged photoproduction events to the low y range, $0.04 < y < 0.24$.

the Electron Tagger (ET) and the Photon Detector (PD), each consisting of an array of crystals. These detectors are placed close to the beam line, in the backward region, far from the interaction area in the tunnel, because the angular distribution is peaked for both electrons and photons, in the electron beam direction. These detectors are positioned on movable platforms which are retracted during ramping and injection of the beam to minimize radiation damage. They measure the electron and photon energies with an energy resolution of $\sigma(E)/E \approx 0.1\sqrt{E} \oplus 0.01$. The layout of the luminosity system is shown in figure 2.8. The scattered electrons with very small scattering angle have slightly lower

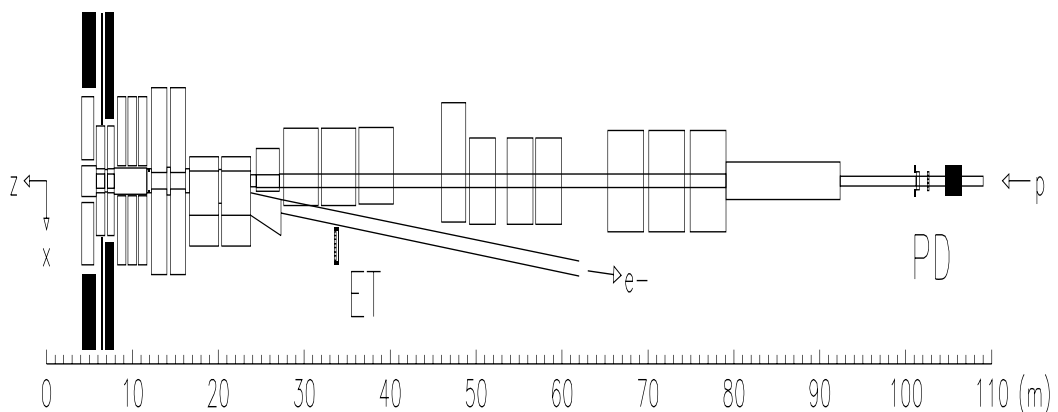


Figure 2.8: Layout scheme of the H1 luminosity system.

energies than the nominal electron beam and are deflected from the electron beam orbit by the magnetic field. They leave the beam pipe through an exit window positioned at $z = -27.3$ m and reach the ET at $z = -33.4$ m. The corresponding photons are not deflected by the magnetic field and pass an exit window at $z = -92.3$ m, where the proton beam-pipe bends upwards, and hit the PD at $z = -102.9$ m. The PD is protected from synchrotron radiation by placing in front a $2 X_0$ lead filter followed by a $1 X_0$ water Čerenkov veto counter (VC), and from behind (proton side) by an iron wall of 2 m in thickness. The VC rejects events with photons interacting in the lead filter. The ET and the PD consist of a 7×7 and a 5×5 crystal matrix respectively, readout by photomultipliers. Photo-production events with $Q^2 < 0.001$ GeV² can be tagged by the ET in the energy range $0.2 < E_{e'}/E_e < 0.8$ ($0^\circ \leq \theta \leq 0.3^\circ$) using the PD and VC as veto. In figure 2.9, the plots for the total integrated luminosities delivered by the HERA machine and accumulated by H1 versus day of the year are shown, from the beginning of regular data taking up to now. The luminosity delivered by HERA must be first corrected for the H1 trigger dead-time, the detector status and beam conditions, resulting in the effective luminosity collected by H1, which can then be used for physics analysis. The plots show a steady increase in luminosity through the years due to improvement of the HERA machine operation and H1 operation efficiency.

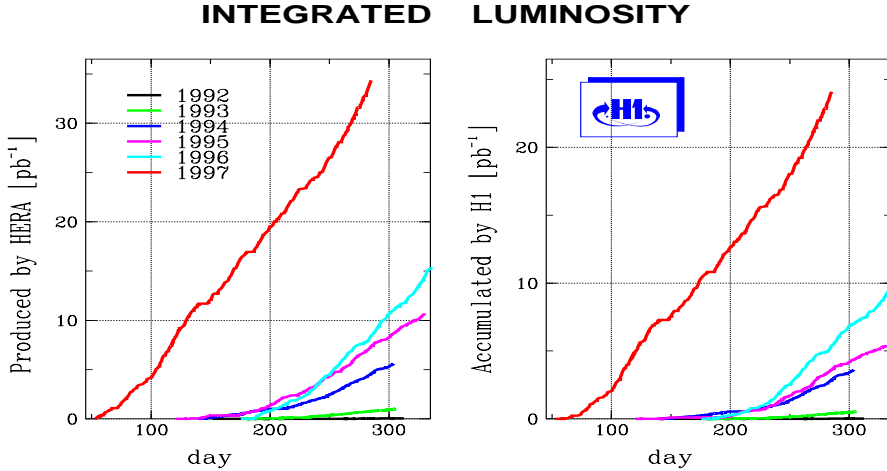


Figure 2.9: The integrated luminosity delivered by HERA and the integrated luminosity collected by H1 are displayed.

2.2.4 TOF-Detectors

Real ep interactions are distinguished from proton induced background interactions occurring upstream from H1 by using the time-of-flight (TOF) method. The idea is that particles produced from ep interactions will arrive at a different time, due to a different path length, from background interactions, relative to the bunch crossing nominal time. The SPACAL calorimeter (see 2.2.2) and some TOF counters are used for this purpose. The TOF counters consist of plastic scintillator of good intrinsic time resolution. They are positioned between the end-cap of the return yoke and the beam pipe BTOF (Backward TOF) at $z \sim -2.7$ m, by the PTOF (Plug TOF) at $z \sim 5.4$ m, and around the beam-pipe nearby the forward muon toroid FTOF (Forward TOF) at $z \sim 7.9$ m. Background events produced near the interaction region cannot be distinguished from ep events using this method, but there is a great reduction of the background rate. Upstream from the interaction area at $z = -6.5$ m and $z = -8.1$ m there are two larger planes of scintillator-veto walls, covering the same area as the backward part of the LAr calorimeter. The outer wall ($z = -8.1$ m) has a timing resolution of ~ 8 ns, while the inner wall ~ 3 ns. These walls work on the same principle as the TOF counters, to monitor and reject background produced from the proton beam, which are mostly muons. The proton beam halo produces muons by inelastic collisions of protons with residual gas in the beam pipe or with the beam pipe walls.

2.2.5 Muon Detection

The outermost parts of the H1 detector are used to detect penetrating muons. The return yoke of the main magnet of H1 is instrumented with limited streamer tubes (LST), with the purpose of tail catcher for the LAr calorimeter and the detection and tracking of penetrating muons. Muon identification is also done by additional wire chambers inside and outside the iron. In the forward direction where there is produced the highest

density of particles, the detection of muons is done by the Forward Muon Detector (FMD) which has an angular range of $3^\circ < \theta < 17^\circ$. The Forward Muon Detector (FMD) is situated outside the iron return yoke in the forward region out of the main body of the detector, positioned $6.4 \text{ m} \leq z \leq 9.4 \text{ m}$. It consists of 6 layers of drift cells, three on either side of the iron toroidal magnet (1.6 T) which deflects particles in the θ direction. The toroidal magnet is necessary to measure muon momenta at small θ since the transverse motion with respect to the main magnet field lines is small. The spatial resolution for measurements using drift time and charge division are $\sim 250 \mu\text{m}$ and 2-6 cm respectively. Due to this large difference in resolution, four layers contain cells arranged to give a better radial coordinate measurement θ -layers, while the other two layers give a better azimuthal coordinate measurement, φ -layers. There is one φ -layer sandwiched between 2 θ -layers on each side of the toroidal magnet. The FMD is used to identify the track left by a muon in the FTD (Forward Tracking Detector) and also measures muon momenta in the range $5 \leq p \leq 200 \text{ GeV}/c$.

2.2.6 Very Forward Detectors

In the very forward region, in the accelerator tunnel, three detector systems are positioned with the purpose of detecting particles in the very forward direction. These are the Proton Remnant Tagger (PRT), the Forward Proton Spectrometer (FPS) and the Forward Neutron Calorimeter (FNC). The FNC is described in chapter 3.

The PRT is located around the beam pipe at $z=26 \text{ m}$, consisting of two scintillator layers sandwiched between lead shielding and readout by photomultipliers. It detects particles originating from proton fragmentation, with a pseudorapidity range $6 \leq \eta \leq 8$.

The FPS[26] is operating since 1995, employing the HERA machine magnets located nearby the interaction region as spectrometer magnets. Scattered protons, that travel at a distance of several millimeters from the nominal orbit, are detected in two stations at z of 81 and 90 m, fitted with scintillating fiber hodoscopes. These detectors are mounted inside movable vacuum sections- Roman Pots, which are retracted during injection and ramping, and are brought close to the beam ($\sim 4 \text{ mm}$) after stable beam conditions have been reached. A permanent installation of the detectors a few mm from the proton beam is not feasible, because during injection and ramping the beam has a wider aperture and the detectors would be cutting into the beam aperture. The HERA proton beam-line in the forward direction uses dipole magnets to bend the protons horizontally at $z \simeq 20 \text{ m}$ and vertically between $z=60$ and 80 m. The two detector stations located at $z=81$ and 90 m are used to make two independent measurements of the position coordinates of the scattered proton. Each Roman Pot station contains two identical subdetectors, each subdetector consists of two planes of scintillating fiber hodoscopes rotated by 90° respect to each other, and sandwiched between two planes of trigger scintillators. These record the two coordinates (x -horizontal, y -vertical) of the scattered proton, which are then used to reconstruct its trajectory. At 650 GeV the typical momentum resolution is $\simeq 4 \text{ GeV}/c$,

with a scale uncertainty of $\simeq 3\%$. In the 1996-97 winter shutdown, two other stations were installed nearer to the interaction point ($z=64$ and 80 m), to increase the momentum acceptance and to improve the position measurement of the track.

2.2.7 The H1 Trigger and Data Acquisition

The interactions at H1 are dominated by background events. The total background rate at H1 is in excess of 100 kHz while the dominant physics process which is photoproduction has a rate of ~ 100 Hz. The purpose of the trigger system is to select a certain class of "interesting" ep collisions and to reject "uninteresting events" which are labeled as background. The typical background events are:

- synchrotron radiation from the electron beam;
- a proton or electron collisions with residual gas in the beam pipe, called also beam gas interactions;
- an interaction between a stray proton or electron (off nominal beam energy particle) and the beam pipe wall- stray protons can hit the beam pipe or the collimators, producing showers of secondary particles which then enter into the H1 detector;
- muons- beam halo muons or muons originating from cosmic rays.

To deal with the low cross sections of ep reactions, large electron and proton beam currents are required, together with a multibunch structure of the beams. At HERA there are 220 circulating bunches for each beam. A proton bunch collides with a corresponding electron bunch with a frequency of 10.4 MHz or every 96 ns- referred to as bunch crossing time, $1BC=96$ ns. The short bunch crossing time and the high background rate needs a fast complex pipelined trigger, consisting of several levels of increasing complexity, with each successive level analyzing the data in more detail and needing more time to make a decision. The trigger decision cannot be made within $1BC$ from a given event, because of the detector complexity and size, and because of the different detection methods used by the different subdetectors. The bunch crossing time is short compared to the response times of the subdetectors; typical times are ~ 0.5 μs , the largest drift times for the CJC is ~ 1 μs and the integration time of the LAr preamplifier is ~ 1.5 μs . This does not pose a pile up problem since the interaction rate probability per bunch crossing is small ($\sim 10^{-4}$). Buffering the front-end information and ignoring the following bunch crossings until the decision to keep the event is made, would introduce dead time for the first level trigger (L1), leading to loss in luminosity provided by HERA. Therefore to build a dead-time free L1 trigger, the detector information for each BC has to be saved until a decision regarding the event is made. The detector information must be pipelined, so called- front end pipeline; pipelining allows to postpone the trigger decision so that there is time to process each of the subdetector signals. Also, the definitive H1 trigger decision can not be taken within the time scale of the first level trigger (L1) of 2.3 μs , with an acceptable rate for data storage logging to tape of ~ 10 Hz. Therefore the H1 multilevel trigger consists

of four trigger levels, two hardware and two software levels, each of greater complexity. The purpose of each level is to reduce the rate of events produced by the lower level, by making a more time consuming and complex decision regarding the event.

- **L1- Level one trigger-** The output L1 trigger rate is of some kHz respect to the background interaction rate of $\gtrsim 10 kHz$. The L1 trigger is a dead-time free pipelined hardware trigger, running at $10.4 MHz$, consisting of a logical combination of hardwired triggers given by the different subdetectors of H1, with a decision time of $2.3 \mu s$. It is subdivided in different trigger systems, each based on the subdetector information, and it is able to identify the bunch crossing time $-t_0-$ associated to the event. The H1 subdetectors produce typically eight bits of digital information at each bunch crossing, named **trigger elements**⁶ (TE), which are stored in a pipeline in synchronization with the HERA clock⁷ and transferred to the central trigger logic (CTL). A subdetector sets a trigger element if a certain threshold is exceeded or hit coincidences are fulfilled etc. The CTL synchronizes the trigger elements to the same BC⁸, which are then logically combined to form up to 128 **subtriggers**. The logical *OR* of all subtriggers produces the L1 trigger decision. After about $2.3 \mu s$ (24 BC) from the interaction, a decision is made and if the level 1 trigger conditions are fulfilled, a *L1-Keep* signal is produced, which stops the pipeline and all subdetectors are read out. Dead-time starts and no further triggers are accepted until the event buffers are read out or a clear from a higher level trigger rejects the event. If the L1 conditions are not fulfilled, the pipelines are left active, the information will move to the end of the pipeline and be removed. The pipeline length varies from 27 to 35 BC depending on the subdetector since further time is needed to distribute the *L1-Keep* signal to the various subdetectors. A maximum of 128 subtriggers can be defined. They are divided in three groups: physics triggers for the selection of physics events, monitor triggers for monitoring of subdetector operation and calibration, and cosmic triggers for calibration purposes using cosmic ray events. Some subtriggers have a higher rate than desired and are so prescaled by a given factor n ; the prescaled trigger is considered in the logical *OR* of all subtriggers only every n^{th} time.
- **L2- Level two trigger-** It is a hardware trigger. Dead-time starts with the *L1-Keep* signal and has a decision time of $20 \mu s$. Its task is to reduce the rate to not more than $\sim 200 Hz$. The trigger elements for level 2 are based on the same information used by L1, but a more "intelligent" use of the trigger data is made. There are two types of L2 triggers in use:

L2NN trigger -level two neural network trigger- the trigger element subdetector information is considered as a pattern or correlation between trigger quantities;

⁶In 1996-97 there were 191 trigger elements.

⁷The HERA clock is the $10.4 MHz$ signal provided by HERA used as a timing reference.

⁸The arrival time of the TE varies due to different cable lengths, response times etc.

L2TT trigger -level two topological trigger- looks at the topology of events.

- **L3 -Level three trigger-** It is a software trigger not yet implemented which starts analyzing data in parallel with L2, to reduce the rate to not more than ~ 50 Hz, with a decision time of $800 \mu s$.
- **L4 -Level four trigger-** It is an asynchronous fast online software event filter, running on a farm of RISC processors, integrated into the H1 central data acquisition system, and has the complete data of the raw event available for application of more complex algorithms. The L4 trigger is also called the L4 filter farm. It is the last filtering step before transferring events to permanent tape storage and does not contribute to dead-time. The output rate can not exceed more than ~ 10 Hz, since it has to be transferred to tape. Several histograms are filled for calibration and monitoring purposes which can be observed directly online (L4 histograms). The L4 decision to accept or reject an event is based on the L1 trigger information, on the whole raw event data and on reconstructed quantities. The reconstructed quantities are calculated either by modules of the standard offline H1 reconstruction program (H1REC) or by specific L4 modules (H1L4). The method used is to verify all L1 subtriggers with the corresponding reconstructed quantities; for example, track subtriggers are checked by requiring hits in the trackers and reconstructed tracks. The subtrigger is reset if it can not be verified, and the whole event is rejected if there exists no other verified subtrigger. Some general cuts are applied after verification of the subtriggers, i.e. a cut on beam-gas collisions and on the z -vertex.

Events that pass all the trigger levels are readout completely and compressed. The time to readout an event is about 1-2 ms depending on the activity of the detector. The trigger system is able to reduce the rate of events from $\gtrsim 10$ kHz to ~ 10 Hz with a dead-time of 10%. The final reconstruction and classification is done offline, called also Level 5. The general scheme of the H1 trigger and data acquisition is displayed in figure 2.10. The H1 events that pass L4 are converted to the H1 offline data format⁹ and saved to tape (*raw data tapes*) in the form of BOS banks. These *raw data tapes* are the input for the quasi-online reconstruction. The events are reconstructed using the standard H1 reconstruction program H1REC typically within a few hours from data taking, and are stored on POT tapes (*Production Output Tapes*). Then these events are further reduced in number by applying further cuts and classifying them into different physics analysis classes (H1ECLASS) and stored on *data summary tapes* (DSTs), which contain the final reconstructed quantities used in the data analysis, such as tracks, calorimeter clusters, energies etc. At the end of each data taking year after: the calibration of each subdetector has been determined, and any modification to the subdetectors or new reconstruction code has been taken in account in the H1REC reconstruction code, the events are reprocessed

⁹H1 uses the dynamic memory management system BOS[31] for management of data, FPACK[32] for input/output transfer of data, and CMZ[33] for code management.

definitively applying the final cuts. This final data is then stored on DSTs. The DSTs are stored on disk providing an easy and rapid access for physics analysis. From these final data, PAW[34] ntuples are created using H1TOX¹⁰ from the DSTs (or some other preferred code) for the final data analysis.

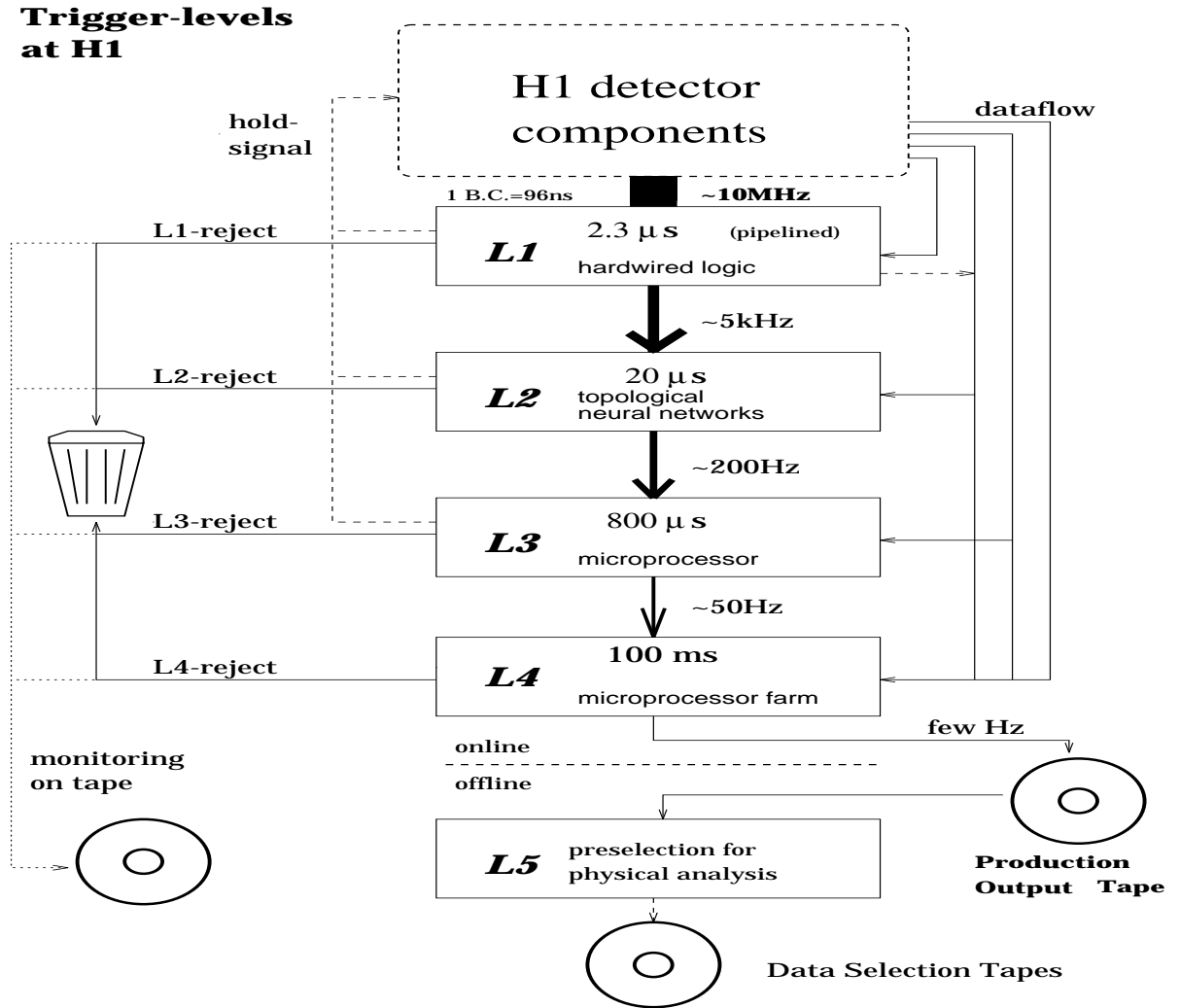


Figure 2.10: The multi-level trigger of H1. L1 and L2 are hardware trigger levels, L3 and L4 are software trigger levels based on programmable processors. The last step in producing the final events, used in physics analysis is done by the offline level L5. Events that are rejected at the different trigger levels, are saved on tape (reject tapes) for monitoring the effect of the trigger cuts. A prescale factor is used when writing the reject events to tape, L4 has typically a prescale of 100.

¹⁰The H1TOX[35] program -H1 physics analysis tool box- offers the possibility to create PAW ntuples, containing the H1 detector information, according to individual purposes.

Chapter 3

THE FORWARD NEUTRON CALORIMETER- FNC

This chapter describes the modification, calibration, installation and performance of the Forward Neutron Calorimeter (FNC) in the H1 experiment at HERA (DESY). Its purpose is to measure the energy and angle of high energy leading neutrons produced in the deep inelastic scattering process $ep \rightarrow e'nX$. The Forward Neutron Calorimeter- FNC, is a spaghetti calorimeter (SPACAL), developed and built by the CERN/LAA[36] project in 1989-90 as a prototype for next generation hadronic calorimeters of high energy collider experiments LHC and SSC¹. From 1991-95 it was used as a neutron detector in the hyperon beam fixed target experiment WA89[37] at CERN. In the last half of 1995, it was modified to fit into its new setup in the H1 experiment and then put in a CERN testbeam for calibration[38]. During the 1995-96 HERA winter shutdown, at the beginning of 1996 it was transported and installed in the HERA tunnel, and started regular data-taking the same year. The FNC replaces a simple test lead sandwich calorimeter that took data in 1995[39]. It had a depth of 1.4 m corresponding to 7 λ_I (λ_I is the nuclear interaction length, see section 3.1.2) and transverse area of 30·30 cm^2 . Two scintillating planes were positioned in front of the calorimeter to veto charged particles; to have a neutron detected, no signal above noise was required in both veto counters.

3.1 Brief Overview of Calorimetry

Calorimetry[40] is an important detection method used in high energy physics experiments primarily for the measurement of energy; but a calorimeter can also provide information on the position and the direction of the detected particle if appropriately segmented, and particle identification by utilizing the different responses of electrons and photons, muons, and hadrons. A calorimeter is essentially an instrumented block of matter, big enough to

¹Large Hadron Collider (LHC) and the aborted Superconducting Supercollider (SSC).

cause the incident particle to interact in it and absorb the particle's energy, by producing a shower of secondary particles and so degrading the energy to the level of atomic ionizations and excitations. A small fraction of the energy is detectable (e.g. scintillation light, ionization charge or Čerenkov light) which is proportional to the initial energy and the rest is mostly dissipated as heat. A calorimeter can be made of only one type of material (e.g. lead-glass) which both absorbs the energy and produces a measurable signal, called- *homogeneous* calorimeter; or of usually two materials, a passive material with high atomic number Z (e.g. lead), which only absorbs the energy producing many shower particles, and an active material with low Z (e.g. scintillator), which absorbs the energy producing a measurable signal, called- *sampling* calorimeter, because the shower energy is sampled periodically. Only the case of sampling calorimeters will be considered, since the FNC is of this type. Some general properties of sampling calorimeters are:

- detection of both neutral and charged particles;
- the shower development is a statistical process, the average number of secondary particles $\langle N \rangle$ is proportional to the incident particle energy E , so in principle the fractional energy resolution σ/E improves as $1/\sqrt{\langle N \rangle} \sim E^{-1/2}$;
- the longitudinal shower length and therefore the calorimeter size required to contain the shower, scales logarithmically with the incident particle energy E ;
- segmentation gives information on the shower development and allows to determine the position and angle of the incoming particle;
- the different response of electrons or photons and hadrons can be exploited for particle identification;
- the fast response times allow operation at high rates and the energy topology can be used for fast online event selection.

Calorimeters are usually classified according to the interaction they are designed to detect: electromagnetic calorimeters and hadronic calorimeters. According to the incident particle type, there are two principal ways a high energy particle² interacts in the calorimeter body: electrons, positrons and photons interact electromagnetically while hadrons interact strongly³. Both types initiate a particle shower, but the secondary particles produced and the interactions that occur result in very different shower characteristics.

²With high energy particle it is intended a particle with energy in the GeV range.

³Charged hadrons interact also electromagnetically when traversing matter, losing energy primarily by ionization (dE/dx), but at quite high energies radiative processes begin to dominate. Muons which interact electromagnetically and lose energy through ionization except at high energies (some 100 GeV) where radiative processes dominate; and neutrinos which interact weakly do not produce showers when passing through matter.

3.1.1 Electromagnetic Showers

An electromagnetic shower is initiated when a high energy electron⁴ or photon enters the calorimeter. A photon initiates the cascade by pair production, while the electron by bremsstrahlung, which in turn generate more photons and electrons of lower energy, until the critical energy ϵ_c is reached, where ionization and excitation are comparable to bremsstrahlung, so ending the shower development. It is useful to describe the shower development in terms that are material independent: radiation length (X_0) and Mollière radius (R_M). The longitudinal shower development is described by the *radiation length* X_0 , i.e. the mean distance that a high energy electron must travel through the material, losing energy by bremsstrahlung, to reach $1/e$ of its original energy⁵. The longitudinal containment of the shower scales logarithmically with energy, when the distance is measured in units of X_0 and is material independent. The lateral shower development is mainly due to multiple Coulomb scattering of electrons that do not radiate but have enough energy to travel far away from the longitudinal axis of the shower and partly by the transverse spread of low energy shower photons (below pair production threshold). The lateral shower development is described by the Molliér radius R_M , i.e. describes the average lateral deflection of electrons of energy ϵ_c after traversing 1 X_0 . Up to the shower maximum the radial shower dimensions is contained in a core of radius $\lesssim 1 R_M$, since at high energy the shower develops principally forwards. Beyond this point electrons are increasingly influenced by multiple scattering and the core is surrounded by a large halo of low energy electrons. About 95% of the shower energy is contained in a $2 R_M$ radius cylinder. The numerical approximations for these quantities are given in (3.1) with an accuracy of $\sim 10\%$ for $Z > 13$, where Z is the atomic number and A the atomic weight:

$$\epsilon_c[MeV] \approx \frac{550}{Z}, \quad X_0[g/cm^2] \approx \frac{180A}{Z^2}, \quad R_M[g/cm^2] \approx \frac{7A}{Z}. \quad (3.1)$$

These characteristic shower quantities for the FNC[41] are:

$$\epsilon_c = 6.3 MeV, \quad X_0 = 7.5 mm, \quad R_M = 25 mm, \quad (3.2)$$

while as a comparison for lead[42] they are:

$$\epsilon_c = 9.51 MeV, \quad X_0 = 5.6 mm, \quad R_M = 12.5 mm. \quad (3.3)$$

⁴With high energy (E) we intend $E > 1 GeV$. The electron and positron behave very similarly when passing through matter and have an almost identically shower development, so no distinction is made between the two of them as regards shower development.

⁵At energies above 1 GeV the principal processes by which electrons (bremsstrahlung) and photons (pair production) interact and lose energy become energy independent. On average high energy photons convert after traveling a distance of $9/7 X_0$.

3.1.2 Hadronic Showers

Hadronic showers are qualitatively similar to electromagnetic ones, but the shower development is far more complex because of the strong interaction; many different processes contribute to the inelastic production of secondary hadrons. A high energy hadron entering the calorimeter loses energy by ionization (dE/dx) until it interacts with a nucleus, roughly after one nuclear interaction length ($1 \lambda_I$) into the calorimeter block of matter. An interaction length is the mean distance traveled by a high energy hadron in matter before an inelastic interaction takes place. In other words, the probability of a hadron not interacting after a thickness of matter t is e^{-t/λ_I} , with λ_I the nuclear interaction length. λ_I is given by:

$$\lambda_I = 1/n\sigma_{ine} \quad \text{with } n = \frac{N_a\rho}{A}, \quad (3.4)$$

where n is the number of nuclei per unit volume, N_a is Avogadro's number, ρ is the density of the material, A is the atomic weight and σ_{ine} is the inelastic nuclear cross section which can be approximated by σ_{tot} (total nuclear cross section) at high energies.

There are a great variety of possible hadronic inelastic interactions between the entering hadron and the nucleons in the material, which produce secondary particles resulting in a hadronic shower. The secondaries consist principally of pions (of which about 1/3 are π^0 's) and nucleons. The number of interactions that occur and therefore the number of particles produced are significantly lower than in electromagnetic showers. Hadronic showers differ in shower composition from one event to another:

- a sizeable part of secondaries are π^0 's, which decay promptly into two photons and give rise to an electromagnetic shower. The number of π^0 's is largely dependent on the particle production in the first interaction and so fluctuates on an event by event basis;
- a large part of the energy is converted into binding energy (nuclear breakup), nuclear excitation and evaporation, of which only a variable fraction of it will be detectable. A small part of the incident energy will be undetected due to escaping particles from the calorimeter, mainly muons and neutrinos.

Hadronic showers have thus two basic components: an electromagnetic component and a hadronic component. Normally the hadronic component response (h) is usually smaller than the electromagnetic component response (e), i.e. $e/h > 1$, and the calorimeter is said to be *undercompensating*. This happens because a large fraction of the incident energy goes undetected in the hadronic part of the shower, and so the energy measurement for the same incident energy will vary from event to event depending on the shower composition. To avoid this problem, calorimeters are built with e/h close to one. A calorimeter is said to be *compensating* if $e/h = 1$ and *overcompensating* if $e/h < 1$. The FNC is a nearly compensating calorimeter with $e/h = 1.15$ [43].

There are several ways to achieve compensation:

- the hadronic response can be increased by using radioactive absorbers (e.g. uranium) where part of the lost energy is regained by nuclear fission;
- the electromagnetic response can be reduced by choosing low Z active material and high Z absorber both of appropriate thickness, so that the low energy short range electrons and photons in the absorber do not reach the active layer;
- the hadronic response can be increased by using hydrogenous material for the active component (e.g. plastic scintillator) since the low energy ($\approx MeV$) neutrons lose more energy by elastic scattering off light nuclei and are thus slowed down more quickly, until an interaction with a nucleus occurs most likely producing ionization.

The nuclear interaction length λ_I describes both the longitudinal and lateral shower development. A cylinder of radius $\sim 1 \lambda_I$ contains radially roughly 95% of the shower. It is approximated as:

$$\lambda_I[g/cm^2] \approx 35A^{1/3}, \quad (3.5)$$

where A is the atomic weight. The effective nuclear interaction length for the FNC[41] is:

$$\lambda = 21 \text{ cm}, \quad (3.6)$$

while, as a comparison, for lead[42]:

$$\lambda = 17.1 \text{ cm}. \quad (3.7)$$

The shower dimensions are used to differentiate between hadronic and electromagnetic showers in calorimeters with big λ_I/X_0 ratio, since hadronic showers are significantly longer and wider than the electromagnetic ones. It is possible to parameterize the longitudinal shower maximum and the longitudinal containment of 95%, i.e. the position in the shower with respect to the longitudinal shower axis at which the multiplicity of secondary particles is at its maximum, and at which 95% of the incoming hadron energy has been deposited, respectively; these are measured from the front face of the calorimeter with $t_{max}(\lambda_I)$ and $t_{0.95}(\lambda_I)$ given in units of λ_I and E in GeV :

$$t_{max}(\lambda_I) \sim 0.2 \ln E + 0.7 \quad t_{0.95}(\lambda_I) \sim t_{max} + 2.5 E^{0.13}. \quad (3.8)$$

In figure 3.1 the equations (3.8) are plotted for the FNC incident particle energy range. Since the hadronic showers have large fluctuations in the deposited energy, a calorimeter should be built with a longitudinal dimension given by $t_{0.95}(\lambda_I)$ plus an extra $3 \lambda_I$ to ensure that 95% of the showers have a containment of 95%. The FNC was built for a lower energy range ($\sim 300 GeV$) with a length of $9.5 \lambda_I$, practically fulfilling this criteria, but at the higher energies present at HERA ($\sim 400-800 GeV$) this criteria is only partially fulfilled (see 3.11.3). Figure 3.2 displays the GEANT simulation for a hadronic shower of a $600 GeV$ neutron entering the FNC. Starting from the right in the picture in sequence there are the incoming neutron track, the two hodoscope planes within the calorimeter enclosing, the calorimeter body, the photomultipliers and the two scintillator tail catchers out the calorimeter enclosing on the left (see figure 3.8 for more detail).

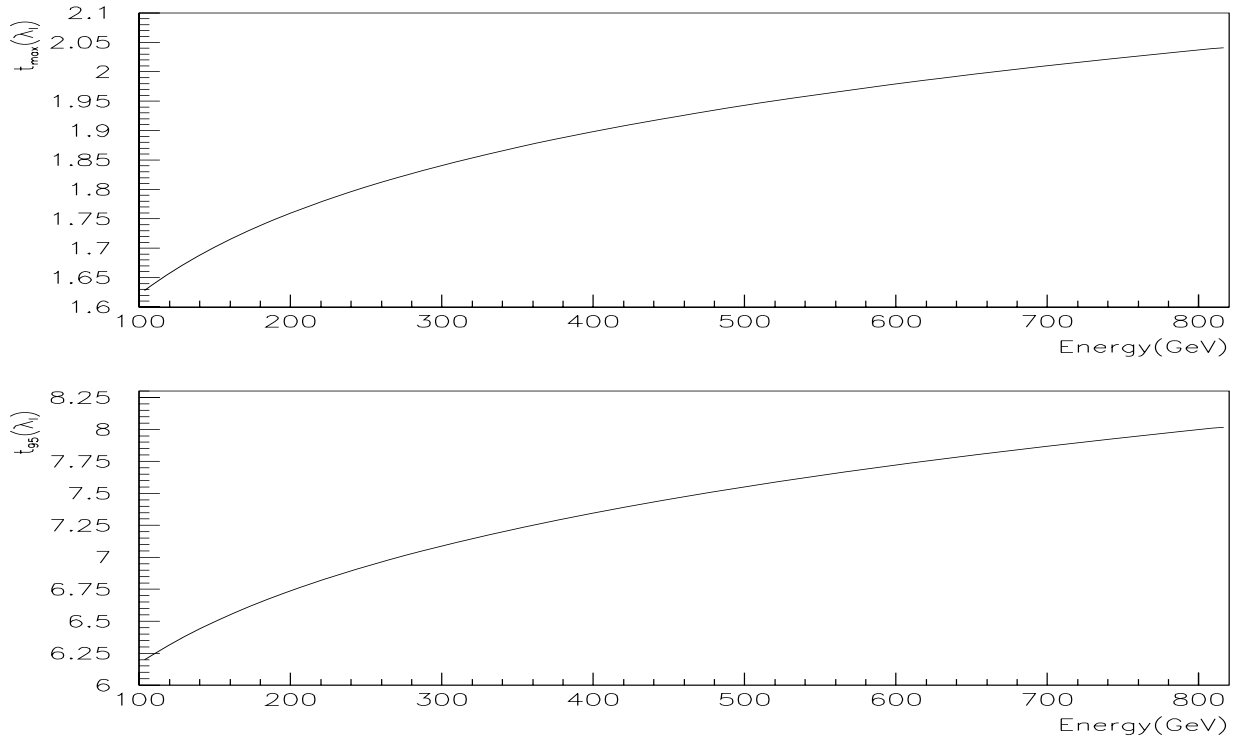


Figure 3.1: The $t_{max}(\lambda_I)$ and $t_{0.95}(\lambda_I)$ are plotted for the FNC energy range.

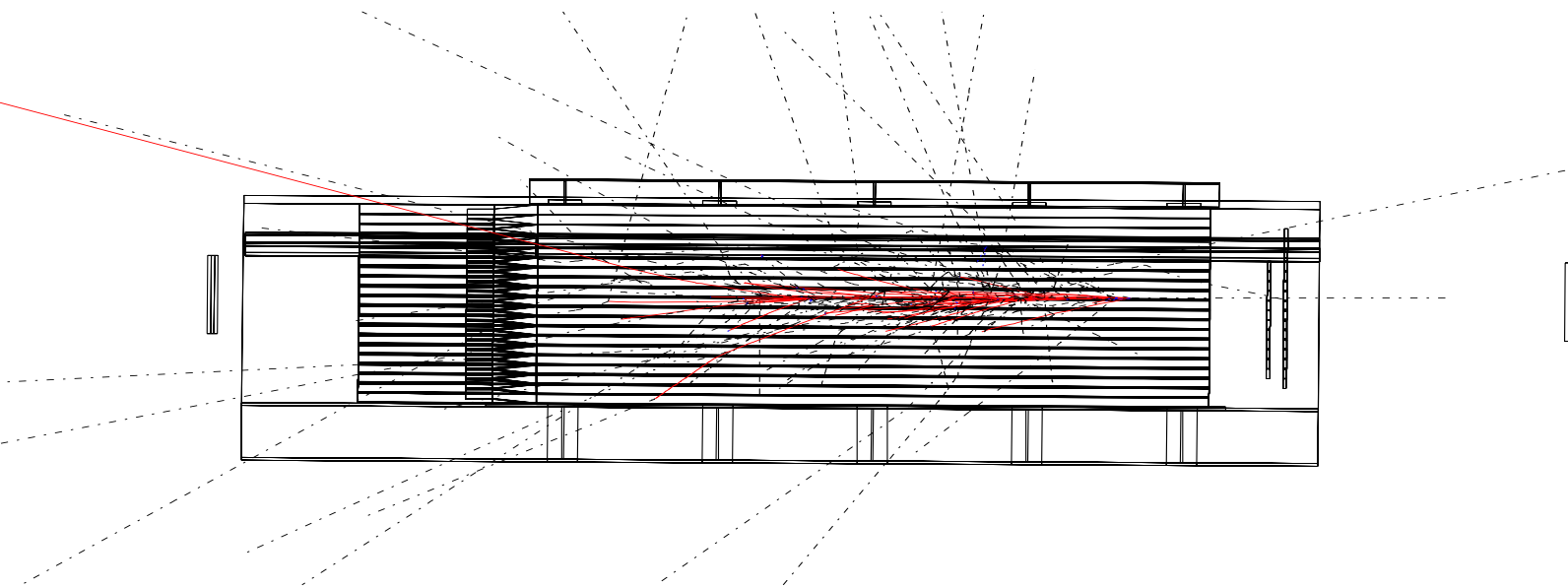


Figure 3.2: The GEANT simulation for a hadronic shower of a 600 GeV neutron entering the FNC in its central module. The neutron enters the FNC from the right in the picture.

3.1.3 Energy Resolution

The uncertainty of an energy measurement made by a calorimeter is given by the energy resolution⁶, denoted by $\sigma(E)/E$. The final signal measured by the calorimeter depends on the number of electrons that are recorded by the electronics. Therefore the resolution is dependent on the fluctuations in the number N of these electrons. These fluctuations are due to intrinsic shower development and sampling fluctuations, photomultiplier statistics and gain variations, detector effects, pile-up etc. If these fluctuations are Poisson distributed the standard deviation is $\sigma = \sqrt{N}$ and the fractional energy resolution is $\sigma(N)/N = 1/\sqrt{N}$. In a linear calorimeter, N is proportional to the incident energy E ($N \propto E$), and the fractional energy resolution can be written as (C is a constant):

$$\frac{\sigma(E)}{E} = \frac{C}{\sqrt{E}}. \quad (3.9)$$

The experimental energy resolution deviates from the above expression and is generally written as sum of two terms in two ways:

$$\frac{\sigma(E)}{E} = \sqrt{\frac{C_1^2}{E} + C_2^2} = \frac{C_1}{\sqrt{E}} \oplus C_2, \quad (3.10)$$

or

$$\frac{\sigma(E)}{E} = \frac{C_1}{\sqrt{E}} + C_2, \quad (3.11)$$

where C_1 and C_2 are constants and E is in GeV. The first term, called the *scaling term*, includes all statistical fluctuations⁷ and the second term, called the *constant term*, includes all other fluctuations (e.g. noise, shower leakage, non-uniformities and non-compensation for case of hadronic showers) which is added in quadrature or linearly. The energy resolution for hadronic showers is worse than for electromagnetic showers because of the great fluctuations in the shower development; the effect of the lateral leakage on the energy resolution is not so important as the longitudinal leakage. The energy resolution of the FNC measured in the CERN test beam and its value for the HERA operation energies, is reported in sections 3.3 and 3.11.1 respectively.

⁶The correct name for $\sigma(E)/E$ is fractional energy resolution, but colloquially it is called energy resolution.

⁷These are predominantly sampling fluctuations. For hadronic showers there is in addition the contribution from the intrinsic fluctuations in the fraction of the incident particle energy that is detected.

3.2 Modification

The original calorimeter consisted of a 13 ton lead-scintillating fiber matrix structure of the spaghetti calorimeter type (SPACAL)[37]. The particles entered the front face nearly parallel to the scintillating fibers. These fibers were grouped together at the backface giving a lateral segmentation of 155 hexagonal towers or modules (figure 3.3). Particles produced in the shower of a hadron hitting the calorimeter gave rise to scintillation light in the fibers, which was then collected by photomultipliers at the back-end of the calorimeter. A scintillating tile hodoscope plane was placed at about 15 cm from the front face of the calorimeter to reject charged particles. This hodoscope plane consisted of 127 hexagonal tiles with same granularity as the calorimeter's towers. To measure the leading neutrons

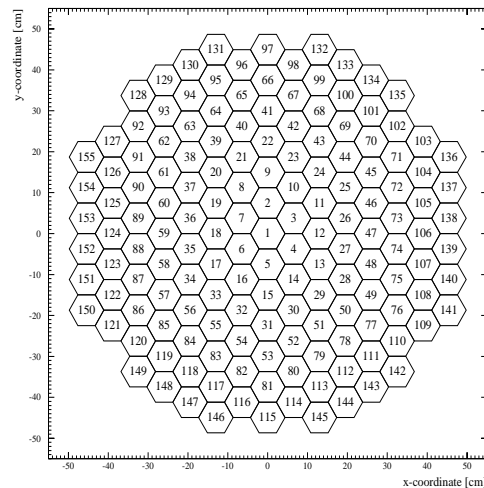


Figure 3.3: Front view of the original calorimeter, composed of 155 towers.

produced in the ep interaction at H1, the FNC was positioned in the forward direction respect to H1, at $z=107$ m, in the HERA tunnel. Due to the limited space available for the calorimeter in the HERA tunnel and the weight limit of 10 t for anything that had to be transported into the tunnel by the HERA Tram⁸, the original SPACAL had to be modified. In addition the proton beampipe is located at about 18 cm above the 0° neutron impact point, requiring a hole for it through the calorimeter. To fulfill the above conditions and attain a simple installation, the calorimeter was reduced in size and split into a lower and upper part with respective weights of ~ 7.5 t and ~ 1.3 t. Once the lower part was placed in position, the upper part was placed on top, leaving a gap the size of one calorimeter module, with just enough space for the proton beampipe to pass through it. The original SPACAL was a lead-fiber matrix, built by stacking long grooved lead sheets containing the scintillator fibers, one on top of the other. This gave the possibility to leave most of the calorimeter modules untouched and only the upper modules had to be rebuilt. The rebuilding of the calorimeter consisted in first opening it

⁸The HERA Tram is a device moving on wheels used to bring and position heavy objects into the HERA tunnel.

up by removing its protective enclosure, the hodoscopes, photomultipliers etc., till there remained only the lead-fiber matrix. Then the lead and fibers were removed starting from the top of the calorimeter, until the height corresponding to the lower edge of the gap for the beampipe was reached. The width was also reduced by removing the lead-fiber matrix from the two lateral sides. The lead was stacked and the fibers belonging to the same module were stored together and separate from the others, so that the same fibers could be used to rebuild each module. The upper modules were rebuilt by relaying the lead and fibers, to form a step structure in both directions respect to the center, when seen from the frontface or backface of the calorimeter⁹. Then a steel support with the similar step structure was laid on top, to form a gap for the beampipe between the lower and upper parts. The top part was built in the same manner as the lower one. Figure 3.4 shows the layout of the rebuilt calorimeter, renamed FNC (Forward Neutron Calorimeter).

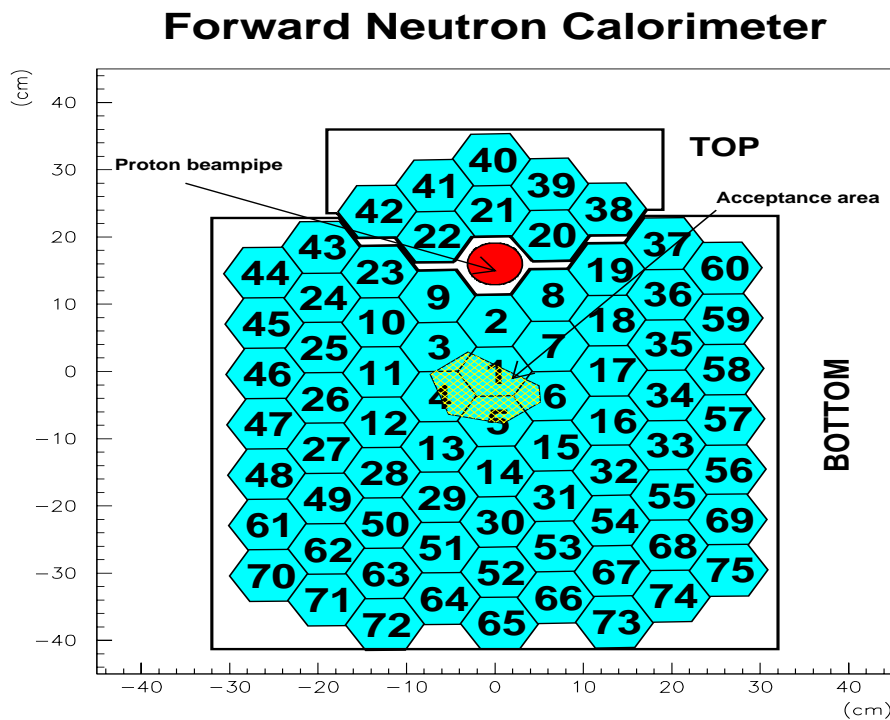


Figure 3.4: Back view of the FNC. The calorimeter module numbering starts in the center with module 1 and goes around counter-clockwise till module 75. The bottom part has 67 modules with a weight of $\sim 7.5 t$ and dimensions $205 \cdot 65 \cdot 64 \text{ cm}^3$, the top part has 8 modules with a weight of $\sim 1.3 t$ and dimensions $205 \cdot 39 \cdot 19 \text{ cm}^3$. The proton beampipe passes through the gap between the top and bottom parts. The acceptance area for the incident neutrons is the hatched area in the center of the calorimeter; it is defined by the dead material of the beam magnets between the FNC and H1. The calorimeter modules are shaded and the thick black line delimitates the lead-fiber matrix body.

⁹The term 'back' refers to the calorimeter end where the PMs are located, and the term 'front' refers to the opposite side, where the incident particle hits and enters the calorimeter body.

3.2.1 Lead-fiber matrix

The lead-scintillating fiber matrix of the FNC consists of 75 calorimeter modules, 67 belonging to the bottom part and 8 to the top part, with a gap in-between for the beampipe. Lead is the passive (absorber) material while the scintillating fibers are the active material acting, also as light guides. The lead-fiber matrix (figure 3.5) is built as one structure held together mechanically, by stacking longitudinally grooved lead sheets (49.5·1.92·2000 mm³) one on top of the other, containing scintillating fibers¹⁰ of 1 mm in diameter and 2.2 m long, with a lead to fiber volume ratio of 4:1. This structure and ratio makes the calorimeter compact (9.5 λ_I) and nearly compensating ($\epsilon/h=1.15$), with a *sampling fraction*¹¹ of 2.3%[41],[43]. The fibers are plastic scintillating fibers[37] consisting

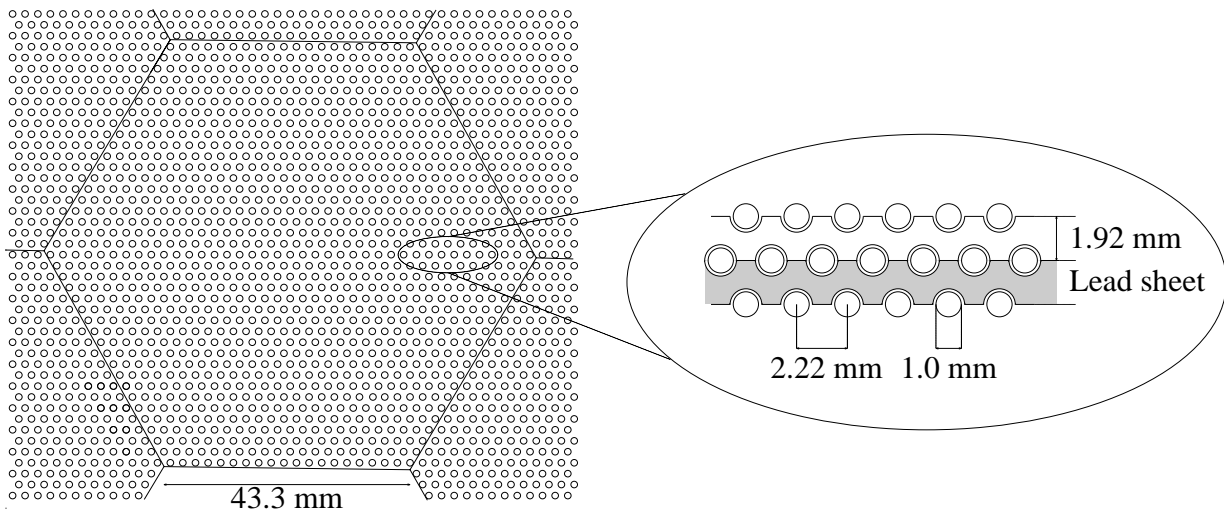


Figure 3.5: Layout of the lead-scintillator fiber matrix. A hexagonal tower (module) is obtained by coupling 1141 fibers, 1 mm in diameter and 2.2 m long, to a common PM. Each module has an area of 48.7 cm² and measures 8.6 cm apex to apex.

of a core of doped scintillating material (polystyrene) surrounded by an outer layer of non-scintillating material (polymethylmethacrylate or PMMA, 29 μm thick) called *cladding*. A charged particle passing through the fiber emits light by exciting the scintillator material, which is then absorbed by the dye in the fiber. The dyes are solutes that are added to the scintillating material (doped scintillator) to absorb the scintillating light and re-emit light at longer wavelengths so that reabsorption is reduced. The fiber acts as a light guide because the refractive index of the cladding ($n_{clad}=1.48$) is smaller than that of the core ($n_{core}=1.59$), so that the light travels through the fiber by total internal reflection. The fibers extend ~ 20 cm from the backend and are bundled hexagonally by a clamp, at the

¹⁰The fiber type is SCSF38, manufactured by Kuraray Co. Ltd., Tokyo, Japan.

¹¹The sampling fraction is the ratio of the incident particle energy that is deposited in both the active and passive material, to the incident particle energy deposited only in the active material.

backend of the calorimeter, in groups of 1141 fibers, to form a calorimeter module 2 m long ($9.5 \lambda_I$), see figure 3.8. Each hexagonal bundle has been machined and polished and is coupled to a Plexiglas light guide¹² of the same hexagonal cross sectional area. The light guide mixes the light by multiple total internal reflections, minimizing the effect of photomultiplier non-uniformities and fiber to fiber fluctuations. To increase the effective attenuation length of the fiber, the fiber end not going to the PM is closed by a mirror¹³ and a yellow filter¹⁴ is placed on the PM's photocathode window with light guide kept in tension against it. The filter cuts out the blue component of the emitted light, which is attenuated due to reabsorption in the fiber. The old PMs were replaced by new ones of the same type. The new PMs are of type XP2282B/01¹⁵; each one was individually tested by Philips for uniform photocathode efficiency. This type of PM has a spectral range of 300 to 650 nm , peaking at 400 nm , which matches the light output from the fiber that has traversed the yellow filter, and it is operated at a gain of $\sim 10^6$. The PM and light guide are housed within the molded foam and mu-metal of an aluminum hexagonal tube with same cross sectional area as the calorimeter modules.

3.2.2 Hodoscope

The hodoscope tiles were rearranged to form two hodoscope planes, called Hodoscope Plane 1 (HP1) and Hodoscope Plane 2 (HP2), and were positioned at 10 cm and 6 cm respectively from the front face of the calorimeter, to veto charged particles. These planes were built by glueing the hodoscope tiles one next to another, on a low density material support plane. HP1 consists of 43 modules, three of which belong to the top part of the calorimeter. Each hodoscope tile of HP1 covers a calorimeter module, except for the outer calorimeter ring modules and the six bottommost calorimeter modules (70 to 75). HP2 consists of 25 tiles, covering a smaller area than HP1. The whole HP2 plane is shifted half a module down and right with respect to HP1 (figure 3.6), so that the gaps between the tiles of HP1 are covered by HP2. A hodoscope module[44] consists of a hexagonal scintillator¹⁶ tile with the same granularity as the calorimeter modules and of 5 wave-length-shifting (wls) fibers, enclosed in a black light protection material. The five wls fibers absorb the scintillation light produced by charged particle crossing the tile and re-emit green light, guiding it by total internal reflection to a PM as shown in figure 3.7. The output ends of the 5 wls fibers are bundled and clamped together, polished and coupled with optical grease to the PM (Hamamatsu R647). The lengths of the hodoscope modules vary since the PM's are positioned below the two hodoscope planes, needing different wls fiber lengths to reach different positions of the calorimeter

¹²The light guide is hexagonal, 79 mm long and 42 mm apex to apex, since this geometry gives the best results for light mixing[37].

¹³These ends of the fibers were polished and made reflective by aluminum sputtering, so that the response is more uniform as function of depth.

¹⁴The filter is KODAK Wratten #3, which cuts wavelengths below 450 nm .

¹⁵Philips, fast 8 stage PM.

¹⁶It was cut out from a 1 cm thick scintillator plate (SCSN-38).

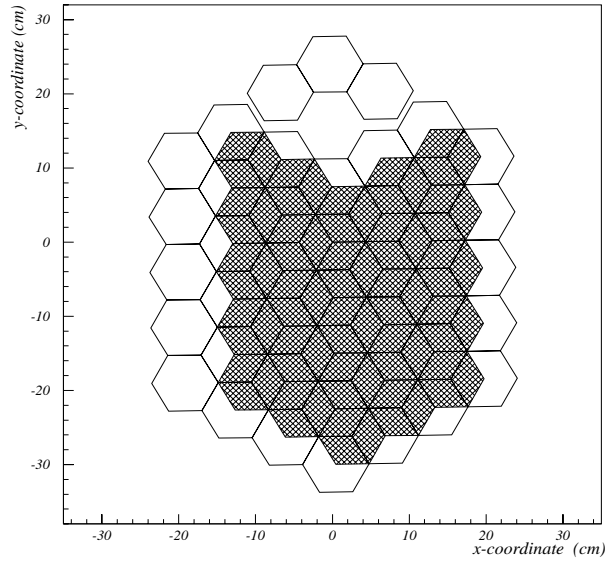


Figure 3.6: The two hodoscope planes. HP2 (hatched area) is shifted respect to HP1 by half a module down and right.

face. The hodoscope tile efficiency for detection of a traversing minimum ionising particle was studied by the WA89 experiment[44] and was found to be $\sim 100\%$. The hodoscope planes serve as a veto for charged particles, but a neutral particle (i.e. neutron) can fake a charged particle when traversing the scintillator tile either by preshowering in the tile or by the *albedo* effect. The tiles are 1 cm thick corresponding to $0.013 \lambda_I$, so about 1.3% of the high energy neutrons will preshower faking a charged particle. The most important effect limiting the hodoscope efficiency for neutral particle identification comes from the albedo effect i.e. shower particles in the calorimeter being scattered backwards and leaking out of the front face of the calorimeter. These particles, if charged, may reach the hodoscope planes and produce a hit, faking a charged particle (see 3.8 for the FNC hodoscope performance).

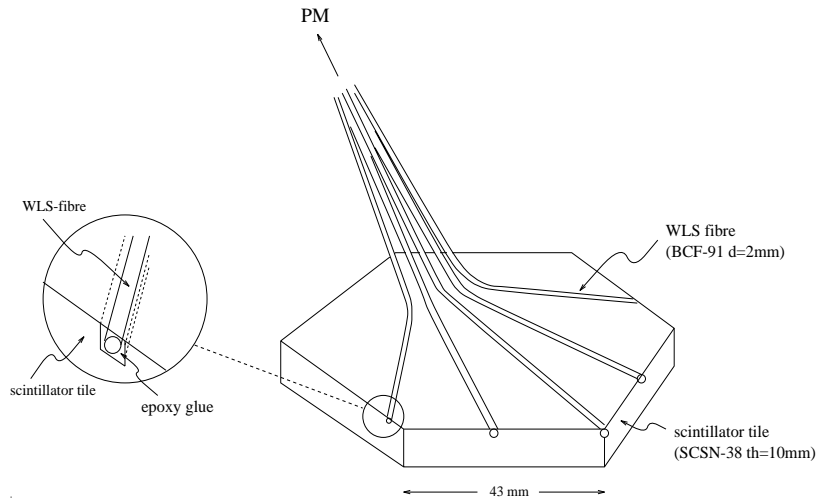


Figure 3.7: Structure of a hodoscope tile.

3.2.3 FNC layout

In table 3.1 a summary of the FNC characteristics is given, while figure 3.8 shows a cut through view of the rebuilt FNC calorimeter. The lead matrix body of the calorimeter is fixed on a steel support frame, allowing for transportability. The bottom and top parts of the calorimeter are separated by the steel support structure of the top part. The top part is fixed to a steel bar with lateral projections, allowing for the removal of the top part, in case the section of the beampipe going through the calorimeter has to be accessed. In the front region, the two hodoscope planes, HP1 and HP2, are located. The hodoscope PMs are positioned directly below the two hodoscope planes, in the space provided by the steel support structure (not drawn). In the back region the fibers are bundled, the light is mixed and guided by the light guides to the PMs. The PMs are cooled by air flow during operation. The pressurized air from an external source (~ 5 atm) is conveyed to the back-end by a pipe and is then distributed to each PM and to the monitoring system (see section 3.9). The whole calorimeter is enclosed in protective aluminum sheets, except for the front and back ends which are closed by thin plastic planes allowing for easy access and providing light protection; a thin plastic plane of low Z material was chosen for the frontend cover (for simplicity also for the backend cover), to have negligible probability for an incident neutron of preshowering in it. With this setup the FNC was put in the CERN test beam for testing and calibration (see section 3.3).

Calorimeter modules	75 (67 bottom, 8 top)	
Hodoscope modules	43 (HP1) and 25 (HP2)	
Calorimeter photomultipliers	Philips XP2282B/01	
Hodoscope photomultipliers	Hamamatsu R647	
Weight	~ 7.5 t (bottom)	~ 1.3 t (top)
Dimension	$205 \cdot 65 \cdot 64$ cm ³ (bottom)	$205 \cdot 39 \cdot 19$ cm ³ (top)
Lead sheets	$49.5 \cdot 1.92 \cdot 2000$ mm ³	
Calorimeter fiber type	SCSF38, 1 mm diameter, 2.2 m long	
Nuclear interaction length (λ_I)	21 cm (9.5 λ_I long)	
Radiation length (X_0)	7.5 mm	
Molière radius R_M	25 mm	
Lead-fiber proportion in volume	4:1	
e/h ratio	1.15 ± 0.02	
Sampling fraction	2.3%	

Table 3.1: Summary of the FNC basic properties and characteristics.

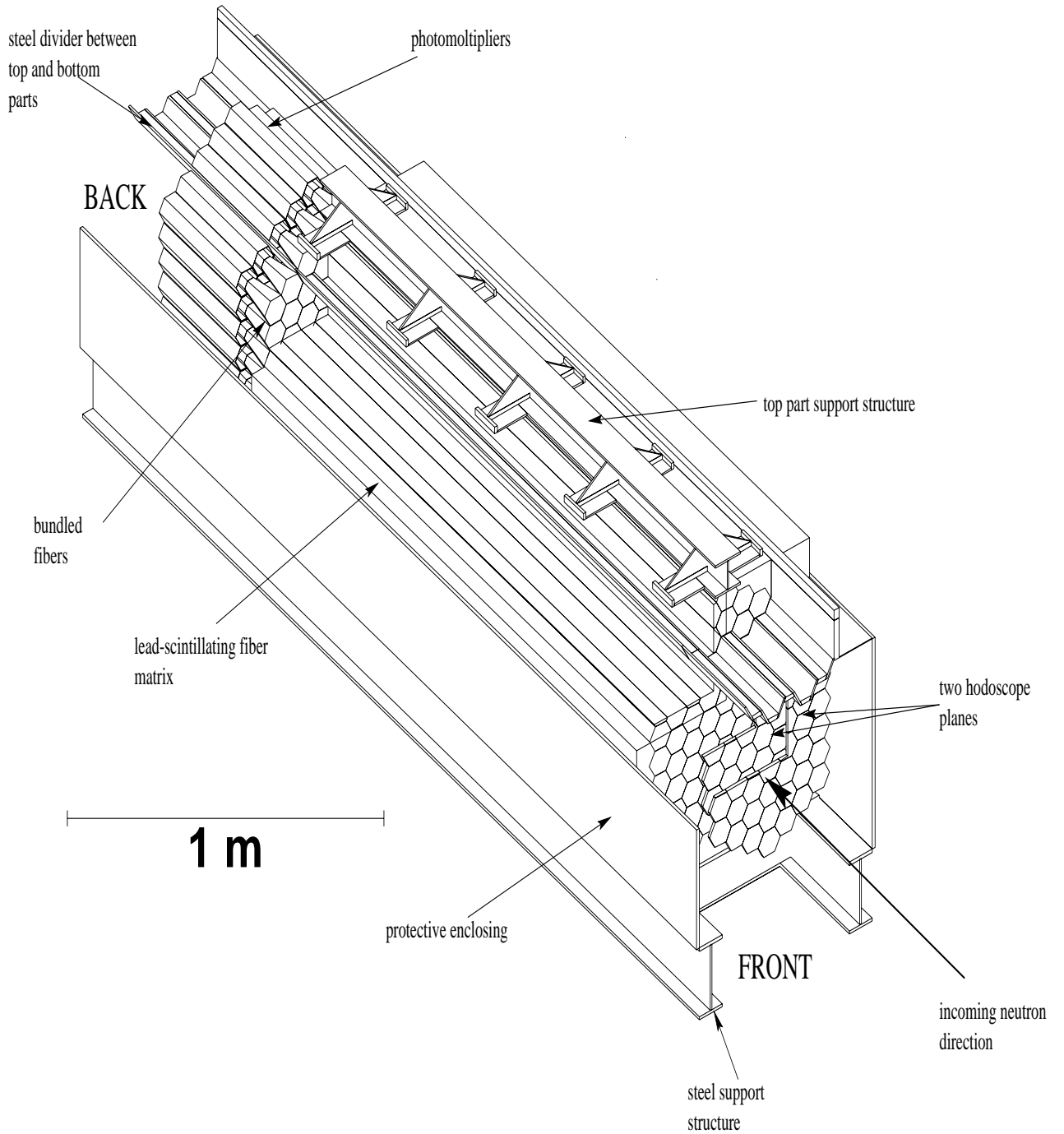


Figure 3.8: Cut through view of the FNC.

3.3 Test Beam Calibration

In autumn 1995 the FNC was put in the T9 test beam fixed target line, in the East Hall, part of the Proton Synchrotron complex at CERN¹⁷ for calibration. Two test beams were used: electrons of 10 GeV and pions (π^-) of 10 and 15 GeV. The FNC was positioned (see figure 3.9) on a movable support table which could be controlled with a precision of ~ 0.1 mm and with the front face directed towards the incoming test beam. Upstream respect to the FNC the following detectors were placed: microstrip chambers for track reconstruction to be used in determining the calorimeter's position resolution of the impact point, two scintillators to be used in coincidence for triggering the event and two Čerenkov gas detectors to distinguish between pions and electrons¹⁸. The same signal cables and FADCs¹⁹ were used to transport and digitize the signals from the FNC, as in its setup in the H1 experiment. A detailed account of the test beam is given in the Diploma Thesis of Thomas Nunnemann[38]. The test beam showed that all calorimeter

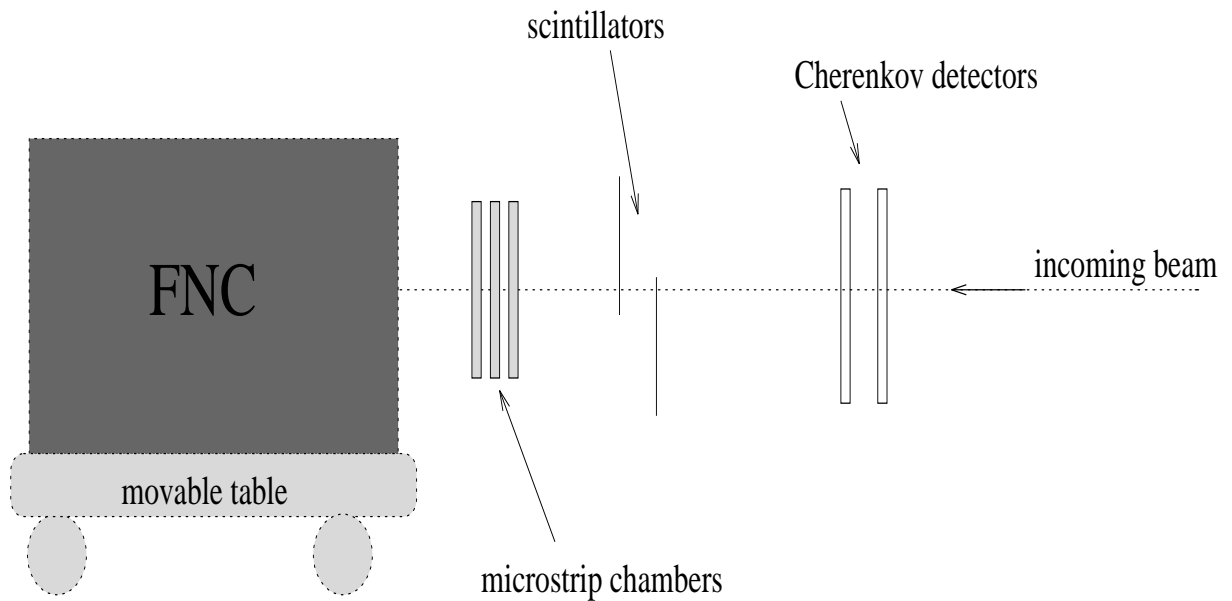


Figure 3.9: Sketch of the test beam setup.

and hodoscope modules were functioning. Figure 3.10 shows a typical calorimeter signal for electrons and pions, both at an energy of 10 GeV. The electron signals are very similar for a given energy, while the pion signals differ due to the fluctuations in the hadronic shower development, leading to fluctuations in the time spectrum of the signals. The

¹⁷The European laboratory for nuclear and particle physics.

¹⁸The experimental line selects particles according to their momentum but not species, so there can be contamination. The pressure in the two Čerenkov detectors (carbon dioxide and helium) was set so that a traversing electron or pion would give a signal in only one of them.

¹⁹FADC-Flash ADC.

light produced in a shower consists of a direct component and a reflected component against the mirror. Deeper inside the calorimeter the light is produced, later the reflected component arrives at the PM, which leads to a broadening of the signal. Hadronic showers have large fluctuations in the longitudinal shower development leading to fluctuations in the time structure of the signals. Neutrons which form a considerable component of the hadronic shower are mainly produced by nuclear evaporation at low energies (\sim few MeV), propagating at $\sim 10^7$ m/s. These lose energy principally by elastic scattering off light nuclei (e.g. hydrogen) in the scintillator fibers, having a mean free path of ~ 0.1 m. This introduces a time constant of about 10 ns which contributes to the broadening of the shower[36].

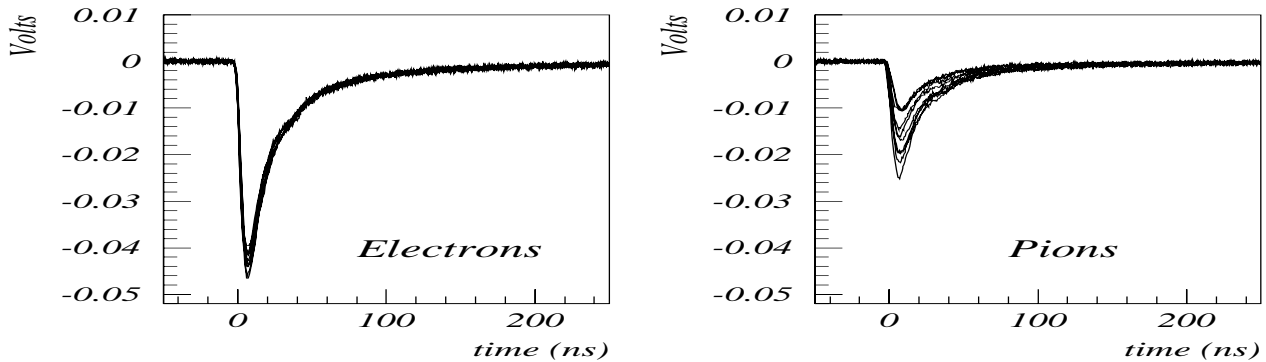


Figure 3.10: Signal recorded by an oscilloscope for electrons and pions both with an energy of 10 GeV for a calorimeter module.

Electromagnetic and hadronic showers can be separated by looking at their lateral shower development. The variable containment C is defined for this purpose, requiring no information about the impact point:

$$C = \frac{\sum_{i \in \{3\}} E_i}{\sum_{i \in \{12\}} E_i}$$

where the numerator is the energy sum of the three neighboring modules containing the highest energy module of the cluster, and the denominator is the energy sum over 12 modules, which consist of the three modules in the numerator plus the first ring of modules surrounding them. Figure 3.11 shows the containment values for the electrons (10 GeV) and pions (15 GeV).

The FNC calorimeter modules were calibrated with 10 GeV electrons. The purpose of the calibration is to find the factor which converts the calorimeter signal into an energy value. By moving the support table, so that the beam would hit the center of a given module, each module's response was measured separately. For each calorimeter module a calibration constant was obtained, that is, for each module a proportionality factor between the energy deposited in the given module and the corresponding calorimeter signal of the given module was found. A preliminary set of calibration constants

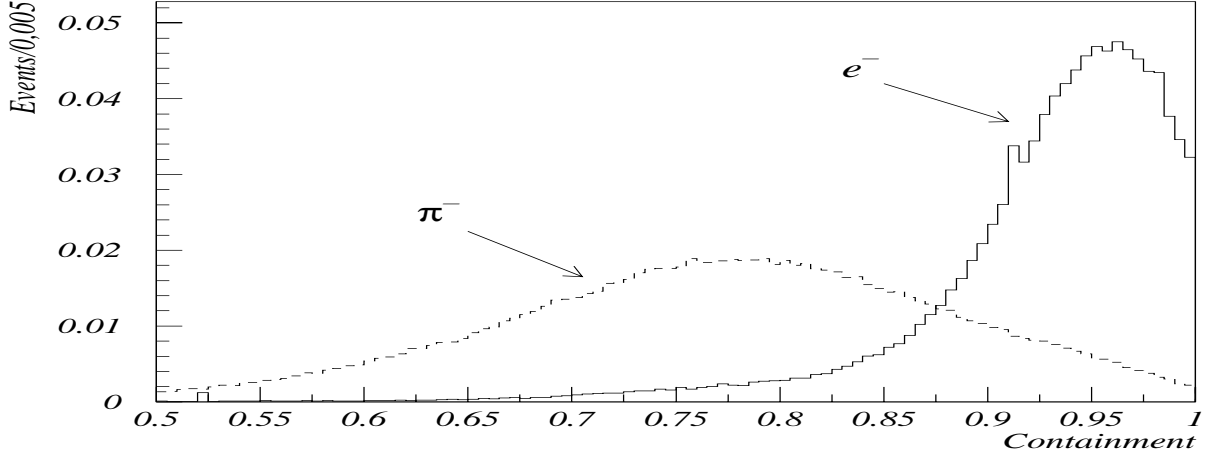


Figure 3.11: Containment value for electrons (10 GeV) and pions (15 GeV). The events are normalized to one.

for the 75 FNC modules was obtained using a matrix inversion method[38]. With this preliminary calibration the FNC had an approximately uniform response, independent from the impact position of the particle (see section 3.10 for final calibration). Once the calibration constants were obtained, the energy resolution was determined from the test beam data[38]:

$$\frac{\sigma_E(10 \text{ GeV})}{E} = (9.8 \pm 0.7)\% \quad \text{for electrons,} \quad (3.12)$$

$$\frac{\sigma_E(15 \text{ GeV})}{E} = (19.1 \pm 1.8)\% \quad \text{for pions,} \quad (3.13)$$

which, when 'extrapolated' to higher energies using equations (3.10) and (3.11), gives for electrons:

$$\frac{\sigma_E(E)}{E} = \frac{(29.8 \pm 4.1)\%}{\sqrt{E}} + (1.2 \pm 0.5)\% \quad (3.14)$$

$$\frac{\sigma_E(E)}{E} = \frac{(30.3 \pm 2.9)\%}{\sqrt{E}} \oplus (2.0 \pm 0.5)\% \quad (3.15)$$

while for pions:

$$\frac{\sigma_E(E)}{E} = \frac{(64.2 \pm 10.8)\%}{\sqrt{E}} + (2.5 \pm 1.0)\% \quad (3.16)$$

$$\frac{\sigma_E(E)}{E} = \frac{(72.2 \pm 8.0)\%}{\sqrt{E}} \oplus (4.1 \pm 1.0)\% \quad (3.17)$$

where E is in GeV and the constant term has been taken from the LAA project with an error ten times greater[43]. At HERA energies the energy resolution is worse than these extrapolated values (see section 3.11.1).

The position resolution was also determined by comparing the reconstructed FNC impact position data and the microstrip chambers data for 15 GeV pions, giving an average value of $\sigma_{xy} \approx 1.3 \text{ cm}$.

3.4 Installation

To detect small angle ($\lesssim 1 \text{ mrad}$) leading neutrons produced in the ep process occurring at the interaction point, the FNC was installed in the forward region of the tunnel respect to the H1 experiment position. This could be done since the proton beam is bent upwards respect to the HERA ring horizontal plane, leaving some place for the installation of a calorimeter around the zero degrees line of flight. The FNC was transported to DESY at the beginning of 1996 and then placed in the tunnel by the HERA tram at the beginning of 1996, in the same location of the previous test-FNC[39], at $z=107 \text{ m}$ downstream (respect to the proton beam) of H1.

Figure 3.12 displays the proton beamline from the interaction region in H1 to the FNC location. The electron and proton beams travel through the same beampipe from the interaction point in H1 up to $z=24 \text{ m}$, where they are separated into two beampipes each having their own magnets. The proton beam is deflected horizontally by the magnets BH04 and then deflected upwards by 5.7 mrad ($\sim 0.3^\circ$) between $z=65$ and 79 m by the bending magnets BU00. The FPS stations (see section 2.2.6) are located immediately after the bending magnets using them as a proton spectrometer. The leading neutrons are produced in $ep \rightarrow e'nX$ with small angles ($\lesssim 1 \text{ mrad}$) with respect to the proton's incoming direction. These small angle neutrons are undeflected by the magnets and travel nearly parallel to the ep collision line (zero degrees line of flight), exiting the proton beampipe through a window (to reduce the amount of dead material) around $z=93 \text{ m}$. The charged particles originating in the interaction region of H1 are deflected by the proton beam magnets and do not reach the FNC, while any neutral particle decays on the way before reaching the FNC (except for photons). To have a large separation between protons and neutrons, a free place along the proton beamline had to be found for the FNC, at some distance after the vertical deflection of the protons. In the region from $z=80$ and 120 m there are no proton beam elements, just vacuum pumps and the FPS stations, then the proton superconducting section begins; so a suitable place for installing the FNC was found²⁰ at $z=107 \text{ m}$. The angular acceptance for the neutrons is defined by the apertures of the proton beamline elements between the FNC and the interaction region; mostly neutrons²¹ that remain within the beampipe until the last vertical proton bending magnet will reach the FNC. Neutrons that have interacted with the dead material along the path before reaching the FNC are rejected by the hodoscope planes.

²⁰The test-FNC was previously installed in the same position.

²¹Also low energy photons ($\lesssim 300 \text{ GeV}$) from π^0 decay can reach the FNC.

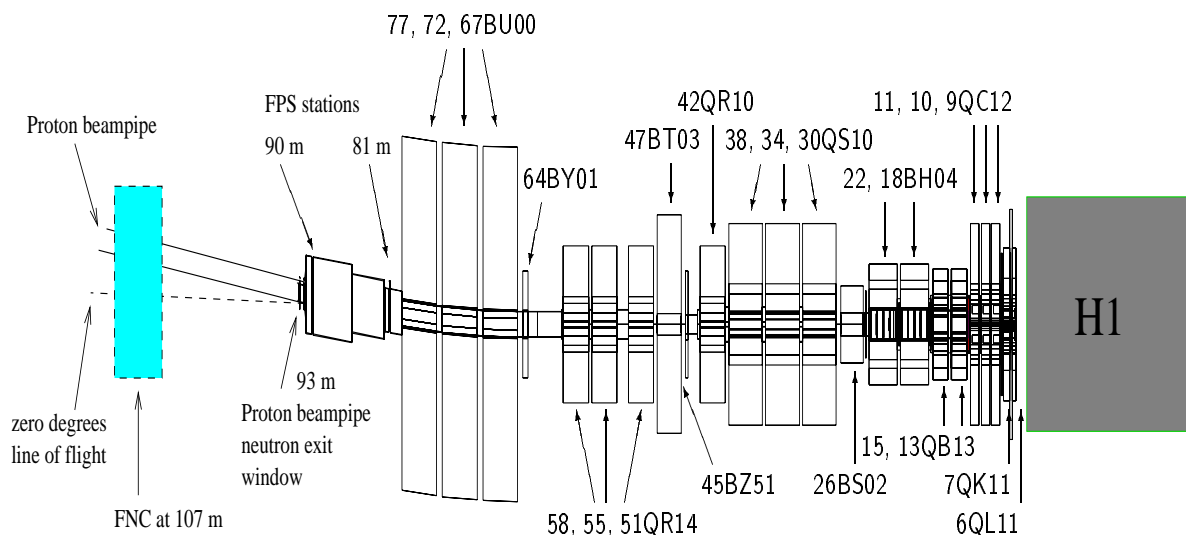


Figure 3.12: Not to scale sketch of the proton beamline from H1 to the FNC position. The names of the magnets are indicated. The first one or two numbers indicate the distance from the interaction point while “Q” and “B” denote quadrupole and bending magnet respectively. The first five magnets ($z=6$ to 11 m) are actually within the forward region of the H1 detector.

Figure 3.13 shows a cross section of the HERA tunnel where the FNC is located. The tunnel has an inner radius of 250 cm and the outer radius (including circular concrete wall) of 280 cm. The FNC is positioned to the right with respect to the electron beampipe and electron magnet, and it is supported by steel bars. The proton beampipe goes through the gap between the bottom and top parts of the FNC. Above, there is the helium transfer line, below left is the quench line into which the evaporating helium can flow if superconductivity collapses in one of the proton magnets. The water cooling system is used by the electron ring to counteract the heating caused by the synchrotron radiation produced by the electron beam. On the left there is the HERA tram lane and walking lane for people, with which the FNC was brought into the tunnel by the HERA tram.

Figure 3.14 shows a top view of the tunnel around the FNC position. The FNC lies between two proton ring vacuum pumps between $z=105$ m and $z=108.5$ m. Through it runs the proton beampipe and on the side there are the radiofrequency cavities and a quadrupole magnet of the electron ring. To protect the FNC from synchrotron radiation from the nearby electron beam, it was covered by lead sheets with a total lead thickness varying from 8 to 15 mm.

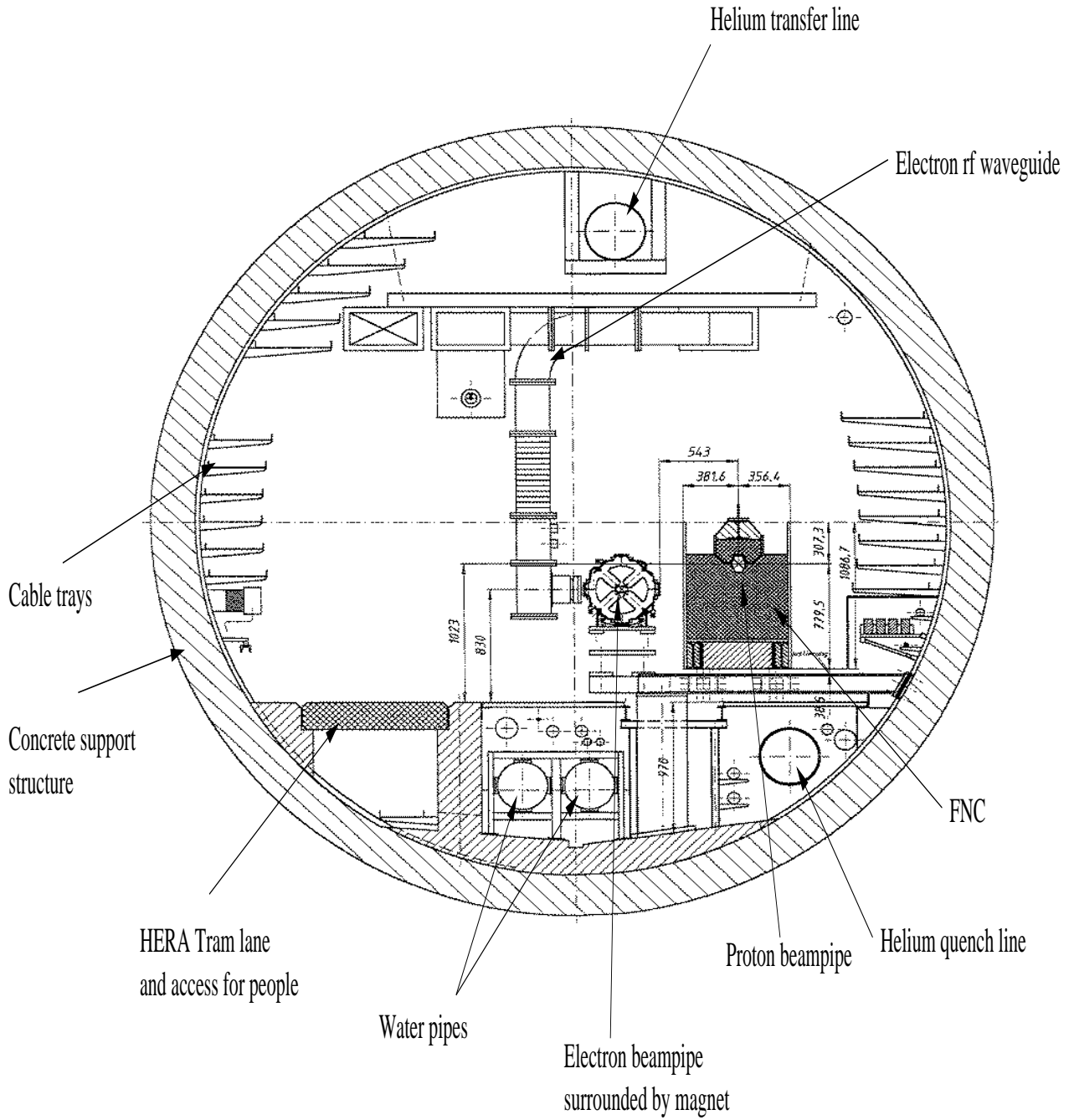


Figure 3.13: Cross section of the HERA tunnel where the FNC is located.

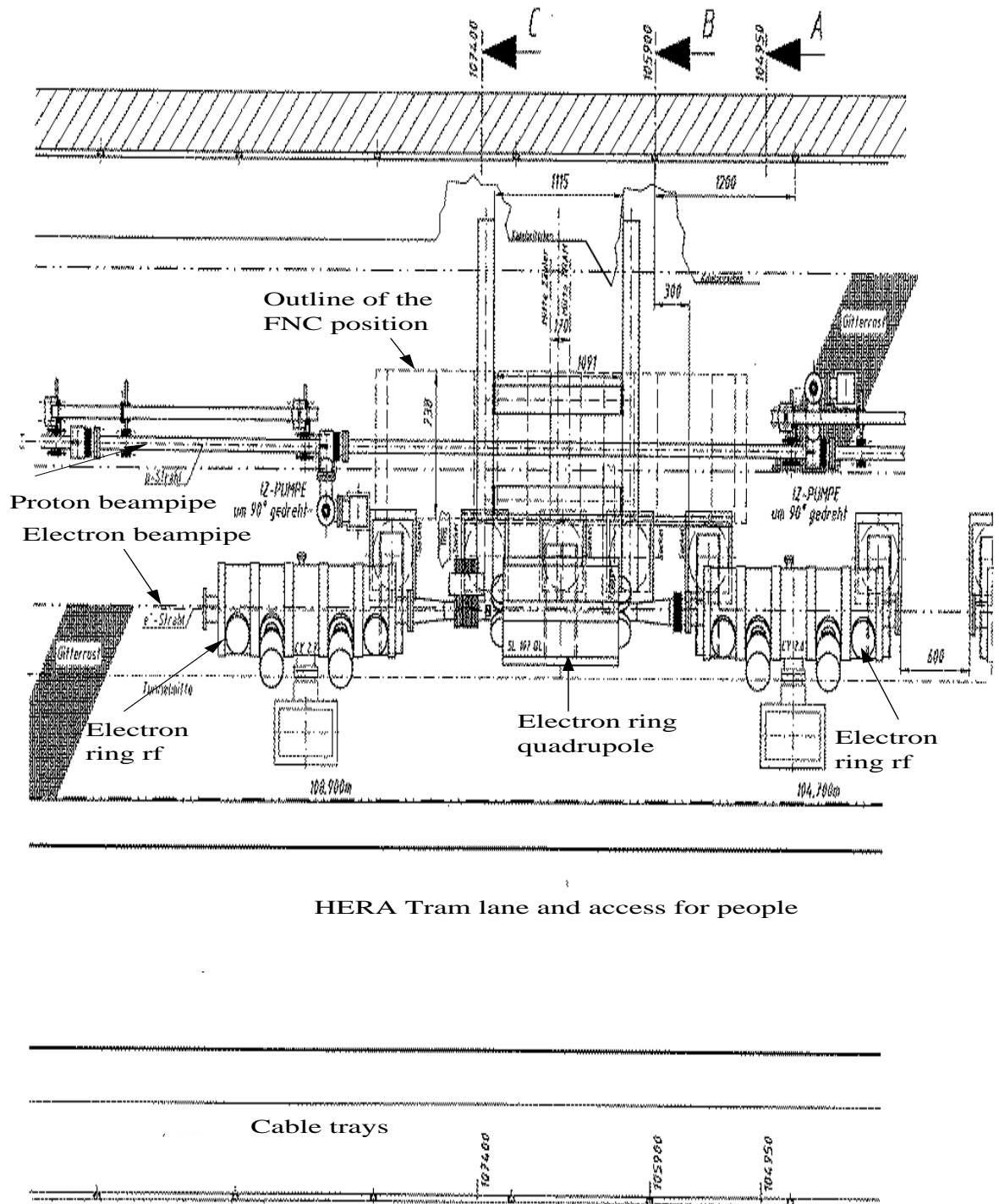


Figure 3.14: Top view of the HERA tunnel where the FNC is located.

Some additional components were added to the FNC after its installation in the tunnel, see figure 3.15:

- Two charged particle veto planes ($230 \cdot 150 \cdot 5 \text{ mm}^3$) are placed 2 m upstream from the front face, with a distance of 10 cm in between them, and covering the acceptance area, to study hodoscope efficiencies for charged particle rejection.
- Two finger counters, to be used in coincidence with the purpose of studying the position resolution of the impact points. Each counter consists of two small scintillators ($3 \cdot 3 \cdot 10 \text{ mm}^3$) about 4 cm apart, a light guide and a photomultiplier of same type as used for the hodoscopes. The two counters are positioned outside of the two hodoscope planes at the lower edge of the acceptance area, one in front of the other so that both cover a common sensitive area of about 5 mm^2 .
- Two tail catchers scintillator plates ($300 \cdot 300 \cdot 10 \text{ mm}^3$) are placed just under the lead covering in the backend region, with a lead plate in between them of same dimensions, to detect any longitudinal shower leakage.
- A lead-scintillator tail catcher is placed outside the lead covering of the back region. It was installed during the 1996/97 winter shutdown to improve the longitudinal shower leakage detection. It consists of a sandwich of alternating plates of lead (12 pieces of $300 \cdot 300 \cdot 14 \text{ mm}^3$) and scintillator (13 pieces of $304 \cdot 304 \cdot (2.6 \cdot 2) \text{ mm}^3$) with wavelength shifters on the two lateral sides, which are conveyed to one PM. It is covered by lead to protect it from synchrotron radiation.

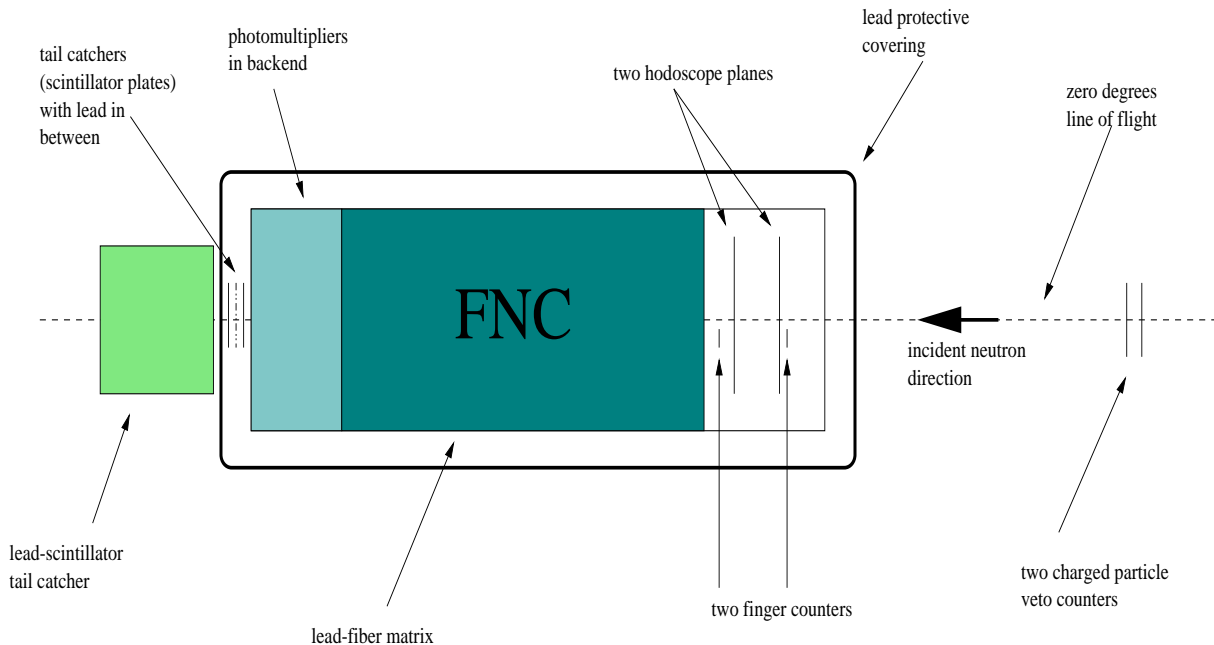


Figure 3.15: Side view scheme of the FNC's components.

3.5 FNC Data Acquisition and Electronics

The FNC's data acquisition, high voltage supply and electronics are installed in room 101 of the H1 experimental hall, also called HERA North. All the various FNC modules receive high voltage by ~ 150 m long high voltage cables, which connect the FNC to the high voltage crate (LeCroy System 1440) in room 101. Similarly the FNC signals are brought by ~ 140 m long coaxial cables to the VME²² crate for digitization by FADC²³ modules. In addition there are also sixteen fast air core (RG213) 150 m signal cables, which are connected to the secondary outputs of the photomultipliers of the sixteen central calorimeter modules, for calorimeter cluster timing studies, and are also digitized by the FADCs in the VME crate.

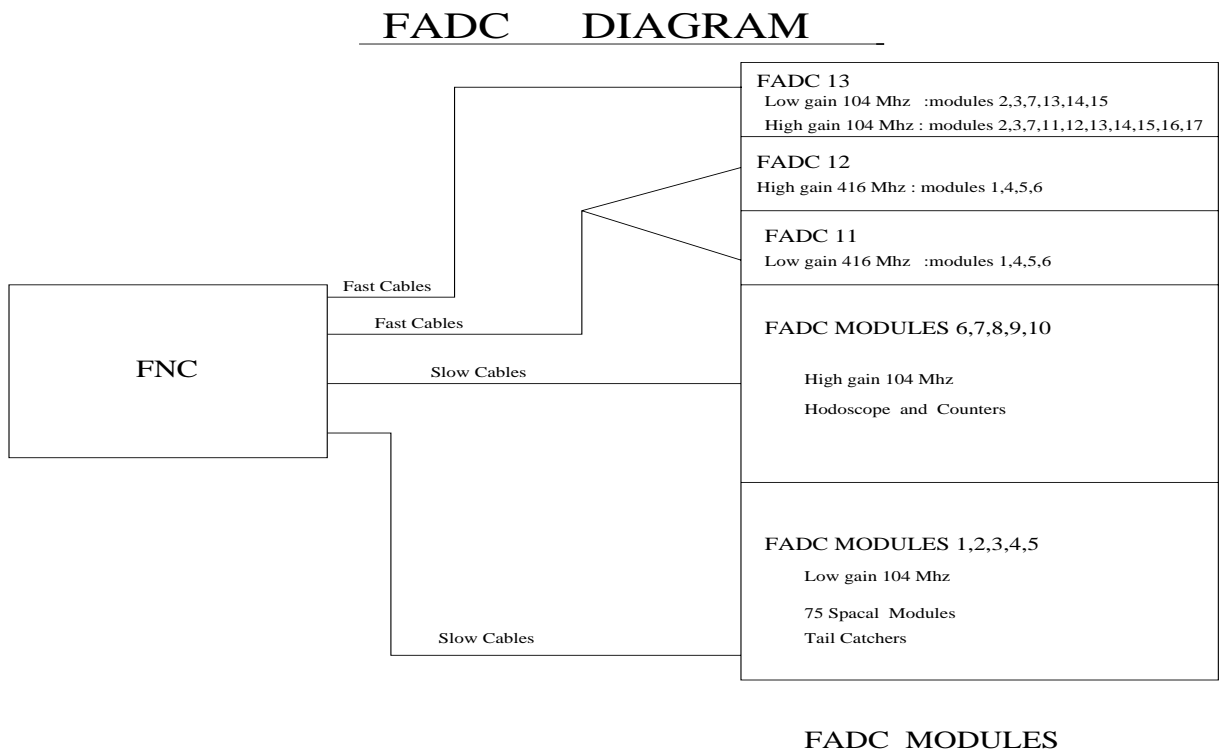


Figure 3.16: The diagram for the 13 FADC connections to various FNC modules. They are divided into three groups FADC1-5, FADC6-10 and FADC10-13. Slow cables refer to the coaxial cables, while fast cables to the air core (RG213) cables.

All the signals produced by the various FNC modules are digitized by a total of 13 FADC modules which are divided in three groups (figure 3.16). The typical digitized signals for these three FADC groups are shown in figure 3.17. Each FADC of the first two groups have sixteen channels, an 8 bit resolution, a 104 MHz frequency and a maximum

²² *Versa Module Europa*- a flexible open ended bus system.

²³ The FADC is a *Flash Analog to Digital Converter* specially built for H1 (Struck F1002).

gate of $2.46 \mu\text{s}$, corresponding to 256 timeslices of 9.6 ns each. The HERA bunch crossing time is 96 ns , and the timeslice length is a tenth of it. The 75 calorimeter modules and the three tail catchers are connected to the first group of five FADCs. These have a low gain preamplifier so that the signal is reduced to $\sim 80\%$ of its initial value, to have the signals within the FADC acceptance. The time window for digitizing the signal is 16 timeslices, 3 timeslices for the pedestal determination and 13 for the actual signal, which allows to register the main part of the signal and limit the FNC data volume. The hodoscope planes, veto planes and finger counters are connected to the second group of five FADCs with high gain preamplifiers, which increase the signal by a factor 8. There are 8 timeslices, 3 timeslices for the pedestal determination and 5 for the actual signal, which are enough to determine whether a given module produced a noticeable signal or not. The third group of three FADCs are connected to the sixteen central modules via the above mentioned fast cables (RG213), for studying low and high energy clusters and their timing. The secondary outputs of the four central calorimeter modules (modules 1,4,5,6) are connected to two 416 MHz FADCs²⁴ of low (~ 0.8) and high gain (~ 8) respectively, which have only four channels, but 2.4 ns timeslices to have a finer digitalization of the signal respect to time. The other 12 modules surrounding these four central modules are connected to a 104 MHz FADC, with some channels at low gain (~ 0.6) and some at high gain (~ 8), to complete the necessary cluster information. These three modules have the 3 and 12 timeslices for the pedestal and 7 and 28 timeslices for the signal respectively for the 104 and 416 MHz FADC, because with the fast cables the signal is narrower.

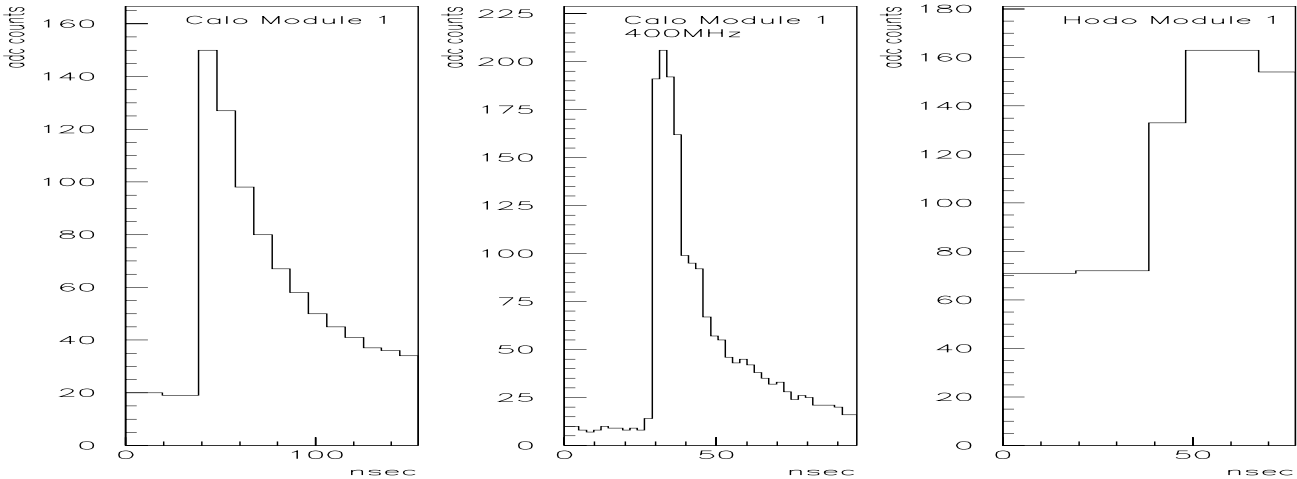


Figure 3.17: The digitized signals of physics events for the three different FADC groups. The left histogram is the digitized signal of calorimeter module 1 connected to FADC1 (first group), the right one is the digitized signal of the hodoscope module 1 of plane 1 (FADC7- second group) and the center one is that of calorimeter module 1 connected to FADC11 with fast cables.

²⁴The 416 MHz FADC is an especially modified version of the normal Struck F1002 104 MHz FADC.

The sensitivity curves, which give the relation between the voltage of the signal and its FADC digitization in adc counts, are shown in figure 3.18 for two different FADC channels. The fit function fits well to the measured data points and is of the type:

$$y = \frac{1}{(\text{par}(1) - (\text{par}(2) * x))} - \text{par}(3) \quad \text{with } y - \text{volts, } x - \text{adccounts, } \text{par} - \text{parameters.} \quad (3.18)$$

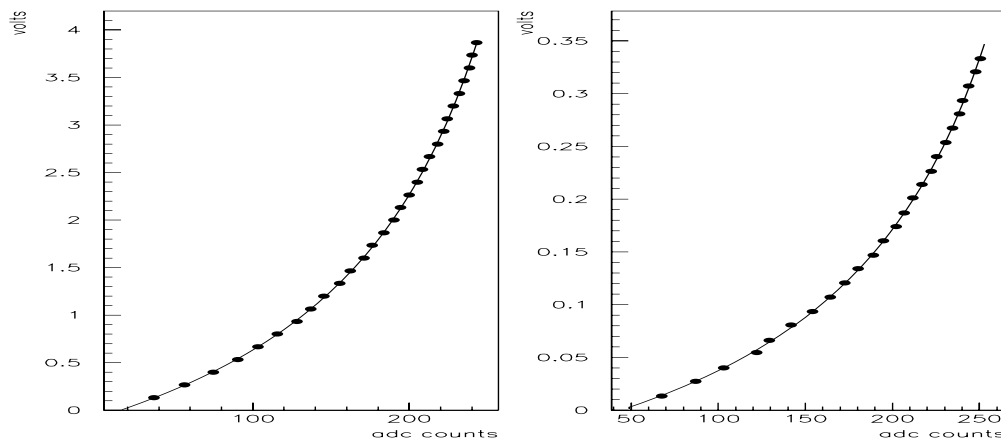


Figure 3.18: Sensitivity curves for two different FADC modules. The left one corresponds to the first channel of FADC1 (low gain- calorimeter modules); the right one to the first channel of FADC7 (high gain- hodoscope modules). The maximum number of adc counts for any FADC channel is 255. The dots correspond to the measured data (errors are within the dot size), while the curve is the fit.

The data acquisition is controlled by the FASTBUS system, which reads out the FADCs and pipelines the data at the HERA clock rate²⁵ to the central H1 data acquisition system and to the local data acquisition that is running on a DEC²⁶ Alpha machine (axhrs1.desy.de). The FASTBUS also controls a CAMAC²⁷ crate which houses the interface for controlling the high voltage system, the ADCs for the monitoring system and for the digitization of the recorded temperatures in the back end of the FNC.

The Slowcontrol[45] system is used to record all data which serve for the monitoring of the detector performance and which are usually produced “slowly” respect to the bunch crossing time, e.g. high voltage values, trigger rates, temperatures, photomultiplier monitoring, etc. It is also running on the same Alpha machine as the data acquisition, and is connected to the electronics by a SCSI²⁸ interface via a CHI²⁹ processor located in the FASTBUS crate. These Slowcontrol variables can be inspected online with an FNC

²⁵A 10.4 MHz gate which corresponds to the HERA bunch crossing time rate.

²⁶Digital Equipment Corporation.

²⁷FASTBUS and CAMAC are data acquisition system standards.

²⁸Small Computer System Interface - an interface between a computer and other devices.

²⁹CERN Host Interface.

Xterminal in the H1 control and electronics room. Figure 3.19 shows the general layout of the FNC data acquisition and electronics.

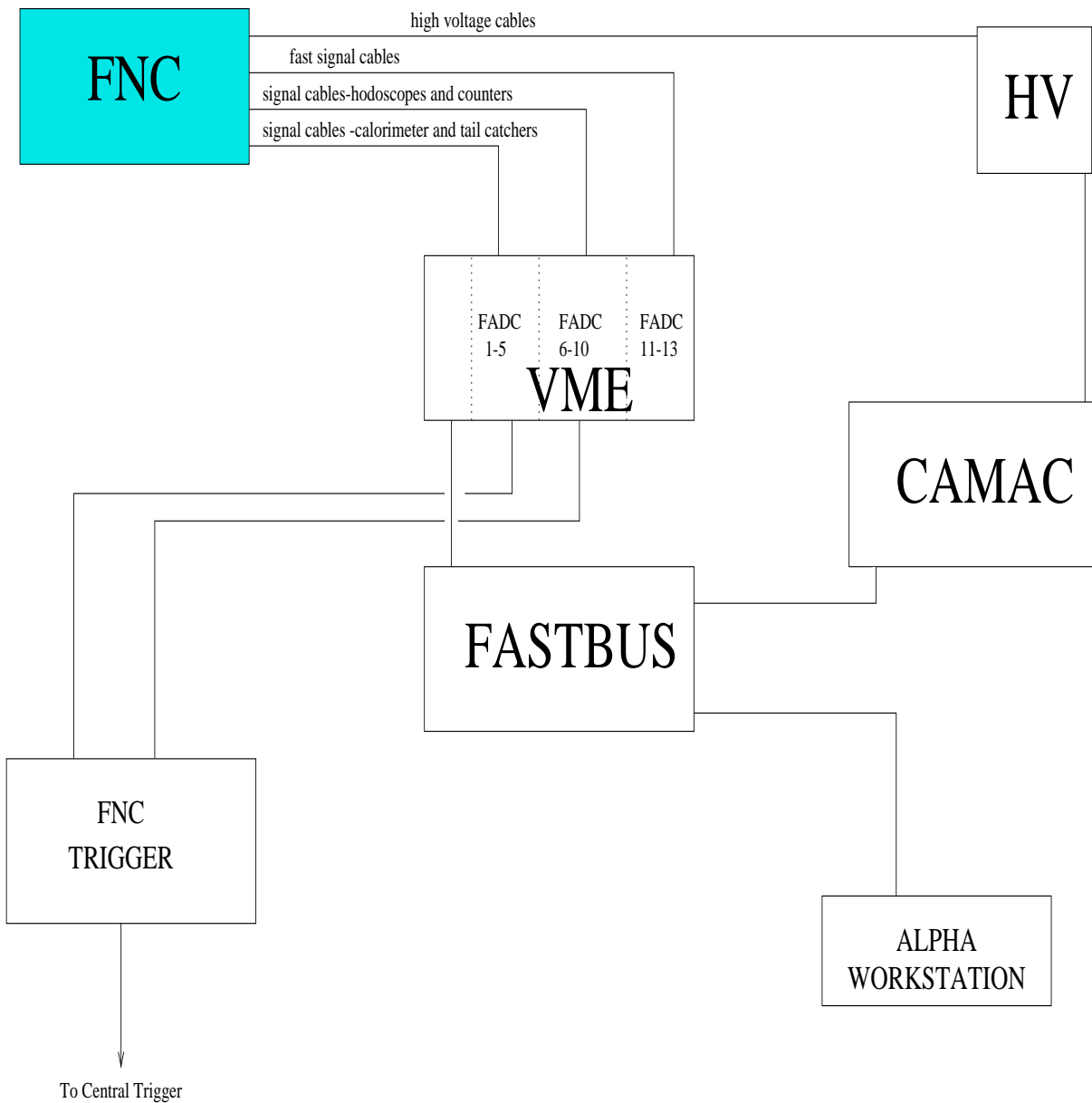


Figure 3.19: FNC data acquisition scheme.

3.6 FNC Trigger

The FNC must provide a trigger to H1, for ep events depositing energy in the calorimeter, of which a considerable part have final state neutrons. The FNC trigger consists of eight trigger elements and of three subtriggers (see section 2.2.7 for clarification of these terms). Four trigger elements are grouped together to form a four bit binary number providing sixteen possible values. These are used to define eight different energy threshold levels for the energy deposited by an event in the FNC³⁰. Each of the other four trigger elements correspond to a one bit binary number giving a yes/no value. They are used respectively to set the LED³¹ monitoring flag, the flag for a coincidence hit in the tail counters, the flag for a coincidence hit in the finger counters and the flag for a hit in the central part of hodoscope plane one. The three subtriggers consist of one monitor subtrigger and two physics subtriggers. The monitor trigger is defined by the FNC monitor trigger element and is used to flag FNC monitor events. The two physics subtriggers are used to differentiate between very low Q^2 events (photoproduction) and deep inelastic events with $Q^2 < 100 \text{ GeV}^2$. The photoproduction FNC subtrigger is defined by a triple coincidence between the electron tagger, the central drift chambers and the FNC energy sum (at least the lowest FNC energy threshold level must be set) trigger elements. The deep inelastic scattering FNC subtrigger is defined by the coincidence of FNC energy sum (here at least the second lowest FNC energy threshold level must be set) trigger element and the SPACAL IET (inclusive electron trigger) subtrigger, which is designed to trigger on the electrons hitting the SPACAL electromagnetic section[29]. In table 3.2 the FNC triggers are listed.

Trigger Elements	Definition
FNC_SUM	trigger elements 176–179: \rightarrow energy deposited in the FNC
FNC_MONI	trigger element 180: \rightarrow LED monitoring flag for FNC
FNC_TAIL	trigger element 181: \rightarrow coincidence hit of the two tail counters
FNC_FINGER	trigger element 182: \rightarrow coincidence hit of the two finger counters
FNC_HODO	trigger element 183: \rightarrow central hit of hodoscope plane 1
Subtrigger	Definition
S89	ETAG && FNC_SUM && DCRPh_Ta: \rightarrow FNC photoproduction subtrigger
S115	FNC_SUM > 1 && SPCLe_IET > 1: \rightarrow FNC DIS subtrigger
S123	FNC_MONI : \rightarrow FNC monitoring subtrigger

Table 3.2: FNC trigger elements and subtriggers.

³⁰The full capacity of 16 thresholds is not used since such subdivision of the energy range 0-820 GeV is too fine.

³¹LED-Light Emitting Diode; see the section 3.9 on monitoring.

The FNC trigger diagram is shown in figure 3.20. The linear summer adds the energy signals from 64 calorimeter modules³². The total energy sum signal is then fed to four linear fan-in/fan-out modules, that split the signal into eight equal signals, which go to an octal discriminator of 8 different thresholds. To distinguish between monitoring and physics events, the discriminators are vetoed in case of a monitor trigger, labeled 'flash' in the diagram. The 8 discriminator thresholds are set with increasing value corresponding to about 80 GeV for the lowest one, to about 1200 GeV for the highest one³³. Each discriminator is connected to a scaler for monitoring purposes, which counts the number of times the threshold is exceeded, and to the SYNC module. The SYNC module is needed to synchronize the arrival of the different signals from the FNC trigger electronics using the HERA clock³⁴ and send them to the GPTP³⁵ module, the later which is the interface to the central trigger for setting the FNC trigger elements. Similarly, the monitor, hodoscope, finger and tail trigger elements are respectively set when: the FNC electronics produce a signal to flash the LEDs; if any of the four central hodoscope modules of HODO1³⁶ is hit; if there is a coincidence hit between the two finger counters and also the hodoscope module between them; and if there is a coincidence hit between the two tail counters.

The FNC energy sum trigger (FNC_SUM), which triggers on the amount of energy deposited in the calorimeter, is the most important FNC trigger since the two FNC physics subtriggers, which will determine if an ep event with energy deposited in the FNC will be readout or not, are defined using it³⁷. FNC events with only one reconstructed cluster (one hit) in the FNC are considered here, since events with more clusters are a small fraction of the total FNC events and are discarded in the physics analysis, because a clean ep scattering leading neutron event is expected to contain only one incident particle (see section 3.7). Its efficiency (FNC_SUM) is shown in figure 3.21 for the different thresholds (the 8th threshold is too high to be seen). It has been calculated by considering the ratio between FNC events (with only one hit) with the FNC_SUM trigger set (for different thresholds) together with any other H1 subtrigger (excluding the FNC subtriggers), and FNC events (with only one hit) with any of the other H1 subtriggers set (excluding the FNC subtriggers). A trigger efficiency of $\sim 100\%$ is obtained for deposited energies in the FNC above 200 GeV; the inefficiency region lies below the pion exchange process energy range (>400 GeV) which we are studying.

³²In 1996 the energy sum was done on 64 out of 75 calorimeter modules, that is on all calorimeter modules except for the 11 outer ones, which anyway are far away from the acceptance area and do not contribute to the signal. In 1997 the energy sum was done only on the 16 central calorimeter modules which contain most of the shower, to reduce the background energy noise contribution from outer modules.

³³Such a high unphysical value was chosen to trigger on double hits.

³⁴A 10.4 MHz gate which corresponds to the HERA bunch crossing time rate.

³⁵General Purpose Trigger Pipe.

³⁶Hodoscope plane one, modules (1,4,5,6).

³⁷Most of the FNC events, as expected, have also other H1 subtriggers set and they would be anyway readout.

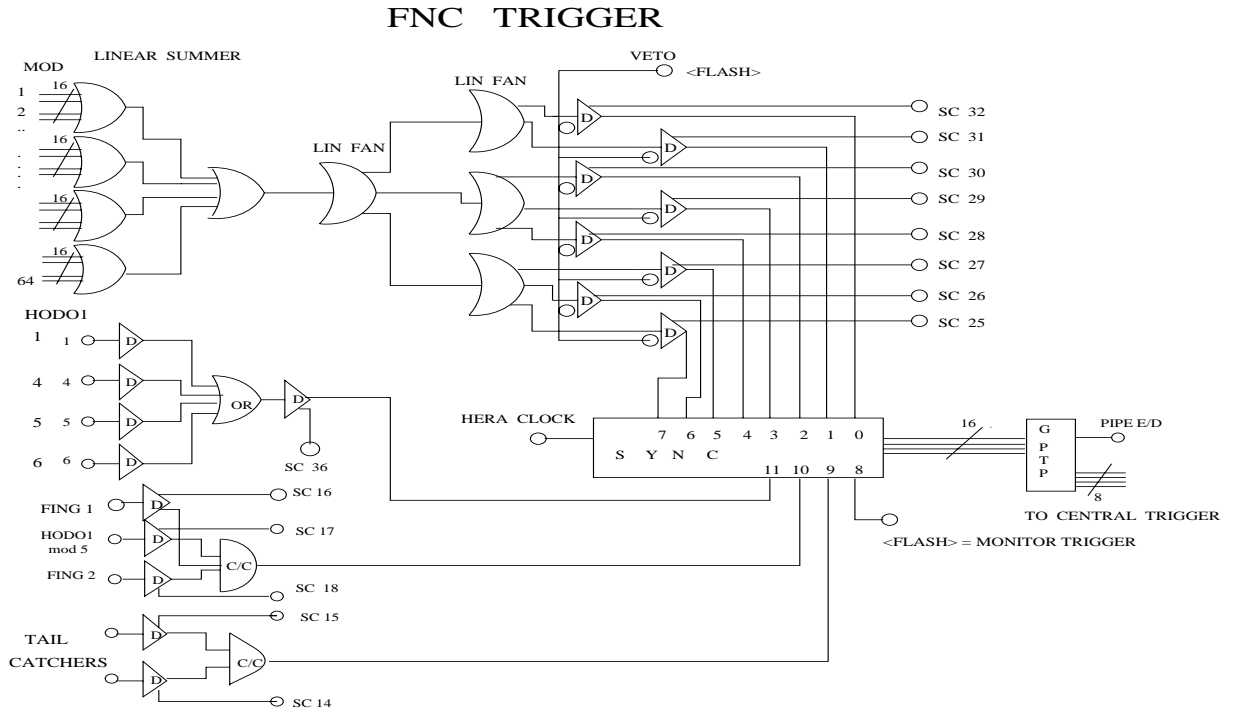


Figure 3.20: The FNC trigger diagram.

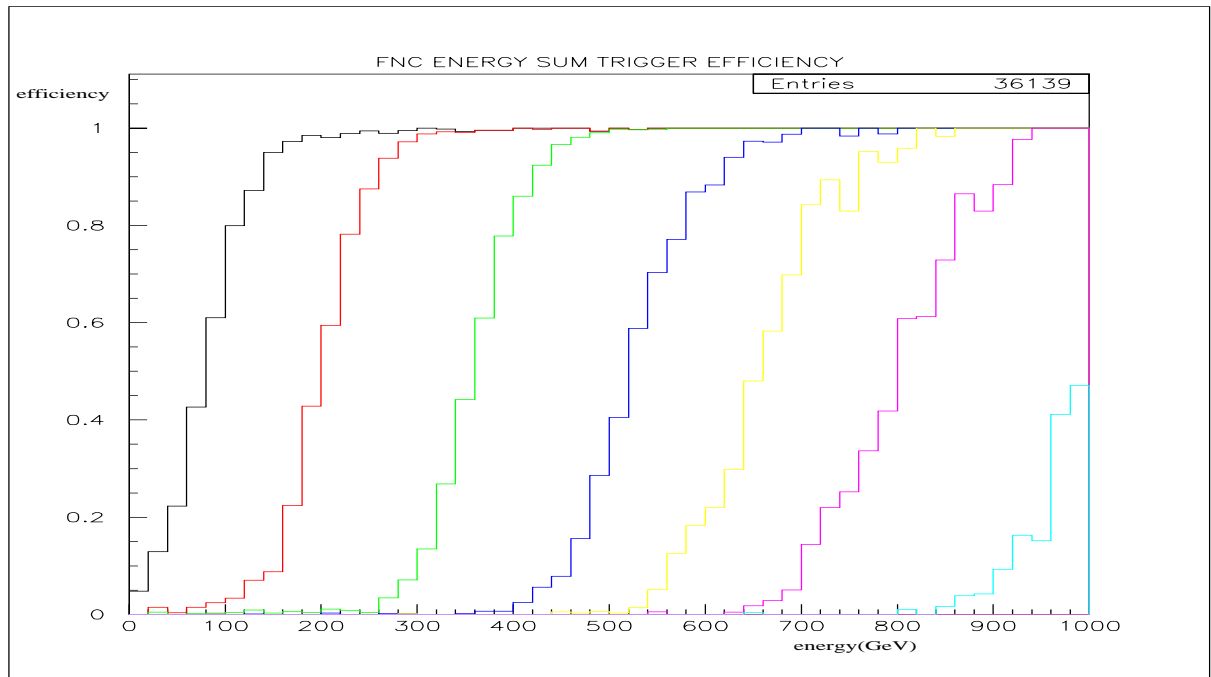


Figure 3.21: The FNC energy sum trigger efficiency (FNC_SUM) for the different energy thresholds (1996 data). The leftmost histogram corresponds to the lowest energy threshold and the rest are in increasing order.

The two physics subtriggers (see figure 3.22) subdivide the FNC events (only one hit): for energies >250 GeV about 20% of the FNC events are set by the FNC photoproduction trigger (S89)³⁸, while for energies³⁹ >350 GeV about 70% of the FNC events are set by the FNC DIS trigger (S115). Not all FNC events have a FNC subtrigger set, $\sim 10\%$ are unset, due to the cuts imposed by the other non FNC trigger elements defining the FNC subtriggers. However, about 15% (>300 GeV) of FNC events are set only by the two FNC subtriggers and by no other H1 subtrigger ($\sim 8\%$ only subtrigger 115 and $\sim 7\%$ only subtrigger 89).

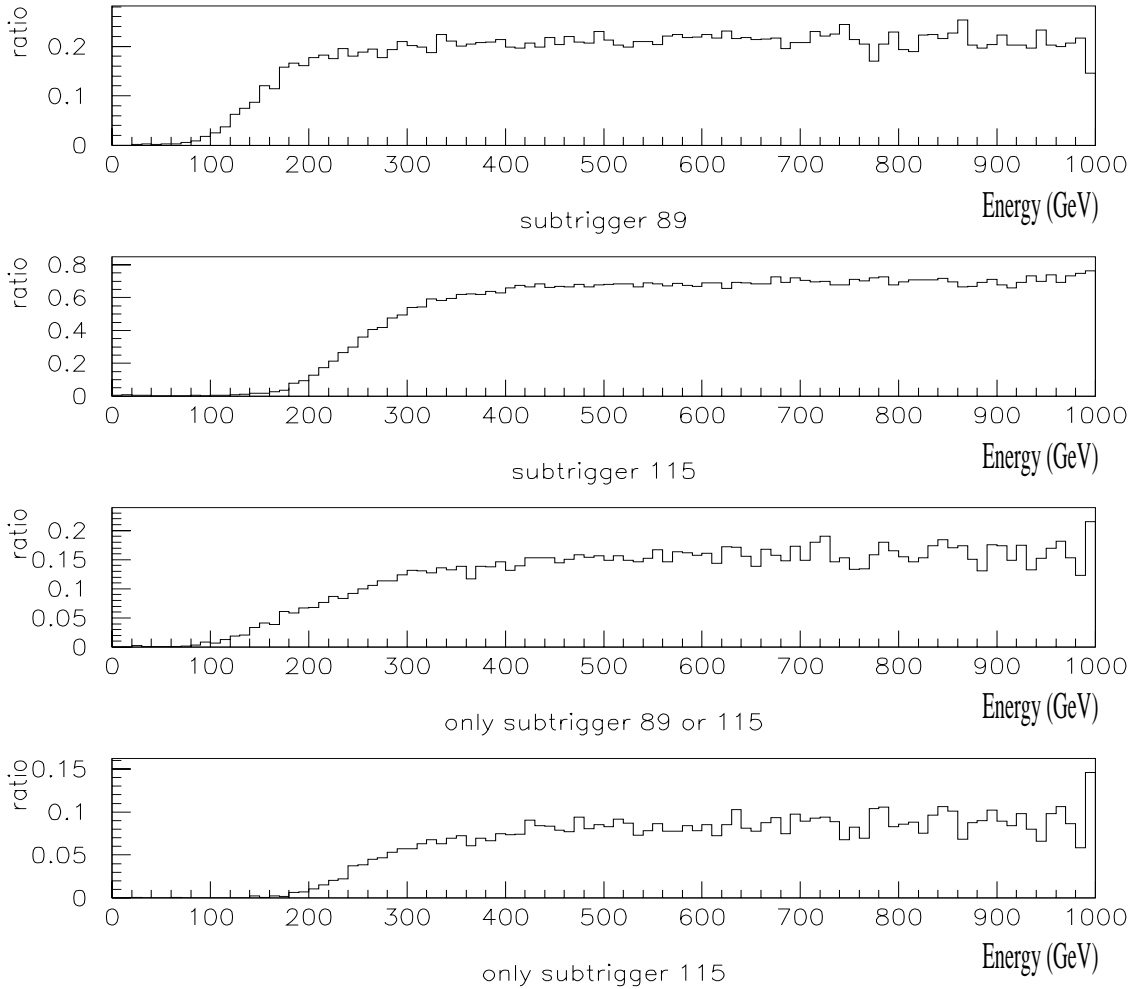


Figure 3.22: From top to bottom, these are the ratios between the FNC events having respectively subtrigger 89 (photoproduction) set, subtrigger 115 (DIS) set, only subtrigger 89 or 115 with no other H1 subtrigger set, and only subtrigger 115 set (no other H1 subtrigger set) and the total FNC events. These ratios are versus the energy deposited in the FNC. 1996 data from the H1 data quality ntuple is used and the considered FNC events have only one hit in the FNC.

³⁸Also other H1 subtriggers can be set contemporaneously.

³⁹The energy is higher because the second lowest threshold of FNC_SUM is used instead of the first.

Figure 3.23 shows the rates for the three FNC subtriggers and trigger element 176, during luminosity data taking of 1997 which are similar to 1996. The monitor subtrigger (S123) has a constant rate of about 0.8-0.9 Hz , which was reduced from the 3 Hz of 1996, when the monitor signal to flash the LEDs became common to both FNC and SPACAL, while the two FNC physics subtriggers (S89 and S115) vary roughly between 0.01 Hz and 1 Hz . The rate of trigger element 176, which is the lowest FNC_SUM threshold and determines if there is a hit or not, varies according to the different luminosity phase beam conditions.

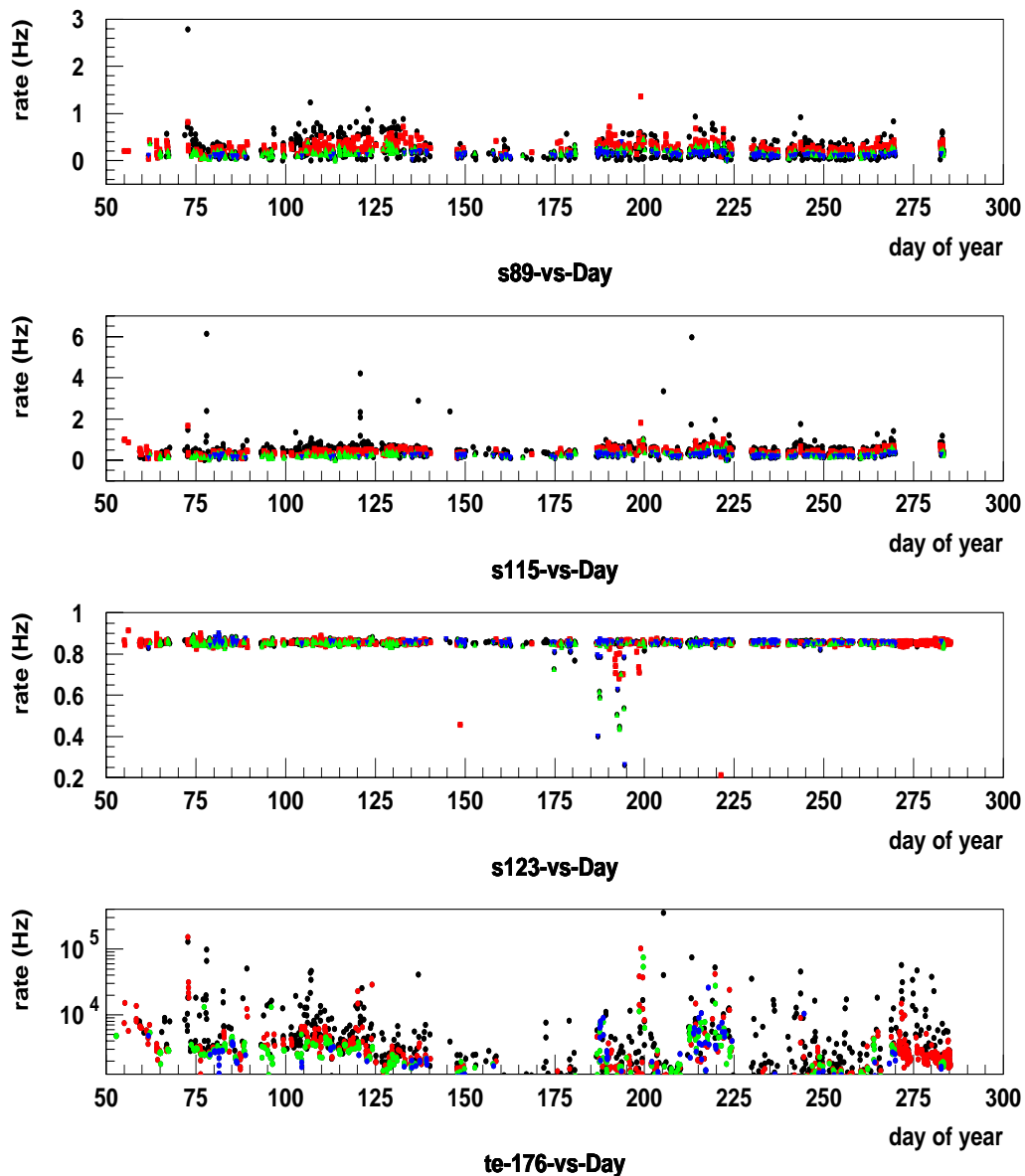


Figure 3.23: The FNC trigger rates versus day of the year for luminosity runs (1997). The different grey-scale of the dots correspond to the different luminosity phases.

3.7 FNC Events

3.7.1 FNC Data Banks and Classification

Whenever one of the FNC subtriggers is set, the whole H1 event information from the various detectors is read out by the H1 data acquisition system and passed through the H1 trigger⁴⁰. Events that survive the H1 trigger are then saved to raw data tapes (RDT). The FNC raw data events, consisting of FADC digitized signals of all the various FNC components, are stored on the RDT tapes, in which each FNC event is saved as a BOS[31] bank, called *LFNC*. These raw FNC events are then reconstructed using the FNC reconstruction program *FNCREC*, which is part of the H1 general reconstruction program *H1REC*. The FNC parameters, such as calibration constants, sensitivity curves, pedestal definition, position of modules, etc., are stored in the NDB database[46] as banks⁴¹ for retrieval during raw data event reconstruction. The FNC reconstructed data is saved in two BOS banks on the POT tapes (see table 3.3): the *FNHT-* contains cluster (hit) information, and the *FNCR-* contains the reconstructed module information. In the final reconstruction and classification of events, also called L5 (Level 5), only FNC events that have the reconstructed impact point falling in the FNC acceptance area are saved to DST tapes⁴². In the L5 classification scheme (*H1ECLASS*) of data there is a separate class for FNC events labeled as: CLASS 14, Physics Class (Diffnc), Head Bank (word 13), bit number 25. The FNC events fall also in the other physics classes and the overlap of the FNC class 14 with the other classes is practically total (see figure 3.24), adding a small fraction (~ 4 per mill in 1996) to the total H1 data volume.

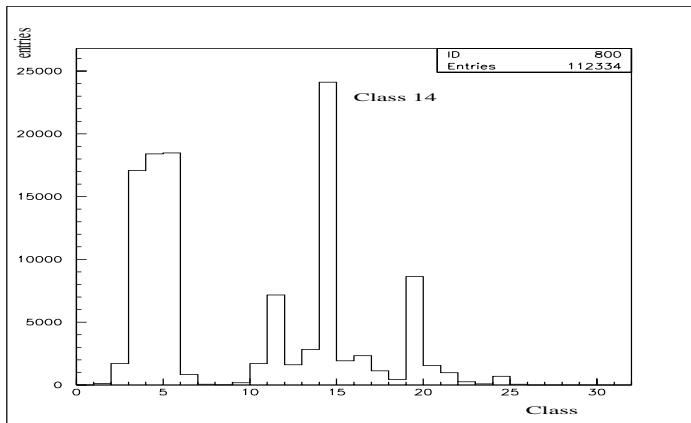


Figure 3.24: The distribution of FNC events in the various classes. Most of the FNC events which constitute class 14 fall also into other classes with a nearly complete overlap.

⁴⁰For details and explanations of terms used in this paragraph see sections 2.2.7 and 3.6.

⁴¹Information on the naming and content of these BOS banks (*fncc*, *fncs*, *fnpd*, *fnxy* etc.) is found in the FNC reconstruction program *FNCREC*.

⁴²For 1996 data, any FNC event with a reconstructed hit was saved to DST; this was changed for 1997 to reduce the data volume.

FNCR bank -module information		
Variable	Bank Column Numbering	Description
ENERGY	1-75	Energy in GeV for the 75 calorimeter modules.
ADC1	76-118	43 ADC values in millivolts for hodoscope plane 1.
ADC2	119-143	25 ADC values in millivolts for hodoscope plane 2.
ADCF	144-148	4 ADC values for the tail and finger counters.
TIME	148-294	Reconstructed time values for the calorimeter, hodoscopes, tail and finger counters.
FADC	295-302	400 MHz FADC information for calorimeter modules 1, 4, 5 and 6 [†] .
FNHT bank -cluster information[‡]		
Variable	Bank Column Numbering	Description
NMOD	1	Number of modules in cluster.
MAXMOD	2	Module with greatest energy in cluster: maxmod.
CHARGE	3	Charge of cluster (neutral = 0, charged = 1).
MAXHOD1	4	Hodoscope module of plane 1 with greatest signal: maxhod1.
MAXHOD2	5	Hodoscope module of plane 2 with greatest signal: maxhod2.
ENERGY	6	Cluster Energy.
MODENG	7	Energy of maxmod module.
CORCGX	8	Corrected Center-of-gravity X.
CORCGY	9	Corrected Center-of-gravity Y.
FNCTIME	10	Cluster time.
TAIL1	11	Signal in Tail hodoscope 1.
TAIL2	12	Signal in Tail hodoscope 2.
SIGHOD1	13	Signal in maxhod1, hodoscope plane 1.
SIGHOD2	14	Signal in maxhod2, hodoscope plane 2.

[†]Present only from last month of 1996 luminosity running onwards.

[‡]The number of FNC reconstructed clusters is contained in the bank header and each cluster has the same number of variables i.e. 14.

Table 3.3: FNC data banks.

3.7.2 FNC Variables

There are seven basic FNC measured variables from which various quantities can be obtained; the most important are the neutron energy and the neutron impact position.

- **nhitfnc**- This variable gives the number of hits per event in the FNC; in other words, the number of FNC reconstructed clusters found in a given event, which is most of the times one. The number of clusters found in the calorimeter is based on the concept of *local equivalence relations*[47], in which all the calorimeter modules are looped over to form equivalence classes. Starting from module one in the center of the FNC, each module is checked to see if the deposited energy in it is above the threshold energy value of 30 GeV for starting a cluster. When such module is found, all modules that belong to the first ring around it and have a deposited energy above the threshold energy (30 GeV) are put in the same equivalence class, forming the nucleus of the cluster. Then two rings of modules are taken around each of the modules belonging to the nucleus of the cluster; and if they do not already belong to another cluster (another class) they can be added to the nucleus of the cluster class in the following manner: all modules of the first ring are added to the class, and modules of second ring are added to the class only if they have a deposited energy above 10 GeV. Figures 3.28 and 3.29 display a DIS event with a neutron detected in the FNC showing the reconstructed cluster and the corresponding activity in H1.
- **iqfnc**- It gives the charge of the cluster (iqfnc=0 neutral, iqfnc=1 charged). The cluster charge is determined by using the two hodoscope planes. If the incoming particle's impact point falls within the area of a hodoscope tile of plane one or plane two, and this hodoscope tile has a signal above threshold (15 mVolts, calculated as the time integrated signal), then the charge is set to 1 (i.e. charged particle), else it is considered neutral.
- **fncetime**- It gives the timing of the cluster. The timing of the cluster is defined by taking the time of the cluster module with the highest energy deposit (also called maxmod). The time of given calorimeter module is a weighted average of the timeslices forming the signal, which is then subtracted by the offset time of the LED pulse of the given module (equation 3.19). This subtraction is done to have a common reference time for all calorimeter modules, taking so in account the different cable lengths. The calorimeter modules are all flashed at the same time by a common LED source (see section 3.9), the time (also a weighted average) of the LED pulse is taken as the offset for the given module. The subtraction of the LED offset gives a negative time, but what is used is the relative time between modules. The time of the signal (nsec) for a given module is:

$$t = \frac{\sum_j t_j (S_j - P_j)}{\sum_j (S_j - P_j)} - L \quad (3.19)$$

with t the time associated to the given module, j timeslice number, t_j the time corresponding to the center of the timeslice j (each timeslice is 9.8 nsec), S_j and P_j the signal and pedestal of timeslice j respectively, and L the LED offset for the given module.

- **fncx and fncy**- These give the x and y coordinates of the impact point on the calorimeter face, which are reconstructed using the corrected center of gravity method. The coordinate system is relative to the center of module one, which is the FNC coordinate system. The usual method for determining the coordinates of the impact point is the center of gravity method, which uses the energy sharing between neighboring modules of a cluster:

$$x_{cg} = \frac{\sum_{i=1}^n E_i x_i}{\sum_{i=1}^n E_i} \quad y_{cg} = \frac{\sum_{i=1}^n E_i y_i}{\sum_{i=1}^n E_i} \quad (3.20)$$

with x_{cg} and y_{cg} the center of gravity coordinates of the impact point, E_i energy of module i , x_i and y_i the coordinates of the center of module i , with the sum done over the cluster modules. The reconstructed impact point using this method tends to be systematically shifted towards the center of the module hit by the incoming particle[37], [36]. This problem can be solved by correcting the center of gravity coordinates (x_{cg}, y_{cg}) by an empirical formula of the type:

$$x_{corr} = A \cdot \arctan(Bx_{cg}) \quad y_{corr} = C \cdot \arctan(Dy_{cg}) \quad (3.21)$$

where x_{corr} and y_{corr} are the corrected center of gravity coordinates, A, B, C, D are empirically determined constants from the test beam, and x_{cg} and y_{cg} the center of gravity coordinates[38].

- **fnc tail**- Gives the total energy deposited in the two tail counters, due to the longitudinal shower leakage, in arbitrary units (a.u.)⁴³.
- **fnc ene**- Gives the energy of the cluster; it is the sum of the energies deposited in the modules composing the cluster.

These FNC variables are displayed in figure 3.25 for the 1996 luminosity DIS data⁴⁴ with the following cuts used for defining a DIS event: the event saved on DST is required to have ep colliding bunches, a reconstructed z coordinate vertex, good running conditions (i.e. good luminosity and H1 detector status), and $5 \text{ GeV}^2 < Q^2 < 100 \text{ GeV}^2$. Most of the DIS FNC events have only one reconstructed cluster (hit), are neutral, have an impact point falling within a radius of 10 cm around the FNC reference coordinate system origin (0,0) and have a negative FNC time, which correspond to a neutron. The number of hits or clusters in the FNC is principally one; $\sim 85\%$ of the FNC beam-gas events⁴⁵ and $\sim 95\%$

⁴³These units correspond to the total time integrated signal in *mVolts*.

⁴⁴The 1996 luminosity run range taken for the FNC analysis considerations is 159000-171156.

⁴⁵See section 3.10 for a definition of beam-gas events.

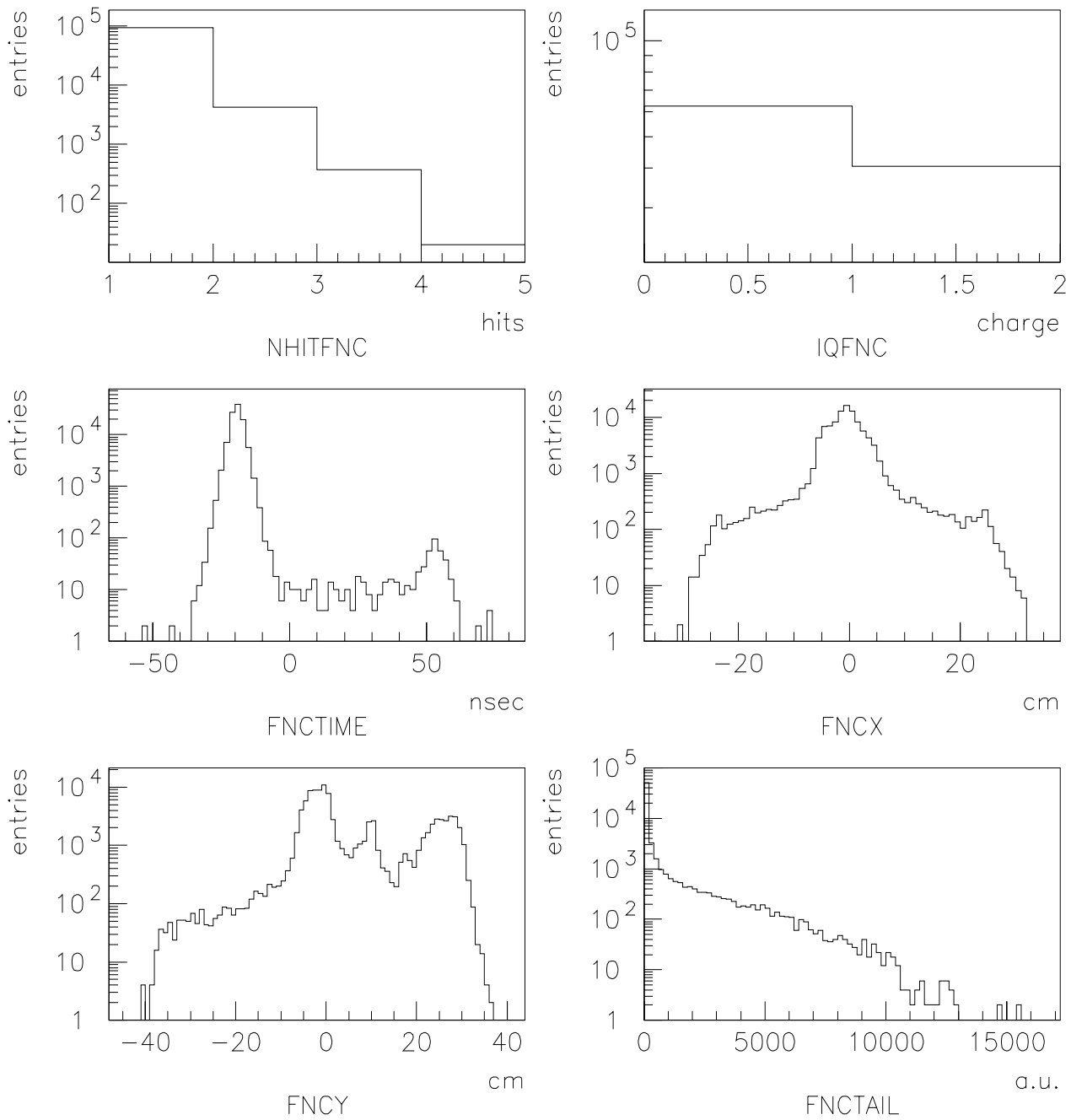


Figure 3.25: The FNC measured variables.

of the 1996 DIS data have only one hit. The difference between the two is due to the different beam conditions and the cuts imposed for DIS data.

Various stray particles (due to particles traveling along the beampipe and interacting with the beampipe, magnets and other dead material) and protons reach the FNC with different timings producing single or multiple hits all over the calorimeter face, as can be seen in figure 3.26. The central region of the calorimeter face, where there is a high density of impact points, corresponds to the FNC acceptance region, where the incoming neutrons hit. In the top part of the FNC there is also a high density of points, due to lower than nominal (<820 GeV) energy protons, which thus have an increased vertical deflection by the magnets, and hit this upper area of the calorimeter. The particles which travel along the beampipe and interact with dead material, hit the calorimeter around the beam hole, and also the rest of the calorimeter's face. The left scatter plot of figure 3.26 corresponds to all FNC events (with at least a hit in FNC) taken during 1996 luminosity running and saved to DST, while the central one corresponds to DIS events (defined above) with at least a hit in the FNC, and the right one to DIS events with one neutral cluster detected in the FNC with the cluster energy ($fncene > 100$ GeV), and a good timing of the cluster ($fnc\text{time} < 0$). The top part of the right plot has a high density of hits that correspond principally to protons and not to neutral particles, since the top part has only three hodoscope tiles around the beampipe hole for charge determination. The imposed cuts for DIS events reduce considerably the stray hits distributed on the calorimeter face, which can be reduced even further by imposing more restrictive cuts (i.e. the acceptance area cut). On the edges of the calorimeter some points are reconstructed slightly out of its body, because particles that hit the edges have only a partial shower containment, shifting the reconstructed impact point outwards.

Figure 3.27 displays the measured energy spectrum for DIS events with FNC hits (charged or neutral) only in the acceptance region. The charged particle spectrum is softer than the neutral one, since neutral particles, which are basically neutrons produced in the ep scattering, arrive directly at the FNC without intermediate interactions which degrade the energy. Also photons from π^0 decay can reach the FNC, but they are converted by the lead shielding positioned on the front face of the FNC producing a signal in the hodoscope planes; other neutral particles decay on the way before reaching the FNC. The basic condition for having a neutron detected by the FNC for luminosity data, is that it must be an ep event, with only one neutral hit which has the impact point in the FNC acceptance region and a good FNC timing. In the case of beam-gas interactions (see section 3.10), all one neutral hit events with a good FNC timing falling in the FNC acceptance area are considered neutrons, since there is no other information available. A cluster energy cut of 100 GeV is applied to eliminate the low energy region, in both DIS and beam-gas events.

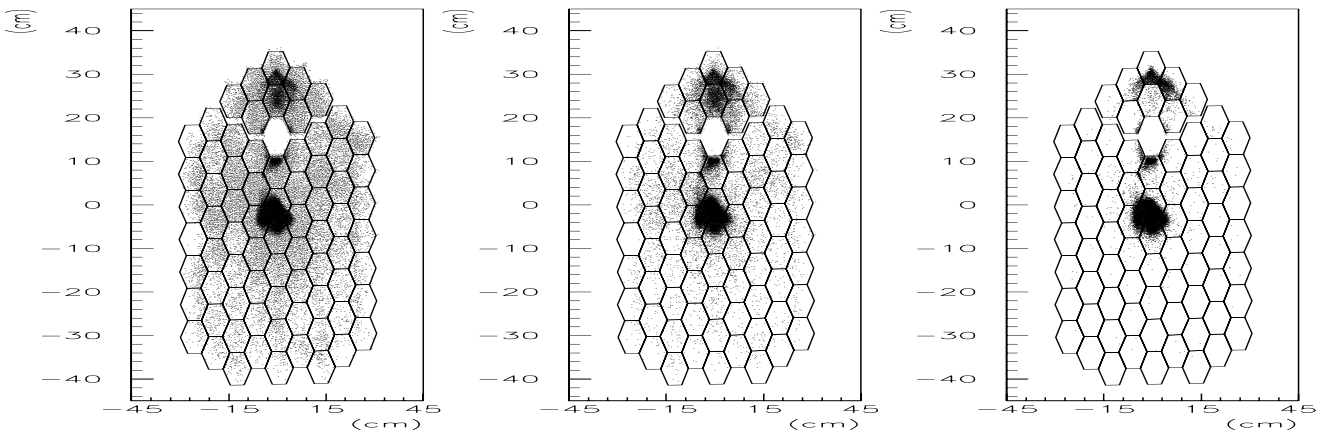


Figure 3.26: Distribution of the hits on the front face of the FNC, for any event saved to DST tape with at least a hit in the FNC (left), DIS events (center) and DIS events with one neutral cluster (>100 GeV and good timing; the top part hits are protons, see text for details) detected in the FNC (right), for 1996 data. The central high density hit region is the acceptance area, while the top part high density hit area corresponds to proton impacts.

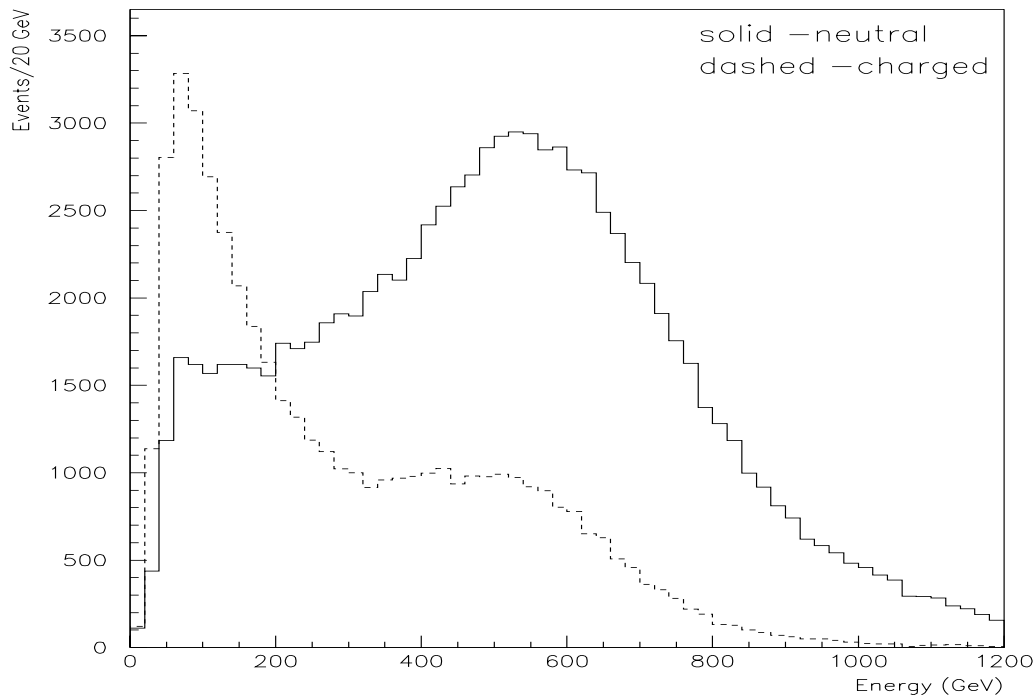


Figure 3.27: The energy spectrum for charged and neutral particles reaching the FNC acceptance region for DIS events, with one reconstructed cluster in the FNC.

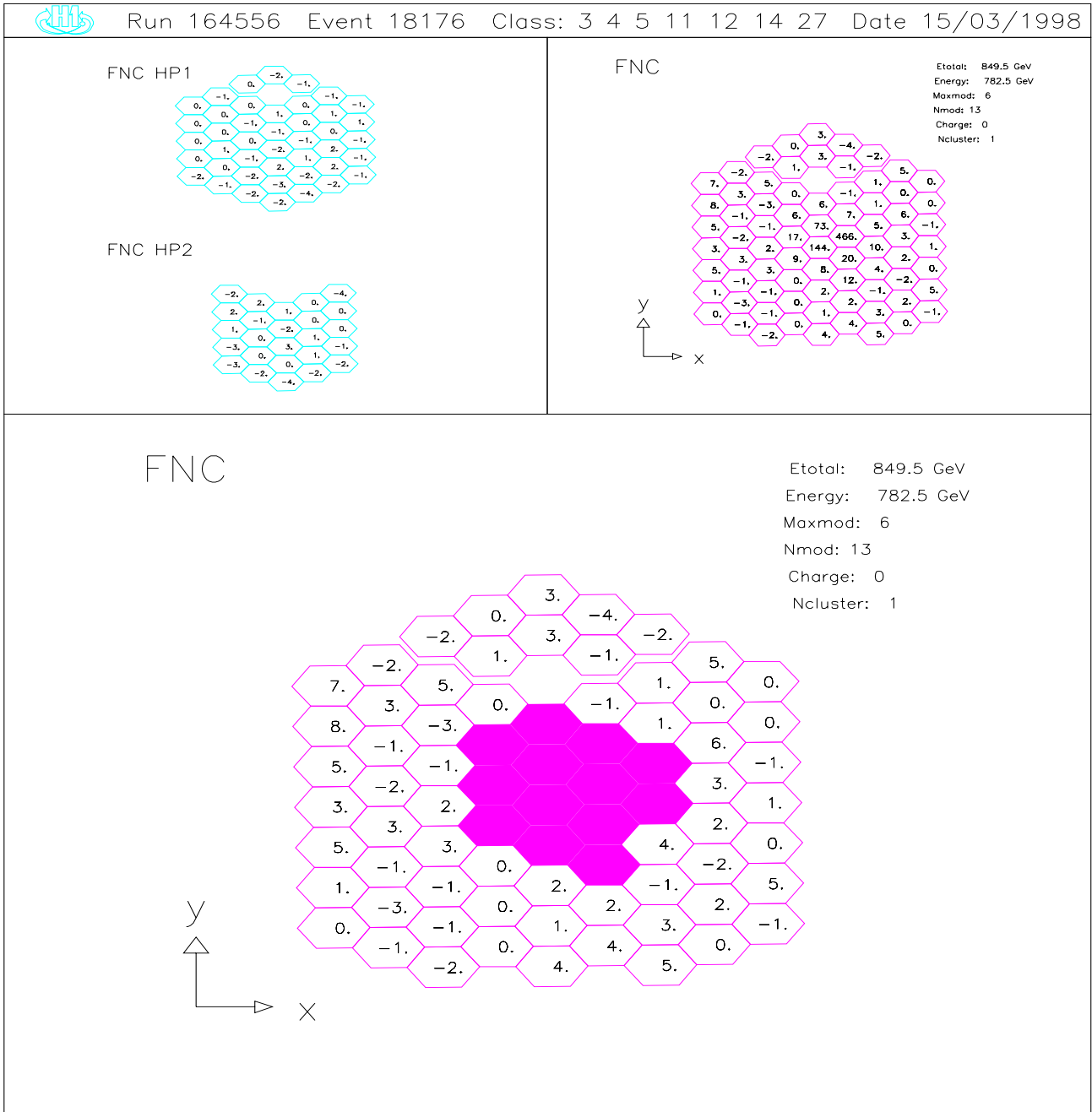


Figure 3.28: The signals (mV) registered in the two hodoscope planes (top left) and the energies (GeV) in the calorimeter (top right) are displayed for a 1996 DIS event with a neutron detected in the FNC. The bottom plot displays the reconstructed cluster (solid area); the other modules have the noise level energies (GeV) displayed. This event has one cluster ($ncluster=1$), is neutral ($charge=0$), has a deposited energy of $782.5 GeV$, with module 6 being the most energetic one ($maxmod=6$), and the cluster consists of 13 modules ($nmod=13$). The total energy deposited in the FNC ($etotal$) includes also the non cluster module background noise contribution.

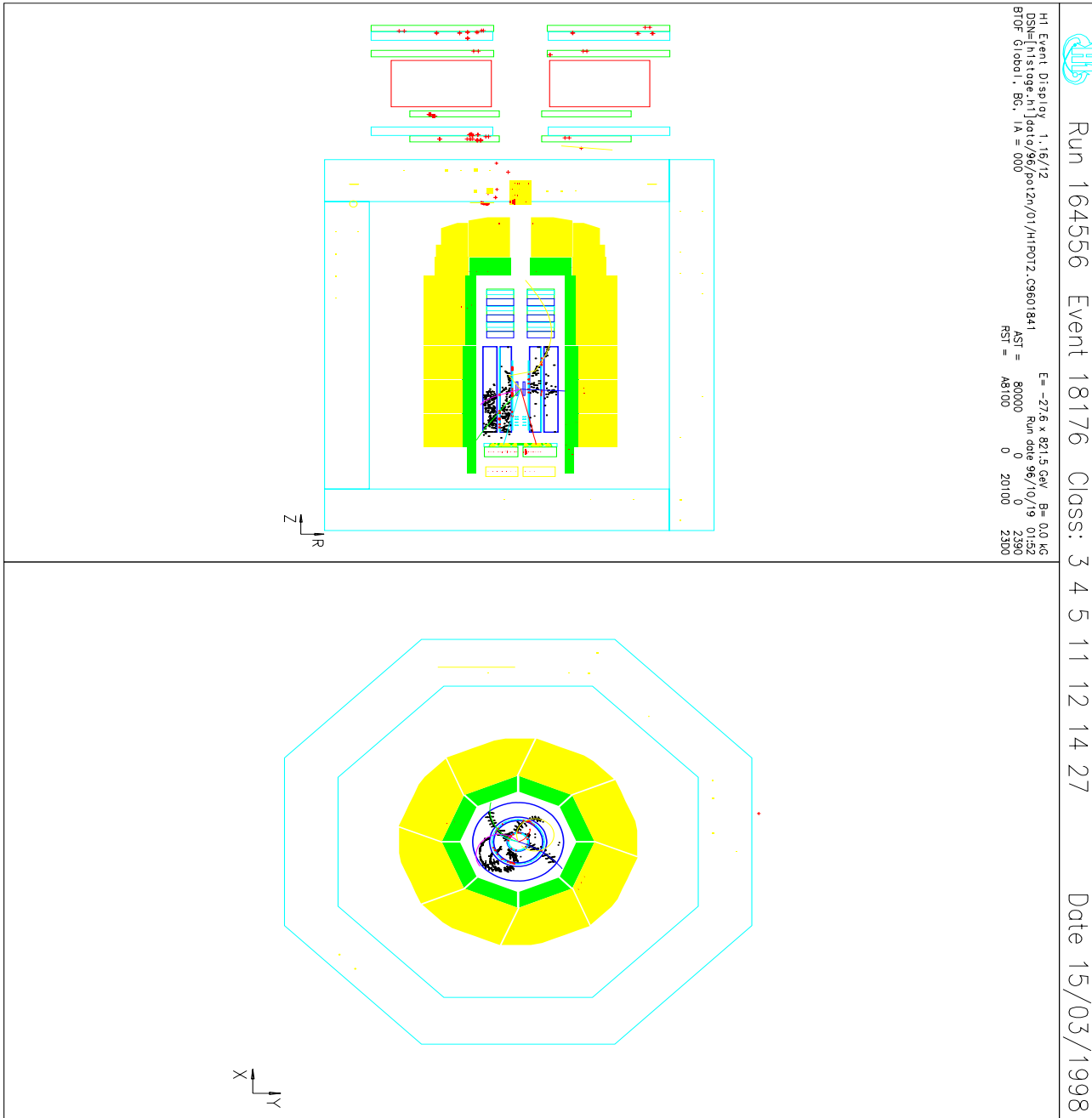


Figure 3.29: The activity in H1 is displayed for a 1996 DIS event (same event as in 3.28) with a neutron detected in the FNC. On the top there is a side view of the H1 detector with the vertex fitted tracks; while on the bottom there is a radial view of the central trackers (inner circles) with vertex fitted tracks and hits, the liquid argon calorimeter with summed energy deposits (solid light and dark grey) and the iron with energies and hits (outer enclosing).

3.8 Hodoscope Efficiency

Two hodoscope planes (see section 3.2.2) are positioned in the frontend of the FNC for charge determination of the incoming particles hitting the FNC, to distinguish between incoming neutrons and various charged particles. These charged particles are created in showers produced by particles interacting with dead material upstream of the FNC or are lower than nominal energy protons ($< 820 \text{ GeV}$) that hit the top part of the calorimeter (around and above the beampipe). For any event detected by the FNC two basic situations are possible:

- The hodoscopes' signal is in the pedestal value range. Then, there are no charged particles hitting the area covered by the hodoscopes, which includes the acceptance area, and the event is classified as a neutron if its impact point is within the acceptance area. This is the only neutral particle produced in an ep collision that does not decay before reaching the FNC. Photons, which can arise from π^0 decay, are mostly converted ($X_0 = 0.56 \text{ cm}$ for lead) by the lead ($\sim 10 \text{ mm}$) covering the front face of the FNC.
- The hodoscopes' signal is above the pedestal value range. Then, a number of relativistic charged particles pass through the hodoscopes (particle shower) hitting various hodoscope tiles, which behave like mips (minimum ionizing particles); but also albedo or backscattering of shower particles produced by an incoming neutron might fake a charged particle.

The signal and timing distributions for a typical hodoscope module (module one of plane one, 1HODO1) are shown in figure 3.30 for beam-gas data. The signal is in $mVolts$ and it is the timeslices integrated signal value. The two top plots display the hodoscope signal spectrum for any particle hit detected by the FNC, on the whole range (left) and on a reduced range (right) near the pedestal region. The signal threshold value of 15 mVolts is chosen for tagging charged particles, which is above the pedestal values (middle left). No clear minimum ionizing peak is observed as would be expected from the relativistic shower particles hitting the hodoscope tiles (middle right), due the energy smearing of the tile and to backscattering events which deposit energy differently from mips. In this plot (middle right) charged particles are tagged by plane two hodoscope tiles: it displays the signal spectrum of hodoscope module one of plane one (1HODO1), for one reconstructed hit in the central calorimeter module 1, and depositing the highest hodoscope tile energy ($>15 \text{ mVolt}$) in any of the three hodoscope tiles of plane two (modules 1, 2 and 3) which together cover the same area of the calorimeter and hodoscope modules one⁴⁶. The bottom left plot shows the timing of the signals ($>15 \text{ mVolts}$), which is determined by the weighted

⁴⁶Hodoscope plane two has tiles of the same size but is shifted respect to plane one, see section 3.2.2.

center of gravity method, and the right one shows the tile signal versus its timing. The oblique relation is artificial, since the signal shape varies with the energy, introducing a systematic of few $nsec$ in the timing. The backscattering contribution can be seen on the right side of this correlation (at greater times); there is a greater contribution of events that arrive later respect to the main distribution than earlier, as would be expected from backscattering events.

Hodoscope Plane One, Module One

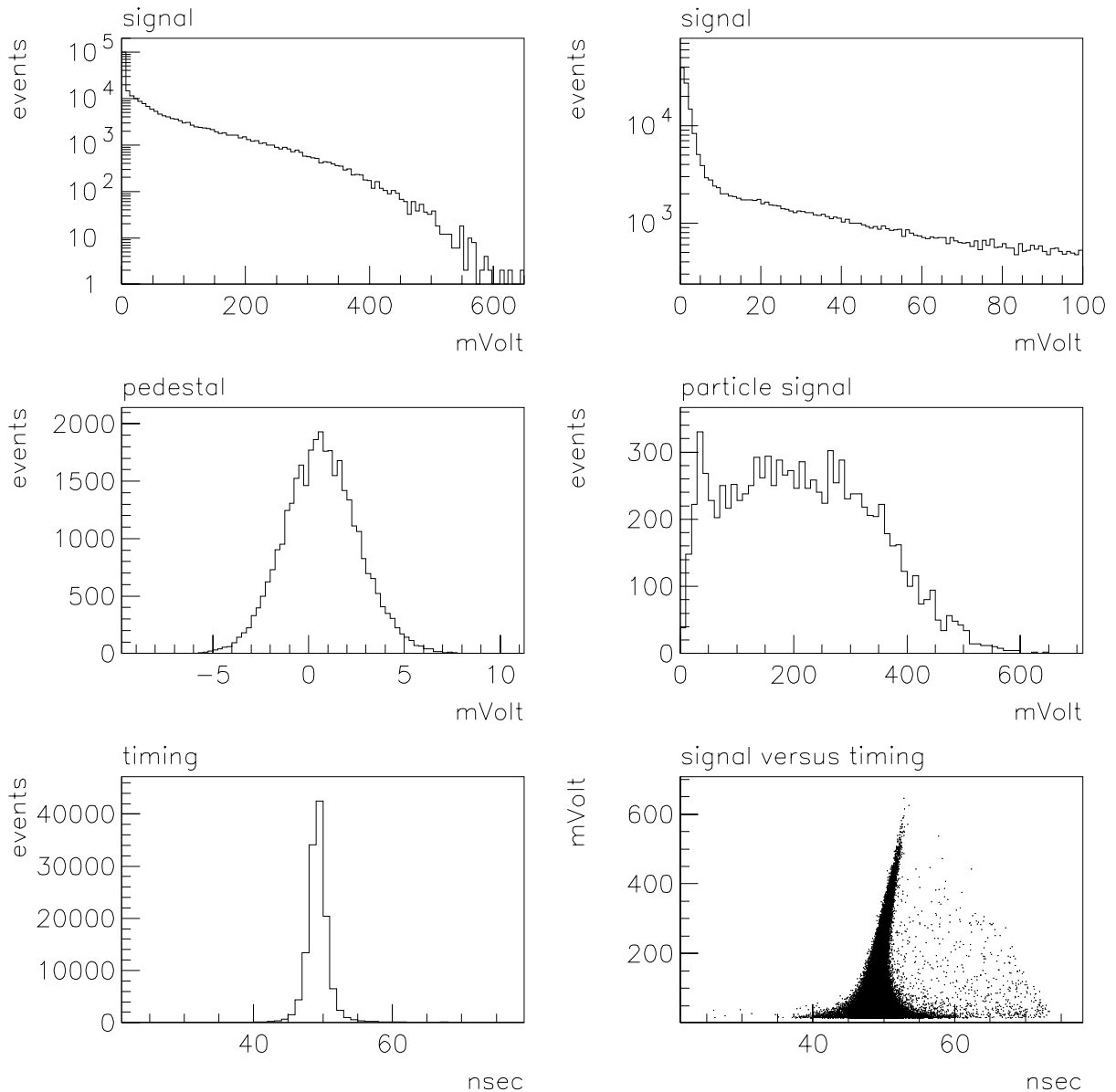


Figure 3.30: The signal and timing distributions of a typical hodoscope module (module one of hodoscope plane 1, 1HODO1).

The hodoscope efficiency for charged particle detection has been measured for both hodoscope planes, using beam-gas data. One plane was used to trigger on incoming charged particles, and the efficiency for detecting these charged particles was measured on the other. Since the two hodoscope planes have different sizes and are shifted one with respect to the other, an enlarged area around the acceptance region, which is covered by both planes, was chosen i.e. the calorimeter reconstructed impact points are between $-12 < x < 12$ and $-16 < y < 8$. To trigger on incoming charged particles a signal threshold was fixed (50 mVolt ⁴⁷) on one plane and then the efficiency for charge recognition was measured on the other at varying signal thresholds (10-50 mVolt). The efficiency versus the signal threshold is shown in figure 3.31 for plane one, plane two, and for the combined planes⁴⁸. The combined plane efficiency for charge particle rejection is $\sim 100\%$ at the 15 mVolt signal threshold cut chosen for particle charge determination, which is in accord with the WA89 studies (see section 3.2.2).

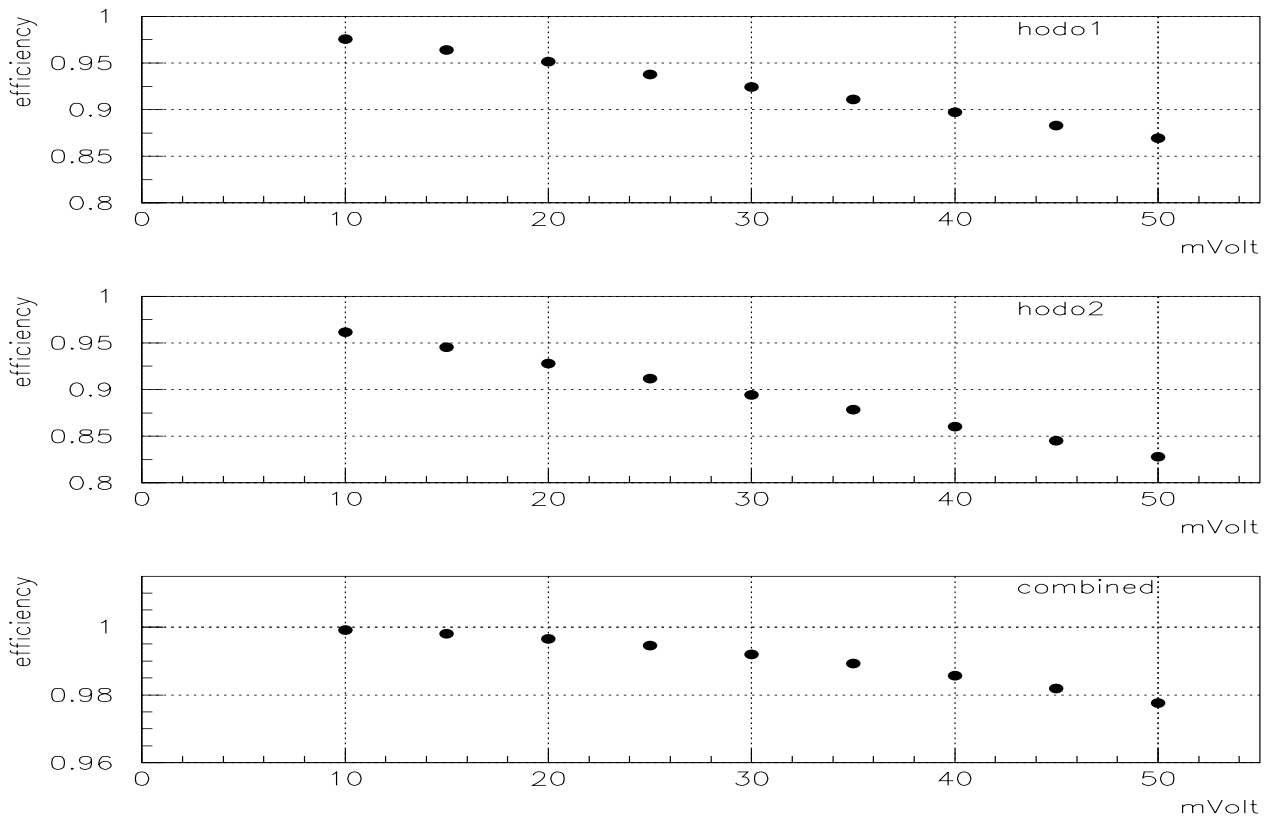


Figure 3.31: The hodoscope efficiencies for hodoscope plane one, two and the combined planes versus the signal threshold cut (statistical errors are neglectable).

⁴⁷This value is away from the pedestal region but lower than the expected average m.i.p. (minimum ionizing particle) signal.

⁴⁸The combined efficiency is determined by $\epsilon = \epsilon_1 + (1 - \epsilon_1)\epsilon_2$, where ϵ_1 , ϵ_2 and ϵ are the hodo1, hodo2, and combined plane efficiencies respectively.

Figure 3.32 shows the fraction of reconstructed charged events, with respect to the reconstructed cluster energy, for one cluster events with the reconstructed impact point in the central area of the FNC ($-12 < x < 12$ and $-16 < y < 8$). The charge reconstruction is determined using only hodoscope plane one, only plane two and the combined planes respectively. The event is considered charged if the reconstructed impact point is within the area of a hodoscope tile which has a signal above threshold (> 15 mVolt). Charged events are found mainly at lower energies, their fraction decreasing steadily as the cluster energy increases. The fraction of charged particles found by plane two is lower than plane one, since plane two is less efficient (see figure 3.31).

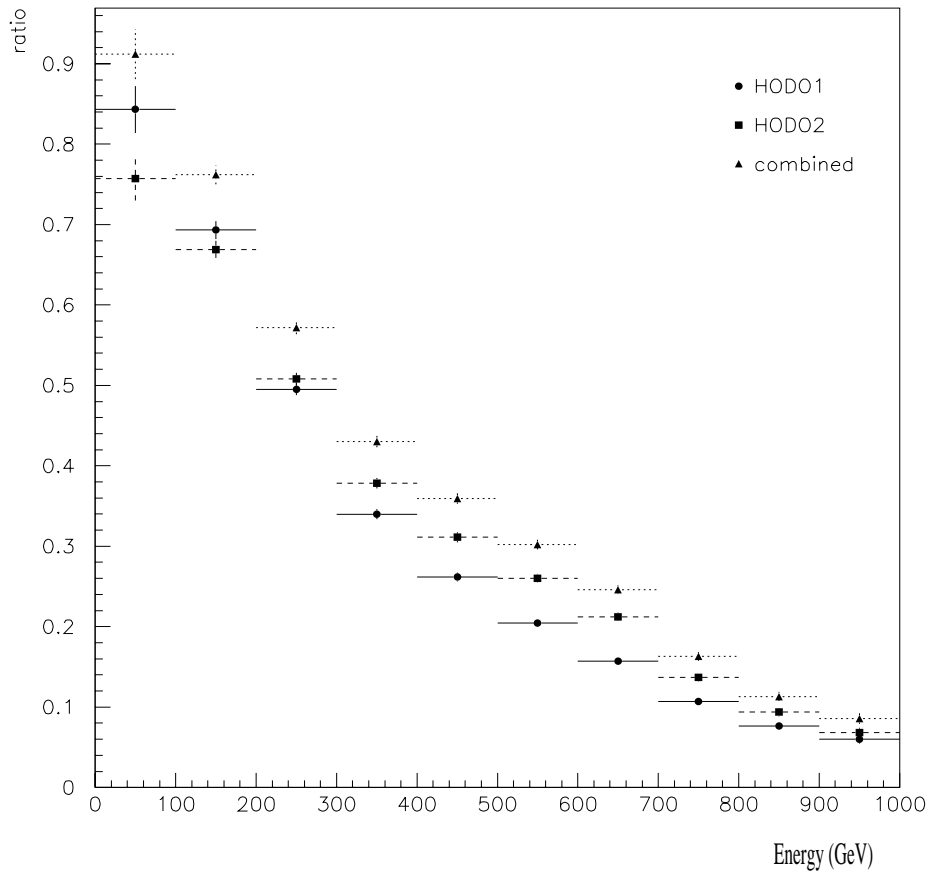


Figure 3.32: The ratio is between charged events (determined using only plane one, two, and both planes combined), hitting the central area around the acceptance region ($-12 < x < 12$ and $-16 < y < 8$), and all events falling in this area. The ratio is versus the FNC reconstructed cluster energy (only statistical errors are displayed).

Backscattering of charged particles (albedo) produced in a hadronic shower initiated by an incoming neutron might fake charged particles, reducing the neutron detection efficiency. Due to the hodoscope tile thickness of 1 cm ($\lambda_I=0.013$), on average 1.3% of

the neutrons will preshower in the hodoscope tile, faking a charged particle. The neutron preshowering in the hodoscopes and the front lead covering is taken in account in the Monte Carlo simulation H1SIM, but not the albedo which has to be estimated. Albedo[44] is typically characterized by the signals arriving later, few to several nanoseconds depending on the type of backscattered particles, and by an increased number of hits in the hodoscope tiles located near and around the impact point of the particle. These additional hits can be used to estimate the albedo effect for an incoming neutron, by looking at the signal hit rate in the hodoscope planes as function of the radial distance from the impact point position, i.e. the fraction of events producing a hit in the hodoscope tiles, with the tile center at certain radial distance R , from the impact point. In figure 3.33 the signal hit rate versus the radial distance R from the impact position, which is in the acceptance area, is plotted for hodoscope planes 1 and 2 over three energy ranges, i.e. the complete energy spectrum, a slice at low energy and one at high energy. Most of the signals in the hodoscope planes are caused by particle showers, and the radial behaviour of the shower hits can be approximated by an exponential (see fit in figure 3.33). It is expected that due to the albedo contribution, there will be additional hits in the tiles around the impact position, increasing the signal hit rate with respect to the expected value obtained from the fit done on the other bins. This difference can be used to estimate the albedo contribution which decreases with increasing energy, as can be seen by comparing the high (right, top and bottom plots) and low energy (middle, top and bottom plots) slices. The estimated albedo varies from $\simeq 2\%$ for high energies ($> 700 \text{ GeV}$) to $\simeq 12\%$ for low energies ($< 300 \text{ GeV}$), with a value of $\simeq 7\%$ for the complete energy range. The neutron detection efficiency can be so estimated to be $93\% \pm 5\%$.

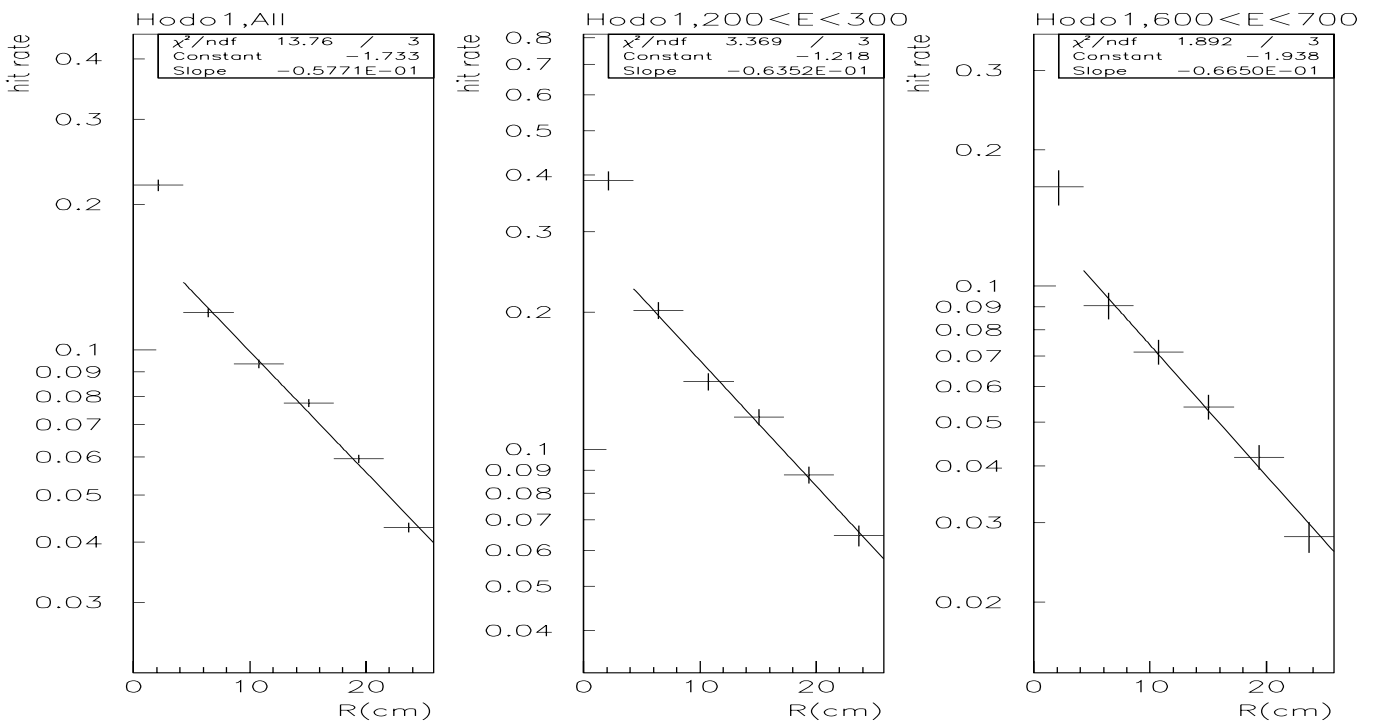


Figure 3.33: Hodoscope plane 1 and 2 signal hit rate versus the radial distance from impact point for three energy ranges. The y-axis is in log scale. The estimated albedo is taken as an average of the two hodoscope planes (their values differ by a fraction of a %), and is $\approx 7\%$, $\approx 12\%$ and $\approx 4.5\%$ for the complete energy range (left plots), the low energy slice (middle plots), and the high energy slice (right plots) respectively; the energy E ranges are in GeV.

H1 data acquisition to be later used for gain variation corrections- so called monitor event. To monitor the possible light variations of the LEDs, the LED light is brought via optical fibers to two photodiodes⁵⁰ and to an alpha source reference system. The reference system consists of a photomultiplier with an alpha source positioned in front of its photocathode and an optical fiber (carrying LED light) also regularly flashing its photocathode. To monitor possible LED light variations the ratio between the alpha source photomultiplier signal and the LED light photomultiplier signal of the reference system is checked for constancy; similarly the photocathodes should provide also a constant ratio.

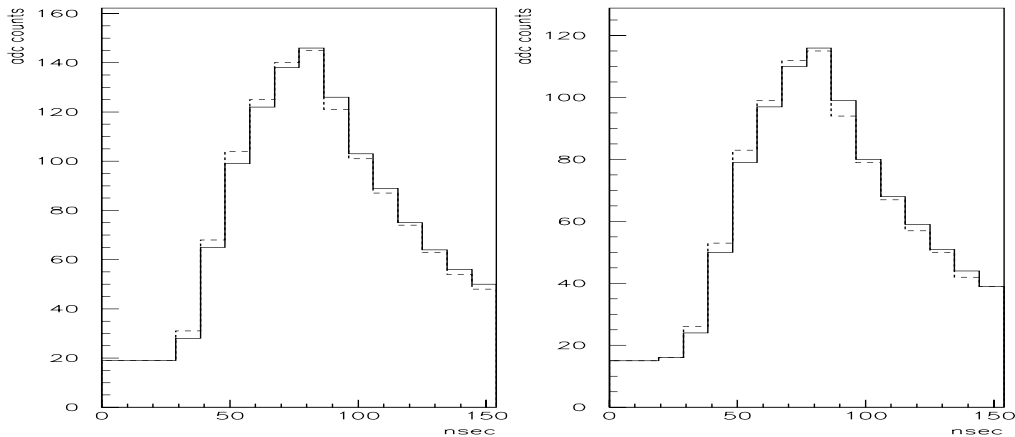


Figure 3.35: Digitized monitor signals for module 1 (left) and module 4 (right) of the calorimeter, belonging to the acceptance region. The solid and semi-continuous histograms are those of two distant monitor events belonging to the same beam-gas run.

The digitized monitor signals⁵¹ (figure 3.35) have a longer rise-time and are wider than the physics signals (figure 3.17). The shape of the monitor signal is similar for all calorimeter modules since all are flashed by the same LED source, but differs in amplitude due to the different response of the photocathode and PM, the different amount of light delivered to it by the optical fibers and the optical coupling between the optical fibers and photocathode. During a run (5-20 minutes) with stable beam conditions, the digitized monitor signals of a given module remain practically unchanged, with the total integrated signal value varying by $\sim 0.01\%$, showing that for a given run the PM gain is quite stable.

Each run is corrected for the PMs gain variations. Each digitized monitor signal is integrated (the first three time slices are used for pedestal determination) to give a number, called monitor factor. These monitor factors are summed up and averaged for each run, to give an averaged monitor factor for each module⁵². A beam-gas run is chosen as a reference run and for this run the reference calibration constant C_i^{ref} is determined

⁵⁰Siemens SFH2030.

⁵¹The signal produced by a PM when flashed by the LEDs due to a monitor trigger.

⁵²As seen in figure 3.35 the monitor signals for a given module vary slightly during a run, so an averaged monitor factor is enough for the whole run.

for each module, i.e. from the preliminary calibration constants obtained in the test beam, a set of reference calibration constants is determined by comparing the beam-gas neutron energy spectrum with the Pompyt Monte Carlo prediction, obtaining run dependent calibration constants. The set of monitor factors for this chosen beam-gas run (one for each module) will be used as reference monitor factors M_i^{ref} . To correct for the PM gain variations for other runs, the calibration constant (C_i^{ref}) of a given module is multiplied by the ratio of the monitor factor M_i for the given run and the reference monitor factor M_i^{ref} :

$$C_i = C_i^{ref} \frac{M_i}{M_i^{ref}}. \quad (3.22)$$

Several beam-gas runs distributed over the data-taking period have been used to obtain these run dependent calibration constants. With this method, the PM gain variations can be corrected on a run by run basis, as can be seen in figures 3.36 and 3.37, where two different beam-gas runs and two different luminosity run ranges⁵³ are compared, each with the same number of events. The spectrums look different for beam-gas compared to DIS since different triggers and cuts were used for collecting the two data samples.

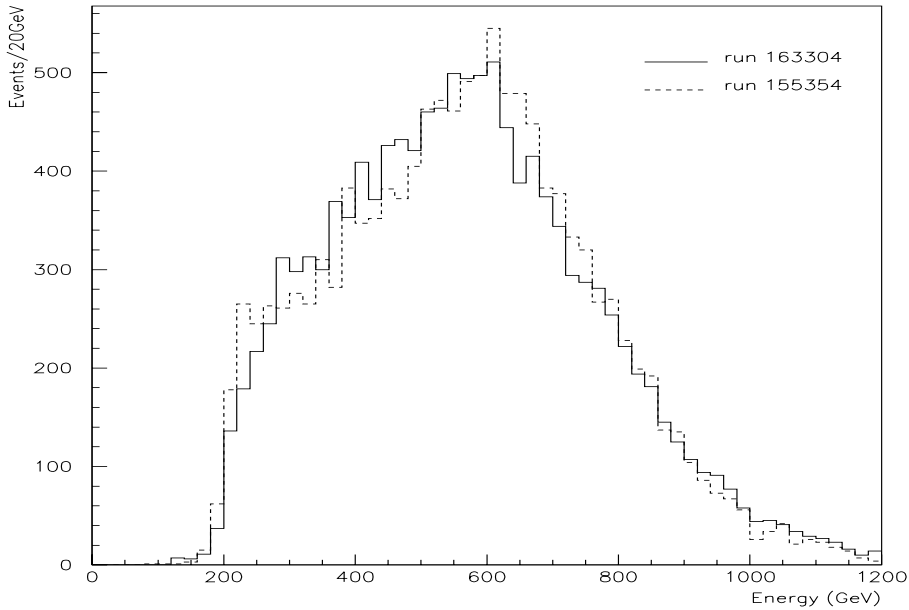


Figure 3.36: The neutron energy spectrum for two 1996 beam-gas runs with same number of events.

During data taking, there is an online extraction of the FNC monitoring factors, done by the local data acquisition, which extracts them directly. Whenever a H1 run ends, the monitor factors are entered into a database (NDB database[46]). In case the

⁵³Several runs have to be taken for the comparison of luminosity data due to the small fraction of DIS events with a neutron in the FNC.

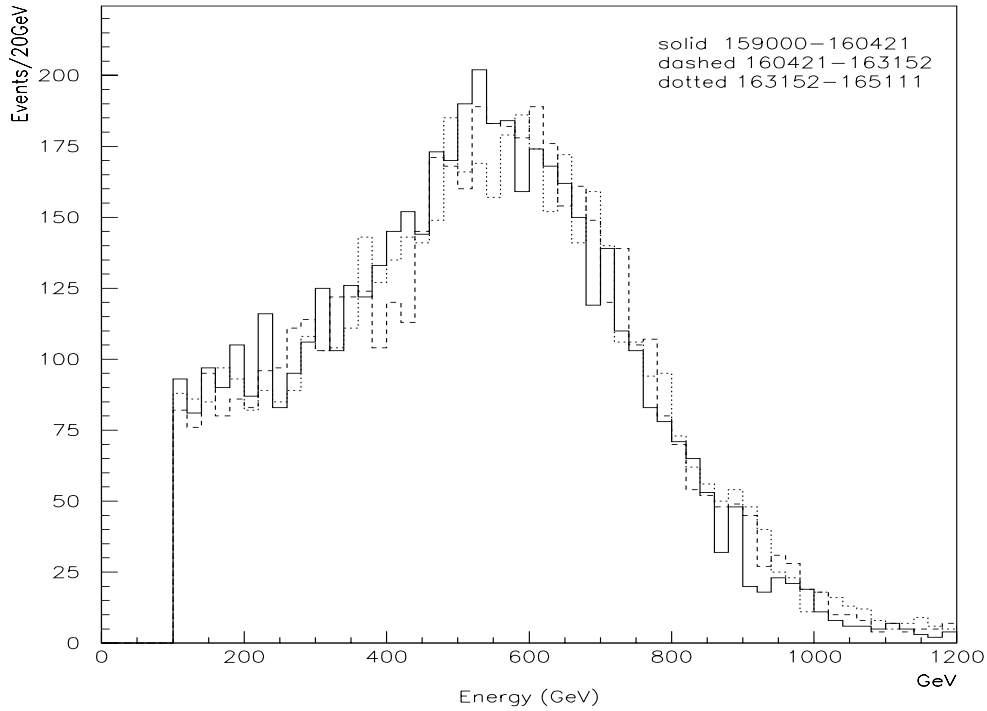


Figure 3.37: The neutron energy spectrum for three 1996 DIS run ranges with same number of events. The number of runs in the samples vary, since the run lengths differ; there is a cut for energies lower than 100 GeV.

online extraction fails, the missing runs are inserted manually into the database from a backup system that stores all FNC monitoring events.

During 1996 luminosity period there was some PM gain loss over the year, which stabilized in 1997, as can be seen by comparing the two top plots and two bottom plots for modules 1 and 4 of figure 3.38. The 1996 data taking was shorter than 1997. In 1997 the high voltage for the PMs was regularly lowered during injection of the beams to protect the PMs from high rates, strongly reducing the monitor factors values, as can be seen by the dotted lines of the two bottom plots; the discontinuities are due the monitoring system being off for some periods of no beam. During HERA luminosity, the PM gain varies over a day period, which is mainly dependent on the different beam conditions, such as the different luminosity phases, beam injection and ramping, as can be seen by comparing the day variation of the monitor factors for module 1 and the day variation of FNC energy sum trigger for the lowest threshold (two central plots of figure 3.38). There is a correlation between the two, the gain variations follow the energy sum trigger rate variations. For higher trigger rates (high hit rate), corresponding to beam injection and ramping, higher is the light rate going to the PM (higher PM currents) so increasing its gain.

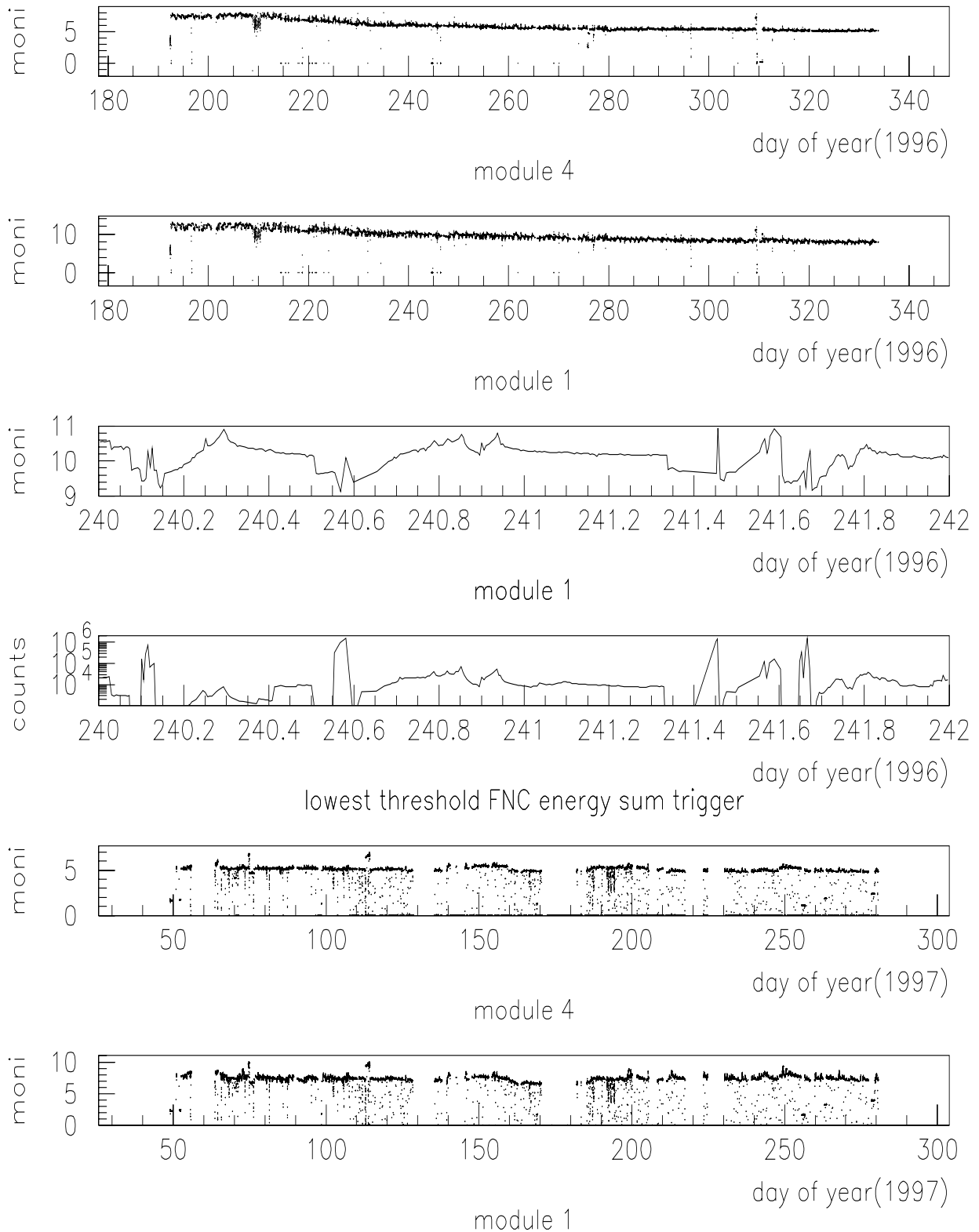


Figure 3.38: The top two plots and bottom two plots display the monitor factors (moni) for calorimeter modules 1 and 4 for the 1996 and 1997 luminosity periods respectively; while the two central ones show the monitor factor (module 1) and the FNC energy sum trigger lowest threshold for a shorter time interval; see text for more detail.

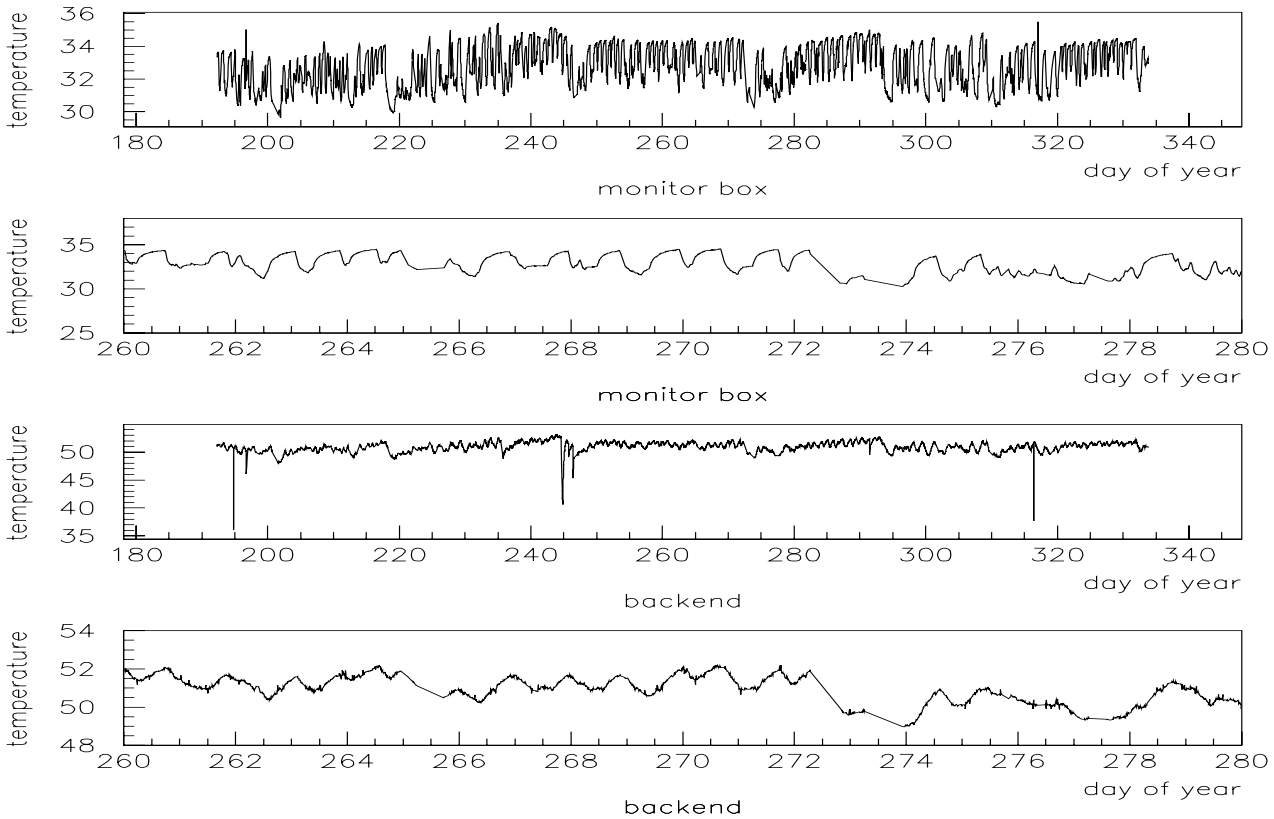


Figure 3.39: Temperature variations in 1996, for the photomultiplier backend region (bottom two) and monitor-box (top two), over the whole running time and on shorter time scale for greater detail. The dips in the backend temperature (third plot from top) correspond to times when the high voltage was momentarily switched off or tripped.

In backend of the calorimeter are located the PMs and the monitor-box; the later contains the photodiodes and the LED matrix with light mixer coupled to optical fibers together with the monitoring control electronics. These must monitored for temperature variations, in order that both the PMs and monitoring system work efficiently. The upper limit for the PMs is $55^{\circ} C$, over which they start to malfunction, and $36^{\circ} C$ for the monitor-box. If these limits are reached, they have to be switched off so that they can cool down; this luckily never happened. The monitor-box and each of the PMs are air cooled by a distributed system of small diameter ($\sim 5 mm$) plastic pipes, since during operation the PMs and the monitoring system heat up; in addition the tunnel also heats up during HERA operation. The temperature variations for 1996 (see figure 3.39) are seen to stay below the limits⁵⁴. The variations follow the different luminosity runs, rising with beam injection and colliding beams, then decreasing with the end of a luminosity run.

⁵⁴For 1997 the temperature variations are similar.

3.10 Calibration

The FNC was tested at low energies (10 GeV electrons and 15 GeV pions) in the 1995 CERN test-beam, since these were the only energies available at the time; high energy test beams in the range we are interested (400-800 GeV) are anyway not available. The calorimeter was calibrated using the 10 GeV electron test beam, from which preliminary calibration constants were obtained (see section 3.3). Assuming a relatively good linear response for the FNC⁵⁵, the test-beam calibration can be used for the higher energy range, with some tuning, i.e. by comparing the observed beam-gas neutron energy spectrum to the Pompyt Monte Carlo prediction. Beam-gas interactions ($p+p \rightarrow n+X$) are used for calibration purposes; since only the FNC trigger is operating, a high rate of events can be obtained ($\sim 10k$ events in 20 minutes). These beam-gas data are taken in-between the luminosity runs when the H1 detector can be used for calibration or test runs. The beam is the proton beam at 820 GeV, after that the protons have been injected and ramped to the 820 GeV nominal energy, while the electrons have yet to be injected and ramped. The gas is the residual gas in the beampipe, which is composed mainly of hydrogen with a small contribution from other light nuclei, and can be considered practically stationary. The beam pipe vacuum is worst in an area of ± 15 m around the interaction region of H1, because there are no vacuum pumps. The vertex for most of the beam-gas interactions will be in this area because of the higher concentration of residual gas and thus a higher interaction rate. The determination of the absolute energy scale is done by comparing the neutron beam-gas spectrum peak to the theoretical prediction of the Pompyt Monte Carlo for pion exchange. Figure 3.40 shows beam-gas data and Pompyt Monte Carlo compared for the absolute energy scale determination, with the FNC resolution effects⁵⁶ taken in account; the comparison between DIS events and Pompyt can be seen in figure 3.43. There is a good agreement for the peak and falling edge (tail) of the spectrum i.e. for energies > 400 GeV. For lower energies other proton fragmentation processes begin to contribute, modifying the purely one pion exchange spectrum. The absolute energy scale is known within the $\pm 5\%$ level. This has been determined by taking the FNC neutron energy spectrum and varying the neutron energy scale by $\pm 5\%$ and $\pm 10\%$ respectively and comparing it to Pompyt (see figure 3.41). The beam-gas interactions at HERA occur at a $\sqrt{S} \approx 38$ GeV which is in the same center of mass energy range as the ($p+p \rightarrow n+X$) data taken at the ISR⁵⁷ at CERN. The inclusive neutron spectrum has been measured for four ISR energies (30.6, 44.9, 52.8, 62.7 GeV) at zero degrees[48] and also in similar energy range (22.5, 30.6, 44.6, 53 GeV) at three different angles (20, 66, 119 mrad)[49]. These ISR data are in agreement with one pion exchange, supporting our comparison of beam-gas with Pompyt for the absolute scale determination.

⁵⁵The previous LAA project[36], [37] measured a good energy linearity for the original SPACAL, which is also confirmed by our measurements in situ by using the proton beam ramping method (see section 3.11.2).

⁵⁶The FNC calorimeter energy response function is used, see section 3.11.1.

⁵⁷Intersection Storage Ring.

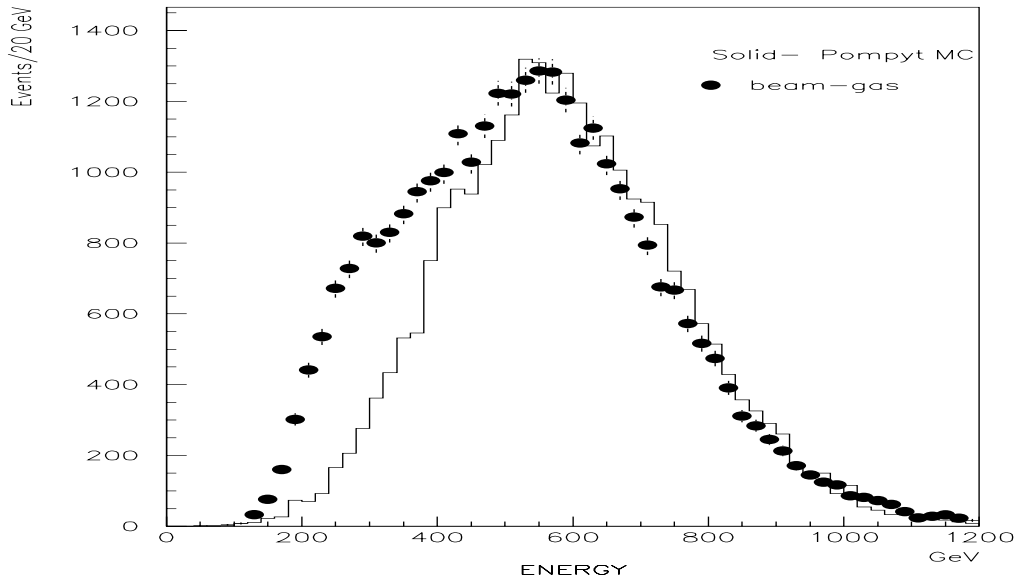


Figure 3.40: The neutron energy distribution for beam-gas data is compared to the theoretical predictions of one pion exchange simulated by the Pompyt Monte Carlo with the FNC resolution taken in account. The Monte Carlo normalization is to peak height; only statistical errors are displayed.

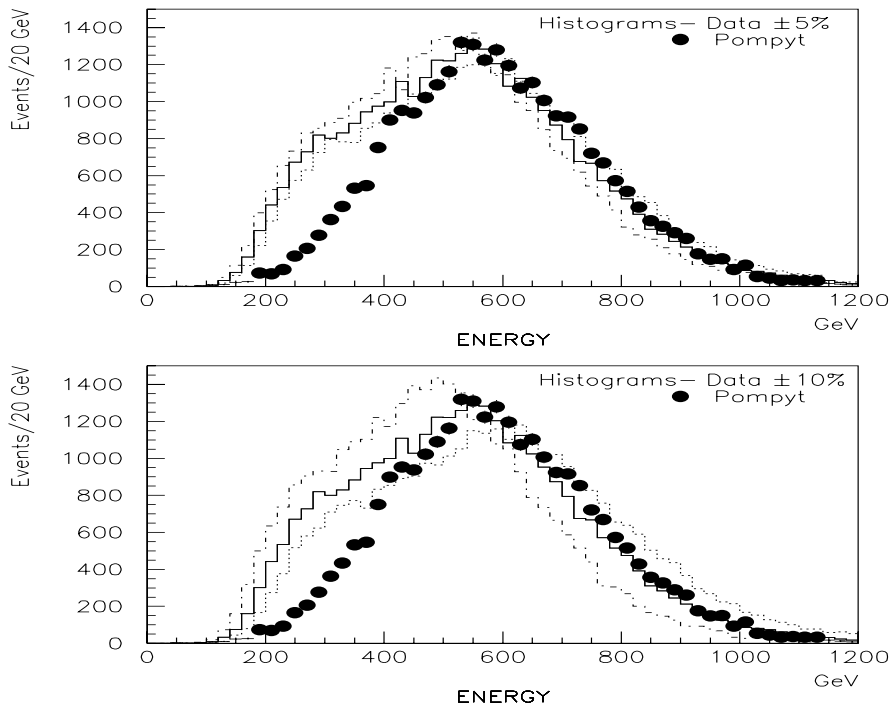


Figure 3.41: The neutron energy spectrum for beam-gas data is plotted (solid histogram) together with the Pompyt prediction and with the absolute energy scale varied by $\pm 5\%$ and $\pm 10\%$ respectively (dashed histograms). The normalization is to peak height, and statistical errors are within the dot size.

To check the relative intermodule calibration at HERA energies, the average lateral shower profile is compared for different beam-gas incident neutron energies. With a good relative intermodule calibration, the shape of the lateral shower profile is similar for different modules and approximately scales with the energy, as can be seen in figure 3.42. The average lateral shower profile for beam-gas neutrons incident on two different acceptance area modules (modules 1 and 4) for different neutron energy ranges is shown. The energy deposited (in GeV) for a given calorimeter module is plotted versus the radial distance R (in cm) of the geometric center of the module from the neutron impact point, averaged over several thousand events. The average shower profile energy increases with the energy range. For large radii ($R > 20$ cm) the shower profiles tend to converge, since there is no real energy deposited in these outer modules, being just the noise level.

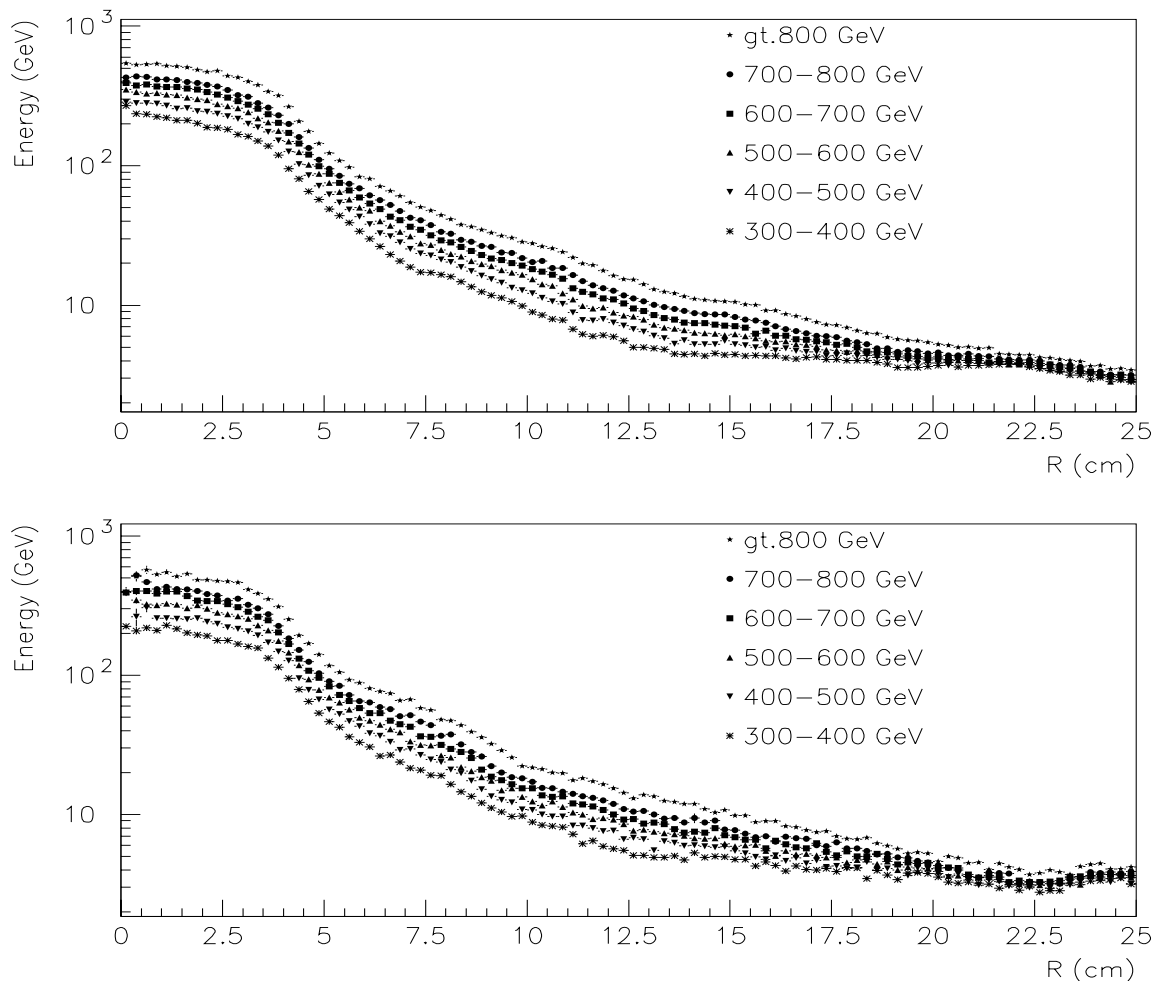


Figure 3.42: The average lateral shower profile for beam-gas neutrons incident on two different acceptance area modules (top- module 1 and bottom- module 4) for different neutron energy ranges (statistical errors are negligible).

3.11 Energy Resolution and Linearity

3.11.1 Energy Resolution

The FNC energy resolution is determined by comparing the observed neutron energy spectrum to the Monte Carlo prediction, which has to be opportunely smeared to be in agreement with the data. Pompyt and Lepto Monte Carlos are used for this purpose, which generate ep scattering events containing leading neutrons. Then the H1SIM program, which simulates the H1 detector and beamline, tracks the leading neutrons from the interaction vertex in H1, through the proton beamline till the FNC. Initially a preliminary energy resolution was determined for the FNC as follows: the observed neutron energy spectrum, both for beam-gas or DIS events, is compared to the simulated neutron energy spectrum with some energy smearing introduced. It is found that data⁵⁸ is well described (see appendix figures A.1 and A.2), also in the high energy tail region, simply by smearing the simulated neutron energy spectrum of Pompyt or Lepto with a 25% Gaussian energy resolution, having a $\pm 5\%$ error (E is in GeV):

$$\sigma(E)/E = 25\% \pm 5\%. \quad (3.23)$$

The high energy tail worsens considerably the energy resolution of the FNC. This tail is principally due to the attenuation length of the calorimeter light scintillating fibers (see section 3.11.3). To have a handle on this high energy tail, a calorimeter energy response function has been determined by GEANT Monte Carlo studies, which simulates the attenuation length of the fibers. For each simulated neutron Monte Carlo (Pompyt or Lepto) event reaching the calorimeter, the response function produces a calorimeter “energy response” neutron event. This response function modifies the simulated neutron energy spectrum by introducing a tail in the high energy region and leaving the lower part of the energy spectrum essentially untouched (figure 3.44); it is of the form:

$$f(x) = A \cdot (x - x_0(e))^{b(e)} \cdot \exp(c(e)(x - x_0(e))) \quad (3.24)$$

with e the input Monte Carlo energy, $b(e)$, $x_0(e)$, $c(e)$ parameterized second order polynomials, A normalization factor; the calorimeter response energy value is obtained by multiplying x by C which is the calibration factor.

The energy resolution is now determined by using this response function of the calorimeter, which accounts for most of the high energy tail observed in data. With this response function applied, an additional 15% Gaussian energy resolution smearing is introduced to obtain the observed neutron energy spectrum, which accounts for all the other contributions affecting the energy resolution (figure 3.43).

⁵⁸In this section both beam-gas and DIS data are from the 1996 HERA running time.

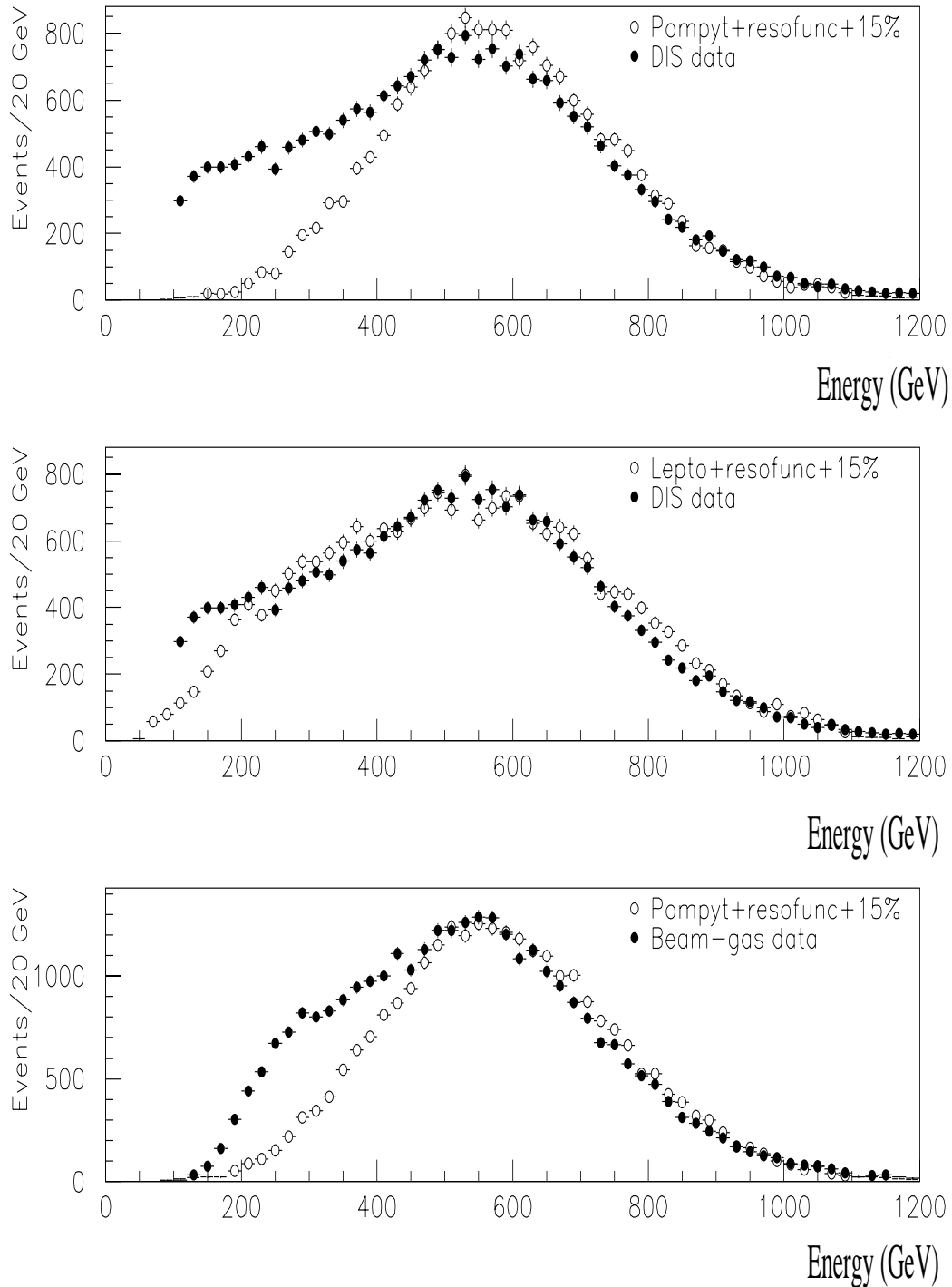


Figure 3.43: The energy spectrums for DIS and beam-gas data are compared to Pompyt Monte Carlo (top and bottom) and DIS is compared to Lepto Monte Carlo (middle); only statistical errors are displayed. The response function is applied to the Monte Carols and an additional smearing of $\sigma(E)/E=15\%$ is applied. Pompyt and Lepto are normalized to the number of data events having energies $E > 400$ GeV and $E > 100$ GeV respectively.

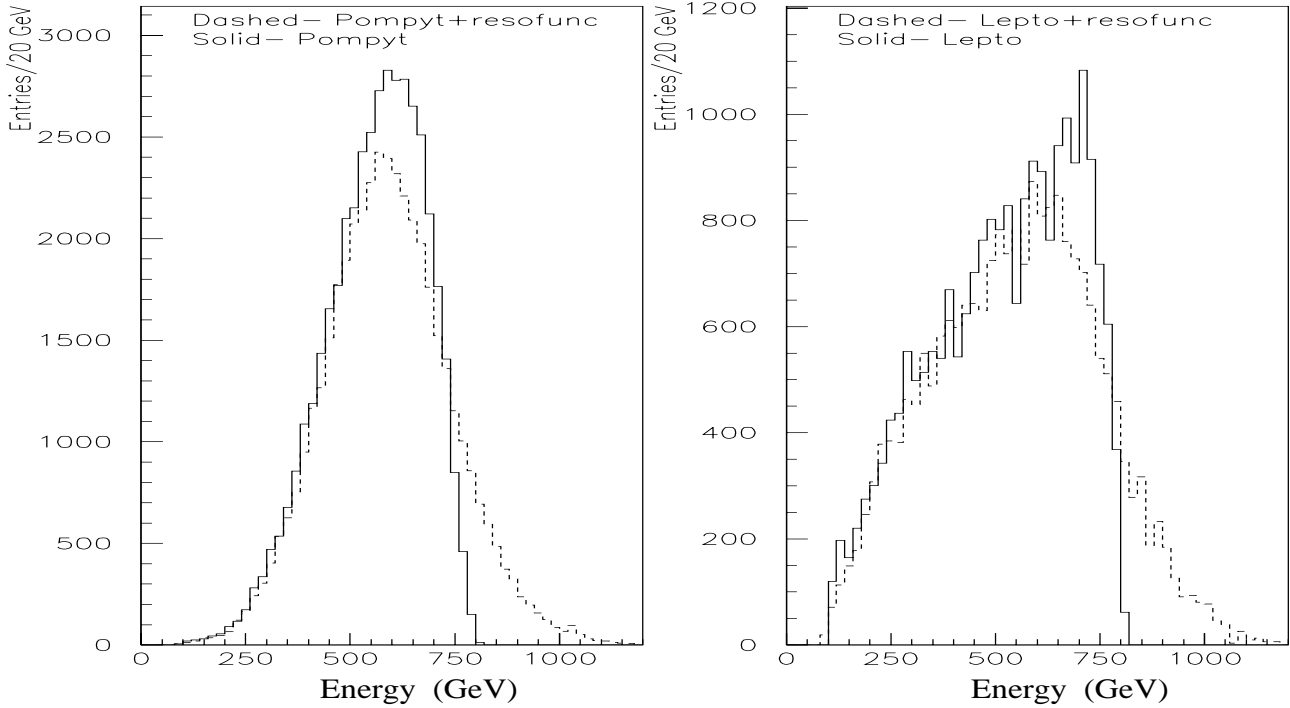


Figure 3.44: The Monte Carlo neutron energy spectrum (Pompyt and Lepto) with (dashed) and without (solid) the FNC calorimeter response function applied.

The energy resolution has been calculated at different energies, by applying the response function on a given number of events at a given energy value, and then smearing the result with a 15% Gaussian. Figure 3.45 displays the resultant energy distribution for 10000 events at four different fixed energies, with the Gaussian fit applied. The peak position is not at the input energy value, but shifted slightly to higher values, because of the response function which produces a distribution which is not fully Gaussian in the higher energy tail region of the plot. The σ value obtained from the fit is taken and the fractional energy resolution σ/E is plotted versus the energy (E) in figure 3.46. The energy resolution gets better with increasing energy as expected (see section 3.1.3), but then reaches a minimum and worsens at higher energies; this because higher energy showers penetrate deeper in the calorimeter so being more sensitive to the fiber attenuation effect. In the energy region of interest (200-800 GeV), the energy resolution (E is in GeV) takes the following value, which is within the error of the previous determination (equation 3.23):

$$\sigma(E)/E = 21\% \pm 0.5\%. \quad (3.25)$$

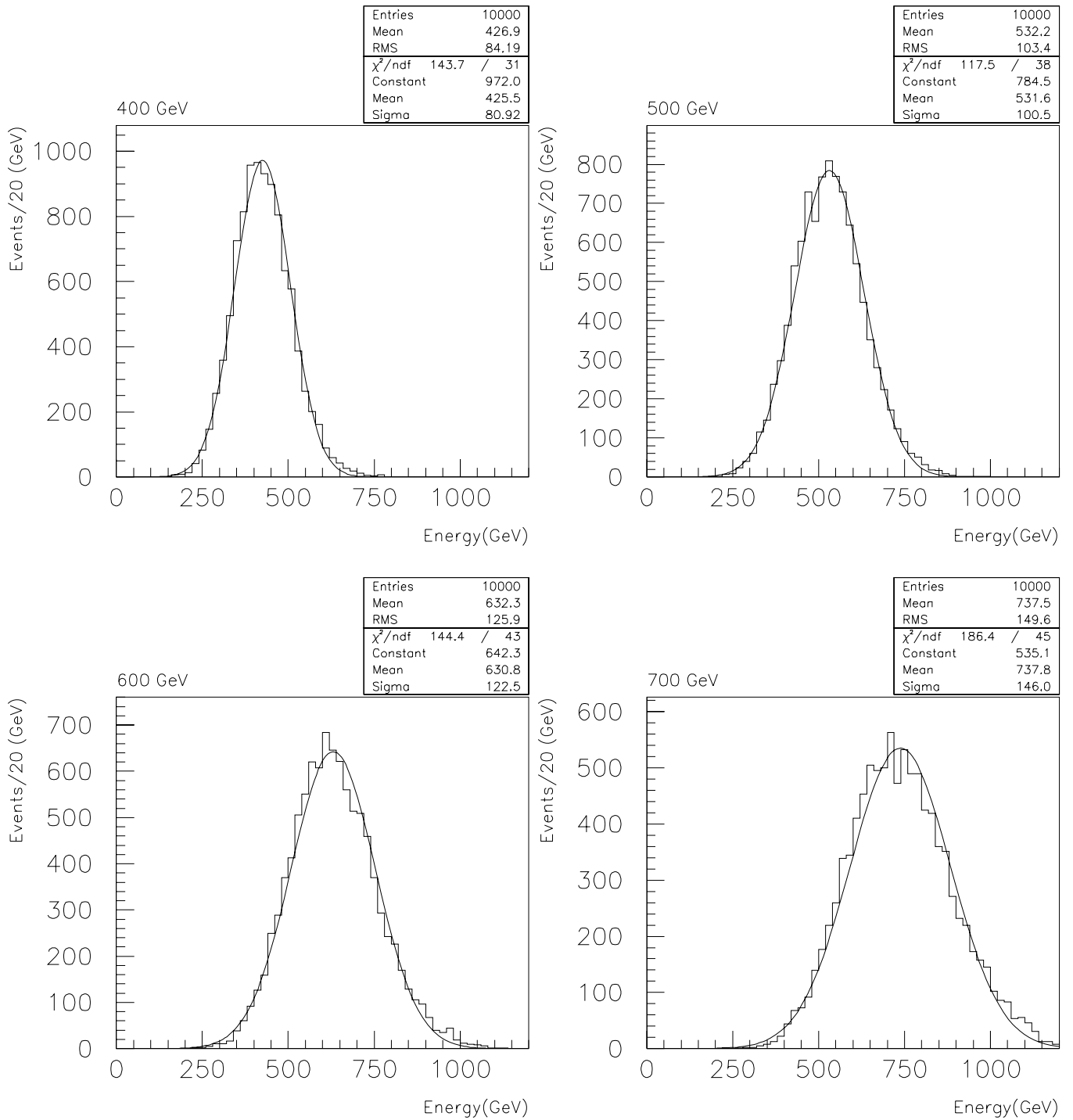


Figure 3.45: The resultant energy distributions for a given fixed input energy (400, 500, 600, 700 GeV) with the response function and 15% Gaussian smearing is applied.

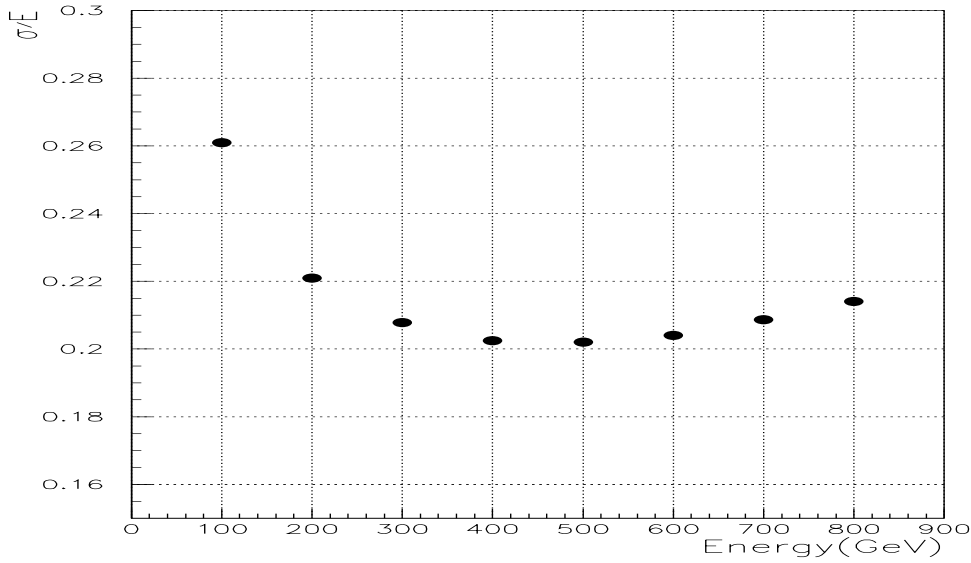


Figure 3.46: The energy resolution calculated at different energies (response function + 15% Gaussian smearing); the errors are neglectable.

3.11.2 Linearity

The linearity of the calorimeter energy response has been measured during the ramping of the HERA proton beam. The protons are injected at 40 GeV and then accelerated to higher energies till the nominal energy of 820 GeV is reached. During this ramping there are short periods during which the energy is kept at a constant value, which can be used for obtaining beam(proton)-gas data at different energies. Figure 3.47 shows the energy spectrum collected during a 1996 proton beam ramping at 4 different energies. The lines indicate the rescaled peak height (assuming linearity) respect to the 820 GeV peak position, i.e. $P_E = P_{820}E/820$, with E the beam energy, P_E, P_{820} the peak height position at E and 820 GeV respectively, while the Gaussian fit estimates the peak position. The peak position at 820 GeV is slightly lower than would be expected because of the chosen monitoring values, which only introduce a shift to lower energies. The linearity relation is obtained by plotting the peak height position derived from the Gaussian fit versus the beam energy (figure 3.48), giving a linear calorimeter energy response better than 5%.

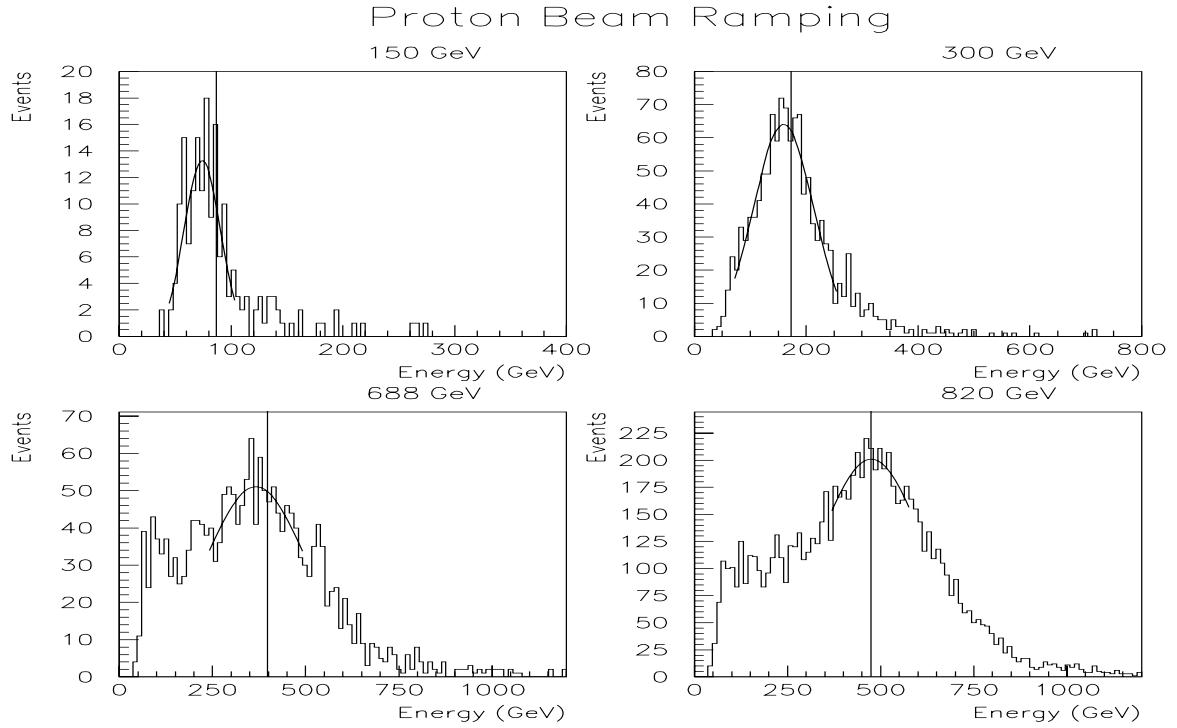


Figure 3.47: The beam-gas neutron energy spectrum taken during the proton beam ramping, at four different energies. The Gaussian fit to the peak position and rescaled peak height positions with respect to 820 GeV (drawn line) are shown.

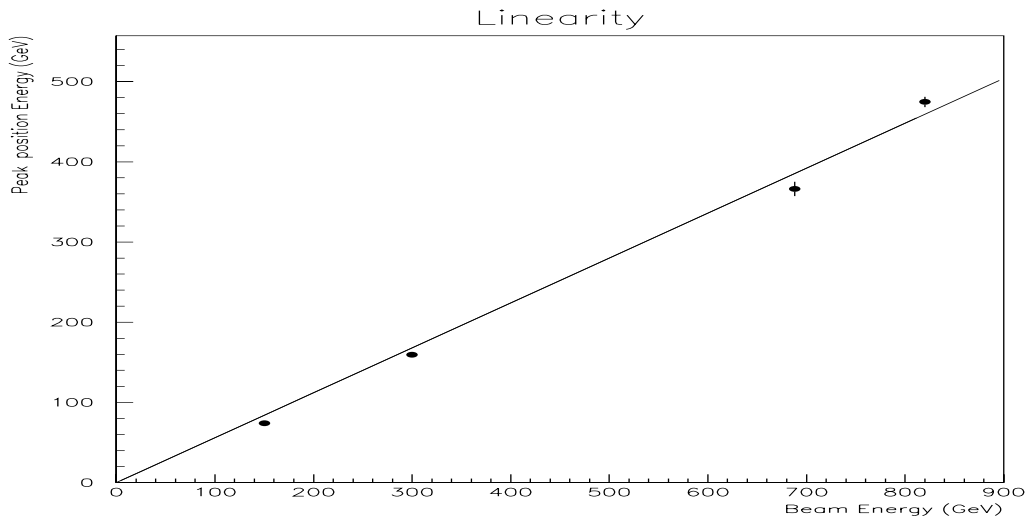


Figure 3.48: The linearity relation of the calorimeter energy response; the linearity of the calorimeter energy response is better than 5%. Only the peak position Gaussian fit error is displayed.

3.11.3 High Energy Tail

The measured neutron energy spectrum has a tail at high energies having a worsening effect on the energy resolution. This high energy tail⁵⁹ can be explained by the deepness of the hadronic shower development into the calorimeter, i.e. how far do the showers reach into the calorimeter body. The major consequence of the shower depth is the attenuation effect of the light produced in the scintillating fibers of the FNC; in other words, the calorimeter signals are influenced by the attenuation characteristics of the scintillating fibers. The deeper the shower develops inside the calorimeter, the nearer to the photomultipliers (backend of calorimeter) the scintillation light is produced, which is therefore less attenuated before reaching the photomultipliers, than scintillation light produced by showers developing in the frontend of the calorimeter. This attenuation effect was also observed by the LAA project[36], [37]: the higher the incident particle energy, the more prominent was the tail. At HERA the energies are higher, so the showers will develop deeper in the calorimeter body⁶⁰ producing a greater attenuation effect. Figure 3.49 shows the Geant simulation of the shower development for a 600 GeV incident neutron showering at the beginning (early) of the calorimeter, and figure 3.50 for a deeper (late) shower of the same incident energy. The neutron enters from the right encountering the two hodoscope planes in the frontend and the calorimeter matrix body; the light produced by the shower reaches the photomultipliers in the backend (left) and any leakage is detected by the tail counters, positioned immediately out of the calorimeter's enclosing box. The scintillation light of the deeper shower will be less attenuated, producing a greater signal than the early shower.

By looking at beam-gas or DIS data, a correlation is found between the total energy deposited in the calorimeter (fncene) by an incident neutron and its timing⁶¹ (fnctime); and also between the energy deposited in the calorimeter (fncene) and the energy deposited in the tail counters (fnctail) due to longitudinal shower leakage (see figures 3.51 and 3.52). This can be understood in the following way. Hits with a high energy deposit, on average develop later and deeper in the calorimeter, producing light in the fibers nearer to the photomultipliers, so being less attenuated, and producing a greater signal (for the same incident energy) with respect to showers developing early and at the frontend. Consequently, these deep and late showers will have a higher longitudinal shower leakage, which is unable to compensate for the lower light attenuation, thus producing a higher signal in the tail counters. Channeling of neutrons along the fibers contributes in having an increased number of deep showers, since the FNC's angle respect to the zero degree

⁵⁹Double hits can also contribute to the higher energy part of the tail; at a typical rate varying from $\sim 10^3$ to 10^4 Hz for the lowest FNC energy sum threshold trigger, the probability of double hits varies from 10^{-2} to 10^{-3} , which can account only for a small fraction of the tail.

⁶⁰A brief description of the hadronic shower development is given in section 3.1.2.

⁶¹The timing, energy and other FNC variables for an incident particle on the FNC are defined in section 3.7.2.

line of flight is 0.42° . Tilting the calorimeter by a few degrees ($\sim 3^\circ$ as in LAA project) is not feasible in the present setup of the FNC in the tunnel, and tilting by a smaller angle of 0.8° , which is the maximum allowable with an upgrade of the FNC setup, gives only a slight improvement according to Geant Monte Carlo studies. The dependence of the neutron energy deposited in the calorimeter and its timing⁶² is displayed in figure 3.51 for DIS events (similarly for beam-gas events). The light in the fibers travels at about $0.5 c$ (c is the speed of light) due to the summed up effect of the fiber index of reflection and the longer distance traveled by scintillation light, since this light is reflected many times on the way before reaching the backend. Early showers will produce a signal later than deep showers, because early showers develop at the frontend and the light produced travels at $\approx 0.5 c$ to the photomultipliers; while for deep showers the neutron travels close to c till it does not interact to produce a shower, then the produced light will travel also at $\approx 0.5 c$ in the fibers. The maximum time difference between a very early and very late shower is $\approx 6\text{-}7$ nsec because the calorimeter is 2 m long⁶³.

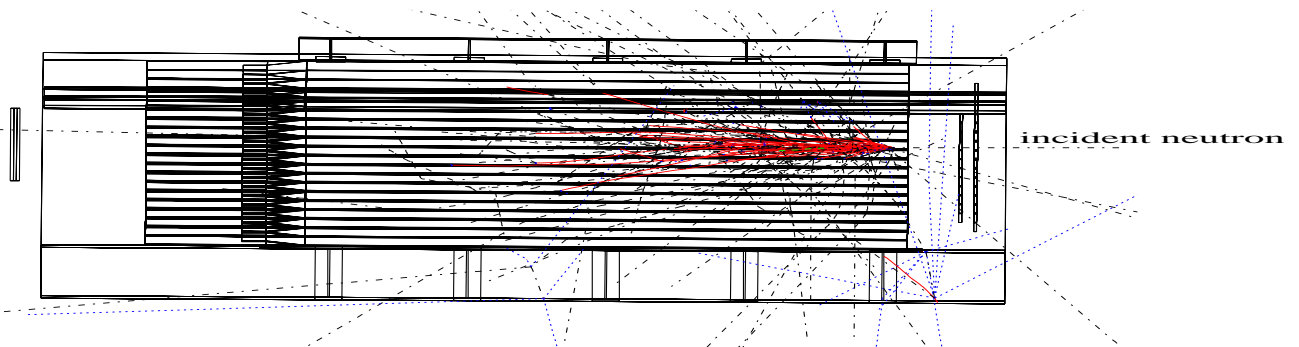


Figure 3.49: The Geant simulation for an early shower of a 600 GeV incident neutron entering the FNC on the right.

⁶²The time is negative because of the chosen FNC reference scale (see section 3.7.2); the more negative the time, the later and deeper the shower develops.

⁶³The time of flight difference between a low (~ 200 GeV) and a high energy neutron (~ 700 GeV), produced at the H1 interaction vertex region (the interaction vertex spread for ep scattering events is of $\sigma \simeq 14$ cm), is of the order of a picosecond, which can not account for the observed time difference of the hits.

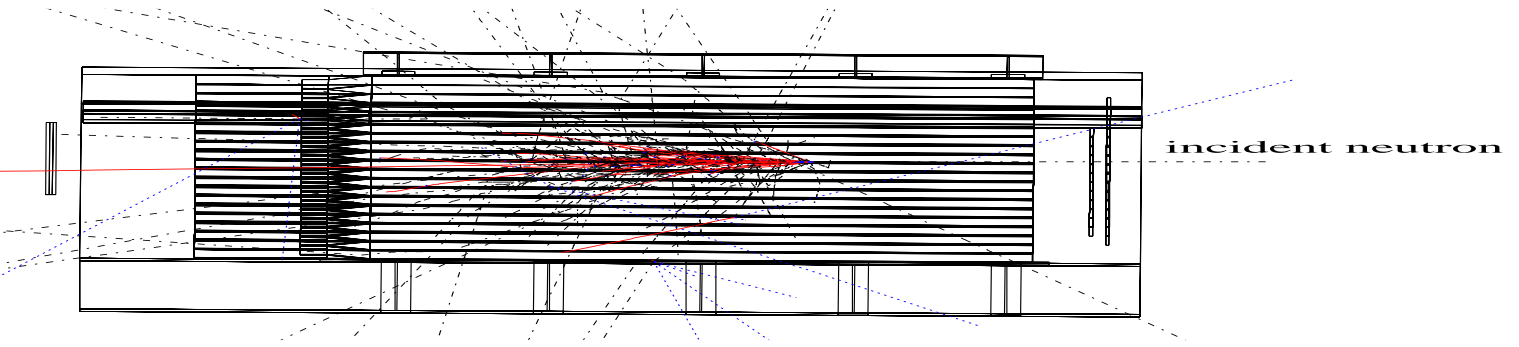


Figure 3.50: The Geant simulation for a late shower of a 600 GeV incident neutron entering the FNC on the right.

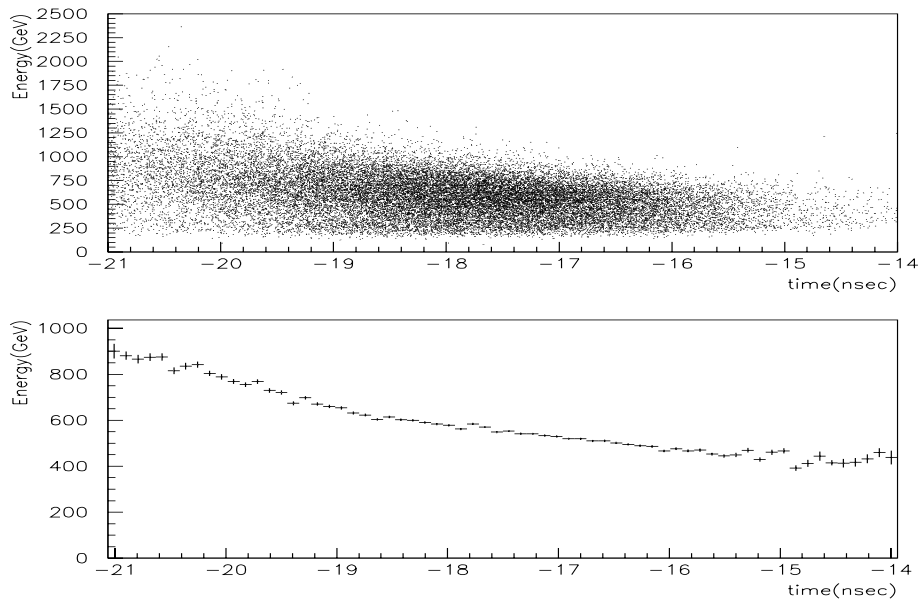


Figure 3.51: The energy deposited in the FNC for an incident neutron versus the time of arrival (in FNC time reference scale) for DIS events; displayed as a scatter plot and a profile histogram (the energies are averaged over the number of events in each time bin). Showers that develop at the beginning of the FNC (early) will have the signals arriving later (less negative times), than showers developing deep (late) in the FNC.

Figure 3.52 shows the approximately linear dependence of the energy deposited in the calorimeter versus the natural logarithm of the energy deposited in the tail counters; “fnc_{tail}” is the summed up signal in the two tail counters and is given in arbitrary units. High energy deposits in the calorimeter have a higher signal in the tail counters, since these showers develop later and deeper (are less attenuated), and have a greater shower leakage, producing a bigger signal in the tail catcher.

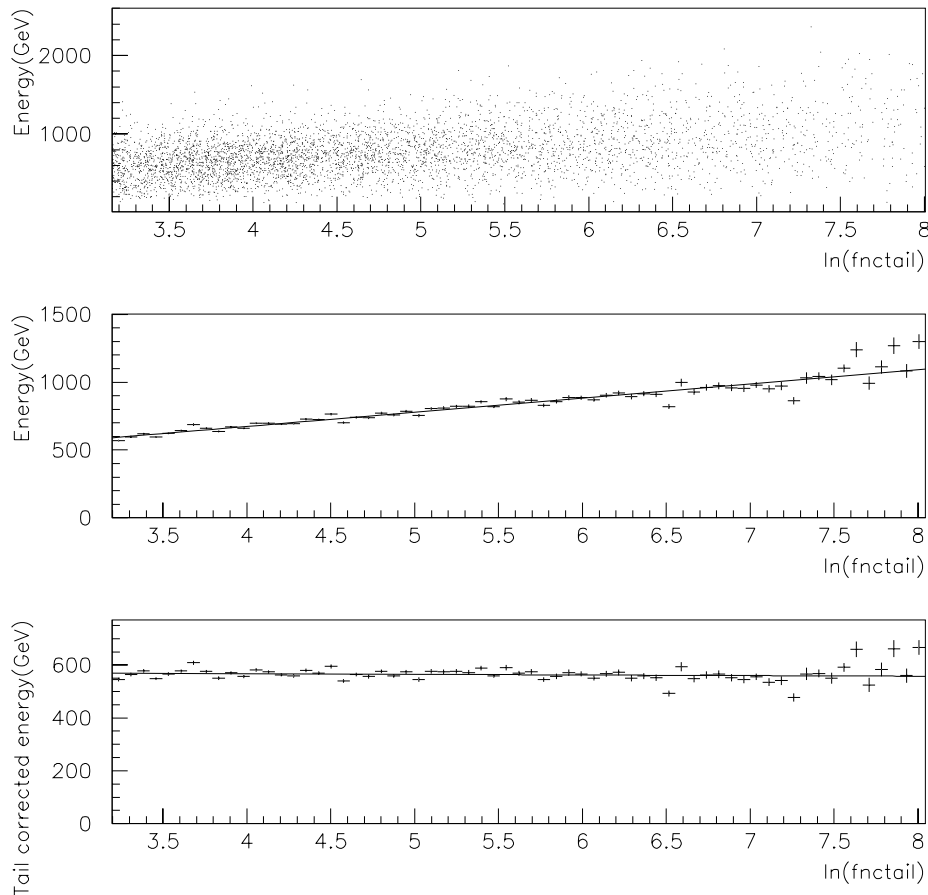


Figure 3.52: The energy deposited in the FNC for an incident neutron versus the natural logarithm of the energy deposited in the tail counters (given in arbitrary units); displayed as a scatter plot and profile histogram with its linear fit. The bottommost plot is the profile histogram with the tail correction for the energy (see equation 3.26).

A small tail catcher was installed in the 1996-97 winter shutdown (see section 3.4) to detect the longitudinal shower leakage, confirming that deep showers cause the high energy tail. The tail in the neutron energy spectrum (figure 3.53) can be reduced by making progressively bigger cuts on the energy deposited in the tail catcher. It can not be reduced completely because there are also showers that develop deep in the calorimeter but deposit very little energy in the tail catcher, since their longitudinal leakage detected in the tail catcher is small.

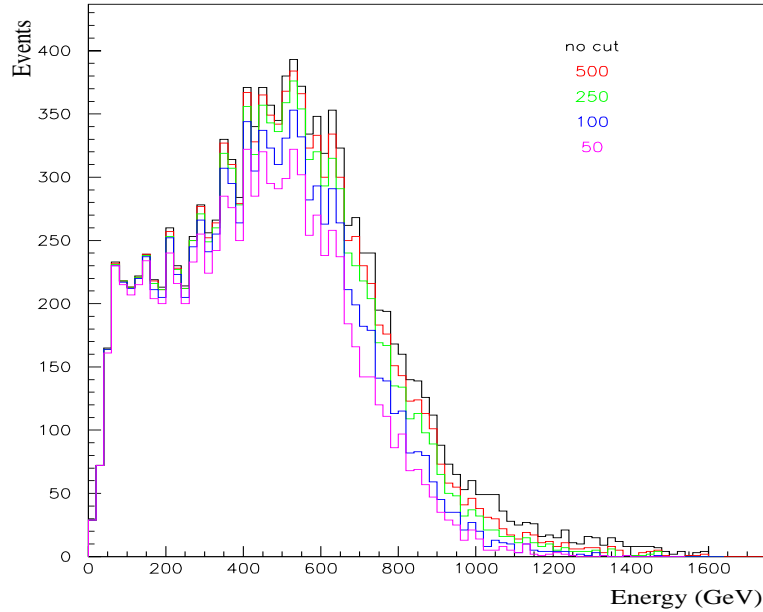


Figure 3.53: The neutron energy spectrum for beam-gas events with various cuts on the tail-catcher signal (arbitrary units). The bigger the cut value, the smaller the number of tail events.

The linear correlation between the FNC energy and the natural logarithm of the fnc_{tail} energy can be used to partially correct the high energy tail⁶⁴, since higher energies have on average greater longitudinal leakage. Figure 3.52 shows the profile histogram for this correlation before (middle plot) and after (bottom plot) the correction for tail is made. The correction utilizes this linear correlation (middle plot) and consists in multiplying the FNC energy by the intercept of the fit and dividing it by the linear correlation $FNC = a + b \cdot \ln(fnc_{tail})$, i.e.:

$$FNC^{cor} = FNC \cdot \frac{a}{a + b \cdot \ln(fnc_{tail})}, \quad (3.26)$$

with FNC^{cor} the tail corrected FNC energy, FNC the FNC energy, a and b the intercept and the slope of the linear fit respectively and fnc_{tail} the combined signal of the two tail counters. The bottommost profile histogram shows that after the correction there is no more a correlation, i.e. the FNC^{cor} is independent from $\ln(fnc_{tail})$. When this correction is applied to data, the high energy tail is reduced progressively by more than 50% (see figure 3.54).

The calorimeter fibers attenuation length was measured during 1997-1998 winter shutdown using cosmic muons. Two scintillator plates were positioned above the calorimeter for triggering on the incoming muon and moved along the calorimeter length in different positions, to measure the calorimeter response to the traversing muon at varying distances from the photomultipliers in the backend. The measured attenuation length

⁶⁴Also the correlation between FNC energy and timing can be used, but the FNC energy versus fnc_{tail} energy was chosen for 1996 data.

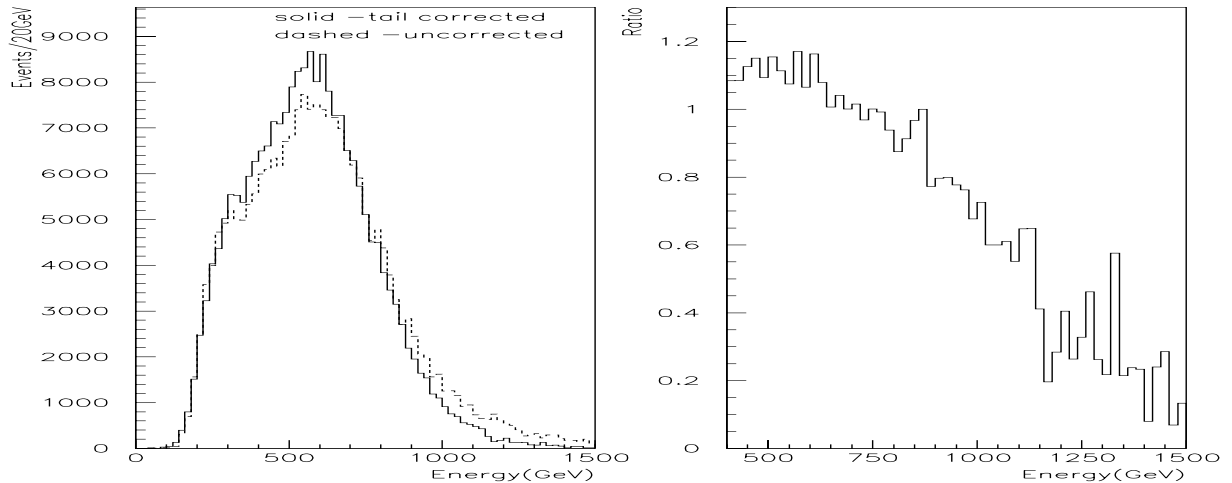


Figure 3.54: On the left is the beam-gas neutron energy spectrum corrected for the tail (solid histogram) and uncorrected (dashed), on the right is the ratio of the corrected to the uncorrected histograms.

was found to be ~ 1.8 m, which decreased considerably from the previous measurement done when it was built ~ 6.6 m[37]. This decrease is not due to radiation damage of the fibers (HERA dose is too low) since the fibers belonging to modules out of the irradiated area have a similar attenuation length. Most likely it could be due to mechanical stress (lead weight) on the fibers, which compresses them modifying their properties. In fact the top part modules rebuilt in 1995 had a higher light output than the untouched ones during the test beam, but now have a similar attenuation length as the others.

Another possible effect, which might contribute to the high energy tail, in addition to the light attenuation, is the Čerenkov light produced in the light guides of the photomultipliers in the backend of the calorimeter, by leakage of deep showers. The average FNC calorimeter photomultiplier signal is produced by $\sim 10^4$ photoelectrons, while $\sim 10^2$ photoelectrons are produced by a relativistic particle passing through the light guide. This effect is still under study since it is not well known how many relativistic particles pass through the light guides.

To try and solve this high energy tail problem, a preshower detector has been built (end 1997 to spring of 1998) and tested at DESY (March-April 1998), with the scope of placing it for the 1998 luminosity run period, upstream of the FNC, in the front end of the calorimeter adjacent to the calorimeter matrix body, covering the whole acceptance region. Its purpose is to trigger on showers initiating in it, so pulling the showers away from the backend, and thus reducing the longitudinal shower leakage in the backend. The preshower is a scintillator-lead sandwich calorimeter ($\sim 2 \lambda_I$ deep), with wavelength shifting fibers glued to the scintillator plates parallel to one another for readout by the photomultipliers. These scintillator plates are oriented with the fibers orthogonally to one another, for impact point reconstruction.

3.12 Position Resolution

The spatial resolution of the impact point position reconstruction can be estimated by using two small scintillator counters, called finger counters, installed in the front end of the device⁶⁵; their layout is displayed in figure 3.55. The charged particles produced in a beam-gas run, which pass through the finger counters producing only one charged reconstructed cluster are used for the estimate. A dedicated beam-gas run was taken for this measurement, with the coincidence between finger counter one and the hodoscope tiles of plane one covering it, defining the data taking trigger.

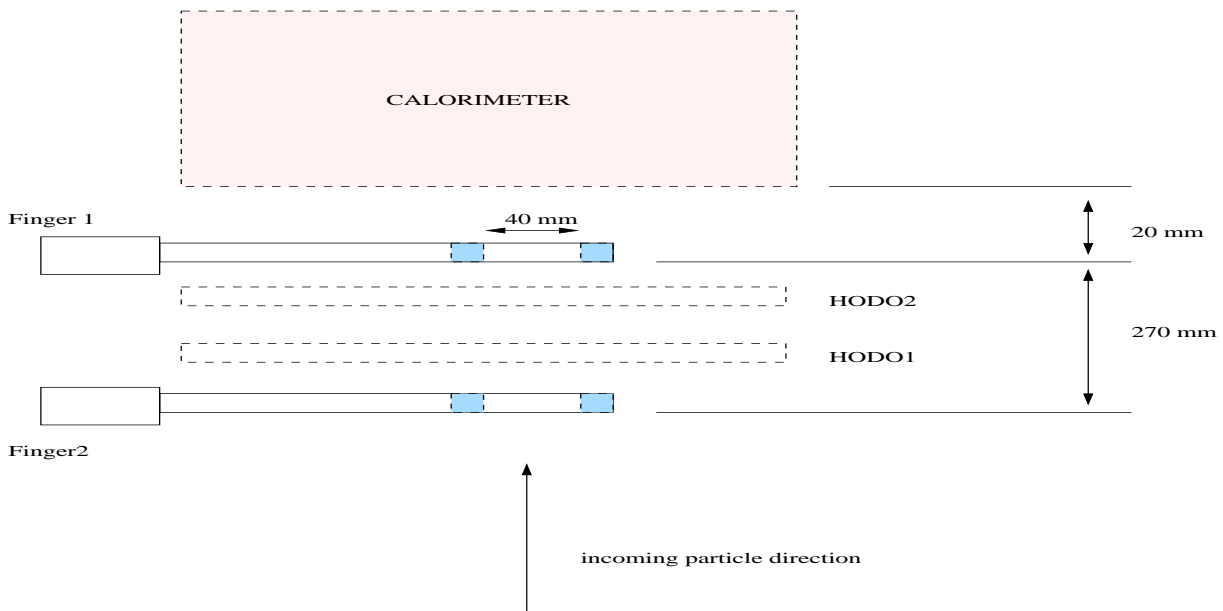


Figure 3.55: The not to scale layout of the finger counters and hodoscope planes in the frontend of the FNC, during the 1997 data taking period. The two small filled in rectangles in each finger counter represent the scintillators.

The energy distribution for the collected finger events (figure 3.56, left plot), which correspond to charged particles, is softer than the neutron energy distribution, as is expected (see section 3.7.2). The impact distributions on the xy plane of the FNC surface belonging to the two scintillators in the finger counter can be seen (figure 3.56 right plot).

⁶⁵Each finger counter is composed of two small scintillators and a light guide, see last part of section 3.4 and figure 3.15 for more detail.

The projection onto the x and y axis respectively (figure 3.57), shows that the distance between the two peaks (x -axis) matches quite well the distance of 4 cm between the two scintillators in the finger counter.

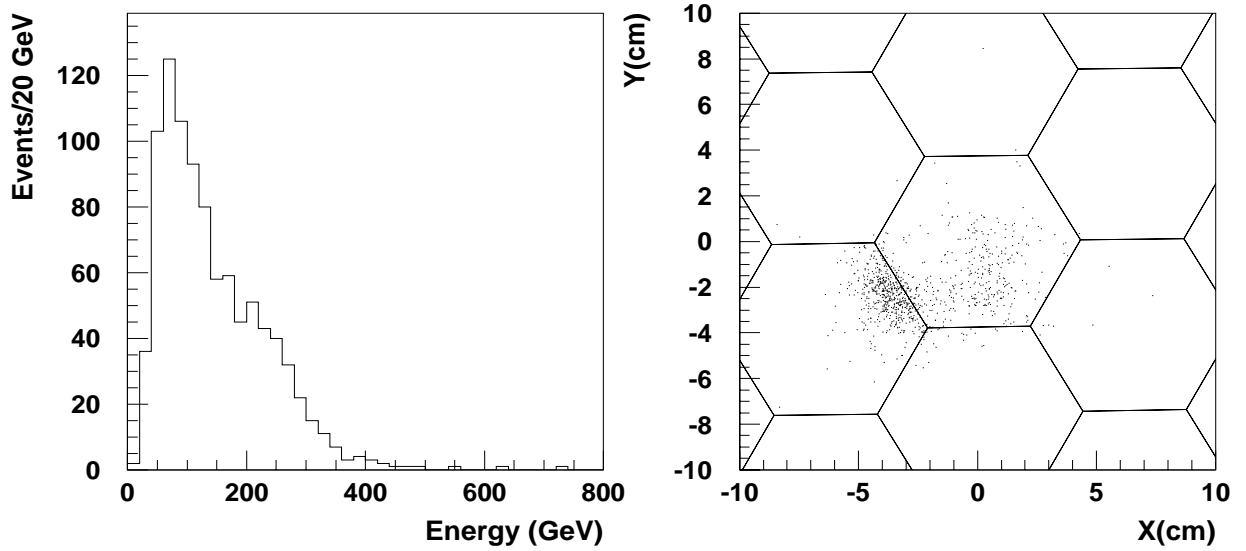


Figure 3.56: The FNC energy distribution for the finger events (left) and the xy reconstructed impact point distribution (right) on the FNC surface plane. The hexagonal calorimeter module structure is also displayed.

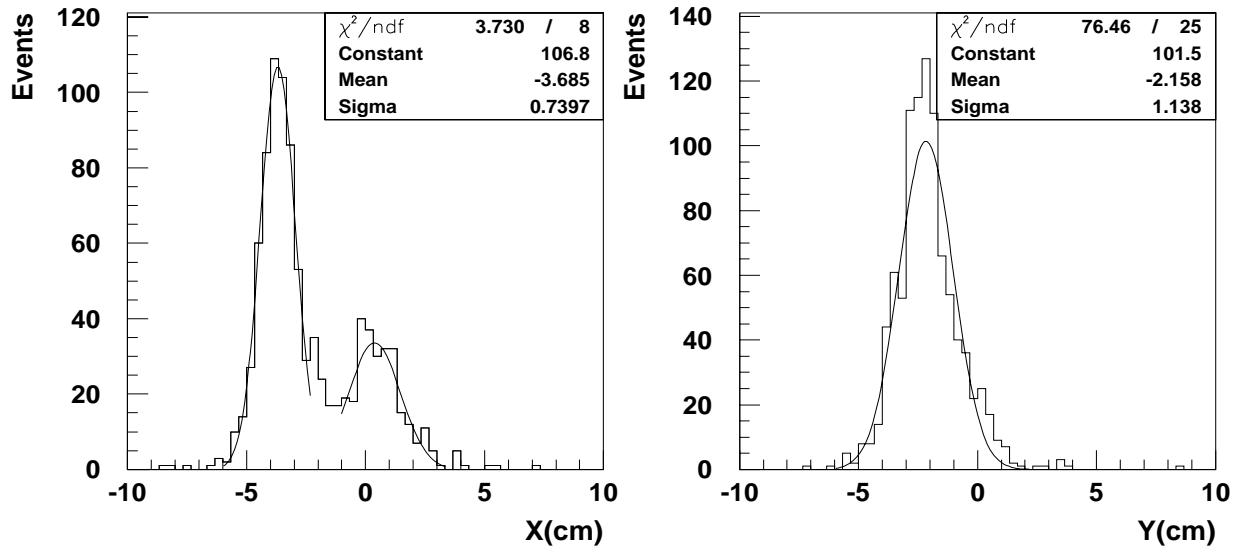


Figure 3.57: The x and y impact point distribution on the FNC surface, with the Gaussian fit applied.

The charged spectrum energy range has been divided into 6 bins, the x and y projections were taken and fitted with a Gaussian obtaining the σ of the fit; then the weighted mean of the x and y projections for each bin was taken. The result is plotted in figure 3.58 for the finger counter data and the test beam data point[38] for 15 GeV pions and fitted with a function of the type[37]:

$$\sigma(E) = \frac{a}{\sqrt{E}} + b, \quad (3.27)$$

with $\sigma(E)$ the position resolution in cm as function of the energy E in GeV , and a, b two constants. The fitted function takes the following values:

$$\sigma(E) = \frac{3.78 \pm 0.86}{\sqrt{E}} + 0.33 \pm 0.09 \text{ cm}; \quad (3.28)$$

by extrapolating this fit to higher energies, an estimate of $\sigma \sim 0.5 \text{ cm}$ for $E > 400 \text{ GeV}$ appears reasonable for the resolution of the impact point position.

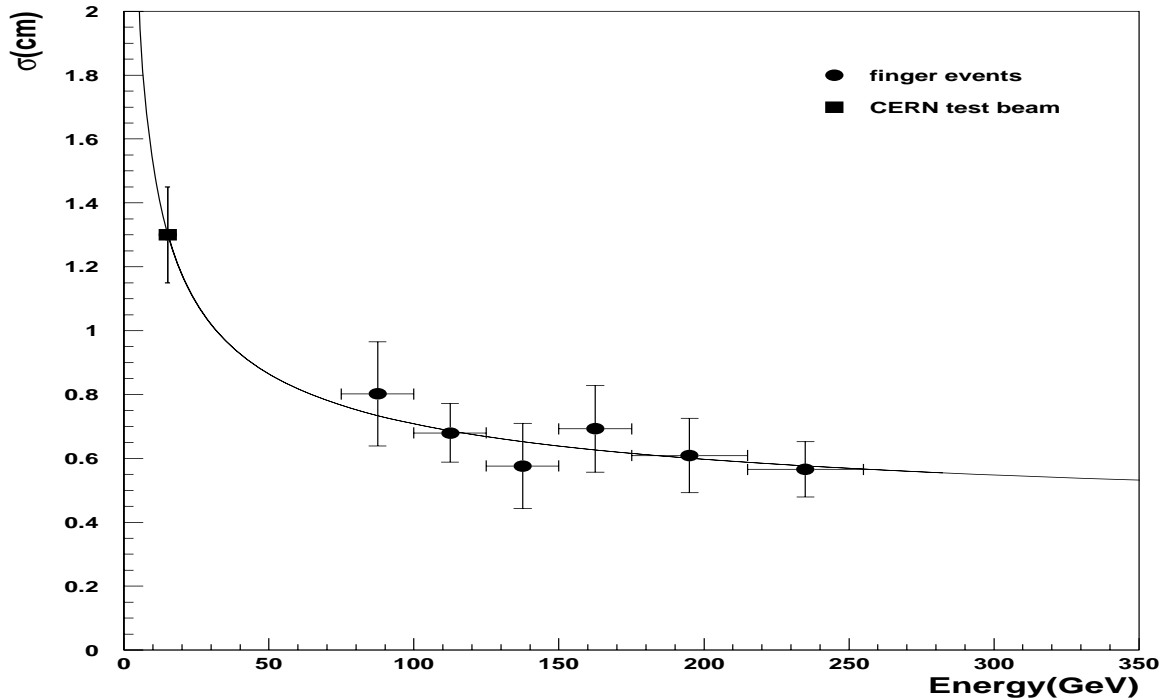


Figure 3.58: The estimated position resolution σ versus the incident charged particle energy. The higher energy bins are larger because of insufficient statistics. Only statistical errors are shown.

3.13 Acceptance

The FNC geometrical acceptance is determined by the apertures of the proton beamline elements located between the H1 detector and the FNC (see fig 3.12), which partially obstruct the neutron flight path around the zero degrees line of flight. The scattering angle θ can stretch out up to $\theta \simeq 0.8 \text{ mrad}$ for a confined region of the azimuthal angle ϕ . The Monte Carlos Pompyt and Lepto have been used to study the acceptance. To simulate the proton beamline the H1SIM⁶⁶ program was used, in which only generated neutrons, that do not interact with the beam elements or other dead material, do reach the FNC. The two Monte Carlo predictions for the neutron energy ($E > 100 \text{ GeV}$) spectrum are quite different at the generator level, but the acceptance strongly modifies the spectrum, giving a similar shape and cross section, as can be seen in figure 3.59.

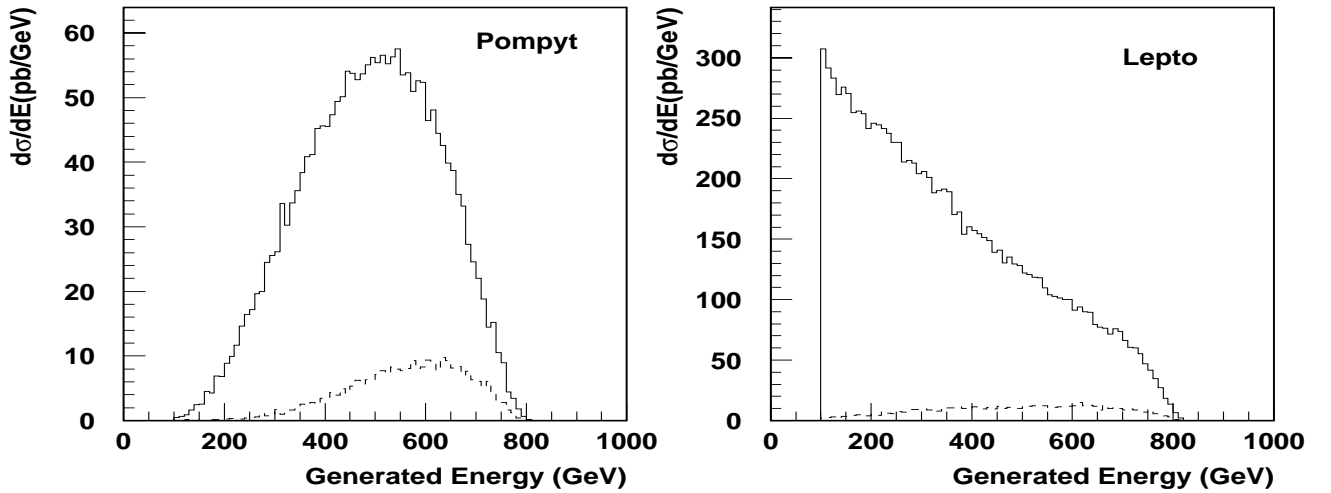


Figure 3.59: The Pompyt and Lepto generated neutron energy spectra (solid) for generated energies $E > 100 \text{ GeV}$ are displayed, together with the effect of the FNC acceptance (dashed) on the energy spectrum.

The FNC acceptance (including the energy resolution) has been estimated⁶⁷ to be $17 \pm 4\%$ for neutron energies $E > 400 \text{ GeV}$. This has been done by taking the average of the Lepto ($13.7 \pm 0.6 \%$) and Pompyt ($20 \pm 0.8\%$) ratios of the number of accepted events (smeared according to the FNC energy resolution) to the generated number of events, with the 4% error accounting for the difference in the two predictions (for $E > 400 \text{ GeV}$ and $|t| < 0.5 \text{ GeV}^2$ the acceptance is $23 \pm 4\%$). Using only Lepto to correct for the acceptance and energy resolution for $E > 100 \text{ GeV}$, the estimate for the acceptance is $7.5 \pm 0.9 \%$.

⁶⁶H1SIM is the simulation program for the H1 detector, which includes also the proton beamline till the FNC.

⁶⁷The Pompyt Monte Carlo is expected to be valid only at $E > 400 \text{ GeV}$, while Lepto can be used also for lower energies $E > 100 \text{ GeV}$.

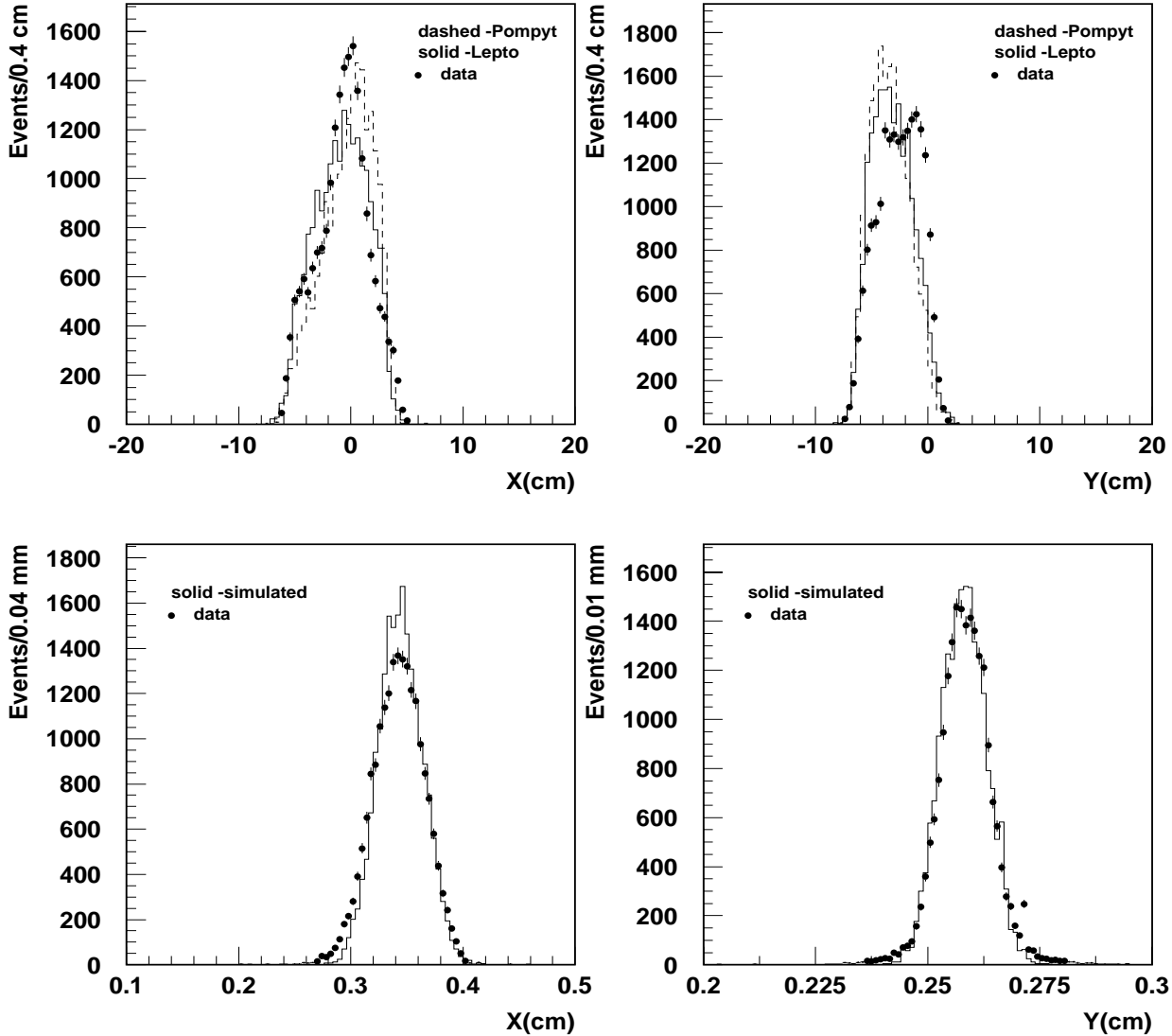


Figure 3.60: The two top plots display the FNC neutron impact point x and y coordinates (in the FNC reference frame) for luminosity data with $E > 400 \text{ GeV}$, compared to Lepto and Pompyt Monte Carlos for $E > 400 \text{ GeV}$ and normalized to the same number of events. The two lower plots display the respective ep scattering vertex positions (H1 reference system) compared to the beam model simulation of the interaction vertexes ($E > 400 \text{ GeV}$).

The neutron (x,y) coordinates of the impact points at the FNC front surface, obtained from luminosity data, are in approximate agreement with the two Monte Carlo predictions for $E > 400 \text{ GeV}$; while the respective neutron ep scattering (x,y) vertex coordinates are in agreement with the beam model simulation of the interaction vertexes (figure 3.60). The FNC position resolution has been taken in account by smearing Gaussianly ($\sigma = 0.6 \text{ cm}$) the Monte Carlo x and y coordinates at the FNC surface. The FNC acceptance as function of position on the FNC surface is shown in figure 3.61, which displays the FNC acceptance area corresponding to the aperture of the beam line elements. The acceptance rises with the neutron energy and decreases with P_T and scattering angle θ (figure 3.62).

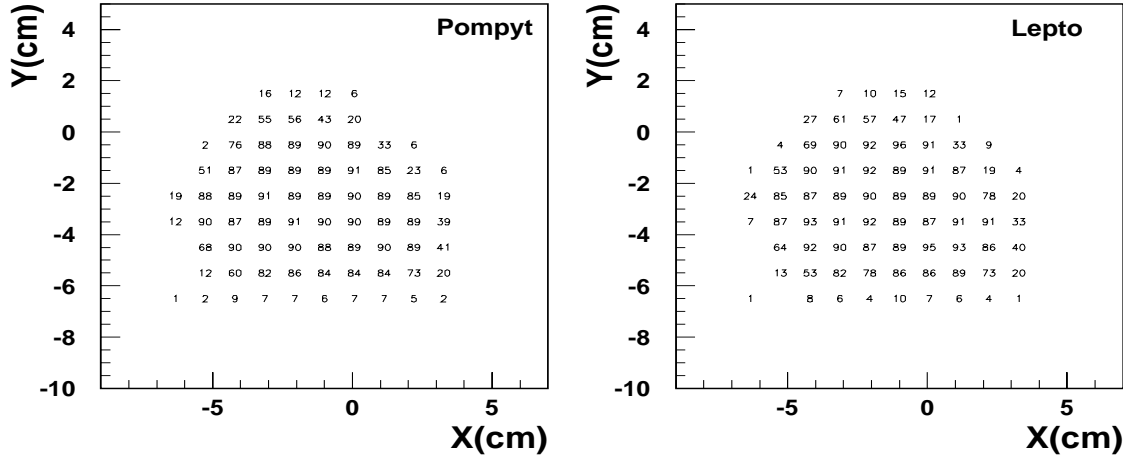


Figure 3.61: The FNC ($E > 400 \text{ GeV}$) acceptance determined from Pompyt and Lepto Monte Carlos as function of the position on the front face of the FNC is displayed. The FNC reference coordinate system is used and the binning is 1 cm^2 .

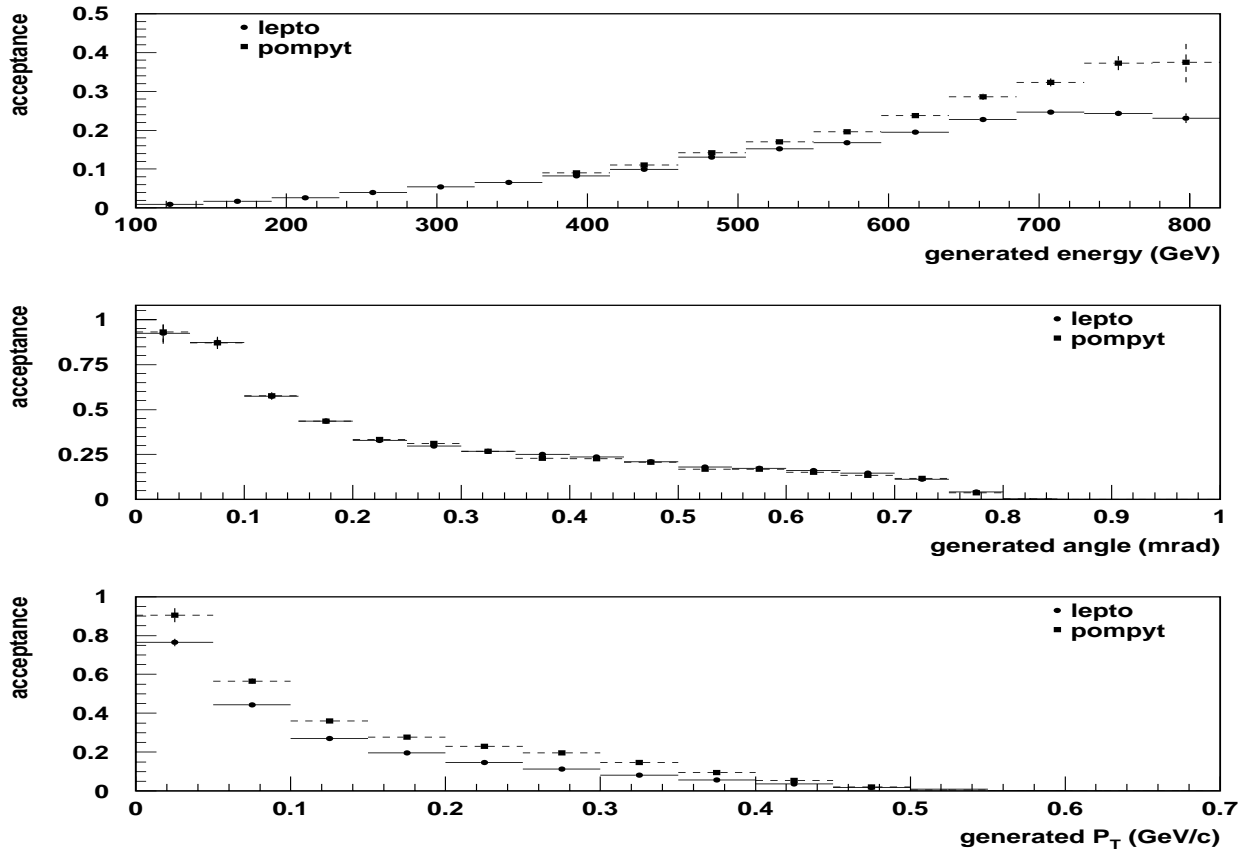


Figure 3.62: The acceptance of the FNC, determined using Pompyt and Lepto Monte Carlos is shown as function of energy, scattering angle θ and P_T (only statistical errors are shown). Pompyt and Lepto generated events with $E > 400 \text{ GeV}$, $E > 100 \text{ GeV}$ respectively, were taken.

Chapter 4

PHYSICS RESULTS

This last chapter describes the reconstruction of the kinematical variables for a given event and the data selection criteria used in this analysis; then the basic properties of leading neutron production will be discussed and data will be compared to the Monte Carlo predictions.

4.1 Event Reconstruction and Selection

Event Reconstruction

The kinematical variables x , y and Q^2 described in section 1.2 can be reconstructed, from the measured electron, the measured hadronic final state or a mixture of the two, using various methods[21]. The optimal method depends on the kinematical range chosen for the analysis. In laboratory coordinates x , y and Q^2 can be expressed simply as:

$$Q_e^2 = 4E_e E'_e \cos^2 \frac{\theta_e}{2}; \quad (4.1)$$

$$y_e = 1 - \frac{E'_e \sin^2 \frac{\theta_e}{2}}{E_e}; \quad (4.2)$$

$$x_e = \frac{Q_e^2}{s y_e}; \quad (4.3)$$

with E_e and E'_e the initial and final electron energy, θ_e the scattered electron angle, s the center of mass energy squared. These variables are expressed using only the scattered electron four-vector information. This method of determining and reconstructing the kinematical variables is called the electron method; for this reason the kinematical

variables x , y and Q^2 have an “ e ” as subscript to denote the method. This method is simple, but the y resolution worsens at low y , due to a $1/y$ factor in the error propagation equation[51], [21].

The sigma method (Σ), which combines both hadronic and electron information, is chosen for the reconstruction of the kinematical variables in this thesis. This method improves the y resolution at low y and reduces the ISR (Initial State Radiation) effects on the measured kinematical variables, and gives a good resolution for the reconstructed variables[51].

If no particles escape detection by H1, from the energy-momentum conservation relation one obtains:

$$2E_e = \sum_h (E_h - p_{z,h}) + (E'_e - p_{z,e}) \quad (4.4)$$

$$= \sum + E'_e(1 - \cos\theta_e) \quad (4.5)$$

with $\sum = \sum_h (E_h - p_{z,h})$ the sum over all the reconstructed hadrons, E_h is the hadron energy, E_e and E'_e the incident electron and scattered electron energy respectively, $p_{z,h}$ and $p_{z,e}$ the hadron and scattered electron longitudinal momenta respectively. It is important to note that any hadronic final state particles escaping detection by going down the forward beam-pipe, gives a small contribution to the sum Σ ; Σ is not sensitive to these undetected particles. In the Σ method, the incident beam electron energy E_e is substituted by E_r , the reconstructed electron energy; E_r is given by (with the same meaning of the variables as above):

$$2E_r = \sum + E'_e(1 - \cos\theta_e). \quad (4.6)$$

The Σ method is less sensitive to the ISR, since the ISR photon normally does not contribute to the calculation because it usually escapes detection by going through the beam-pipe; thus E_r is nearer to the energy of the electron which interacts with the proton, resulting in “truer” reconstructed values. Replacing E_e with E_r in equations 4.1-4.3, the reconstructed kinematical variables take the following form with the Σ method:

$$y_\Sigma = \frac{\Sigma}{\Sigma + E'_e(1 - \cos\theta_e)}; \quad (4.7)$$

$$Q_\Sigma^2 = \frac{E_e'^2 \sin^2\theta_e}{1 - y_\Sigma}; \quad (4.8)$$

$$x_\Sigma = \frac{Q_\Sigma^2}{s y_\Sigma}. \quad (4.9)$$

Event Selection

The 1996 luminosity data was used in this analysis. The H1TOX[35] program, modified to contain the FNC event information, was used to create ntuples which could then be analyzed using PAW (see section 2.2.7). The following cuts were applied for the data selection.

- **run conditions**:- The Runselect program[50] was used to select runs that were considered of good or medium quality (run quality 1-2, i.e. when all of the main detector systems are operational) and of good luminosity conditions (trigger phase 2-4).
- **$2 < Q^2 < 100 \text{ GeV}^2$** :- The low Q^2 DIS selection which is within the acceptance of the SPACAL calorimeter.
- **$0.02 < y < 0.6$** :- The kinematic region with a good y reconstruction[51].
- **z vertex**:- A reconstructed vertex in H1 is required, with the z position of the event being at $z=5\pm 30 \text{ cm}$, corresponding to the spread of the interaction vertex due to the proton bunch length.
- **$E'_e > 12 \text{ GeV}$** :- This cut is required for the scattered electron energy (E'_e) detected in the SPACAL, to reject low energy SPACAL clusters originating from background events and reduce the photoproduction background[29] (i.e. the scattered electron escapes detection by going through the beampipe and a fake electron cluster is identified in the SPACAL).
- **$E - P_z > 40 \text{ GeV}$** :- $E - P_z = \sum_k (E_k - p_{z_k})$ with the sum done over all the detected particles; E and P_z stand for energy and longitudinal momentum respectively. This cut reduces the radiative and photoproduction background. For DIS events, where both the scattered electron and the hadronic final state are detected in H1, the $E - P_z$ distribution is peaked around twice the electron beam energy $2E_e \simeq 55 \text{ GeV}$ (see equation 4.4), while photoproduction background events have smaller values due to the undetected scattered electron escaping through the beampipe. For radiative events (ISR), the radiated electron escaping down the beampipe modifies the energy-momentum conservation equation 4.4 to $2E_e - 2E_\gamma = E - P_z$, with E_γ the radiated photon energy; this allows to reduce partly the radiative background by limiting the ISR photon energy.
- **S(4) subtrigger**:- It is a SPACAL subtrigger used to trigger on events with the scattered electron depositing energy in the SPACAL and reject beam induced background. Its efficiency has been calculated to be $94.3 \pm 0.1\%$, by taking the ratio

between N with subtrigger S4 set and N : $(N \text{ and S4})/N$, where N is the total number of events of the complete data sample 1996 that survive the above described cuts with any non SPACAL subtrigger set.

The requirements relative to the FNC are (see section 3.7.2 for a description of the FNC variables) the following.

- **nhitfnc=1**:- Only one reconstructed cluster in the FNC; about 95% of the ep data FNC events have only one cluster.
- **iqfnc=0**:- The electric charge of the cluster is zero (i.e. neutral cluster).
- **(fncx,fncy)**:- The impact point position of the reconstructed cluster is within the FNC's acceptance area.
- **fncene > 100 GeV**:- The FNC reconstructed cluster energy is $> 100 \text{ GeV}$.
- **fnc time < 0**:- A good timing of the reconstructed cluster.

Luminosity

The analyzed data is from the 1996 luminosity running period, and corresponds to an integrated luminosity of $3.38 \pm 0.07 \text{ pb}^{-1}$; a total of 21468 events remain after the above mentioned cuts (general DIS cuts and FNC cuts). Figure 4.1 displays the accumulated 1996 luminosity, useful for the analysis, while figure 4.2 shows the (x_{BJ}, Q^2) kinematical plane for all the events accumulated in 1996 that passed the DIS and FNC selection criteria.

Background

The main background for the DIS events with a neutron detected in the FNC, originates from beam-gas collisions, i.e. protons interacting with the residual gas in the beam-pipe produce neutrons which can randomly overlap with DIS events. The contribution from this background can be estimated in the following way. In beam-gas runs about a third of the FNC triggered events are neutrons, and the average FNC trigger rate¹ during luminosity data taking is 2-3 kHz , giving a beam-gas neutron rate of $\sim 0.66\text{-}1 \text{ kHz}$. In 1996 there were on average 184 proton bunches out of the 220 HERA buckets, each bucket being 96 nsec long; thus the probability for a beam-gas neutron to fall in a bunch

¹This trigger is the lowest energy sum FNC trigger (FNC_SUM, see section 3.6) which has a threshold $\lesssim 100 \text{ GeV}$.

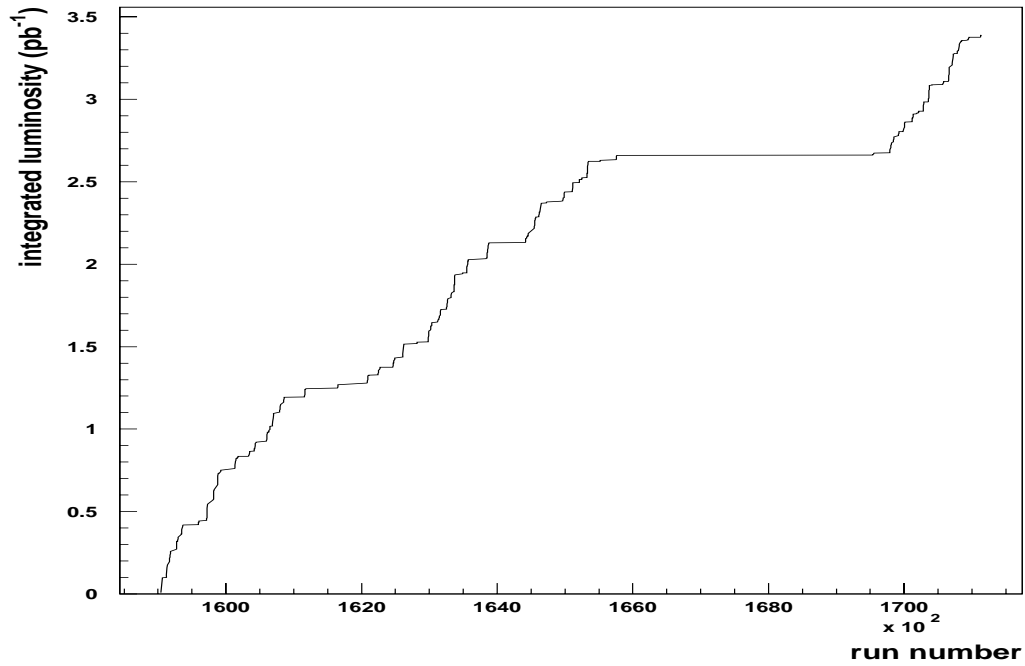


Figure 4.1: The integrated luminosity versus the run number for 1996 FNC luminosity data. The total integrated luminosity is $3.38 \pm 0.07 \text{ pb}^{-1}$. The flat part of the graph corresponds to runs that were excluded due to trigger timing problems of the SPACAL sub-detector.

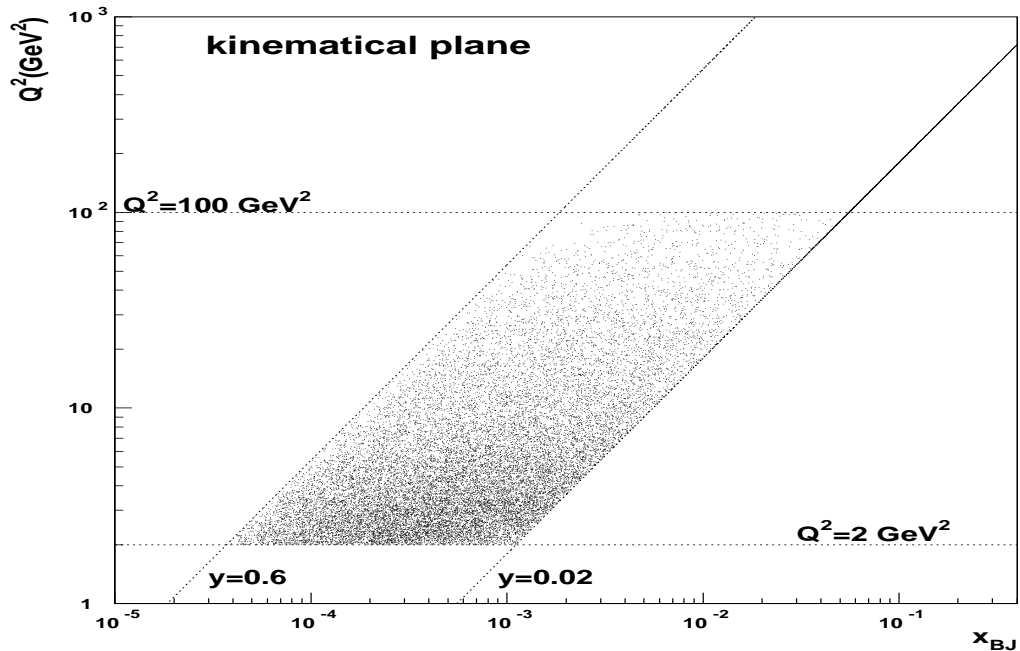


Figure 4.2: The kinematical (x_{BJ}, Q^2) plane with the selected cuts described in section 4.1 for DIS events with a FNC neutron.

is $\sim 10^{-4}$. About 2.7% (see section 4.2) of the DIS events (with the above cuts) have a FNC neutron of energy $E > 100 \text{ GeV}$, so the background/signal ratio is estimated to be $\sim 4 \cdot 10^{-3}$ ($\sim 0.4\%$).

The two main contributions to the background of low Q^2 DIS events are non- ep and photoproduction background. The non ep background is mainly due to beam (proton or electron) interactions with residual gas in the beampipe (beam-gas interactions) and with the beam line components (beam-wall interactions). This background is strongly suppressed by the vertex and timing cuts. The remaining background can be estimated[52] by comparing proton-pilot (p-pilot), electron-pilot (e-pilot), empty (to study cosmic muon background) and ep colliding bunches². The events from 1996 data surviving the above described DIS cuts are 19, 484, 1, 806846 for p-pilot, e-pilot, empty and colliding bunches respectively; taking in account that in 1996 the bunch ratios were on average 10/174 for p-pilot/ ep , 15/174 for e-pilot/ ep , and 21/174 for empty/ ep , the background from non- ep events is estimated to be less than 1%. The photoproduction background can be estimated by looking at the $E - P_z$ distribution for all the above DIS cuts except the $E - P_z > 40 \text{ GeV}$ cut (figure 4.3). DIS events peak around twice the electron beam energy $\sim 55 \text{ GeV}$, while any contamination of photoproduction events should be found at lower $E - P_z$ values, decreasing towards higher $E - P_z$ values to due to the escaping electron. By counting the events in the left tail the possible estimated contamination with a cut of $E - P_z > 40 \text{ GeV}$ is $\lesssim 1\%$.

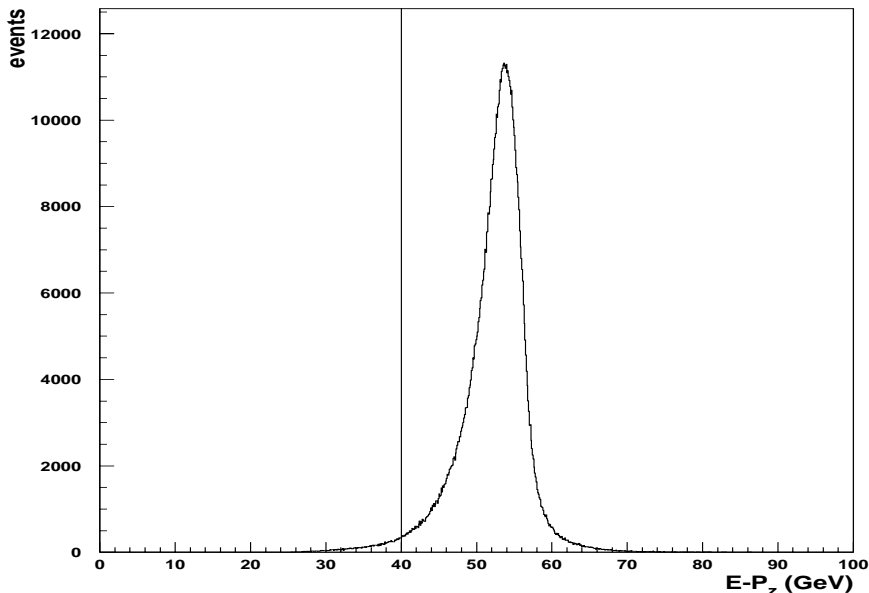


Figure 4.3: The $E - P_z$ distribution for events that survive all the above DIS cuts except the $E - P_z > 40 \text{ GeV}$ position. The line displays the $E - P_z = 40 \text{ GeV}$ cut.

²See section 2.1 for the definition of these bunches.

4.2 Properties of DIS Events with a Leading Neutron

4.2.1 Dependence on the Kinematical Variables

Deep inelastic scattering events with a leading neutron (i.e. leading neutron production) display the same x , W , Q^2 and track multiplicity dependence as the complete DIS sample³. The observed ratio between DIS events with a leading neutron (also called FNC tagged events) and all DIS events in the data sample, as function of the kinematical variables, is approximately constant for neutron energies $E > 100 \text{ GeV}$ or $E > 400 \text{ GeV}$ as can be seen in figure 4.4. The ratio uncorrected for acceptance, energy resolution and neutron detection efficiency, of DIS events with a leading neutron of energy $E > 100 \text{ GeV}$ or $E > 400 \text{ GeV}$ to all the DIS events is $2.66 \pm 0.02 \pm 0.02\%$ and $1.81 \pm 0.02 \pm 0.08\%$ respectively; the first error is statistical and the second is systematic due to the energy scale uncertainty of $\pm 5\%$. The corrected ratio for FNC tagged neutrons with energy $E > 100 \text{ GeV}$ is $38_{-4}^{+6}\%$, which is in agreement with Lepto's prediction of $\simeq 36\%$, while for $E > 400 \text{ GeV}$ it is $11.4_{-2.4}^{+2.6}\%$. The ratio has been corrected for the neutron detection efficiency ($93 \pm 5\%$, see section 3.8), and for the acceptance and energy resolution using only Lepto for $E > 100 \text{ GeV}$ ($7.5 \pm 0.9\%$) and both Lepto and Pompyt for $E > 400 \text{ GeV}$ ($17 \pm 4\%$, see section 3.13), which are the dominant uncertainties. The percentage of DIS events with a leading neutron with $E > 400 \text{ GeV}$ and $|t| < 0.5 \text{ GeV}^2$ is $7.9_{-1.5}^{+2.0}\%$; the energy resolution and acceptance have been corrected using Pompyt and Lepto Monte Carlos ($23 \pm 4\%$). These ratios are listed in table 4.1.

Uncorrected Ratio	Selection
$2.66 \pm 0.02 \pm 0.02\%$	$E > 100 \text{ GeV}$
$1.81 \pm 0.02 \pm 0.08\%$	$E > 400 \text{ GeV}$
Corrected Ratio	Selection
$38_{-4}^{+6}\%$	$E > 100 \text{ GeV}$
$11.4_{-2.4}^{+2.6}\%$	$E > 400 \text{ GeV}$
$7.9_{-1.5}^{+2.0}\%$	$E > 400 \text{ GeV}, t < 0.5 \text{ GeV}^2$

Table 4.1: FNC uncorrected and corrected leading neutron ratios. For the uncorrected ratios the first error is statistical while the second is systematic (energy scale uncertainty of $\pm 5\%$). For the corrected ratios the errors (statistic and systematic) have been added in quadrature.

The uncorrected ratio of DIS events with a leading neutron to all DIS events versus the kinematical variables Q^2 and x_{BJ} , is approximately constant showing no functional dependence, in the different neutron energy bins, and varies between ~ 0.2 - 0.5% (figures 4.5, 4.6). The same occurs if the ratio is made for FNC tagged events with $E > 100 \text{ GeV}$ in bins of Q^2 as function of x_{BJ} and vice versa (figure 4.7).

³Some previous papers are [54], [39], [55].

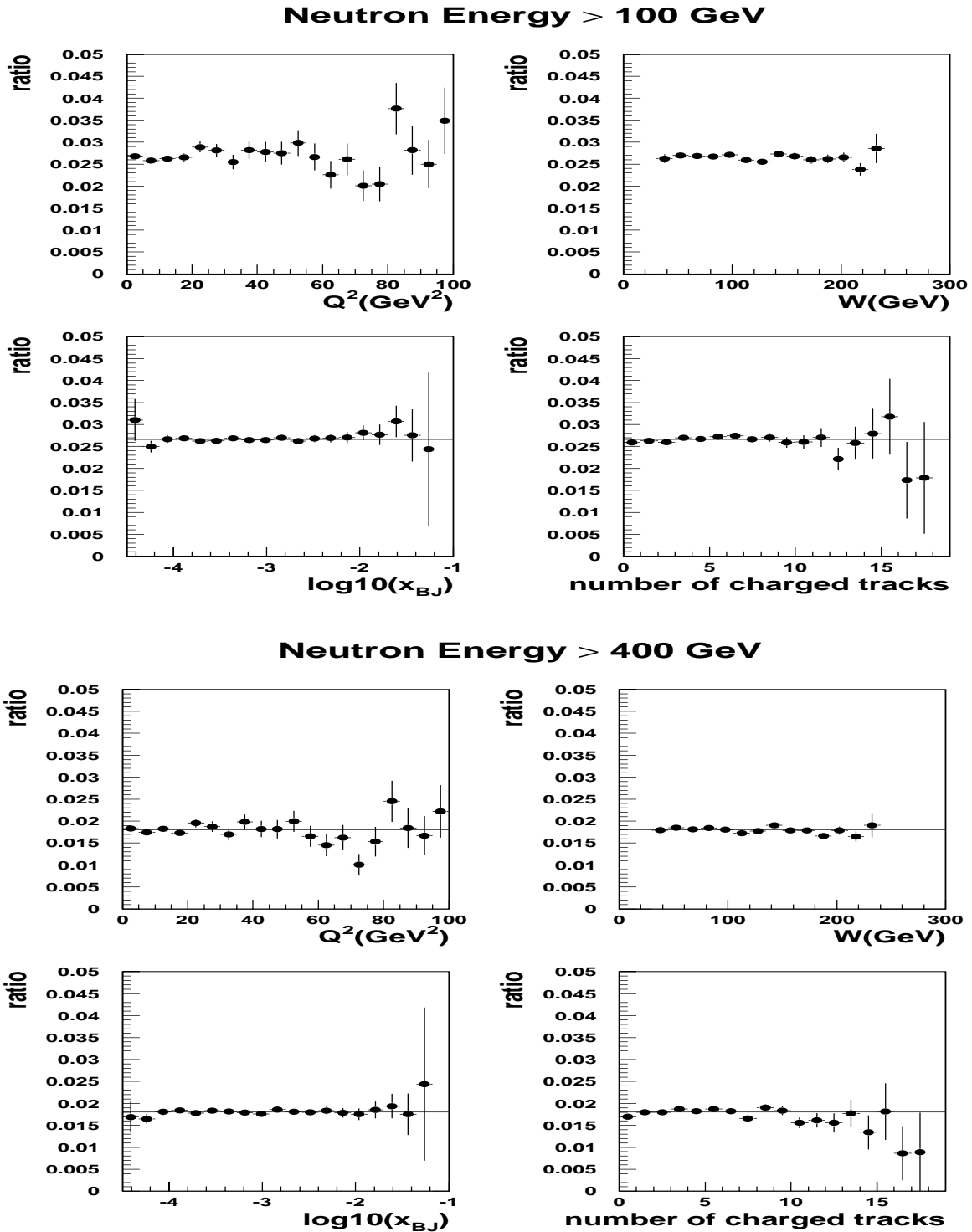


Figure 4.4: The uncorrected ratio between FNC tagged neutron events ($E > 100 \text{ GeV}$ and $E > 400 \text{ GeV}$) and all DIS events, for the three kinematical variables x_{BJ} , W , Q^2 and the track multiplicity. The drawn line indicates the average ratio value of 2.66% ($E > 100 \text{ GeV}$) and 1.81% ($E > 400 \text{ GeV}$); within the errors there is no functional dependence of the ratio from these variables. Only statistical errors are displayed.

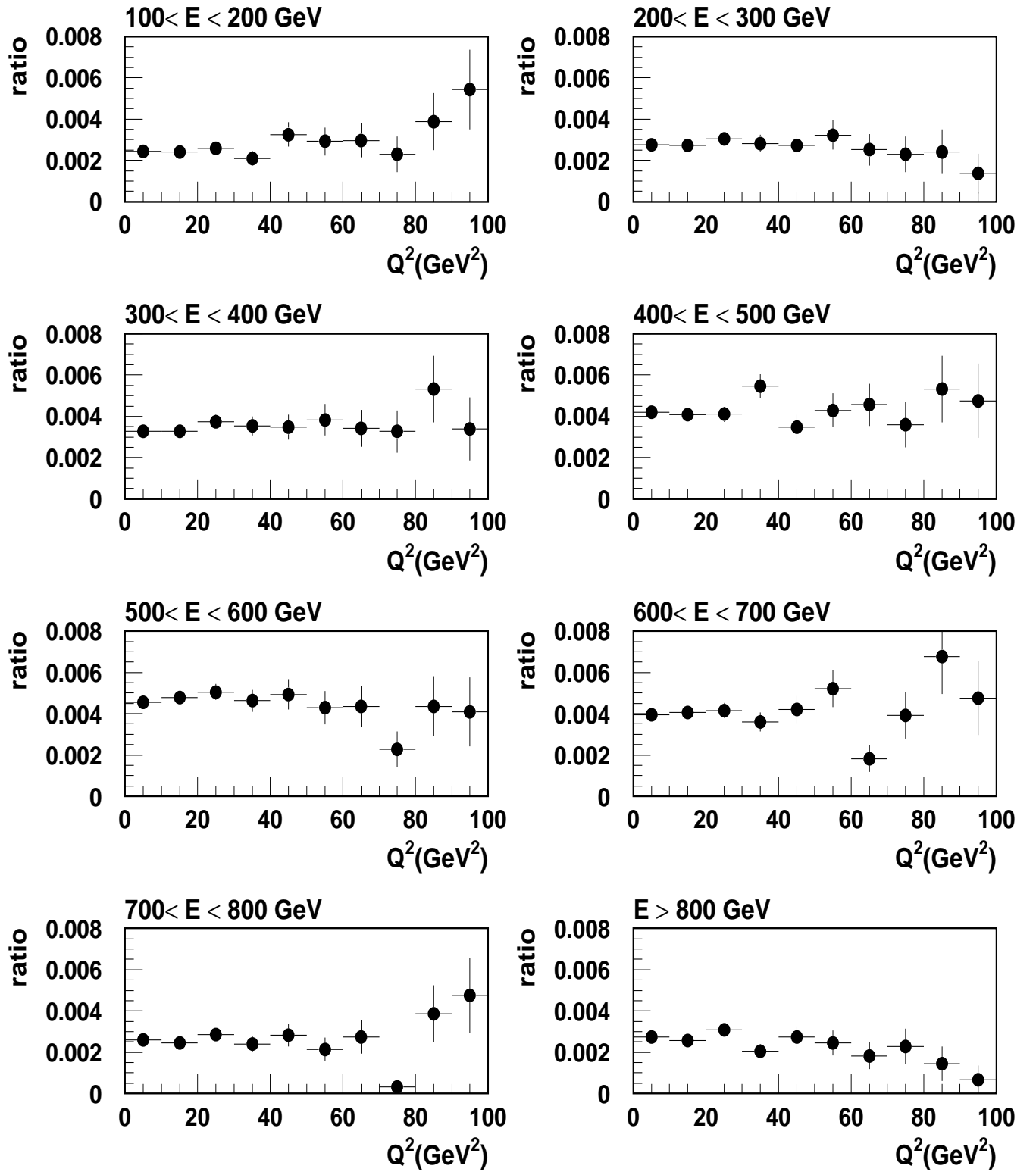


Figure 4.5: The uncorrected ratio of FNC tagged neutrons and all DIS events as function of Q^2 in eight neutron energy (E) bins. Within errors the ratio is practically constant in each bin, varying from ~ 0.2 - 0.5% in the different energy bins. Only statistical errors are displayed.

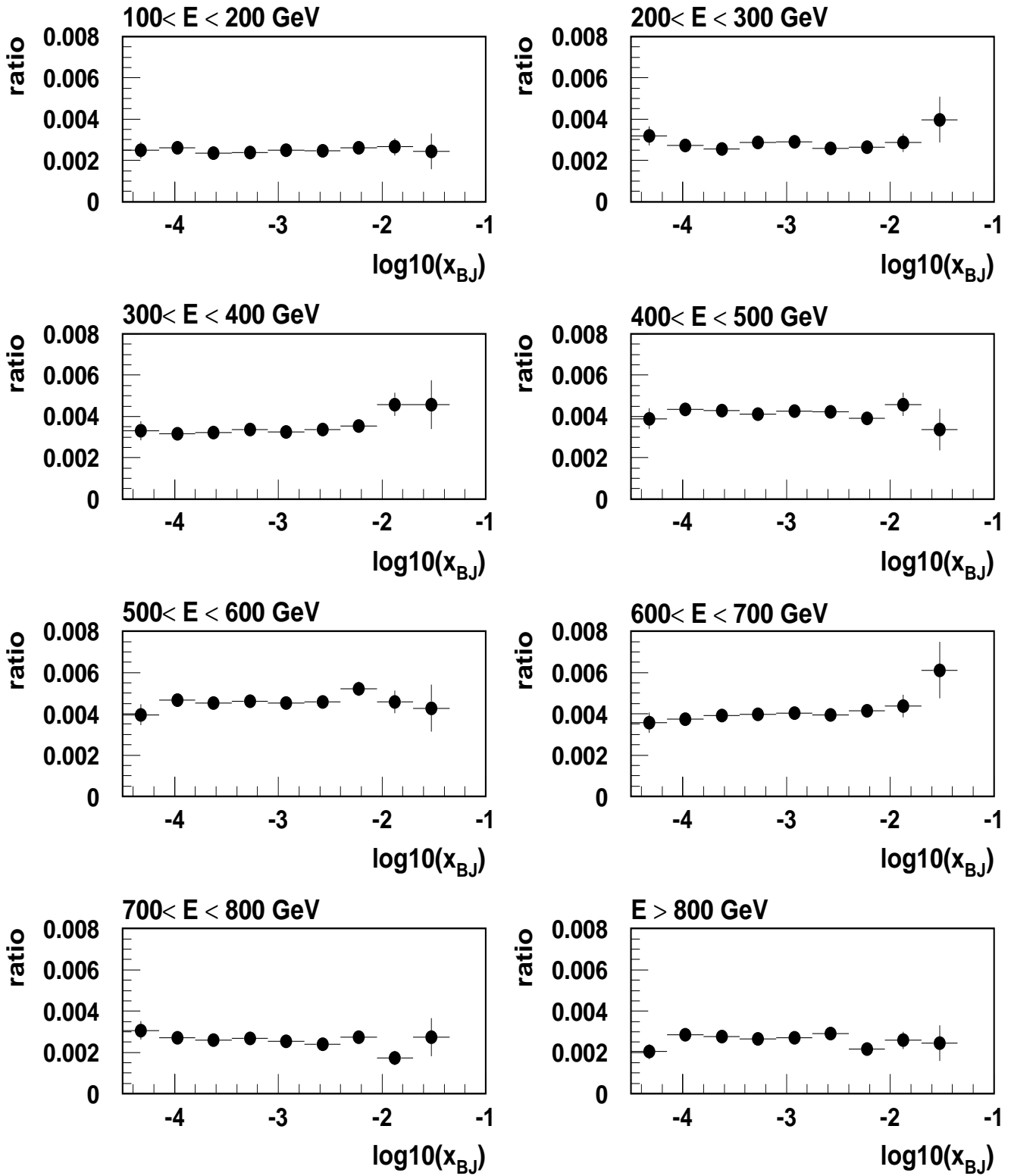


Figure 4.6: The uncorrected ratio for FNC tagged neutrons and all DIS events as function of $\log_{10}(x_{BJ})$ in eight neutron energy (E) bins. Within errors the ratio is practically constant in each bin, varying from ~ 0.2 - 0.5% in the different energy bins. Only statistical errors are displayed.

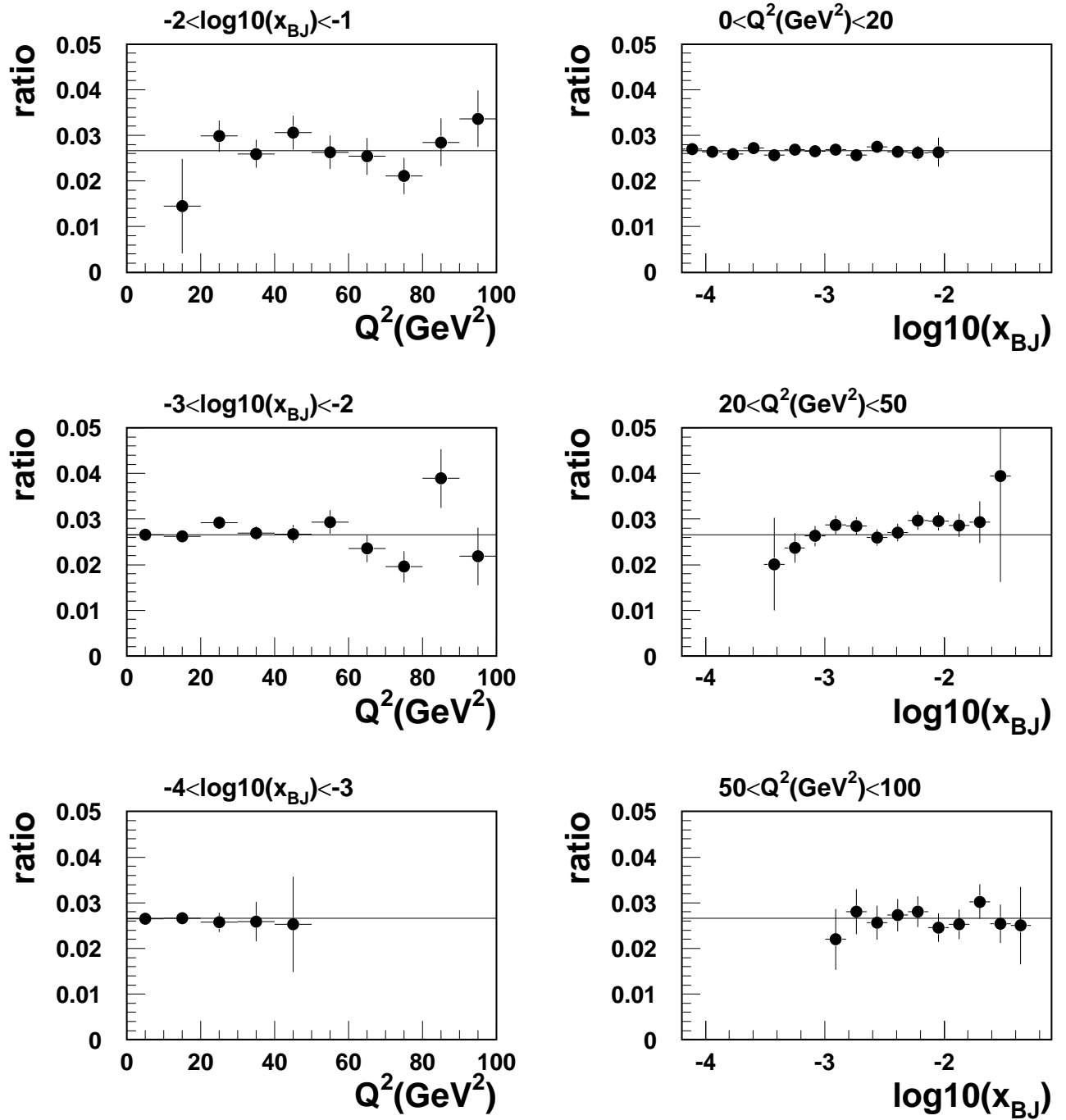


Figure 4.7: The uncorrected ratio between FNC tagged neutrons ($E > 100 \text{ GeV}$) and all DIS events as function of Q^2 in three $\log_{10}(x_{BJ})$ bins, and as function of $\log_{10}(x_{BJ})$ in three Q^2 bins. The line displays the average 2.66% ratio value, indicating a practically constant ratio; only statistical errors are displayed.

4.2.2 η_{max} Distribution

The uncorrected ratio between FNC tagged events and all DIS events as function of η_{max} ⁴ is not flat (figure 4.8); for $\eta_{max} < 2$ the ratio is approximately flat, with an average ratio value of $\simeq 1.2\%$ for $E > 100 \text{ GeV}$ and $\simeq 0.9\%$ for $E > 400 \text{ GeV}$, but for higher η_{max} values it rises. The observed η_{max} distributions (figure 4.9) for the DIS event sample and the FNC tagged neutron events have a similar shape at large η_{max} ($\eta_{max} > 2$) rising exponentially, while for $-2 \lesssim \eta_{max} \lesssim 2$ both distributions are relatively flat; by "observed", it is intended that the distribution is not corrected for the detector effects. About 2% of the DIS event sample falls in the $\eta_{max} < 2$ region; while for the FNC tagged DIS events, $0.88 \pm 0.07\%$ ($E > 100 \text{ GeV}$) and $0.95 \pm 0.08\%$ ($E > 400 \text{ GeV}$) of the events are in the $\eta_{max} < 2$ region (the errors are only statistical). The fact that there are less FNC tagged neutrons in the $\eta_{max} < 2$ region can also be seen in figure 4.10, where a shape comparison is made between the two samples (FNC tagged and DIS) by renormalizing the DIS sample to the uncorrected fraction of FNC tagged neutrons in the inclusive DIS sample. The corrected ratio⁵ for FNC tagged DIS events ($E > 400 \text{ GeV}$ and $\eta_{max} < 2$) to all DIS events ($\eta_{max} < 2$) is $4.2^{+0.9}_{-0.7}\%$. Figure 4.11 shows that $\eta_{max} < 2$ events are a small fraction of the total sample and that they are concentrated at low values of the observed invariant mass of the hadronic final state.

Diffractive data are selected experimentally by looking for a large rapidity gap (LRG) event[53], which is quantified by the variable η_{max} . Large rapidity gap events are events that have a large region of rapidity without any hadronic activity, so that there is a large gap in rapidity between the proton direction and the first detected particle produced in the ep scattering[17]. Leading neutrons with a large rapidity gap ($\eta_{max} < 2$) display an approximately flat tail in the observed η_{max} distribution. This effect can be explained as diffractive production of leading neutrons: i.e. the diffractive excitation of the proton (pomeron exchange) into N^* resonances which then decay into fast neutrons or the Deck mechanism[3] where a pomeron is exchanged between the virtual pion emitted from the proton and the virtual photon emitted from the scattered electron. Since these events ($\eta_{max} < 2$) are a small fraction of the total leading neutron sample $\simeq 0.9\%$, it can be concluded that diffractive production of leading neutrons is not the dominant mechanism, but is a rather negligible mechanism.

⁴The variables rapidity (y) and pseudo-rapidity (η) for a given particle are defined by the relations: $y = \frac{1}{2} \ln \left(\frac{E+P_z}{E-P_z} \right)$ and $\eta = -\ln \tan(\theta/2)$, with E , P_z and θ the energy, the longitudinal momentum and the polar angle of the particle respectively. If $E \gg m$ then $\eta \simeq y$, with m the mass of particle. In the H1 coordinate system (see section 2.2), the proton beam direction defines the positive z -axis direction (forward); the polar angle θ is defined relative to the z -axis, so that pseudo-rapidity (η) is positive in the forward direction. The pseudo-rapidity of the detected particle (clusters in calorimeter) closest to the proton beam direction is called η_{max} [17].

⁵It is corrected for the neutron detection efficiency ($93 \pm 5\%$) and for the FNC detector acceptance and energy resolution by using Lepto and Pompyt ($17 \pm 4\%$).

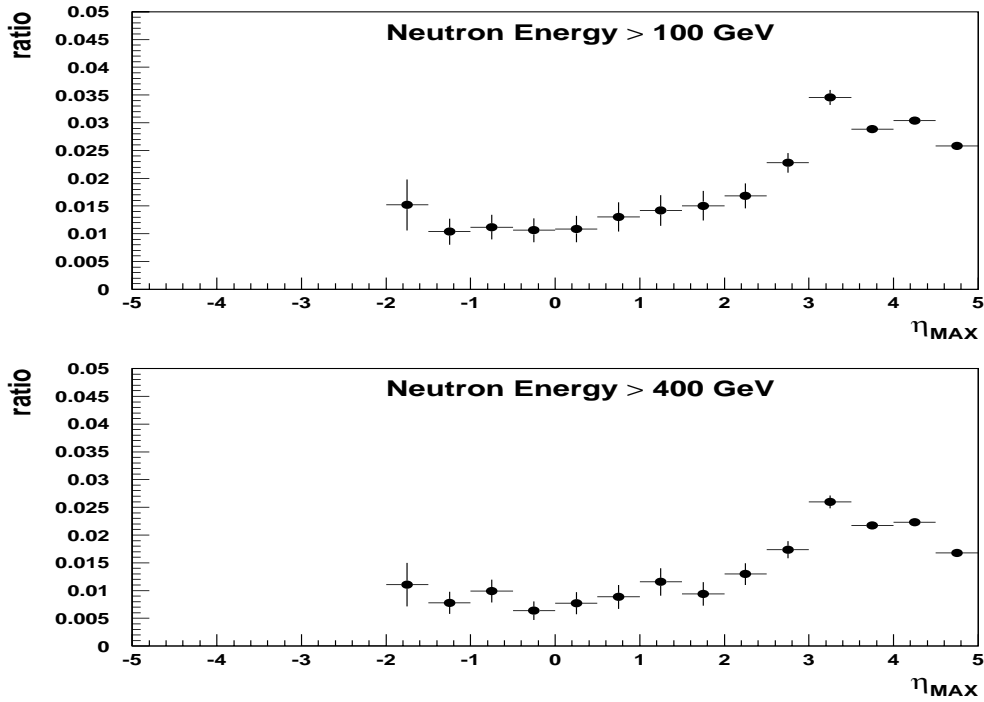


Figure 4.8: The uncorrected ratio between FNC tagged neutron events ($E > 100$ GeV and $E > 400$ GeV) and all DIS events as function of η_{max} . The average ratios for $\eta_{max} < 2$ are $\simeq 1.2\%$ and $\simeq 0.9\%$ for $E > 100$ and 400 GeV respectively. Only statistical errors are displayed.

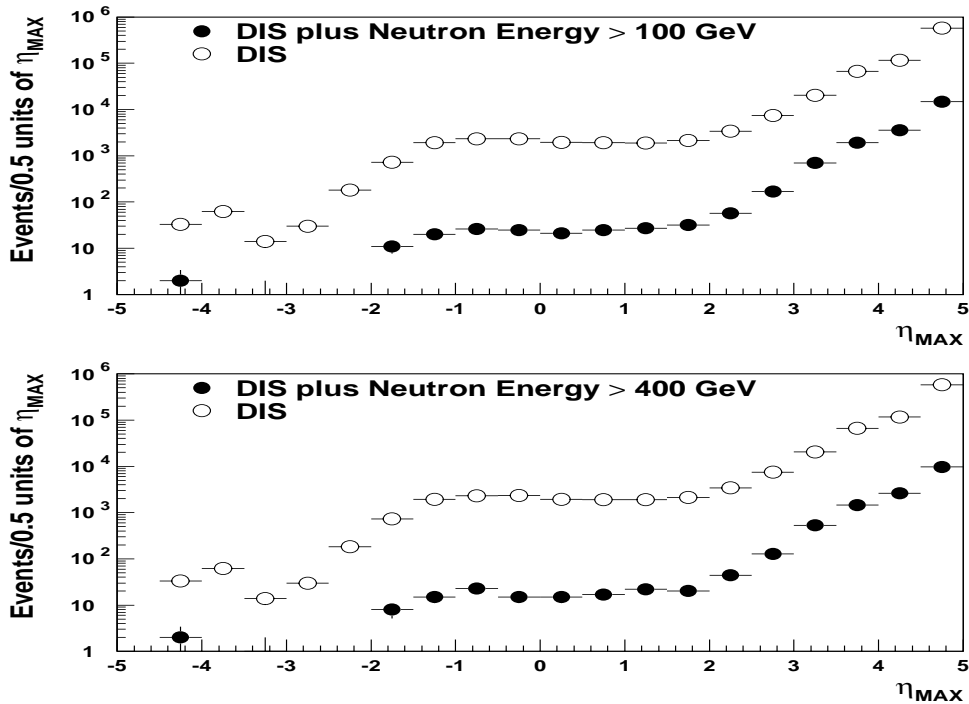


Figure 4.9: The observed η_{max} distributions for FNC tagged ($E > 100$ GeV and $E > 400$ GeV) and all DIS events. The statistical errors are within the dot size.

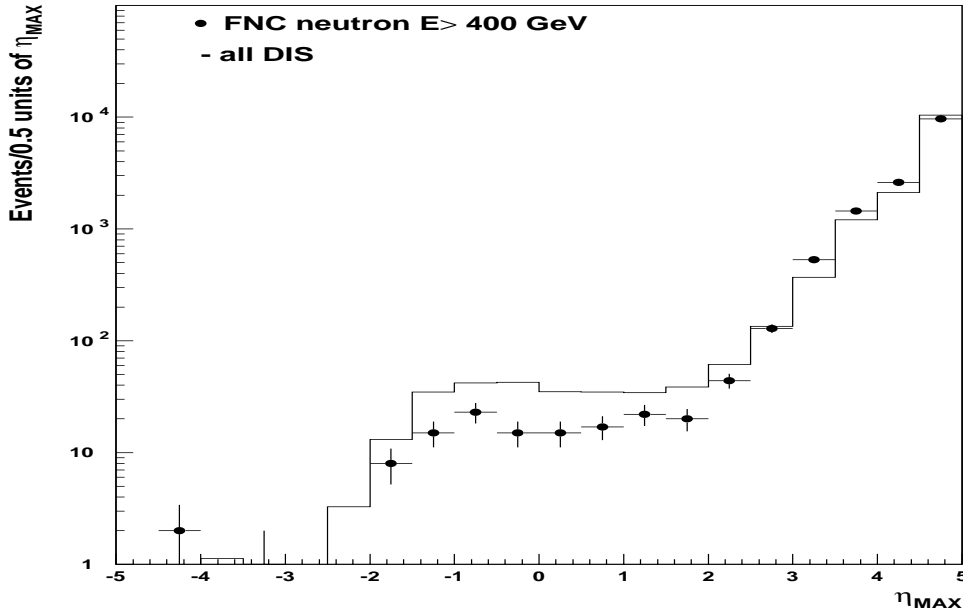


Figure 4.10: Shape comparison between the observed η_{max} distributions of FNC tagged DIS events (neutron energy $E > 400 \text{ GeV}$) and all DIS events. The η_{max} distribution for all DIS events has been renormalized to 1.8% (the uncorrected fraction of tagged neutrons of energy $E > 400 \text{ GeV}$ in the DIS sample). The shapes of the distribution are similar for $\eta_{max} > 2$ and rise exponentially; for $\eta_{max} < 2$ there is a relatively flat tail but there are fewer neutrons. Only statistical errors are displayed.

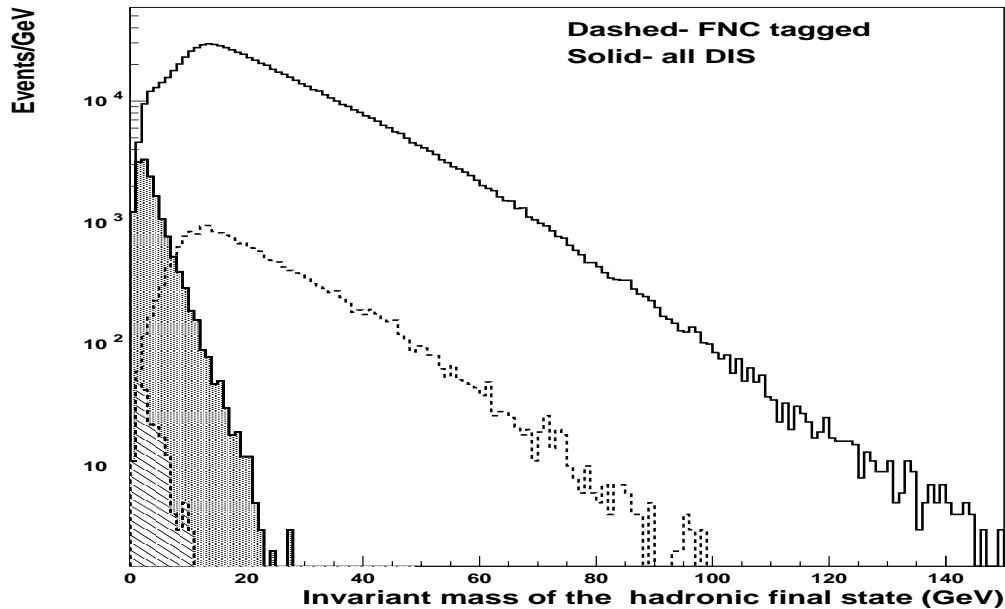


Figure 4.11: The observed hadronic final state invariant mass distributions for FNC tagged (dashed) and for all DIS events (solid). The filled areas correspond to events having $\eta_{max} < 2$, the large rapidity gap (LRG) events (the smaller one is for FNC tagged events). The LRG events fall in the low final state invariant mass region and are a small fraction of the sample.

4.3 Leading Neutron Distributions

The observed leading neutron distributions are compared to two different Monte Carlo models: Pompyt and Lepto. Lepto introduces soft colour interactions to produce final state neutrons, while Pompyt⁶ simulates one pion exchange (see sections 1.3.1 and 1.3.2). At the generator level, the energy spectra of the two Monte Carlos are quite different, but due to the FNC acceptance their predictions are similar in the high energy region $E > 400 \text{ GeV}$ (see section 3.13). The FNC acceptance effect and the FNC energy resolution (FNC resolution function plus 15% smearing, see section 3.11.1) have been taken in account in the Monte Carlos. In the comparison between data⁷ and Monte Carlo, the Lepto Monte Carlo is normalized to the number of data events with energy $E > 100 \text{ GeV}$, while for Pompyt the normalization is to the number of data events with energy $E > 400 \text{ GeV}$. This is done because Lepto is a general DIS Monte Carlo, while Pompyt simulates the one pion exchange process which is expected to dominate only at higher energies i.e. $E > 400 \text{ GeV}$. The two Monte Carlo predictions are compared to the observed leading neutron energy spectrum in figure 4.12, and both give a good description for $E > 400 \text{ GeV}$.

DIS data and beam-gas data display the same observed neutron energy spectrum when compared, indicating that the proton fragmentation is independent from the incident beam (figure 4.13). By beam-gas it is intended scattering of protons belonging to the proton beam with the residual gas in the beam-pipe, which is principally hydrogen; see section 3.10 for more detail and for a comparison between beam-gas and Pompyt Monte Carlo.

In the kinematic range considered, the observed leading neutron energy spectrum is independent of both kinematical variables x and Q^2 . In figure 4.14, for each of the kinematical variables x and Q^2 , the range has been divided in three bins containing the same number of events, and then the observed neutron energy spectrum is compared, giving a very similar spectrum in the different kinematical bins. Large rapidity gap FNC tagged DIS events ($\eta_{max} < 2$) are a small fraction of the total FNC tagged events and span most of the neutron energy range (figure 4.15).

The observed $|t|$, rapidity and p_T distributions are compared to Lepto and Pompyt Monte Carlos for $E > 100 \text{ GeV}$ and $E > 400 \text{ GeV}$, and in different neutron energy bins (figures 4.16-4.18). There is a general agreement between data and Monte Carlo for most of the energy bins. The observed p_T is measured with respect to the proton beam direction and the relation between $|t|$ and p_T is given by equation 1.9.

⁶The GRV-LO parton density function for the pion is used.

⁷The data selection criteria are defined in section 4.1.

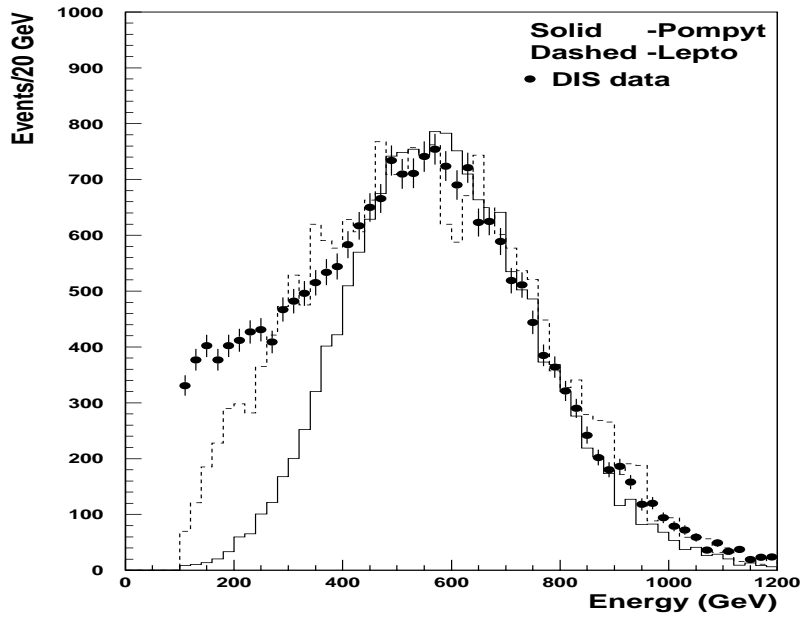


Figure 4.12: The observed leading neutron energy spectrum for energies $E > 100 \text{ GeV}$. The Lepto Monte Carlo (dashed) is normalized to the number of data events with $E > 100 \text{ GeV}$, while for Pompyt (solid) the normalization is to the number of data events with $E > 400 \text{ GeV}$. Both Monte Carlos give a good description of data for $E > 400 \text{ GeV}$. Only statistical errors are shown.

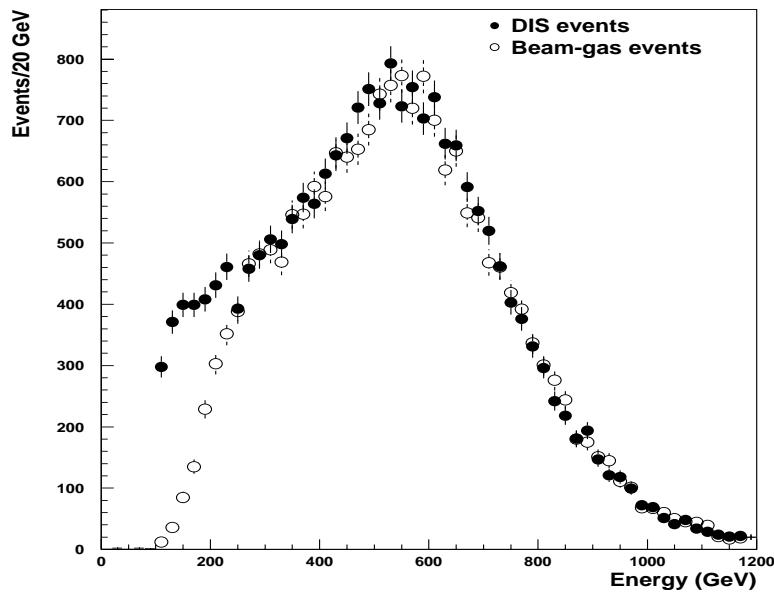


Figure 4.13: The observed beam-gas neutron energy spectrum is compared to the observed neutron energy spectrum of DIS events, both for $E > 100 \text{ GeV}$. The distributions are normalized to the same number of events for neutron energies $E > 400 \text{ GeV}$. The beam-gas spectrum has been collected using the FNC trigger which is not 100% efficient at low energies.

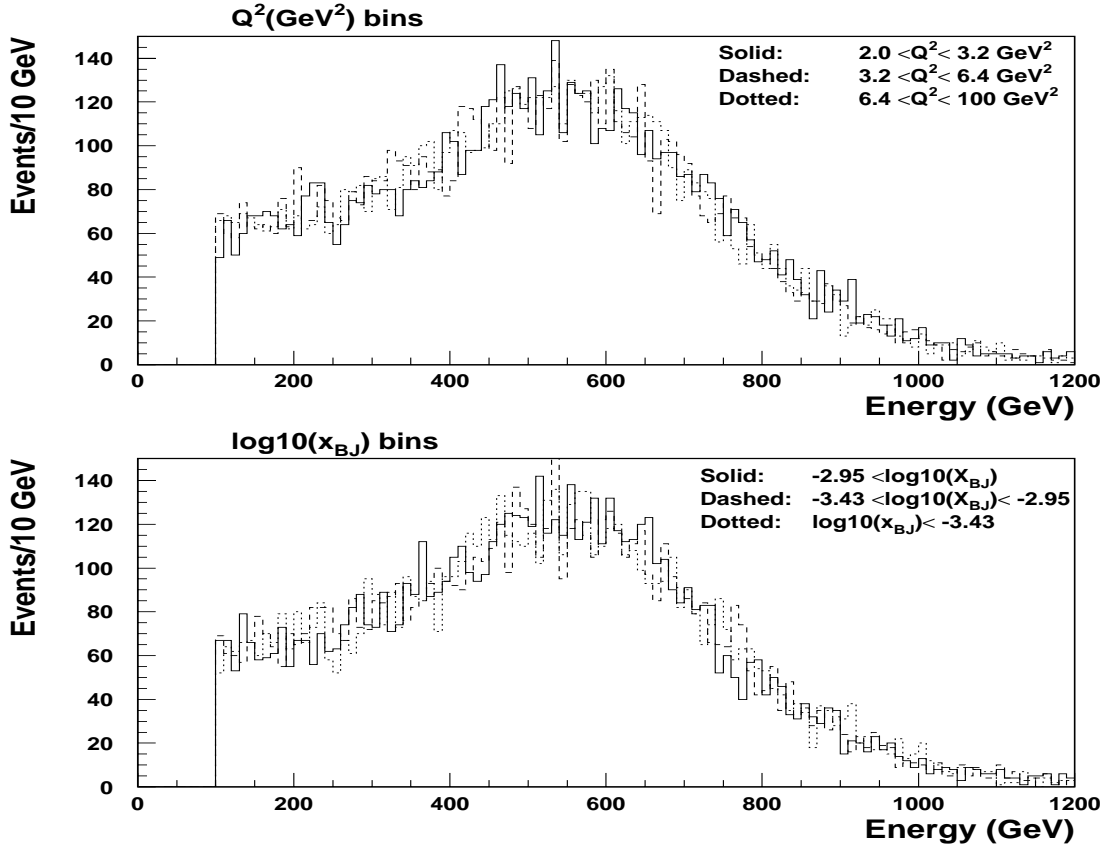


Figure 4.14: The neutron energy spectrum ($E > 100 \text{ GeV}$) for different Q^2 and x_{BJ} bins. The Q^2 and x_{BJ} bins have been chosen so that each Q^2 and x_{BJ} bin has the same number of events. The neutron energy spectrum is very similar in the different kinematical bins.

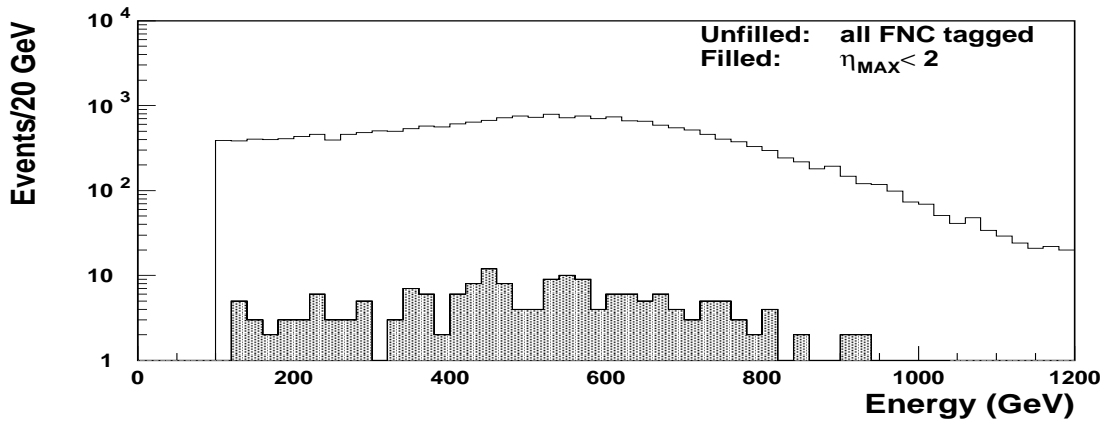


Figure 4.15: The observed neutron energy spectrum of all FNC tagged DIS events (unfilled) is compared to FNC tagged DIS events with $\eta_{max} < 2$ for $E > 100 \text{ GeV}$. These large rapidity gap ($\eta_{max} < 2$) events constitute a small fraction ($0.88 \pm 0.07\%$ for $E > 100 \text{ GeV}$) of the total FNC tagged events, and are distributed over most of the energy range.

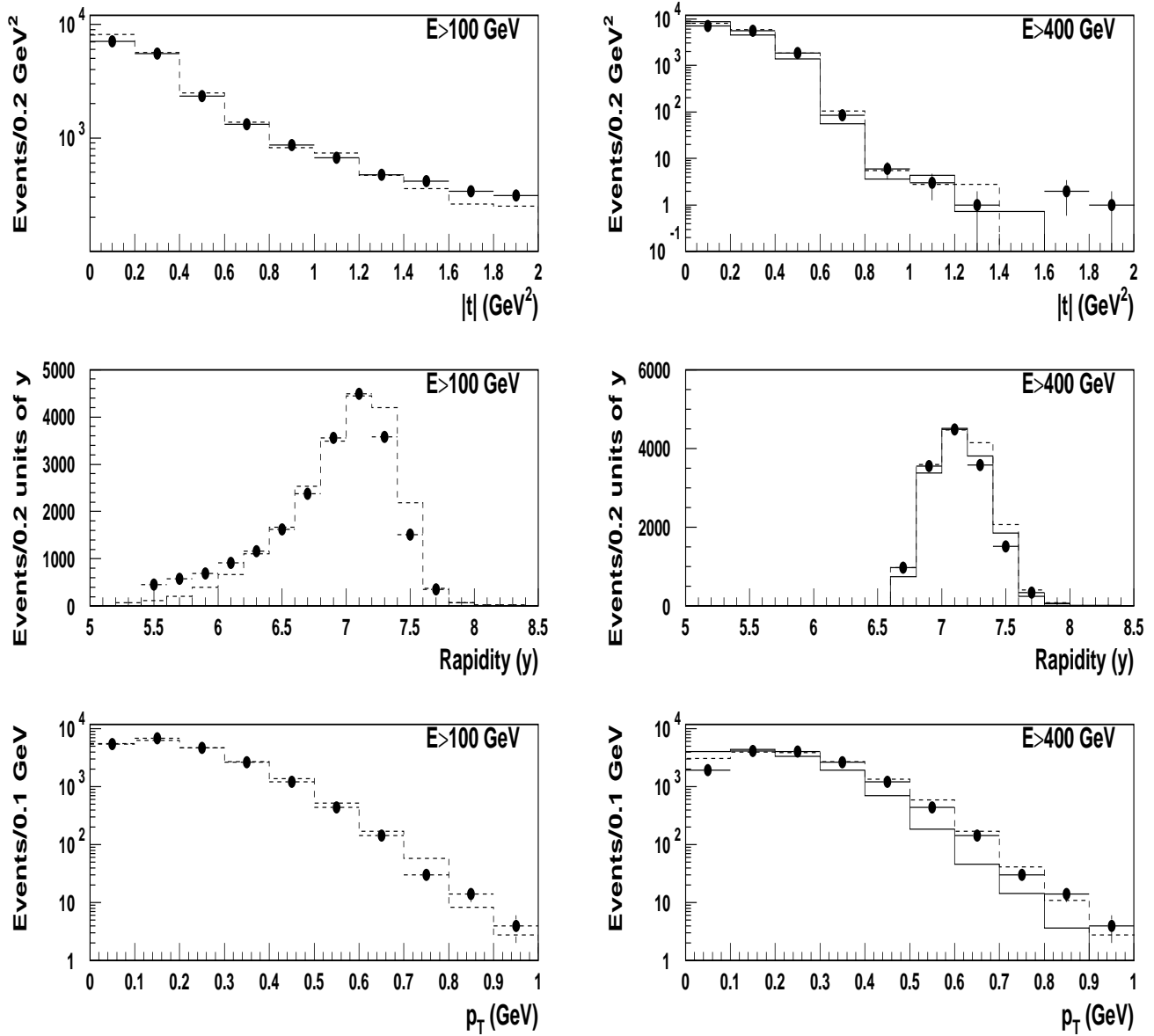


Figure 4.16: The observed $|t|$, rapidity and p_T distributions are compared to Lepto and Pompyt Monte Carlos. In the three left plots data is compared to Lepto (dashed) for $E > 100 \text{ GeV}$, while in the three right plots data is compared to Lepto (dashed) for $E > 100 \text{ GeV}$ and Pompyt (solid) for $E > 400 \text{ GeV}$. There is a good agreement between data and Monte Carlo except for the rapidity distribution where there is some disagreement, and for the p_T distribution which is underestimated by Pompyt. Lepto and Pompyt are normalized to the number of data events with $E > 100 \text{ GeV}$ and $E > 400 \text{ GeV}$ respectively. Only statistical errors are shown.

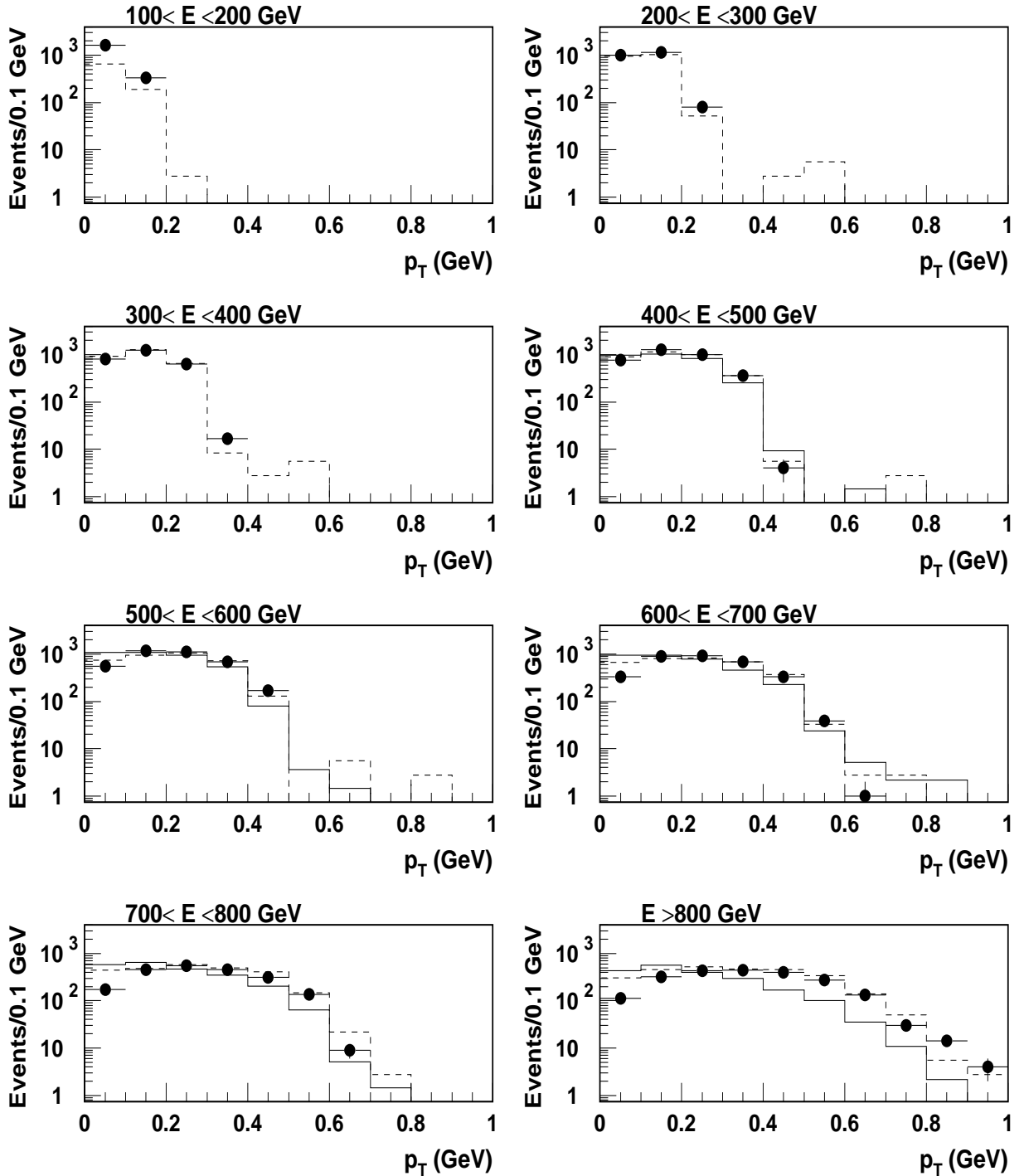


Figure 4.17: Data is compared to the Lepto Monte Carlo (dashed) for $E > 100 \text{ GeV}$ and to both Lepto and Pompyt (solid) for $E > 400 \text{ GeV}$. There is a good agreement between data and Monte Carlo except for first bin where data is slightly underestimated by Lepto and the last bin where Pompyt underestimates data. Lepto and Pompyt are normalized to the number of data events with $E > 100 \text{ GeV}$ and $E > 400 \text{ GeV}$ respectively. Only statistical errors are displayed.

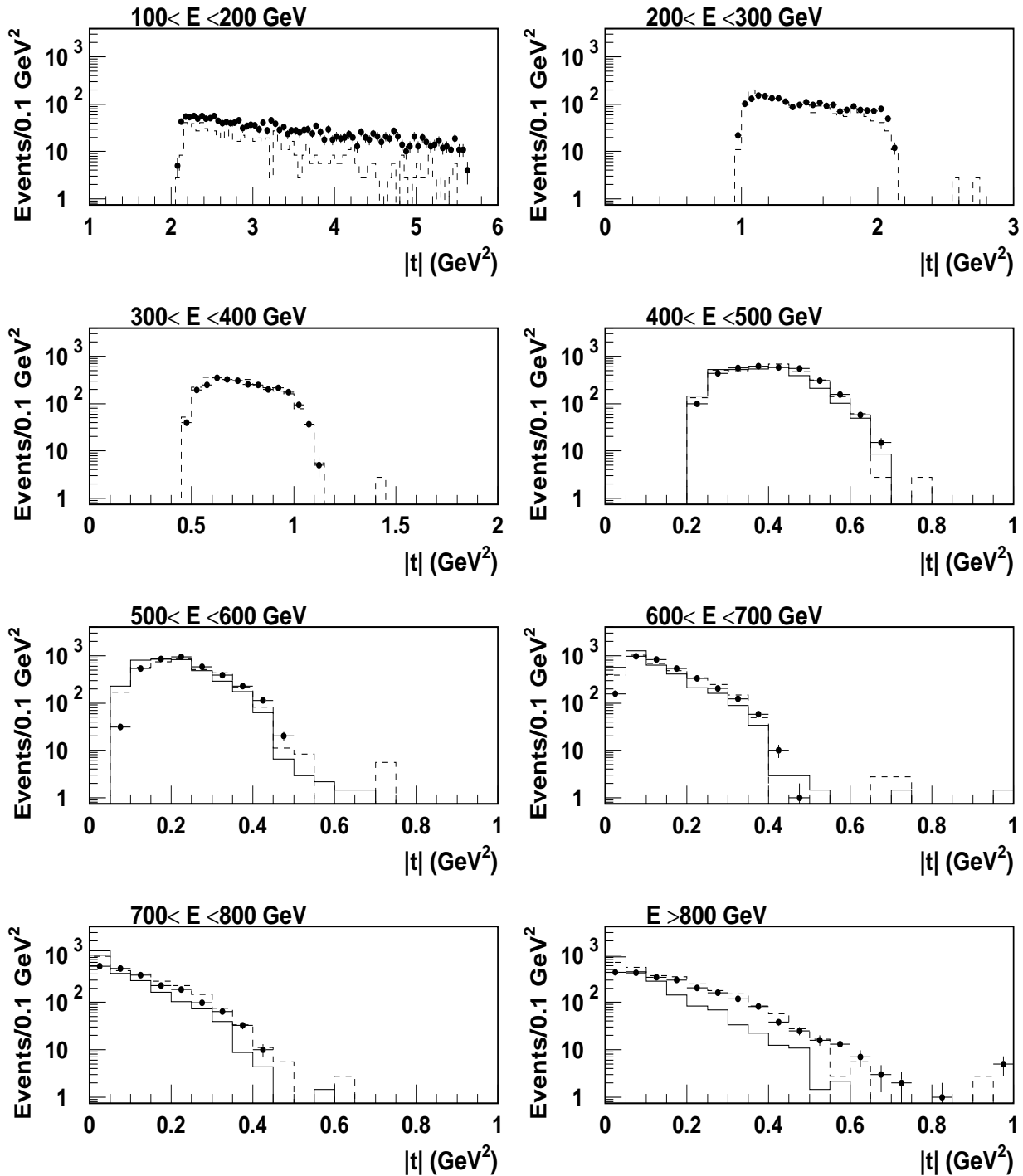


Figure 4.18: Data is compared to the Lepto Monte Carlo (dashed) for $E > 100 \text{ GeV}$ and to both Lepto and Pompyt (solid) for $E > 400 \text{ GeV}$. There is a good agreement between data and Monte Carlo except for the first bin where Lepto slightly underestimates data and the last bin where Pompyt underestimates data. Lepto and Pompyt are normalized to the number of data events with $E > 100 \text{ GeV}$ and $E > 400 \text{ GeV}$ respectively. Only statistical errors are displayed.

4.4 The Total $ep \rightarrow e'nX$ Cross Section

The total cross section for leading neutron production $\sigma_{ep \rightarrow e'nX}$, in the kinematical range $2 < Q^2 < 100 \text{ GeV}^2$ and $0.02 < y < 0.6$, can be determined by the following formula:

$$\sigma_{ep \rightarrow e'nX} = \frac{N}{A_{FNC} N_{eff} T_{eff} L}; \quad (4.10)$$

with N the total number of FNC tagged neutron events above a given neutron energy value satisfying the selection criteria in section 4.1, A_{FNC} the correction for the FNC resolution and acceptance (corrected according to the energy range, section 3.13), N_{eff} the neutron detection efficiency ($93 \pm 5\%$, section 3.8), T_{eff} the S(4) trigger efficiency ($94.3 \pm 0.1\%$, section 4.1) and L the total integrated luminosity ($3.38 \pm 0.07 \text{ pb}^{-1}$, section 4.1). The main contribution to the systematic error originates from the A_{FNC} and the N_{eff} uncertainties. The errors associated to N are the statistical error and the systematic error due to the energy scale uncertainty of $\pm 5\%$, while the beam-gas background ($\lesssim 0.4\%$) is subtracted. The number of FNC tagged neutrons with energies $E > 100 \text{ GeV}$, $E > 400 \text{ GeV}$, and $E > 400 \text{ GeV}$ with $|t| < 0.5 \text{ GeV}^2$ are 21468, 14574 and 13969 respectively. The respective total cross sections are given in table 4.2.

Cross Section	Selection
$96_{-14}^{+12} \text{ nb}$	$E > 100 \text{ GeV}$
29_{-9}^{+6} nb	$E > 400 \text{ GeV}$
20_{-5}^{+4} nb	$E > 400 \text{ GeV}, t < 0.5 \text{ GeV}^2$

Table 4.2: The total $ep \rightarrow e'nX$ cross sections are given for the kinematical range $2 < Q^2 < 100 \text{ GeV}^2$ and $0.02 < y < 0.6$. The errors (statistical and systematic) have been added in quadrature.

CONCLUSIONS

The installation of the Forward Neutron Calorimeter (FNC) has given the possibility of observing and studying leading neutron production at HERA. These high energy neutrons are detected at very small angles ($\lesssim 1$ mrad) with respect to the proton beam direction due to the aperture defined by the beamline elements positioned between the FNC and the interaction region in H1.

Within the statistics leading neutrons constitute a constant fraction of deep inelastic scattering events, independent from the kinematical variables Q^2 and x_{BJ} in the measured range. The observed neutron energy spectrum shows no dependence on Q^2 and x_{BJ} in the selected binning and is independent from the beam as can be seen by comparing beam-gas and DIS data. These leading neutron properties are an indication of factorization. The η_{max} distribution for leading neutrons is similar to the DIS η_{max} distribution for $\eta_{max} > 2$, while for smaller values (large rapidity gap events) both have a flat tail but there are fewer neutrons. These large rapidity gap events are concentrated at small values of the observed invariant mass of the hadronic final state. The small percentage of leading neutrons with a large rapidity gap, indicates that diffractive leading neutron production is not the dominant process. The observed neutron energy spectrum, the $|t|$ and P_T distributions are in general agreement for neutron energies $E > 400$ GeV with both Pompyt Monte Carlo, which simulates one pion exchange, and Lepto Monte Carlo, which includes soft colour interactions.

The soft colour interactions (SCI) were introduced in the Lepto Monte Carlo as an alternative novel mechanism to explain the large rapidity gap events observed at HERA. The SCI mechanism is based on the assumption that SCI can occur in addition to perturbative interactions, which modifies the colour topology and consequently the hadronization of the proton remnant, producing rapidity gaps. This SCI mechanism can also be applied to leading neutron production, giving a fair description of data. The one pion exchange (OPE) model, which also gives a good description of the data, is based on the concept of virtual pions being present in the nucleon. This OPE model is supported by previous hadron-hadron scattering data and there is good reason to believe that OPE should also occur in ep scattering, giving rise to leading neutrons.

An improvement in the energy resolution of the FNC is expected with the installation of the pre-shower detector in front of the FNC, which should reduce the high energy tail of the observed neutron energy spectrum. This would allow the measurement of the $|t|$, p_T , z leading neutron distributions with an improved accuracy. A more advanced analysis by the H1-FNC group, which investigates leading baryon (neutron and proton) production at HERA, already indicates some failure of Lepto in describing the data. Further analysis together with the FNC upgrade should give the possibility to clearly discriminate between the two models and signal the presence of the one pion exchange process.

Appendix A

Appendix: Energy Resolution

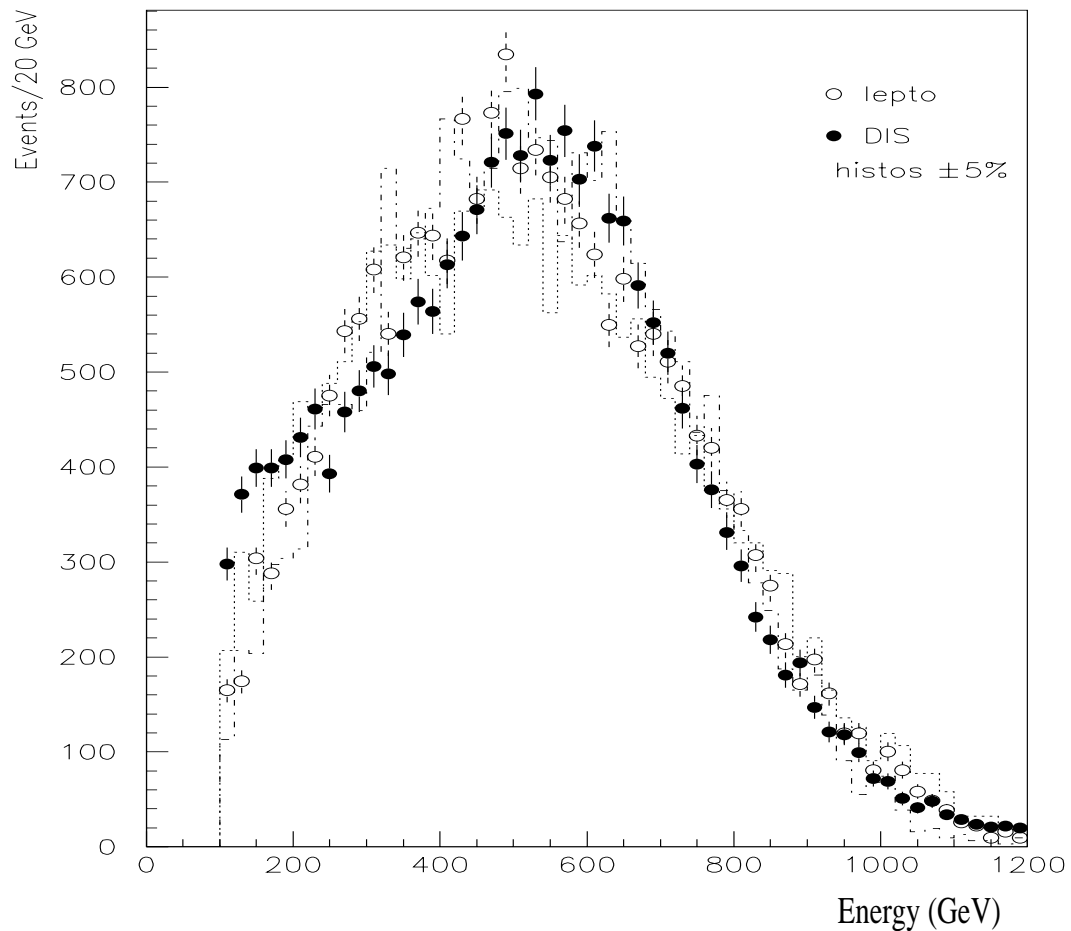


Figure A.1: The Lepto neutron energy spectrum smeared by $\sigma(E)/E=25\%$ is compared to DIS data (statistical errors only). The dotted and dashed histograms display the Lepto prediction smeared by an extra $\pm 5\%$. The Lepto prediction is normalized to the number of data events having energies $E > 100$ GeV.

Figures A.1 and A.2 show DIS data compared to Lepto, and beam-gas and DIS data compared to Pompyt, respectively. The Lepto prediction is in general agreement with data on the whole energy range. According to the pion exchange model, the Pompyt prediction is expected to be valid only at energies $E > 400$ GeV, where pion exchange is dominant. In the lower part of the energy spectrum (A.2), the beam-gas data points differ from the DIS data points, since when beam-gas data is taken, only the FNC triggers are active which are not 100% efficient at low energies, while for DIS data other H1 supplementary trigger requirements are introduced.

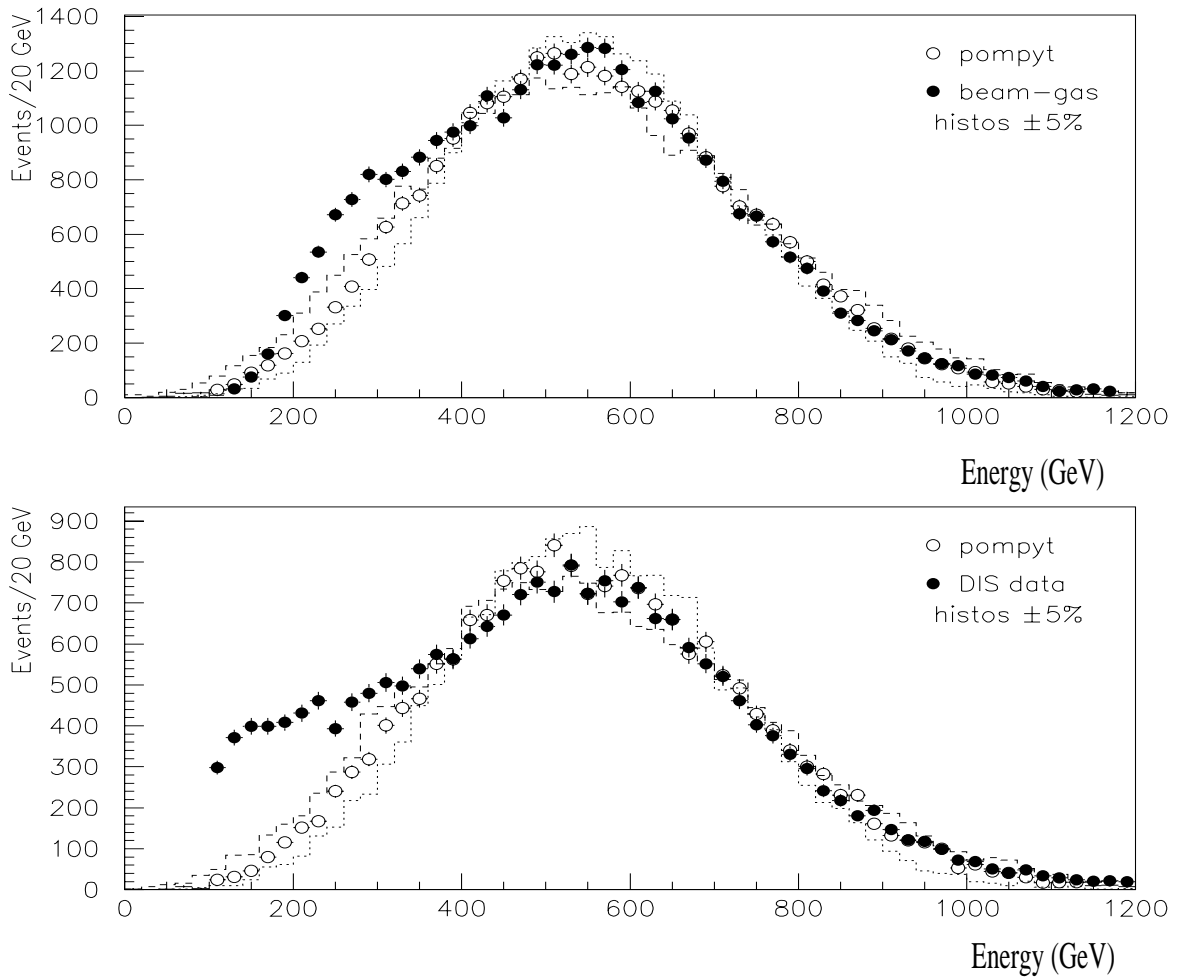


Figure A.2: The Pompyt neutron energy spectrum smeared by $\sigma(E)/E=25\%$ is compared to data (beam-gas and DIS). The dotted and dashed histograms display the Pompyt prediction smeared by an extra $\pm 5\%$. The Pompyt prediction is normalized to the number of data events having energies $E > 400$ GeV. Only statistical errors are shown.

Bibliography

- [1] B. Povh, K. Rith, C. Scholz, F. Zetsche,
Particles and Nuclei: An Introduction to the Physical Concepts,
Springer, 1995.
- F. Halzen and A.D. Martin,
Quarks and Leptons: An Introductory Course in Modern Particle Physics,
J. Wiley & Sons, Inc, Toronto(1984).
- D.H. Perkins,
Introduction to High Energy Physics,
Addison-Wesley Publishing Company, Inc, Don Mills, Ontario(1987).
- O. Nachtmann,
Elementary Particle Physics: Concepts and Phenomena,
Springer, 1990.
- D.J. Griffiths,
Introduction to Elementary Particles,
Wiley, 1987.
- D.C. Cheng and G. K. O'Neill,
Elementary Particle Physics. An Introduction,
Addison-Wesley, 1979.
- [2] A. Levy (Tel Aviv U.),
DESY-97-013, Feb 1997,
Lectures given at Strong Interaction Study Days,
Kloster Banz, Germany, 10-12 Oct 1995.
- [3] B. Kopeliovich, B. Povh, I. Potashnikova,
Deep Inelastic Electroproduction of Neutrons in the Proton Fragmentation Region,
Z.Phys.C73:125-131,1996,
DESY-96-011, Jan 1996.

- [4] G. Levman, K. Furutani,
Virtual Pion Scattering at HERA,
DESY-95-142, Jul 1995.
- [5] H. Holtmann et al.,
How to Measure the Pion Structure Function at HERA.
Phys.Lett.B338:363-368,1994.
- [6] M. Przybycien, A. Szczurek, G. Ingelman,
Properties of HERA Events from DIS on Pions in the Proton,
DESY-96-073, Apr 1996,
Z. Phys. C74 (1997) 509-515.
U. D'Alesio,
Target Fragmentation of the Nucleon at High Energies,
Talk given at the 6th International Workshop on Deep Inelastic Scattering and QCD,
(DIS 98), Brussels, Belgium,
hep-ph/9805444.
- [7] H1 Collaboration (M. Beck et al.),
Proposal for a Forward Neutron Calorimeter for the H1 Experiment at DESY,
H1 Collaboration proposal, August 1995.
- [8] R. Zoller,
Peripheral Structure of Nucleons when Probing with High Q^2 Photons,
Z.Phys. C53,443(1992).
J.D. Sullivan,
One-Pion Exchange and Deep-Inelastic Electron Nucleon Scattering,
Phys. Rev. D5,1732(1972).
M. Bishari,
Pion Exchange and Inclusive Spectra,
Phys.Lett.B38,510(1972).
- [9] H. Holtmann, A. Szczurek and J. Speth,
Testing the Meson Cloud in the Nucleon in Drell-Yan Processes,
Nucl. Phys. A596(1996)631.
- [10] A. Baldit et al.,
Study of the Isospin Symmetry Breaking in the Light Sea of the Nucleon from the Drell-Yan Process,
Phys. Lett. B332(1994)244.
- [11] P. Amaudruz et al.,
Gottfried Sum from the Ratio F_2^n/F_2^p ,
Phys. Rev. Lett. 66(1991)2712.

- M. Arneodo et al.,
Reevaluation of the Gottfried Sum,
 Phys. Rev. D50(1994)1-3.
- [12] T. Ericson et al., CERN-preprint CERN-TH/95-158,(1995).
 R. Arndt et al., Phys. Rev. C49,2729(1994).
 R. Arndt et al., Phys. Rev. Lett. 65,157(1990).
 R. Timmermans et al., Phys. Rev. Lett. 67,1074(1991).
 R. Klomp et al., Phys. Rev. C44,1258(1990).
 R. Koch et al., Nucl. Phys. A336,331(1980).
 W.Koepf et al., Phys. Rev. D53,2586(1996).
- [13] P. Bruni, A. Edin, G. Ingelman,
Pompyt version 2.6 - A Monte Carlo to Simulate Diffractive Hard Scattering Processes,
<http://ulrik.tsl.uu.se/thepp/pompyt/>.
- [14] Torbjörn Sjöstrand,
Pythia 5.7 AND Jetset 7.4: Physics and Manual,
 LU-TP-95-20, Aug 1995,
 CERN-TH-7112-93.
- [15] B. Andersson, G. Gustafson, G. Ingelman, T. Sjöstrand,
Parton Fragmentation and String Dynamics,
 LU-TP-83-10, Phys.Rept.97:31,1983.
- [16] M.Glück et al.,
Pionic Parton Distributions,
 Z. Phys. C53,651(1992).
- [17] H1 Collab., T. Ahmed et al.,
Deep Inelastic Scattering Events with a Large Rapidity Gap at HERA,
 DESY-94-133,
 Nucl. Phys. B429(1994)477.
- [18] G. Ingelman and P. Schlein,
Jet Structure in High Mass Diffractive Scattering,
 Phys. Lett. 152B(1985)256.
- [19] G. Ingelman, A. Edin, J. Rathsmann,
LEPTO 6.5: A Monte Carlo Generator for Deep Inelastic Lepton - Nucleon Scattering,
 DESY-96-057,
 Comput.Phys.Commun.101:108-134,1997.

- [20] G. Ingelman, A. Edin, J. Rathsman,
Soft Color Interactions as the Origin of Rapidity Gaps in DIS,
 Phys.Lett.B366:371-378,1996.
Rapidity Gaps in DIS Through Soft Color Interactions,
 Paris DIS 1995(24-28 Apr):391-394 (QCD162:D41:1995),
 DESY-95-145.
- [21] Proceedings of the workshop, Hamburg, October,
Physics at HERA,
 October 29-30, 1991, Editors W. Buchmuller and G. Ingelman, DESY,
 Hamburg(1992).
- [22] H1 Collaboration,
The H1 Detector at HERA,
 Internal Report DESY-H1-96-01 March 96,
 (updated version of Report DESY 93-103),
 Nucl. Instr. and Meth. A386, 1997 (in 2 parts pages) 310-347 and 348-396.
- [23] ZEUS Collaboration,
The ZEUS Detector: Status Report 1993,
 ZEUS-Status-Rept-1993, Feb 1993. 597pp,
 and
 ZEUS Collab., M. Derrick et al., Phys.Lett. B316(1993)412.
- [24] M. Dueren,
The HERMES Experiment: From the Design to the First Results,
 (Erlangen U., Theorie III), 1995,
 Hamburg DESY - Int.Rep.HERMES-95-02 (95/07,rec.Aug.) 234 p.
- [25] HERA-B Collaboration (W. Schmidt-Parzefall, for the collaboration), 1995,
*HERA-B: An Experiment to Study CP Violation at the HERA Proton Ring Using
 an Internal Target*,
 Nucl. Instrum. Methods A368 (1995) 124-132.
- [26] B. List,
*Tiefunelastische ep-Streuung bei HERA unter Nachweis eines vorwaerts gestreuten
 Protons*,
 H1 Thesis(7/97)- Universität Hamburg.
- [27] J. Bürger et al.,
Technical Proposal to Build Silicon Tracking Detectors for H1,
 H1 internal report 226 (1992) and DESY PRC92/01.
- D. Pitzl et al., IEEE Nucl. Science Symp. 1992, unpublished.

- J. Gassner,
Messung der Ortsauflösung des H1-Siliziumvertexdetektors,
 Diplomarbeit Inst. f. Teilchenphysik ETH Zürich,
 ETHZ-IPP Internal Report 96-4. Dez. 1996.
- W. Eick et al.,
Development of the H1 Backward Silicon Strip Detector,
 DESY-Preprint.
- [28] H1 SPACAL Group,
The H1 Lead/Scintillating-Fiber Calorimeter,
 DESY Report, DESY 96-171, August 1996.
- [29] T. Nicholls,
A Measurement of the Diffractive Proton Structure Function at HERA,
 Univ. Birmingham Dissertation 4/97 (H1-Thesis).
- [30] Bernhard Schwab,
Das Rückwärtsdriftkammersystem des H1-Experiments,
 (6/96)(H1-Thesis).
- Judith Katzy,
Messung der Strukturfunktion F_2 bei kleinen Bjorken- x und kleinen Impulsüberträgen am H1 Experiment bei HERA,
 (6/97)(H1-Thesis).
- [31] V. Blobel,
The BOS System, Fortran 77 Version,
 DESY, December 1987.
- [32] V. Blobel,
The F-Package for Input-Output,
 Proc. Int. Conf. on Computing in High Energy Physics 92, Annency, France (1992),
 eds. C. Verkerk and W. Wojcik, CERN-Report 92-07, Geneva(1992), page 755.
- [33] M. Brun, R. Brun, A.A. Rademakers,
CMZ - A Source Code Management System,
 Proc. Int. Conf. on Computing in High Energy Physics, Oxford (1989), R. C. E.
 Devenish, T. Daniels eds., Comp. Phys. Comm. 57(1989) 235.
- [34] *PAW Physics Analysis Workstation*,
 CERN Program Library Long Writeup Q121, Geneva, Switzerland.
- [35] M. Wobisch et al.,
H1TOX: H1 Physics Analysis Tool Box,
<http://www-h1.desy.de/h1/iww/icas/imanuals/h1tox.html>.

- [36] D. Acosta et al.,
Results of Prototype Studies for a Spaghetti Calorimeter,
Nucl. Instr. and Meth. A294(1990) 193.
- M. Livan et al.,
Scintillating-Fiber Calorimetry,
CERN Yellow Report CERN 95-02, 28 February 1995.
- [37] Christine V. Scheel,
The Spaghetti Calorimeter,
Dissertation, University of Amsterdam (1994).
- [38] T. Nunnemann,
Aufbau und Test eines Kleinwinkel-Neutronen-Kalorimeters für das Experiment H1.
Diplomarbeit im Studiengang Physik, Universität Heidelberg, 1996.
- [39] H1 Collaboration,
Leading Neutron Production in Deep Inelastic ep Scattering at HERA,
Paper pa02-063, submitted to the 28th International Conference on High Energy
Physics ICHEP'96, Warsaw, Poland, July 1996.
- [40] U. Amaldi,
Fluctuations in Calorimetry Measurements,
Physica Scripta, Vol. 23, pp. 409-424(1981).
- [41] D. Acosta et al.,
Localizing Particles Showering in a Spaghetti Calorimeter,
Nucl. Instr. and Meth. A305,55(1991).
- [42] Particle Data Group,
Review of Particle Properties,
Phys. Rev. D50, Part 1 (1994).
- [43] D. Acosta et al.,
Electron, Pion and Multiparticle Detection with Lead/Scintillating Fiber Calorimeter,
Nucl. Instr. and Meth. A308,481(1991).
- [44] M. Beck et al.,
A Scintillating Tile Hodoscope with WLS Fiber Readout,
Preprint MPIH-V22-1994, Nucl. Instr. Meth. A 355 (1995) 351-358.
- M. Beck et al.,
Online Detection of Neutrons with a Lead/Scintillating Fiber Calorimeter and a Scintillating Tile Hodoscope,
Preprint MPIH-V22-1994, Nucl. Instr. Meth. A 381 (1996) 330-337.

- [45] R. Todenhagen,
Introduction to the FNC Slow Control System,
Internal FNC documentation: on the 3W at <http://axhrs1.desy.de/local/local.html>.
- [46] http://www-h1.desy.de/h1/iww/icas/imanuals/ndb_man.html.
- [47] S. Youssef,
Clustering with Local Equivalence Relations,
Computer Physics Communications 45 (1987) 423-426.
- [48] W. Flauger and F. Mönnig,
Measurement of Inclusive Zero Angle Neutron Spectra at the CERN ISR,
Nuclear Physics B109(1976)347-356.
- [49] J. Engler et. al.,
Measurement of Inclusive Neutron Spectra at the ISR,
Nuclear Physics B84(1975)70-82.
- [50] S. Egli,
Userguide for Program Runselect, H1 Internal Note, 12/6/96.
- [51] U. Bassler and G. Bernardi,
On the Kinematic Reconstruction of Deep Inelastic Scattering at HERA: the Σ Method,
DESY 94-231.
- [52] H1 Collaboration S. Aid et al.,
A Measurement and QCD Analysis of the Proton Structure Function $F^2(x, Q^2)$ at HERA,
Nucl. Phys. B470(1996) 3.
- [53] H1 Collaboration S. Aid et al.,
Energy Flow in the Hadronic Final State of Diffractive and Non-Diffractive Deep-Inelastic Scattering at HERA,
DESY-96-14; Z.Phys. C70 (1996) 609.
- [54] H1 Collaboration C. Adloff et al.,
Leading Neutron Production in Deep-Inelastic Scattering at HERA,
Submitted to the International Europhysics Conference on High Energy Physics,
HEP97, August 9-26 1997 Jerusalem, Israel.
- [55] ZEUS Collaboration M. Derrick, et al.,
Observation of Events with an Energetic Forward Neutron in DIS at HERA,
Phys.Lett.B384:388-400,1996.

List of Figures

1.1	Feynman diagrams for NC and CC deep inelastic ep scattering.	2
1.2	Feynman diagram for NC DIS.	3
1.3	Feynman diagram for one pion exchange leading neutron production in DIS. . .	6
1.4	The string structure for a DIS boson-gluon-fusion event with and without SCI.	8
2.1	The Q^2 - x^{-1} plane, showing the areas covered by the fixed target experiments and the HERA ones.	10
2.2	DESY site accelerator complex for HERA.	11
2.3	Layout of the H1 detector.	14
2.4	A side view of the H1 trackers.	15
2.5	A $r - \phi$ view of the central trackers.	16
2.6	A $r - z$ view of the H1 calorimeters.	17
2.7	Partial side view of the H1 detector.	19
2.8	Layout scheme of the H1 luminosity system.	21
2.9	The integrated luminosity delivered by HERA and collected by H1.	22
2.10	The multi-level trigger of H1.	27
3.1	The $t_{max}(\lambda_I)$ and $t_{0.95}(\lambda_I)$ are plotted for the FNC energy range.	34
3.2	The GEANT simulation for a 600 GeV neutron hadronic shower in the FNC.	34
3.3	Front view of the original calorimeter, composed of 155 towers.	36
3.4	Back view of the FNC.	37

3.5	Layout of the lead-scintillator fiber matrix.	38
3.6	The two hodoscope planes.	40
3.7	Structure of a hodoscope tile.	40
3.8	Cut through view of the FNC.	42
3.9	Sketch of the test beam setup.	43
3.10	Test beam electron and pion signals.	44
3.11	Containment value for electrons (10 GeV) and pions (15 GeV).	45
3.12	Sketch of the proton beamline from H1 to the FNC position.	47
3.13	Cross section of the HERA tunnel where the FNC is located.	48
3.14	Top view of the HERA tunnel where the FNC is located.	49
3.15	Side view scheme of the FNC's components.	50
3.16	The FNC FADC diagram.	51
3.17	The digitized signals of physics events for the three different FNC FADC groups.	52
3.18	Sensitivity curves for two different FADC modules.	53
3.19	FNC data acquisition scheme.	54
3.20	The FNC trigger diagram.	57
3.21	The FNC energy sum trigger efficiency (FNC_SUM).	57
3.22	FNC subtrigger ratios.	58
3.23	The FNC trigger rates.	59
3.24	The distribution of FNC events in the various classes.	60
3.25	The FNC measured variables.	64
3.26	Distribution of the hits on the front face of the FNC.	66
3.27	The energy spectrum for charged and neutral particles reaching the FNC acceptance region.	66
3.28	A FNC event display.	67
3.29	The activity in H1 for an FNC event is displayed.	68

3.30	The signal and timing distributions of a typical hodoscope module.	70
3.31	The hodoscope planes efficiencies.	71
3.32	The ratio between charged events and all events falling around the acceptance region.	72
3.33	Hodoscope plane 1 and 2 signal hit rate versus the radial distance from impact point.	74
3.34	Schematic diagram of the FNC monitoring system.	75
3.35	The digitized monitor signals for two calorimeter modules.	76
3.36	The neutron energy spectrum for two 1996 beam-gas runs.	77
3.37	The neutron energy spectrum for three 1996 DIS run ranges.	78
3.38	FNC monitoring factors versus day of the year.	79
3.39	Temperature variations in 1996, for the photomultiplier backend region and monitor-box.	80
3.40	The beam-gas data neutron energy distribution is compared to Pompyt.	82
3.41	The neutron energy spectrum scale is varied by $\pm 5\%$ and compared to Pompyt.	82
3.42	The average lateral shower profile for beam-gas neutrons.	83
3.43	The energy spectrums for DIS and beam-gas data are compared to Pompyt and Lepto.	85
3.44	The Monte Carlo neutron energy spectrum (Pompyt and Lepto) with and without the FNC calorimeter response function applied.	86
3.45	The resultant energy distributions for a given fixed input energy with the response function and 15% Gaussian smearing applied.	87
3.46	The energy resolution calculated at different energies (response function + 15% Gaussian smearing).	88
3.47	The proton beam ramping neutron energy spectrum.	89
3.48	The linearity relation of the calorimeter energy response.	89
3.49	The Geant simulation for an early shower of a 600 GeV neutron.	91
3.50	The Geant simulation for a late shower of a 600 GeV neutron.	92

3.51	The energy deposited in the FNC for an incident neutron versus the time of arrival.	92
3.52	The energy deposited in the FNC for an incident neutron versus the natural logarithm of the energy deposited in the tail counters.	93
3.53	The neutron energy spectrum for beam-gas events with various cuts on the tailcatcher signal.	94
3.54	The beam-gas neutron energy spectrum corrected for the tail and uncorrected.	95
3.55	Layout of the finger counters and hodoscope planes in the front end of the FNC.	96
3.56	The FNC energy distribution for the finger events and the xy reconstructed impact point distribution on the FNC surface plane.	97
3.57	The x and y impact point distribution on the FNC surface.	97
3.58	The estimated position resolution σ versus the incident charged particle energy.	98
3.59	The Pompyt and Lepto generated neutron energy spectra for generated energies $E > 100 \text{ GeV}$, together with the effect of the FNC acceptance is shown.	99
3.60	The FNC neutron vertex and impact points are compared to Monte Carlo.	100
3.61	The FNC ($E > 400 \text{ GeV}$) acceptance as function of the position on the front face of the FNC.	101
3.62	The FNC acceptance as function of energy, scattering angle θ and P_T	101
4.1	The 1996 total integrated luminosity versus run number.	107
4.2	The kinematical (x_{BJ}, Q^2) plane for DIS events with a FNC neutron.	107
4.3	$E - P_z$ distribution.	108
4.4	The uncorrected ratio between FNC tagged and all DIS events for neutron energies of $E > 100 \text{ GeV}$ and $E > 400 \text{ GeV}$	110
4.5	Uncorrected ratio between FNC tagged and all DIS events for different energy bins, as function of Q^2	111
4.6	Uncorrected ratio between FNC tagged and all DIS events for different energy bins, as function of $\log_{10}(x_{BJ})$	112

4.7	Uncorrected ratio between FNC tagged and all DIS events for $E > 100 \text{ GeV}$, in three x_{BJ} bins, as function of Q^2 and vice versa.	113
4.8	Uncorrected ratios between FNC tagged and all DIS events as function of η_{max}	115
4.9	The observed η_{max} distributions for FNC tagged neutrons ($E > 100 \text{ GeV}$ and $E > 400 \text{ GeV}$) and all DIS events.	115
4.10	Shape comparison between the observed η_{max} distributions of FNC tagged DIS events and DIS events.	116
4.11	The observed hadronic final state invariant mass distributions for FNC tagged and for all DIS events.	116
4.12	The neutron energy spectrum for DIS events compared to Monte Carlo. . .	118
4.13	The observed neutron energy spectrum for beam-gas events compared to DIS events.	118
4.14	Neutron energy spectrum for different Q^2 and x_{BJ} bins.	119
4.15	Observed neutron energy spectrum for all FNC tagged DIS events and for only FNC tagged LRG events.	119
4.16	The observed $ t $, rapidity and p_T distributions are compared to Lepto and Pompyt Monte Carlos.	120
4.17	The observed p_T distribution in different neutron energy bins.	121
4.18	The observed $ t $ distribution in different neutron energy bins.	122
A.1	The Lepto neutron energy spectrum smeared by $\sigma(E)/E=25\%$ is compared to DIS data.	127
A.2	The Pompyt neutron energy spectrum smeared by $\sigma(E)/E=25\%$ is compared to data (beam-gas and DIS).	128

List of Tables

2.1	HERA design parameters.	11
3.1	Summary of the FNC basic properties and characteristics.	41
3.2	FNC trigger elements and subtriggers.	55
3.3	FNC data banks.	61
4.1	FNC uncorrected and corrected leading neutron ratios.	109
4.2	The total $ep \rightarrow e'nX$ cross sections.	123

Acknowledgements

First, I would like to acknowledge my advisor, Prof. Dr. Bogdan Povh, whom gave me the opportunity to work on this thesis within the H1 collaboration and the Max Planck Institute für Kernphysik of Heidelberg. I also thank him for his guidance, support and advice during the preparation of the thesis.

I thank Dr. Doug Jansen for reading the thesis and for giving valuable comments. I am also grateful for his guidance, especially during my initial working period on the FNC project.

I would like to remember and thank Dr. Ralf Todenhausen for the interesting discussions, particularly about the FNC calorimeter, during the time he belonged to the FNC group.

I also thank Dipl. Phys. Thomas Nunnemann for his very useful comments given after reading the draft of this thesis; and for his cooperation during the years of the thesis, from the period we spent together at CERN up to now.

I thank Dr. Leonid Lytkin for the useful discussions about FNC calorimeter and for his cooperation.

I am grateful to both Dr. Mathias Beck and Dr. Thomas Haller for their friendliness during the months we spent working together in 1995 at CERN (Geneva), for the modification and test of the calorimeter.

I would like to thank the H1 collaboration and DESY for participating in the experiment.

I thank Mrs. Claudia Schroeder, MPI-HD secretary, for her kindness and helpfulness during my stay in Heidelberg.

I wish to thank also Mrs. Hella Kleinebenne and Mrs. Hildegard Haertel, secretaries of H1, for their kindness during all the time I spent at DESY.

Finally, I would like also to thank Mr. Dieter Schaller, the German language teacher at the course for foreigners organized by Desy, who introduced me to the basics of the German language during the months I spent in Hamburg.